



Diese Dissertation haben begutachtet:

Prof. K. HELD

Prof. S. BIERMANN

DISSERTATION

Spectral Properties of Strongly Correlated Materials

ausgeführt zum Zwecke der Erlangung des akademischen Grades eines
Doktors der Naturwissenschaften
unter der Leitung von

Univ.-Prof. Dr. Karsten Held

E 138 – Institut für Festkörperphysik

sowie Mitbetreuung von

Prof. Dr. Giorgio Sangiovanni

Institut für Theoretische Physik und Astrophysik, Universität Würzburg

eingereicht an der Technischen Universität Wien,
Fakultät für Physik

von

Elias Assmann

Matrikelnummer: 0331122
Stiftingtalstraße 133/2, 8010 Graz

Graz, am 27. August 2015

Deutschsprachige Kurzfassung

Stark korrelierte Materialien sind solche, in denen die Abstoßung zwischen Elektronen nur unzureichend abgeschirmt ist. Dadurch entsteht eine Vielzahl bemerkenswerter Eigenschaften, als Beispiel sei die Hochtemperatur-Supraleitung genannt. Auf theoretischer Seite erfordern elektronische Korrelationen eine differenzierte Modellierung dieser Wechselwirkung, die über Standardmethoden wie semilokale Dichtefunktionaltheorie (DFT) hinausgeht. Daher verspricht ein verbessertes Verständnis solcher Materialien nicht nur ungeahnte technische Anwendungen; es zu erreichen ist auch eine der großen Aufgaben der zeitgenössischen Physik.

Die vorliegende Dissertation beschäftigt sich einerseits mit Methoden der theoretischen Festkörperphysik für stark korrelierte Materialien, insbesondere LDA+DMFT, die Verbindung von DFT mit dynamischer Molekularfeld-Theorie (DMFT). Als Brückenschlag zwischen diesen beiden Ansätzen muss eine minimale Basis aus lokalisierten Funktionen aufgestellt werden, was hier mithilfe maximal-lokalisierter Wannierfunktionen (MLWF) gelingt.

Es werden zwei Computerprogramme beschrieben, die Teilaufgaben des LDA+DMFT-Verfahrens übernehmen, und die im Rahmen der Dissertation weiterentwickelt und zur Veröffentlichung gebracht wurden:

- WIEN2WANNIER stellt eine Schnittstelle zwischen dem DFT-Paket WIEN2k und dem MLWF-Paket Wannier90 bereit.
- WOPTIC berechnet die optische Leitfähigkeit, die statische Leitfähigkeit, und den Seebeck-Koeffizienten aus einer LDA+DMFT-Rechnung. Da die Beiträge zu diesen Größen typischerweise innerhalb kleiner Teile der Brillouinzone lokalisiert sind, kommt eine adaptive k-Integration zum Einsatz.

Die genannten Methoden werden darüber hinaus auf oxidische Heterostrukturen angewandt, insbesondere auf $\text{LaVO}_3|\text{SrTiO}_3$, das ist eine dünne Schicht Lanthanvanadat auf einem Substrat aus Strontiumtitanat. Diese Heterostruktur wurde im Rahmen der vorliegenden Doktorarbeit zur Anwendung in hocheffizienten Solarzellen vorgeschlagen [Phys. Rev. Lett. 110, 078701], wozu es bereits erste experimentelle Resultate gibt [z.B. L. Wang *et al.*, Phys. Rev. Applied 3, 064015].

Abstract

In strongly correlated materials, the inter-electron repulsion is only weakly screened. This property yields a multitude of remarkable phenomena; high-temperature superconductivity, to name but one prominent example. On the theoretical side, electronic correlation necessitates a sophisticated description of the electron-electron interaction, above and beyond such standard methods as semilocal density-functional theory (DFT). Thus, an improved understanding of such materials not only promises novel applications and technologies, it also represents one of the big challenges in contemporary physics.

The present dissertation is concerned, on the one hand, with methods of theoretical solid state physics adapted to strongly correlated materials; in particular LDA+DMFT, the combination of DFT with dynamical mean-field theory (DMFT). To connect these two approaches, a minimal basis of localized functions must be constructed. In the present case, this is accomplished using maximally localized Wannier functions (MLWF).

In the course of this thesis, two computer codes have been improved and released to the scientific community, which perform parts of the LDA+DMFT program:

- WIEN2WANNIER acts as an interface between the DFT package WIEN2k and the MLWF code Wannier90.
- WOPTIC computes the optical conductivity, dc conductivity, and thermopower from LDA+DMFT. Since the contributions to these quantities are often strongly localized in the Brillouin zone, an adaptive k-integration algorithm is used.

On the other hand, an application to oxide heterostructures is presented, in particular to $\text{LaVO}_3|\text{SrTiO}_3$, which is a thin film of lanthanum vanadate on a strontium titanate substrate. This heterostructure has been suggested as an absorber material for high-efficiency solar cells as part of the present thesis [Phys. Rev. Lett. 110, 078701]. Experimental results building on this proposal have already appeared [e.g. L. Wang *et al.*, Phys. Rev. Applied 3, 064015].

Introduction

The present thesis deals with methods of theoretical solid-state physics, with a focus on strongly correlated materials; and their application to a particular instance of such a material, the $\text{LaVO}_3|\text{SrTiO}_3$ heterostructure. Let us begin with a definition of these terms.

Solid-state physics, or the more general term *condensed-matter physics*, is the physics of the everyday, in a sense. We human beings, and the objects that we interact with, are (mostly) condensed matter: solid or liquid. Even so, theories that could describe the “internals” of these objects only came within reach in the twentieth century. The idea of “atoms” is an old one [Ber11; Wik15a], but what binds them together? And, given such a cohesive force, what keeps them from collapsing into one place? Satisfactory answers to these questions had to await the discovery of quantum mechanics and the Pauli principle [Mes15].

What do we mean by *strong correlations*, then? The advent of quantum mechanics and a better understanding of atoms made it possible to construct a very simple model of a solid, where electrons are considered to be completely independent, that is, uncorrelated. This means that the electric interaction between electrons is neglected (the electrons’ negative charge is considered to be “canceled out” by the ions’ positive charge). Obviously, this is an oversimplification; the interaction energy between electrons at points \mathbf{r}' and \mathbf{r}'' , to a good approximation given by Coulomb’s law (in natural units)

$$V(|\mathbf{r}' - \mathbf{r}''|) = \frac{1}{|\mathbf{r}' - \mathbf{r}''|}, \quad (1)$$

depends strongly on the distance and is not small compared to other relevant energy scales. If we simply neglect it, we have no right to expect sensible predictions. Yet, for many materials and observables, this model works surprisingly well.

The secret ingredients are the Pauli principle, which strongly reduces the phase space of possible electron–electron scattering, and *screening*. That is,

each electron's charge is screened by a cloud of other electrons, and when this screening is effective, the independent electron model works well. On the other hand, strongly correlated materials may be characterized as those where this mechanism is not effective enough for such a simple description. Understanding strongly correlated materials is one of the big challenges of contemporary physics. Since they exhibit a wide range of unusual phenomena, a better understanding also promises important technological applications. Perhaps the most iconic example are high-temperature superconductors and the dream of room-temperature superconductivity. In the example studied here, high-efficiency solar cells provide the motivation.

Oxide heterostructures are artificial materials pieced together from different bulk materials composed of oxygen anions and metal cations. They have been at the focus of much attention in the past years because the combination of materials may give rise to new phenomena, which are not present in any of the constituents. The classical example is the emergence of a conducting layer at the interface of two insulators [OH04; Oht+02]. There is also a large space of possible heterostructures to explore, because the manufacturing processes (typically, pulsed laser deposition or molecular beam epitaxy) are extremely flexible. Theoretical insight on which heterostructures are most promising is therefore in high demand.

To conclude these introductory notes, let us return to the big picture. For decades now, we have had a complete knowledge of the fundamental laws underlying condensed-matter physics and everyday phenomena more generally [Car10]. But that does not mean that we *understand* these phenomena in any meaningful sense, a realization epitomized in a classic essay by Anderson [And72]. The ideas and methods adequate for describing a single electron bound to a nucleus become hopelessly insufficient when we turn to the multitude of electrons in a solid. At the same time, new laws often “emerge” from the apparent chaos, and they may be quite robust with respect to the details of the underlying system [Lau05]. This turns out to be a pervasive concept in modern science.

On the large scale, it is at work where chemistry emerges from physics, and biology from chemistry and physics, and so on — not too long ago, the notion of deriving chemical laws from physical ones would have seemed far fetched. On a smaller scale, the Hubbard model emerges from the band structure of strongly correlated materials. In each case, it is quite possible to work on the “higher-level” system without considering the details of the

levels “below”. Indeed, to make progress, we would do well to discover the “fundamental laws” of the abstracted system and study their implications, in much the same way as we study the “more fundamental” laws underlying them.

Outline

The present thesis is divided into three main parts. First, Chapters 1 to 4 introduce the computational techniques to be used thereafter: *Density-functional theory* (DFT) provides the basis, in this work and in much of solid-state theory, on top of which more sophisticated theories are built if required. The *maximally localized Wannier function* (MLWF) formalism provides the transition to localized orbitals. While DFT for crystalline materials is most naturally formulated in terms of delocalized basis states, a localized basis is often necessary for a better treatment of electronic correlations. This is because correlated electrons are relatively localized and may be adequately described in terms of local physics. Conversely, localized states are what gives practical DFT the most trouble. The correlation effects are described by dynamical mean-field theory (DMFT) in the Wannier basis, or rather, its combination with DFT, LDA+DMFT.

The purpose of these chapters is to give a brief outline of each subject and establish a notational basis for the chapters to follow. For a more detailed introduction, the interested reader is referred to the excellent literature covering each of these methods. For instance, Pavarini et al. [Pav+11] compile introductory lecture notes to all mentioned topics, freely available for download. Capelle [Cap06] and Kohn [Koh99] give accessible concise introductions to DFT, while Jones and Gunnarsson [JG89] contribute a scholarly review, albeit somewhat dated. Marzari et al. [Mar+12] provide a review of MLWF and their applications. Georges et al. [Geo+96] review DMFT for model systems; Held [Hel07] and Kotliar et al. [Kot+06] the application to LDA+DMFT. Georges [Geo04] supplies lecture notes on the latter.

Second, Chapters 5 and 6 focus on computer codes developed in the framework of this thesis. Two preexisting scientific program packages have been revised and expanded, namely: WIEN2WANNIER [Kun+10; Wis12], an interface between WIEN2k [Bla+01] and Wannier90 [Mos+08a]; and WOPTIC [Ass+15; Wis12], which calculates optical conductivities and transport properties from

LDA+DMFT. These chapters give a description of WIEN2WANNIER and WOPTIC with an emphasis on the new contributions made in the present thesis. Both packages are free software [FSF] and available at <http://www.ifp.tuwien.ac.at/forschung/arbeitsgruppen/cms/software-download/>. But note that they are mostly useful in conjunction with WIEN2k, which is not free.

Third, in Chapter 7, several of the above-mentioned methods are applied to the correlated oxide heterostructure $\text{LaVO}_3|\text{SrTiO}_3$, in particular: DFT and semilocal DFT augmented by a Hubbard- U term in mean-field approximation (LDA+ U) in the implementation of WIEN2k; MLWF with WIEN2WANNIER and Wannier90; and LDA+DMFT using the w2dynamics package [Par+12]. This chapter expands on [Ass+13], a first publication of the present Ph.D. work, but focuses on new results.

Finally, in App. A the WIEN2WANNIER and WOPTIC user's guides are reproduced, and in App. B, the journal articles published in the course of the present thesis.

Contents

Introduction	vii
Acronyms and mathematical symbols	xvii
I. Theoretical background	
1. Density-functional theory	3
1.1. The Hohenberg-Kohn theorem	3
1.2. The Kohn-Sham equations	5
1.3. Local approximations to V_{xc}	7
2. Wien2k and the APW basis set	9
3. Maximally localized Wannier functions	13
3.1. Disentanglement	15
3.2. Wannier interpolation	17
4. Augmenting DFT with explicit Coulomb interaction	19
4.1. Static correlations: LDA+U	21
4.2. Dynamical correlations: LDA+DMFT	22
4.2.1. Dynamical mean-field theory	22
4.2.2. CTQMC as an impurity solver	25
4.2.3. Interfacing DMFT to LDA	26
4.2.4. LDA+DMFT charge self-consistency	27

II. Software Development

5. Wien2Wannier: MLWF from Wien2k	33
5.1. Arbitrary orientation of initial projections	34
5.2. Discussion and outlook	36
6. Woptic: optical conductivity with MLWF	39
6.1. Strontium vanadate, testbed material	40
6.2. Computing the integrand	42
6.2.1. Wannier-interpolating the momentum matrix elements	45
6.2.2. Interpolating the mixed momentum matrix elements .	48
6.2.3. Interpolation and disentanglement	52
6.3. Numerical results for the optical conductivity	56
6.3.1. Noninteracting models	57
6.3.2. Interacting models	61
6.4. Discussion and outlook	66

III. Results on Correlated Heterostructures

7. The $\text{LaVO}_3 \text{SrTiO}_3$ heterostructure	71
7.1. Bulk SrTiO_3 and LaVO_3	73
7.2. Models and methods	75
7.3. Structural relaxation and DFT results for $\text{LaVO}_3 \text{SrTiO}_3$	77
7.4. LDA+DMFT results for $\text{LaVO}_3 \text{SrTiO}_3$	81
7.4.1. An elementary heterostructure	81
7.4.2. A more realistic model	83
7.5. Discussion and outlook	84

Conclusion	87
-------------------	-----------

Appendix

A. Software documentation	91
A.1. WIEN2WANNIER user's guide	93
A.2. WOPTIC user's guide	115
B. Reproduced journal articles	137
B.1. woptic: optical conductivity with Wannier functions	139
B.2. Cubic interaction parameters for t_{2g} Wannier orbitals	153
B.3. Unfolding the band structure of disordered solids	161
B.4. Oxide Heterostructures for Efficient Solar Cells	169
References	177
Acknowledgements	191
Vita	193

List of Figures

4.1.	DFT and DMFT self-consistency flowcharts	27
4.2.	A metaphor for LDA+DMFT charge self-consistency	29
6.1.	Crystal structure of SrVO ₃	40
6.2.	Bandstructure and density of states of SrVO ₃	41
6.3.	Comparison of Wannier band structures for SrVO ₃	42
6.4.	Exponential decay of the Wannier momentum matrix elements	46
6.5.	Imaginariness of the Wannier momentum matrix elements	47
6.6.	Momentum matrix elements compared to Peierls approximation	47
6.7.	Decay of the mixed matrix elements $ W_{uv}^{\alpha\alpha}(\mathbf{R}, \omega = -2 \text{ eV}) $	49
6.8.	Realness of the mixed matrix elements $ W_{uv}^{\alpha\alpha}(\mathbf{R}, \omega = -2 \text{ eV}) $	50
6.9.	Decay of the mixed matrix elements $ W_{uv}^{\alpha\neq\beta}(\mathbf{R}, \omega = -2 \text{ eV}) $	51
6.10.	Decay of the mixed matrix elements $ W_{uv}^{\alpha\alpha}(\mathbf{R}, \omega = -4.5 \text{ eV}) $	52
6.11.	Noninteracting optical conductivity from different algorithms	58
6.12.	Optical conductivity with and without disentanglement	58
6.13.	Contributions to the noninteracting optical conductivity	60
6.14.	Self-energy of SrVO ₃ from a 3-band DMFT calculation	61
6.15.	Interacting optical conductivity with 3 WF	62
6.16.	Contributions to the interacting optical conductivity	63
6.17.	Interacting optical conductivity with 14 WF	65
6.18.	Interacting 14-WF optical conductivity using the original $\mathcal{U}(\mathbf{k})$	65
7.1.	Crystal structures of SrTiO ₃ and LaVO ₃	74
7.2.	Rotation and tilt of the VO ₆ octahedra in bulk LaVO ₃	74
7.3.	Density of states of bulk LaVO ₃ in LDA+U	75
7.4.	Relaxed 4 6×2-p,o (AF) and 4 4×2-o (PM) structures	78
7.5.	In-plane M-O-M bond angles in LaVO ₃ SrTiO ₃	79
7.6.	M-M layer distances in LaVO ₃ SrTiO ₃	79

7.7.	Density of states of $4 6\times 2$ $\text{LaVO}_3 \text{SrTiO}_3$ in LDA+U	80
7.8.	The $1 1\times 1$ -p heterostructure	81
7.9.	Spectral function of the $1 1\times 1$ -p heterostructure	82
7.10.	LDA+DMFT d occupation of Ti and V in the $4 4\times 2$ -o heterostructure	82
7.11.	Spectral functions and orbital order in the $4 4\times 2$ -o heterostructure	84

Acronyms and mathematical symbols

A	spectral function (matrix)
a_0	the Bohr radius, $a_0 \approx 52.9 \times 10^{-12}$ m
AF	antiferromagnetic
AF-C	C-type antiferromagnetic (“checkerboard”) order
AF-G	G-type antiferromagnetic order (staggered in all directions)
AIM	Anderson impurity model
APW	augmented plane wave
APW+lo	augmented plane waves + local orbitals
β	inverse temperature, $\beta = 1/T$ (Boltzmann’s constant set to 1)
BZ	Brillouin zone
CLDA	constrained LDA
CRPA	constrained random-phase approximation
CTQMC	continuous-time quantum Monte Carlo [Gul+11]
DC	double-counting correction
DFT	density-functional theory
DMFT	dynamical mean-field theory
DOS	density of states
ϵ_0	the vacuum permittivity, $\epsilon_0 = 8.854 \dots \text{pF m}^{-1}$ in the international system of units (SI)
FLL	(double counting correction in the) fully-localized limit
$F[\phi]$	$F : (\mathbb{R}^3 \rightarrow \mathbb{C}) \rightarrow \mathbb{C}$, $\phi \mapsto F[\phi]$ is a functional

$\delta F[\phi]/\delta\phi(\mathbf{r})$	a functional derivative
$F[\phi](\mathbf{r})$	$F : (\mathbb{R}^3 \rightarrow \mathbb{C}) \times \mathbb{R}^3 \rightarrow \mathbb{C}$, $(\phi, \mathbf{r}) \mapsto F[\phi](\mathbf{r})$ is given as a functional of ϕ at every \mathbf{r}
G	a Green function (matrix)
GGA	generalized gradient approximation
HK	Hohenberg-Kohn (theorem)
$i\omega_\nu$	Matsubara frequencies; the discrete imaginary frequencies obtained at finite temperature by Fourier transforming the (bounded) imaginary time [Wik15b]
KS	Kohn-Sham (equations, state)
LAPW	linearized augmented plane wave
LDA	local-density approximation
LDA+DMFT	combination of semilocal DFT with DMFT
LDA+U	semilocal DFT augmented by a Hubbard- U term in mean-field approximation
LO	local orbital to supplement LAPW
lo	another type of local orbital
MAXENT	maximum-entropy method of analytic continuation [JG96; Sang8]
MLWF	maximally localized Wannier function
MT	muffin tin (sphere, radius)
OBC	open boundary conditions
PBC	periodic boundary conditions
PBE	Perdew-Burke-Ernzerhof density functional [PBE96]
PBESOL	revised PBE density functional [Per+08]

PM	paramagnetic
PV	photovoltaic
QE	the Quantum ESPRESSO DFT code [Gia+09]
QMC	quantum Monte Carlo
R^{MT}	muffin-tin radius
$R^{\text{MT}} \cdot K_{\text{max}}$	or “RK-max”, a measure for the quality of an APW basis set
τ	imaginary time, $\tau = it$, obtained by a “Wick rotation” in the complex time plane [NO98, Sec. 2.2]
τ	the circle constant: ratio of the circumference of a circle to its radius (in legacy notation, $\tau = 2\pi$) [Har10; Palo1]; for an opposing viewpoint see [MSC11]
TDDFT	time-dependent density-functional theory
$\mathcal{U}(\mathbf{k})$	the unitary matrices taking the Kohn-Sham gauge to the Bloch gauge in maximally localized Wannier function (MLWF)
$\mathcal{V}(\mathbf{k})$	the rectangular matrices selecting the optimal subspaces in disentanglement
WC	Wu-Cohen density functional [wco6]
WF	Wannier function
Y_{ℓ}^m	spherical harmonic of degree (angular quantum number) ℓ and order (magnetic quantum number) m

Part I.

Theoretical background

1. Density-functional theory

The prototypical problem in theoretical solid-state physics is to find solutions

$$\hat{H}\Psi(\mathbf{r}_1, \dots, \mathbf{r}_N) = E\Psi(\mathbf{r}_1, \dots, \mathbf{r}_N) \quad (1.1)$$

to a Hamiltonian of the form

$$\hat{H} = \sum_i \left\{ -\frac{1}{2}\nabla_i^2 - \sum_\alpha \frac{Z_\alpha}{|\hat{\mathbf{r}}_i - \mathbf{R}_\alpha|} \right\} + \frac{1}{2} \sum_{i \neq j} \frac{1}{|\hat{\mathbf{r}}_i - \hat{\mathbf{r}}_j|} \quad (1.2)$$

where i, j enumerate the electrons in a solid, and α labels the ions, with positions \mathbf{R}_α and charges Z_α . As usual, we will use the Born-Oppenheimer approximation and take the \mathbf{R}_α to be fixed, leaving the positions \mathbf{r}_i of the electrons as dynamic variables. To avoid clutter, we use natural units, setting the electron's mass and charge, the reduced Planck constant, the appropriate multiple of the vacuum permittivity, and (when the need arises) Boltzmann's constant to unity: $m_e = e = \hbar = 2\tau \varepsilon_0 = k_B = 1$. Here and throughout, the upright τ denotes the circle constant, i.e. the circumference of the unit circle [Har10; Pal01].

Density-functional theory (DFT) amounts to a reformulation of (1.1) which replaces the many-body wave function Ψ as the basic variable by the electron density

$$\begin{aligned} n(\mathbf{r}) &= \langle \Psi | \sum_i \delta(\mathbf{r}_i - \mathbf{r}) | \Psi \rangle \\ &= N \int d\mathbf{r}_2 \cdots d\mathbf{r}_N \Psi^*(\mathbf{r}, \mathbf{r}_2, \dots, \mathbf{r}_N) \Psi(\mathbf{r}, \mathbf{r}_2, \dots, \mathbf{r}_N). \end{aligned} \quad (1.3)$$

1.1. The Hohenberg-Kohn theorem

Let us split \hat{H} into the kinetic part \hat{T} , the potential \hat{V} , and the electron-electron interaction \hat{U} :

$$\hat{H} = \hat{T} + \hat{V} + \hat{U}. \quad (1.4)$$

We see that \hat{T} and \hat{U} are “universal”; all the specifics of the material are contained in $\hat{V} = \sum_i V(\hat{\mathbf{r}}_i)$, i.e. given by the ionic lattice $\{(Z_\alpha, \mathbf{R}_\alpha)\}$. Consider now the ground state Ψ_0 , and in particular its electronic density n_0 . These objects follow from the Hamiltonian. Since the Hamiltonian in turn is fully specified by the external potential V , we can view the ground state density n_0 as a functional of the potential: $n_0 = n_0[V]$; the basis of DFT is the inversion of this relation, given by the Hohenberg-Kohn (HK) theorem [HK64; Lev79].

That is to say, HK guarantees that, given the ground-state density of a system of interacting electrons in an unknown external potential V , that potential is uniquely determined: $V = V[n_0]$. As we have seen, this suffices to determine the Hamiltonian—at least in principle, it is enough to give either the potential V or the ground-state density n_0 in order to specify the Hamiltonian (1.2). In this sense we can view the ground state as a functional $\Psi_0[n_0]$ of its density, and write the ground-state energy as

$$E_0 = \langle \Psi_0[n_0] | \hat{T} + \hat{U} + \hat{V} | \Psi_0[n_0] \rangle. \quad (1.5)$$

Let us generalize this relation to an energy functional of an arbitrary density n

$$\begin{aligned} E_V[n] &:= \langle \Psi_0[n] | \hat{T} + \hat{U} + \hat{V} | \Psi_0[n] \rangle \\ &= F[n] + \int d\mathbf{r} V(\mathbf{r})n(\mathbf{r}) \end{aligned} \quad (1.6)$$

where

$$F[n] := \langle \Psi_0[n] | \hat{T} + \hat{U} | \Psi_0[n] \rangle \quad (1.7)$$

is the universal part of the *ground-state* energy associated with n . Note in the latter definition we made a representability assumption: in order to write $\Psi_0[n]$ for an arbitrary electron density n , we have to assume that some potential $V[n]$ exists which yields n as a ground-state density. This condition is called *v-representability*.

It can be shown that a variational principle for n exists [HK64] in analogy to the Rayleigh-Ritz variational principle for wave function. Namely, E_V takes its minimum at the true ground-state density,

$$E_V[n] > E_0 = E_V[n_0] \quad \text{when } n \neq n_0. \quad (1.8)$$

1.2. The Kohn-Sham equations

It is difficult to work with the variational principle (1.8) directly in terms of the density because we do not know how to evaluate the energy functional $F[n]$. In order to exploit (1.8), we will rewrite it in terms of auxiliary orbitals, the Kohn-Sham (KS) states [KS65].*

We begin by rearranging the energy functional (1.6) as

$$E_V[n] = \tilde{T}[n] + \int d\mathbf{r} V_H[n](\mathbf{r}) n(\mathbf{r}) + \int d\mathbf{r} V(\mathbf{r})n(\mathbf{r}) + E_{xc}[n], \quad (1.9)$$

where the first term,

$$\tilde{T}[n] := \langle \Psi_0[n] | \hat{T} | \Psi_0[n] \rangle, \quad (1.10)$$

is the ground-state kinetic energy of a fictitious system of noninteracting electrons with density $n(\mathbf{r})$; the second term is the *Hartree* (mean-field) part of the interaction,

$$V_H[n](\mathbf{r}) = \frac{1}{2} \int d\mathbf{r}' \frac{n(\mathbf{r}')}{|\mathbf{r} - \mathbf{r}'|}; \quad (1.11)$$

the third term is the external potential; and the last term is “all the rest”, the *exchange-correlation energy* $E_{xc}[n]$, which is defined by (1.9). To introduce this new unknown will be useful to the extent that \tilde{T} and V_H , which can be computed exactly, are reasonable approximations for the interacting system, and E_{xc} itself is comparatively small.

Applying a variational principle leads to a Euler-Lagrange equation of the form

$$\left\{ \frac{\delta}{\delta n(\mathbf{r})} \tilde{T} + V(\mathbf{r}) + \int d\mathbf{r}' \frac{n(\mathbf{r}')}{|\mathbf{r}' - \mathbf{r}|} + V_{xc}[n](\mathbf{r}) - \varepsilon \right\} \delta n(\mathbf{r}) = 0 \quad (1.12)$$

with the *exchange-correlation potential*, defined as the functional derivative of E_{xc} ,

$$V_{xc}[n](\mathbf{r}) := \frac{\delta E_{xc}[n]}{\delta n(\mathbf{r})}, \quad (1.13)$$

* The alternative, *orbital-free density-functional theory*, is practiced mainly as an approach to large-scale systems. The main difficulty is the evaluation of the kinetic energy from the density alone [LC05].

and Lagrange multipliers ε to constrain the particle number.

We see that (1.13) is identical to the Euler-Lagrange equation of a non-interacting electron gas in an *effective external potential* V_{eff} composed of the physical external potential, the Hartree part of the interaction, and the exchange-correlation potential:

$$V_{\text{eff}}[n](\mathbf{r}) = V(\mathbf{r}) + \int d\mathbf{r}' \frac{n(\mathbf{r}')}{|\mathbf{r}' - \mathbf{r}|} + V_{\text{xc}}[n](\mathbf{r}). \quad (1.14)$$

By this analogy, the variational problem (1.12) can be solved using an ansatz

$$n(\mathbf{r}) = n[\{\psi\}](\mathbf{r}) = \sum_i \psi_i^*(\mathbf{r})\psi_i(\mathbf{r}) \quad (1.15)$$

where the ψ_i are solutions of the *Kohn-Sham Hamiltonian*,

$$\hat{H}_{\text{KS}} \psi_i(\mathbf{r}) = \varepsilon_i \psi_i(\mathbf{r}) \quad \text{with} \quad (1.16)$$

$$\hat{H}_{\text{KS}} = -\frac{1}{2}\nabla^2 + V_{\text{eff}}[n](\mathbf{r}). \quad (1.17)$$

The corresponding total energy can be written

$$E_{\text{KS}} = E_V[n] = \sum_i \varepsilon_i + E_{\text{xc}} - \int d\mathbf{r} V_{\text{xc}}[n](\mathbf{r}) n(\mathbf{r}) - \frac{1}{2} \int d\mathbf{r}' d\mathbf{r}'' \frac{n(\mathbf{r}')n(\mathbf{r}'')}{|\mathbf{r}' - \mathbf{r}''|}. \quad (1.18)$$

This is the KS formulation of DFT. The structure of these equations is quite similar to the Hartree formalism: the “single-particle energies” ε_i are Lagrange multipliers that enforce the correct particle number, and the effective potential depends on the solutions ψ_i , so that the equations have to be solved “self-consistently” (in practice, iteratively). This self-consistency cycle is summarized in Fig. 4.1 (left).

V_{eff} inherits the periodicity of the lattice from the original problem (1.2). Therefore, after a Fourier transformation, we can solve (1.16) separately for each reciprocal vector $\mathbf{k} \in \text{BZ}$ (restricted to the first Brillouin zone), and choose solutions in the form of Bloch waves

$$\psi_i(\mathbf{r}) = \psi_{nk}(\mathbf{r}) = e^{i\mathbf{k}\mathbf{r}} u_{nk}(\mathbf{r}) \quad (1.19)$$

composed of a plane wave e^{ikr} and a lattice-periodic part u_{nk} , with eigenvalues

$$\varepsilon_n(\mathbf{k}). \quad (1.20)$$

It should be noted that the ψ_{nk} and ε_{nk} are, in the first instance, mathematical constructs without physical meaning, except for the relations given by (1.18) and (1.15), and the fact that the highest occupied ε_N gives the ionization energy [AB85].

In practice, the $(\varepsilon_{nk}, \psi_{nk})$ are habitually interpreted as the quasi-particle band structure of the Hamiltonian (1.2); and often, they do provide a good approximation. The most important mode of failure of this interpretation is the *band-gap problem* in insulators: if the difference between the highest occupied $\varepsilon := \varepsilon_N$ and lowest unoccupied eigenvalue $\underline{\varepsilon}$ is taken as the band gap, its value is systematically too small (this is called the “HOMO-LUMO gap”, corresponding to the highest occupied and lowest unoccupied molecular orbitals).

Even so, the wave functions ψ_{nk} are often in good agreement with more sophisticated calculations [GSS88], and, all things considered, the band structure interpretation is a good approximation for many materials. It is also indispensable for many of the common applications of DFT (such as computing optical spectra, where the band-gap problem can be alleviated in an ad-hoc manner using a *scissors operator*, i.e. rigidly shifting conduction states up in energy).

1.3. Local approximations to the exchange-correlation potential

What have we accomplished so far? We started with the eigenproblem (1.1), which is difficult because the wave function $\psi : \mathbb{R}^{3N} \rightarrow \mathbb{C}$ must describe a huge number N of electrons. Using HK, we were able to change variables from the wave function to the density $n : \mathbb{R}^3 \rightarrow \mathbb{R}$. This alone may be regarded as a significant simplification. Thereupon, KS provided a convenient variational ansatz (1.15), together with an appealing interpretation in terms of an effective single-particle model (1.16).

This transformation is exact, but it required us to introduce the unknown exchange-correlation potential V_{xc} . In fact, after removing all the “easy” parts

of the problem (i.e. the external potential, the Hartree potential, and the noninteracting kinetic energy), V_{xc} is left with all the “hard” parts. The last step to make DFT practical, then, is to find a good approximation to V_{xc} .

It can be shown [KM98] that the exchange-correlation energy, which so far was a completely general functional of the electron density n , can be written as an integral over n and an exchange-correlation energy density $e_{\text{xc}}[n]$,

$$E_{\text{xc}}[n] = \int d\mathbf{r} n(\mathbf{r}) e_{\text{xc}}[n](\mathbf{r}). \quad (1.21)$$

The simplest non-trivial approximation to this form is to suppose that $e_{\text{xc}}[n](\mathbf{r}) \leftarrow e_{\text{xc}}^{\text{LDA}}(n(\mathbf{r}))$ depends only on the value of the density at point \mathbf{r} , and hence

$$E_{\text{xc}}^{\text{LDA}}[n] = \int d\mathbf{r} n(\mathbf{r}) e_{\text{xc}}^{\text{LDA}}(n(\mathbf{r})), \quad (1.22)$$

with $e_{\text{xc}}^{\text{LDA}}$ taken from the homogeneous electron gas at density n . This is the *local-density approximation* (LDA) [KS65]. Despite its simplicity, it has proven to be “remarkably serviceable” [Koh99] and enjoys continued use.

Nonetheless, many more sophisticated approximations have been constructed. In a classic article, Perdew and Schmidt classify the various types of approximations on a hierarchy they call “Jacob’s ladder of density functional approximations”, leading from the “Hartree World” to “Chemical Accuracy” [PS01]. On this ladder, LDA is the lowest rung. To climb another rung, we use the density gradient in addition to the density itself to parametrize $e_{\text{xc}}[n](\mathbf{r}) \leftarrow e_{\text{xc}}(n(\mathbf{r}), \nabla n(\mathbf{r}))$. This type of functional is called *generalized gradient approximation* (GGA). While the LDA is uniquely defined by the simple prescription given above, there are many different GGAs, each with its own strengths and weaknesses. Of these, the Perdew-Burke-Ernzerhof (PBE) functional [PBE96] is perhaps the most widely known and applied. New GGAs continue to appear. For instance, the revised PBE (rPBE) [Per+08] and Wu-Cohen (WC) [WCO6] functionals are geared specifically towards a good description of solids. For guidance along the rest of the way to DFT heaven, the interested reader is referred to the relevant literature.

2. Wien2k and the APW basis set

An important distinguishing feature of practical DFT implementations is the basis set in which the KS states (1.16) are expanded. The WIEN2k code [Bla+01] employed in the present work uses a basis of the *augmented plane wave* (APW) type. This section provides a brief description of the WIEN2k basis set [largely based on Coto2].

What makes a good basis set? Ideally, (1) we should be able to reproduce the ψ_{nk} with sufficient accuracy using only a “small” number of basis states, and (2) the basis states should be “simple” in that matrix elements and scalar products are easy to evaluate. APW emphasize the first point, a pure plane wave basis the second. Excellent DFT codes exist using a variety of different basis sets, but the choice of basis does have important consequences; for instance, plane waves are associated with pseudopotentials whereas linearized augmented plane waves (LAPW) lend themselves to a full-potential approach as implemented in WIEN2k.

In APW-type basis sets, criterion (1) above is achieved by combining plane waves

$$e^{i\mathbf{g}\cdot\mathbf{r}} \quad (2.1)$$

with the solutions of the Schrödinger equation for a free atom

$$u_\ell(\rho; E) Y_\ell^m(\hat{\rho}). \quad (2.2)$$

Here, $\boldsymbol{\rho} := \mathbf{r} - \mathbf{R}_\alpha$ is the position relative to the nucleus, $\rho := |\boldsymbol{\rho}|$ is its length, $\hat{\boldsymbol{\rho}} := \boldsymbol{\rho}/\rho$ its direction and Y_ℓ^m is the spherical harmonic function of angular quantum number ℓ and magnetic quantum number m . The rationale is that, near the nuclei at \mathbf{R}_α , the ψ_{nk} will be similar to atomic states, and the u_ℓ will make for an efficient basis; far away, they will be similar to free-electron states, i.e. plane waves.

Therefore we partition the unit cell into “*muffin-tin*” (MT) spheres S_α of radius R_α^{MT} , centered around each nucleus α ; and the *interstitial region* \mathcal{I} , i.e.

2. Wien2k and the APW basis set

the remaining space. In the interstitial, we will use plane waves (2.1) as basis states; within the spheres, we would like to use the atomic states (2.2), linked by a boundary condition to ensure continuity on the sphere boundary $\partial\mathcal{S}_\alpha$. This is the original APW basis [Sla37].

Note that we need the atomic solution only in the MT sphere. Thus the usual boundary condition at $\rho \rightarrow \infty$ is replaced with the continuity condition and the energy is not quantized. To indicate this, we wrote the energy dependence in (2.2) with a continuous energy E instead of a quantum number n . But which value should E take? To get a good basis, it should be close to the relevant ks eigenvalue ε_{nk} . Since this energy is unknown at the beginning, the basis has to be determined in an inner self-consistency cycle during each iteration of the DFT cycle. To avoid this complication, the energy dependence of the APW is usually linearized.

Using the energy derivative $\dot{u} := \partial u / \partial E$, we write a *linearized augmented plane wave* [And75; KA75] as

$$\phi_{\mathbf{K}}^k(\mathbf{r}) = \begin{cases} \sum_{\ell m} \{ A_{\ell m}^{\alpha g} u_{\ell}^{\alpha}(\rho; E_0^{\alpha \ell}) + B_{\ell m}^{\alpha g} \dot{u}_{\ell}^{\alpha}(\rho; E_0^{\alpha \ell}) \} Y_{\ell}^m(\hat{\rho}) & \mathbf{r} \in \mathcal{S}_{\alpha}, \\ 1/\sqrt{V_{\text{uc}}} e^{i\mathbf{g}\mathbf{r}} & \mathbf{r} \in \mathcal{I}. \end{cases} \quad (2.3)$$

At the risk of overloading the notation, we have written out the dependencies of the various terms on position $(\mathbf{r}, \rho, \hat{\rho})$, the reciprocal lattice vector \mathbf{K} , $\mathbf{k} \in \text{BZ}$, atoms α , and quantum numbers ℓ, m in full. The notation “ $\phi_{\mathbf{K}}^k$ ” is meant to indicate that the basis used to expand ψ_{nk} depends on k , and its members are enumerated by \mathbf{K} . The sum in principle runs over all quantum numbers ℓ, m ; in practice, it is truncated by imposing an appropriate ℓ_{max} . The coefficients A and B are fixed by continuity in value and slope on $\partial\mathcal{S}_{\alpha}$. Furthermore, V_{uc} is the unit cell volume, E_0 is a suitable linearization energy, and $\mathbf{g} := \mathbf{K} + \mathbf{k}$.

An alternative APW linearization scheme is given by combining the APW at a linearization energy $E_0^{\alpha \ell}$

$$\phi_{\mathbf{K}}^k(\mathbf{r}) = \begin{cases} \sum_{\ell m} C_{\ell m}^{\alpha g} u_{\ell}^{\alpha}(\rho; E_0^{\alpha \ell}) Y_{\ell}^m(\hat{\rho}), & \mathbf{r} \in \mathcal{S}_{\alpha} \\ 1/\sqrt{V_{\text{uc}}} e^{i\mathbf{g}\mathbf{r}} & \mathbf{r} \in \mathcal{I}; \end{cases} \quad (2.4a)$$

with *local orbitals* (lo) on each atom α ,

$$\phi_{\ell m}^{\text{lo}\alpha}(\mathbf{r}) = \begin{cases} \{A_{\ell m}^{\alpha} u_{\ell}^{\alpha}(\rho; E_0^{\alpha\ell}) + B_{\ell m}^{\alpha} \dot{u}_{\ell}^{\alpha}(\rho; E_0^{\alpha\ell})\} Y_{\ell}^m(\hat{\rho}) & \mathbf{r} \in \mathcal{S}_{\alpha}, \\ 0 & \mathbf{r} \notin \mathcal{S}_{\alpha}, \end{cases} \quad (2.4\text{b})$$

whose coefficients A and B (independent from those in (2.3)) are determined by normalization and $\phi^{\text{lo}}|_{\partial\mathcal{S}_{\alpha}} = 0$. This is the APW+lo basis [Mad+01; SNS00].

To further increase the flexibility of the basis, it is advantageous in certain cases to add another type of *local orbitals* (LO)

$$\phi_{\ell m}^{\text{LO}\alpha}(\mathbf{r}) = \begin{cases} \{A_{\ell m}^{\alpha} u_{\ell}^{\alpha}(\rho; E_0^{\alpha\ell}) + B_{\ell m}^{\alpha} \dot{u}_{\ell}^{\alpha}(\rho; E_0^{\alpha\ell}) + C_{\ell m}^{\alpha} u_{\ell}^{\alpha}(\rho; \tilde{E}_0^{\alpha\ell})\} Y_{\ell}^m(\hat{\rho}) & \mathbf{r} \in \mathcal{S}_{\alpha}, \\ 0 & \mathbf{r} \notin \mathcal{S}_{\alpha} \end{cases} \quad (2.5)$$

for some atoms α and orbitals ℓ , at a different linearization energy $\tilde{E}_0^{\alpha\ell}$. The additional coefficients C are used to ensure that ϕ^{LO} has vanishing derivative as well as value on $\partial\mathcal{S}_{\alpha}$.

In WIEN2k, LAPW (2.3), APW+lo (2.4), and LO (2.5) states are combined in order to construct an efficient basis for the case at hand. Specifically, for each atom α and angular quantum number ℓ , either LAPW or APW+lo is chosen, and may be supplemented by LO as needed.

The *muffin-tin radii* R_{α}^{MT} are important parameters for an APW-based calculation—in particular, the product of the smallest radius and the plane-wave cutoff, $R^{\text{MT}} \cdot K_{\text{max}}$, gives a good dimensionless measure of the completeness of the basis employed.

3. Maximally localized Wannier functions

The Bloch waves of (1.19) are in a sense the natural basis in a crystal; they are eigenstates of the Hamiltonian and at the same time exploit the translational symmetry of the lattice. But by their nature they extend throughout the whole crystal, whereas for many applications (e.g. LDA+DMFT, see Chapter 4) a basis of localized functions is preferable. Wannier functions (WF) provide a natural way to obtain such a localized basis.

To construct these, we Fourier transform the reciprocal vectors $\mathbf{k} \in \text{BZ}$ indexing the Bloch waves to lattice vectors \mathbf{R} ,

$$|\mathbf{w} \mathbf{R}\rangle := \frac{V_{\text{uc}}}{\tau^3} \int_{\text{BZ}} d\mathbf{k} e^{-i\mathbf{k}\mathbf{R}} |\psi \mathbf{k}\rangle. \quad (3.1)$$

This is the Wannier construction [Wan37] in its most basic form; note that the transformation is in the index rather than the argument of $\psi_{\mathbf{k}}(\mathbf{r})$ —in accordance with the lattice periodicity, $\mathbf{k} \in \text{BZ}$ is transformed to a direct lattice vector \mathbf{R} .

But $\psi_{\mathbf{k}}$, which we defined as the solution of an eigenproblem, has an undefined phase $\varphi(\mathbf{k})$. For a single wave function, a global phase factor $\psi \rightarrow e^{i\varphi}\psi$ may be unimportant, but in (3.1),

$$\frac{V_{\text{uc}}}{\tau^3} \int_{\text{BZ}} d\mathbf{k} e^{-i\mathbf{k}\mathbf{R}} |\psi \mathbf{k}\rangle \rightarrow \frac{V_{\text{uc}}}{\tau^3} \int_{\text{BZ}} d\mathbf{k} e^{-i(\mathbf{k}\mathbf{R} - \varphi(\mathbf{k}))} |\psi \mathbf{k}\rangle \quad (3.2)$$

can have important consequences for the shape and localization of $|\mathbf{w} \mathbf{R}\rangle$. To use WF in practice, we must resolve this ambiguity.

But first, (3.1) is a transformation from one band $\psi_{\mathbf{k}}$ to one WF $w_{\mathbf{R}}$; in the more general case where we want to transform J bands $\psi_{m\mathbf{k}}$ into J WF $w_{n\mathbf{R}}$,

3. Maximally localized Wannier functions

the phase factor $e^{i\varphi(\mathbf{k})}$ must be generalized to a unitary $J \times J$ matrix $\mathcal{U}(\mathbf{k})$:

$$|\mathbf{w} \ n\mathbf{R}\rangle := \frac{V_{\text{uc}}}{\tau^3} \int_{\text{BZ}} d\mathbf{k} e^{-i\mathbf{k}\mathbf{R}} \sum_{m=1}^J |\psi \ m\mathbf{k}\rangle \mathcal{U}_{mn}(\mathbf{k}). \quad (3.3)$$

In Marzari and Vanderbilt's *maximally localized Wannier function* (MLWF) formalism [MV97], the $\mathcal{U}(\mathbf{k})$ (in other words, the *Wannier gauge*) are fixed by taking the *spread functional* of the wF

$$\Omega := \sum_n \left[\langle \mathbf{w} \ n\mathbf{0} | \hat{r}^2 | \mathbf{w} \ n\mathbf{0} \rangle - |\langle \mathbf{w} \ n\mathbf{0} | \hat{r} | \mathbf{w} \ n\mathbf{0} \rangle|^2 \right] \quad (3.4)$$

to its minimum. In the rest of this section, we will briefly sketch this procedure and the corresponding formalism. For details, see the original literature [MV97; SMV01] or the review [Mar+12].

The spread functional Ω can be written as the sum of two contributions,

$$\Omega[\mathcal{U}] =: \Omega_I + \tilde{\Omega}[\mathcal{U}], \quad (3.5)$$

each of which is positive definite, but of which only

$$\tilde{\Omega} = \sum_{nm\mathbf{R}}^{Rm \neq 0n} |\langle \mathbf{w} \ Rm | \hat{r} | \mathbf{w} \ 0n \rangle|^2 \quad (3.6)$$

depends on $\mathcal{U}(\mathbf{k})$, whereas

$$\Omega_I = \sum_n \left[\langle \mathbf{w} \ 0n | \hat{r}^2 | \mathbf{w} \ 0n \rangle - \sum_{Rm} |\langle \mathbf{w} \ Rm | \hat{r} | \mathbf{w} \ 0n \rangle|^2 \right] \quad (3.7)$$

is *gauge invariant*.

By a Fourier transformation, \hat{r} in the matrix elements translates to $\nabla_{\mathbf{k}_i}$; going to a discrete \mathbf{k} -mesh and applying a finite-difference formula, it can be shown [MV97] that all the information about the Bloch states needed to calculate the spread is a set of *overlap matrices*

$$M_{mn}^{kb} := \langle \mathbf{u} \ nk | \mathbf{u} \ n(\mathbf{k} + \mathbf{b}) \rangle \quad (3.8)$$

where $|\mathbf{u} \ nk\rangle$ is the lattice periodic part of the Bloch states (1.19), \mathbf{k} labels a uniform Monkhorst-Pack mesh of the BZ [MP76], and \mathbf{b} points to one of a set of suitably chosen neighbors of \mathbf{k} on the finite mesh (we will briefly discuss

the choice of neighbors at the end of Sec. 6.2.3; for details see [mv97, App. B] and [Mos+08b, Sec. 3.2]).

Using these matrices, the $\mathcal{U}(\mathbf{k})$ can be determined by minimization of $\tilde{\Omega}$ (3.6). The de facto standard program used to perform this optimization is Wannier90 [Mos+08b; Wan], which uses a conjugate gradient/steepest descent algorithm.

Since we are facing a complicated many-dimensional optimization problem, it comes as no surprise that local minima can be problematic. Therefore, to guide the algorithm, Wannier90 accepts as a secondary input *initial projections*

$$A_{mn}^k := \langle \psi \, m\mathbf{k} | f_n \rangle, \quad (3.9)$$

where f_n is a suitable function which must be chosen for the case at hand [e.g., it might be an atomic xy wave function centered on an atom α , $f_n(\mathbf{r}) = u_2^\alpha(\rho)Y_{xy}(\hat{\rho})$].

A judicious choice of initial projections together with an orthonormalization step is often sufficient to achieve a good set of wf without an explicit minimization of the $\mathcal{U}(\mathbf{k})$. This observation is the basis of the *projector wf* approach [Ani+05; Ku+02], which may be viewed as an alternative to MLWF.

3.1. Disentanglement

Eq. (3.3) defines a unitary transformation from J states $|\psi \, n\mathbf{k}\rangle$ to J other states $|\mathbf{w} \, m\mathbf{R}\rangle$; so far, we have tacitly assumed the $|\psi \, n\mathbf{k}\rangle$ are the Bloch waves, and that it is obvious which of them should be included in the transformation. In practice, this means that an isolated set of bands (i.e. separated at every \mathbf{k} by finite gaps from all other bands) is being transformed—the occupied bands of an insulator constitute an important example.

If the target bands are crossed or touched by other, extraneous bands in some region of the BZ, the unwanted bands must be projected out before applying (3.3). In such a case the bands are said to be “entangled”, and the *disentanglement* procedure [SMV01] provides a systematic way of constructing J states for (3.3). At the same time, it minimizes the gauge independent part Ω_I (3.7) of the spread. By construction, such a transformation cannot be unitary (or even invertible) anymore.

To construct J wf, we now allow the number $\mathcal{J}_k \geq J$ of bands to be different at different k-points, and we introduce $\mathcal{J}_k \times J$ matrices $\mathcal{V}(\mathbf{k})$ to

3. Maximally localized Wannier functions

select a subspace of functions

$$|\tilde{\psi} n\mathbf{k}\rangle = \sum_{m=1}^{\mathcal{J}_k} |\psi m\mathbf{k}\rangle \mathcal{V}_{mn}(\mathbf{k}) \quad (3.10)$$

to which the transformation (3.3) will apply; in other words,

$$|w n\mathbf{R}\rangle = \frac{V_{\text{uc}}}{\tau^3} \int_{\text{BZ}} d\mathbf{k} e^{-i\mathbf{k}\mathbf{R}} \sum_{lm}^J |\psi l\mathbf{k}\rangle \mathcal{V}_{lm}(\mathbf{k}) \mathcal{U}_{mn}(\mathbf{k}). \quad (3.11)$$

The $\mathcal{V}(\mathbf{k})$ must be “rectangular unitary” in the sense that

$$\mathcal{V}^+(\mathbf{k})\mathcal{V}(\mathbf{k}) = \mathbb{1}_{J \times J} \quad (3.12)$$

to keep the $\tilde{\psi}$ orthonormal. They are found by minimizing Ω_I : Instead of (3.5), we now view the spread as a functional of both \mathcal{U} and \mathcal{V} ,

$$\Omega[\mathcal{U}, \mathcal{V}] = \Omega_I[\mathcal{V}] + \tilde{\Omega}[\mathcal{U}], \quad (3.13)$$

and minimize first Ω_I by varying \mathcal{V} , then $\tilde{\Omega}$ by varying \mathcal{U} . Strictly speaking, this procedure is not equivalent to minimizing Ω on the combined space of \mathcal{U} and \mathcal{V} ; however, since Ω_I is usually the greater contribution by far, we may expect to get close to the global minimum, and practical experience confirms this [SMVO1].

In a sense, it is redundant to have both \mathcal{V} and \mathcal{U} , since the latter could be subsumed in $\mathcal{V}'(\mathbf{k}) = \mathcal{V}(\mathbf{k})\mathcal{U}(\mathbf{k})$. Geometrically, the columns of $\mathcal{V}(\mathbf{k})$ give a basis of the optimal subspace, and $\mathcal{U}(\mathbf{k})$ rotates to the MLWF basis. But Ω_I is independent of the choice of basis; just as well, $\mathcal{V}(\mathbf{k})$ could specify the MLWF basis directly. Instead, the differentiation between \mathcal{V} and \mathcal{U} is given by the prescription of successive optimization.

Intuitively, what do we expect of \mathcal{U} and \mathcal{V} ? To have Fourier transforms $|w n\mathbf{R}\rangle$ that are well localized in \mathbf{R} , the states in the “Wannier gauge” should be smooth functions of \mathbf{k} . The role of \mathcal{U} and \mathcal{V} is thus to transform the $|\psi n\mathbf{k}\rangle$, with arbitrary \mathbf{k} -dependence, to functions

$$|w n\mathbf{k}\rangle := \sum_{lm} |\psi l\mathbf{k}\rangle \mathcal{V}_{lm}(\mathbf{k}) \mathcal{U}_{mn}(\mathbf{k}) \quad (3.14)$$

which vary smoothly with \mathbf{k} .

The rectangular $\mathcal{V}(\mathbf{k})$ can be seen to select an “optimally smooth subspace” (3.10) within which $\mathcal{U}(\mathbf{k})$ picks the smoothest gauge (3.14). More formally, it can be shown that on a discrete \mathbf{k} -mesh with $N_{\mathbf{k}}$ points, (3.7) can be written as [SMV01]

$$\Omega_I = \frac{1}{N_{\mathbf{k}}} \sum_{\mathbf{k}\mathbf{b}} g_{\mathbf{b}} \operatorname{tr} P_{\mathbf{k}}(1 - P_{\mathbf{k}+\mathbf{b}}), \quad (3.15)$$

where $g_{\mathbf{b}}$ is a weight factor and $P_{\mathbf{k}} = \sum_{n=1}^J |\tilde{\mathbf{u}} n\mathbf{k}\rangle \langle \tilde{\mathbf{u}} n\mathbf{k}|$ is the projector onto the optimal subspace at \mathbf{k} . ($P_{\mathbf{k}}$ is gauge invariant.) In this sense, Ω_I is given by the mismatch of subspaces between neighboring \mathbf{k} -points \mathbf{k} and $\mathbf{k} + \mathbf{b}$.

Using (3.15), it can be shown that the stationarity condition for Ω_I is equivalent to a set of eigenproblems [SMV01, cf. Sec. 6.2.3]; because they couple neighboring \mathbf{k} -points, they have to be solved iteratively until self-consistency is reached. This is how Wannier90 implements disentanglement [Mos+08b].

3.2. Wannier interpolation

One application which directly takes advantage of the localization of the $\mathbf{w}_{\mathbf{F}}$, and which will become important in later chapters, is interpolation in \mathbf{k} [cf. Mar+12; Yat+07].

Assume that we are interested a quantity $O_{mn}(\mathbf{k}) = \langle \psi n\mathbf{k} | \hat{O} | \psi m\mathbf{k} \rangle$, given in terms of the matrix elements of some operator \hat{O} which are known on a coarse \mathbf{k} -mesh \mathcal{K} . To interpolate O_{mn} to an arbitrary \mathbf{k} -point \mathbf{q} , we first transform it to the Wannier gauge and Fourier transform to \mathbf{R} , yielding

$$\begin{aligned} O_{uv}^{\mathbf{w}}(\mathbf{R}) &= \frac{1}{|\mathcal{K}|} \sum_{\mathbf{k} \in \mathcal{K}} e^{-i\mathbf{k}\mathbf{R}} \sum_{mn} \mathcal{U}_{um}^+(\mathbf{k}) O_{mn}(\mathbf{k}) \mathcal{U}_{nv}(\mathbf{k}) \\ &= \langle \mathbf{w} u\mathbf{0} | \hat{O} | \mathbf{w} v\mathbf{R} \rangle. \end{aligned} \quad (3.16)$$

Here, \mathbf{R} is a lattice vector in the (small) supercell \mathcal{K}^* corresponding to the (coarse) \mathbf{k} -mesh \mathcal{K} . Since $O_{uv}^{\mathbf{w}}(\mathbf{R})$ is a matrix element between MLWF, it will decay quickly (normally exponentially) in $|\mathbf{R}|$. Therefore, we can inverse Fourier transform to a finer \mathbf{k} -mesh \mathcal{Q} based only on the smaller supercell \mathcal{K}^* , rather than the larger \mathcal{Q}^* which ordinarily corresponds to \mathcal{Q} :

$$O^{\mathbf{w}}(\mathbf{q}) = \frac{1}{|\mathcal{K}^*|} \sum_{\mathbf{R} \in \mathcal{K}^*} e^{i\mathbf{R}\mathbf{q}} O^{\mathbf{w}}(\mathbf{R}); \quad (3.17)$$

3. Maximally localized Wannier functions

The terms with $\mathbf{R} \in \mathcal{Q}^* \setminus \mathcal{K}^*$ can be left out because O^w is small there.

This interpolation technique can be viewed as a generalization of the tight-binding idea, where the eigenvalues of the Hamiltonian can be calculated on arbitrary \mathbf{k} -points by including only a small number of real-space hoppings of sufficiently localized orbitals [sk54].

4. Augmenting DFT with explicit Coulomb interaction

LDA, GGA, and related approximations give a good description of a wide range of materials, but for many strongly correlated systems, they fail. These failures manifest in qualitatively wrong ground states (e.g., a nonmagnetic metal instead of an antiferromagnetic insulator), severely underestimated magnetic moments, and similar problems.

Generically, these approximate functionals work well as long as the electrons are delocalized and their interactions are strongly screened. Conversely, when they become problematic, it is often in the presence of localized orbitals, where screening is weaker. (Recalling that they are based on the homogeneous or slowly varying electron gas, this should not be surprising.)

From this point of view, it seems natural to try to improve the description of strongly correlated materials by adding the “missing” interaction of the localized states explicitly to the potential. In this section and the next, we will discuss two schemes which do this with varying levels of sophistication: semilocal DFT augmented by a Hubbard- U term in mean-field approximation (LDA+ U) and combination of semilocal DFT with DMFT (LDA+DMFT). Their common starting point is a multiband *Hubbard model* with a Hamiltonian

$$\hat{H}_U = \sum_{\substack{\alpha\beta ij \\ \sigma}} t_{ij}^{\alpha\beta} c_{\alpha i \sigma}^+ c_{\beta j \sigma} + \frac{1}{2} \sum_{\substack{\alpha ijkl \\ \sigma\sigma'}} U_{ijkl} c_{\alpha i \sigma}^+ c_{\alpha j \sigma'}^+ c_{\alpha k \sigma'} c_{\alpha l \sigma} \quad (4.1)$$

where α, β enumerate lattice sites; i, j, k, l orbitals on site α ; σ, σ' spin directions; and c^+ and c are creation and annihilation operators. The hopping parameters t will be formally defined in (4.21). First, let us focus on the interaction U .

Two delicate issues are implicit in this ansatz. First, we must choose a single-particle basis for (4.1). Adding a Hubbard interaction will be appropriate and necessary only for a subset of the single-particle states in a given system;

4. Augmenting DFT with explicit Coulomb interaction

specifying those states is an important step. The remaining states, it is supposed, are adequately described in LDA (here and below, we will use “LDA” as a shorthand for any similar approximation). Second, since we consider only site-local interactions U_{ijkl} , we must suppose that the “target” orbitals are indeed well localized, and that intersite interactions are satisfactorily accounted for by the Hartree term (1.11). (It is the leading contribution in $1/z$, where z is the coordination number [Mül89].)

In practical calculations, the full generality of the on-site interaction term in (4.1) is normally limited by symmetry or approximation. A common form is the *Kanamori interaction* [Kan63]

$$\frac{1}{2}U \sum_{i\sigma} \hat{n}_{i\sigma} \hat{n}_{i\bar{\sigma}} + \frac{1}{2}U' \sum_{\substack{i \neq j \\ \sigma \sigma'}} \hat{n}_{i\sigma} \hat{n}_{j\sigma'} - \frac{1}{2}J \sum_{\substack{i \neq j \\ \sigma}} (\hat{n}_{i\sigma} \hat{n}_{j\sigma} + c_{i\sigma}^+ c_{i\bar{\sigma}} c_{j\bar{\sigma}}^+ c_{j\sigma} + c_{i\sigma}^+ c_{i\bar{\sigma}}^+ c_{j\sigma} c_{j\bar{\sigma}}) \quad (4.2)$$

with three independent parameters: intra- and interorbital repulsion $U := U_{iiii}$ and $U' := U_{ijji}$, and Hund’s rule coupling $J = U_{ijij} = U_{iijj}$. This parametrization assumes that the orbitals are independent of spin; for the last equality to hold, they must also be real-valued. In (4.2) the site index has been suppressed and $\bar{\sigma} := -\sigma$. Often, this is further reduced to two just parameters using the relation

$$U = U' + 2J, \quad (4.3)$$

which is exact for t_{2g} orbitals in spherical symmetry (as in a free atom) See [Rib+14], reproduced in App. B.2, for more about the symmetries and approximations that lead to (4.3).

Let us mention two problems inherent in this approach. Perhaps the most fundamental is the *double-counting problem*: some part of the interaction is already contained in V_{xc} at the LDA level and should be subtracted from (4.1) so that it will not be counted twice. This *double-counting correction* (DC) takes the form of an additional term

$$- \sum_i \Delta \varepsilon_i \hat{n}_i \quad (4.4)$$

in (4.1). The problem is that the DC values $\Delta \varepsilon_i$ are not known exactly, since the exchange-correlation potential is a rather opaque object, and it is difficult

to determine which part of (4.1) is contained in a particular approximation. One frequently used for of DC is the *fully-localized limit* (FLL) [Ani+93] where the correction to the total energy reads

$$E_{\text{DC}} = \frac{1}{2}\bar{U}N(N-1) + \frac{1}{4}\bar{J}N(N-2), \quad (4.5)$$

with spherically averaged interaction parameters \bar{U} and \bar{J} and the total number of electrons N to which the Hubbard interaction is applied.

Second, to construct the basis orbitals for the model (4.1) we must select a “correlated” subset of states, which is to some degree arbitrary. In more complicated cases, constructing the basis can also be technically difficult. Once the orbitals are constructed, the hopping t is easily derived from them (4.21), but the interaction U less straightforward. This is because the “bare” interaction $\langle \psi_i \psi_j | 1/\hat{r} | \psi_k \psi_l \rangle$ is inappropriate; the interaction as screened by the “uncorrelated” states (i.e., those not appearing in (4.1)) must be used instead. There are schemes to calculate U from LDA (notably *constrained* LDA (CLDA) [AG91; CG05; KKV12] and *constrained random-phase approximation* (CRPA) [Ary+04; IM10; Nom+12]), but in many calculations, it is treated as a phenomenological parameter.

One may find these ambiguities aesthetically unappealing (they represent a step away from the “ab initio” ideal), but the approach has proven useful for the description of strongly correlated materials.

4.1. Static correlations: LDA+U

The idea behind the LDA+U method [AAL97; AZA91] is to apply a mean-field approximation

$$\langle \hat{n} \hat{n}' \rangle = \langle \hat{n} \rangle \langle \hat{n}' \rangle + \langle (\hat{n} - \langle \hat{n} \rangle) (\hat{n}' - \langle \hat{n}' \rangle) \rangle \approx \langle \hat{n} \rangle \langle \hat{n}' \rangle \quad (4.6)$$

to the extra interaction in Hamiltonian (4.2). In conjunction with this, the Hamiltonian is normally simplified beyond (4.2): the spin-flip and pair-hopping terms are neglected, and only one “effective U ” and an “effective J ” are used, or even just a single repulsion \bar{U} . Including $U = U'$ and J , as originally proposed [AZA91], the LDA+U interaction energy reads (with $n_{i\sigma}^\alpha := \langle \hat{n} \rangle$, and reinstating the site indices)

$$E_U = \frac{1}{2}U \sum_{\alpha i \sigma} n_{i\sigma}^\alpha n_{i\bar{\sigma}}^\alpha + \frac{1}{2}U \sum_{\substack{\alpha i \neq j \\ \sigma \sigma'}} n_{i\sigma}^\alpha n_{j\sigma'}^\alpha - \frac{1}{2}J \sum_{\substack{\alpha i \neq j \\ \sigma}} n_{i\sigma}^\alpha n_{j\sigma}^\alpha. \quad (4.7)$$

Using this expression, the LDA+U total energy is written as

$$E_{\text{LDA+U}} = E_{\text{LDA}}[n] + E_U[\{n_{i\sigma}^\alpha\}] - E_{\text{DC}}[\{n_{i\sigma}^\alpha\}] \quad (4.8)$$

where E_{LDA} is the LDA energy (1.18).

Since $E_{\text{LDA+U}}$ depends on the orbital occupations rather than just the total density, it leads to an *orbital-dependent effective potential* $V_{\text{eff}}^{\alpha i\sigma}(\mathbf{r}) = \delta E / \delta n_{i\sigma}^\alpha(\mathbf{r})$ (i.e., this is not strictly density-functional theory anymore).

In practical LDA+U calculations, the states i, j are usually chosen in terms of ℓ -subshells of certain atoms (e.g., the V-d states). To give precise meaning to this definition, the projection on the ℓ states must be made in some region around the nucleus where the states are supposed to be similar enough to a free atom for this division to make sense. In an APW framework, this will be the MT sphere.

What effect relative to LDA can we expect from the added Hubbard term? The orbital energies $\varepsilon_{i\sigma}^\alpha = \partial E / \partial n_{i\sigma}^\alpha$ afford some insight. With the FLL DC (4.5) term,

$$\varepsilon_{i\sigma}^\alpha - \varepsilon_{i\sigma}^{\alpha(\text{LDA})} = (U - J)(1/2 - n_{i\sigma}^\alpha) - \frac{1}{2}J(N_\sigma - N_{-\sigma}). \quad (4.9)$$

We see that “empty” ($n < 1/2$) states will be pushed further down in energy, while “filled” ($n > 1/2$) states will be pushed up, creating a gap of order U .

4.2. Dynamical correlations: LDA+DMFT

To go beyond the simple mean-field treatment of LDA+U, we may turn to *dynamical mean-field theory* (DMFT) [Geo+96; GK92; MV89], an approach which has become known as LDA+DMFT. In this section, we will provide an outline of DMFT before we see how it connects to DFT.

4.2.1. Dynamical mean-field theory

Dyson's equation,

$$G^{-1}(\mathbf{k}, \omega) = G_0^{-1}(\mathbf{k}, \omega) - \Sigma(\mathbf{k}, \omega), \quad (4.10)$$

links the self-energy Σ to the full (G) and the noninteracting (G_0) Green functions. It can be viewed as a definition of Σ [see e.g. NO98, Secs. 2.4 and

5.3]. In multiorbital models, G , G_0 , and Σ are complex-valued matrices. The *Green function* is defined as the propagator

$$G_{ij}(t, t') := -i \langle \mathcal{T} c_i(t) c_j^+(t') \rangle \quad (4.11)$$

using the *time-ordering operator*

$$\mathcal{T} c_i(t) c_j^+(t') = \begin{cases} c_i(t) c_j^+(t') & t > t' \\ -c_j^+(t') c_i(t) & t < t' \end{cases}. \quad (4.12)$$

In DMFT, Σ is taken to be \mathbf{k} -independent,

$$\Sigma(\mathbf{k}, \omega) \leftarrow \Sigma(\omega), \quad (4.13)$$

or, equivalently, local in direct space. In terms of Feynman diagrams, this means that only purely local irreducible diagrams are included in the summation for Σ . In this sense, local (“temporal”) correlations are included while non-local correlations are treated on the mean-field level; hence the name *dynamical mean-field theory*.^{*} Thus, for example, DMFT yields mean-field critical exponents [Roh+11], and becomes exact in the limit of “infinite dimensions”, or more properly, diverging coordination number $z \rightarrow \infty$, provided the proper scaling for the hopping amplitudes, $t \leftarrow t/\sqrt{z}$, is imposed.

The self-energy generated by this prescription turns out to be identical to that of an *Anderson impurity model* (AIM) with the same interaction as the original model [GK92]. That is to say, \hat{H}_U (4.1) is mapped to

$$\begin{aligned} \hat{H}_{\text{AIM}} = & \sum_{ki\sigma} \epsilon_i(\mathbf{k}) a_{ki\sigma}^+ a_{ki\sigma} + \sum_{kij\sigma} [V_{ij}(\mathbf{k}) a_{ki\sigma}^+ c_{j\sigma} + V_{ij}^*(\mathbf{k}) c_{j\sigma}^+ a_{ki\sigma}] \\ & + \frac{1}{2} \sum_{\substack{ijkl \\ \sigma\sigma'}} U_{ijkl} c_{i\sigma}^+ c_{j\sigma'}^+ c_{k\sigma'} c_{l\sigma} \quad (4.14) \end{aligned}$$

with additional parameters to be determined self-consistently in conjunction with (4.16).

^{*} Including non-local corrections on top of DMFT leads to methods such as cluster DMFT [Kot+01; LK00] or dynamical cluster approximation [Het+98], often grouped as “cluster extensions” of DMFT [for a review see Mai+05]; or to “diagrammatic extensions” such as the dynamical vertex approximation [TKH07] and the dual fermion approach [RKLO8].

4. Augmenting DFT with explicit Coulomb interaction

The AIM describes electrons which interact on an impurity site (c, c^+), embedded in a “bath” of noninteracting electrons (a, a^+) with dispersion $\epsilon_i(\mathbf{k})$. Hopping between bath and impurity is governed by the *hybridization strengths* $V_{ij}(\mathbf{k})$. The ϵ and V are the parameters that must be adjusted to select that AIM which corresponds to the lattice model we started with. This correspondence is achieved when the AIM Green function \mathcal{G} equals the local part of the lattice Green function G ,

$$\mathcal{G}(\omega) = G_{\text{loc}}(\omega) := G^{aa}(\omega). \quad (4.15)$$

where G_{loc} is calculated by integrating Dyson’s equation (4.10) over $\mathbf{k} \in \text{BZ}$,

$$\begin{aligned} G_{\text{loc}}^{-1}(\omega) &= \frac{1}{N_k} \sum_{\mathbf{k}} [G_0^{-1}(\mathbf{k}, \omega) - \Sigma(\omega)] \\ &= \frac{1}{N_k} \sum_{\mathbf{k}} [\omega + \mu - H^w(\mathbf{k}) - \Sigma(\omega)], \end{aligned} \quad (4.16)$$

where μ is the chemical potential.

In the path integral formalism, the noninteracting electrons, which enter only quadratically in the AIM, can be integrated out. As a consequence, the dispersion and hybridization strengths can be subsumed in the *hybridization function* Δ [Hew97], which reads, in Matsubara frequencies $i\omega_\nu$,

$$\Delta_{ij}(i\omega_\nu) := \sum_{kl} \frac{V_{il}^+(\mathbf{k}) V_{lj}(\mathbf{k})}{i\omega_\nu + \mu - \epsilon_l(\mathbf{k})}. \quad (4.17)$$

In particular, the noninteracting Green function of the AIM can be written as

$$[\mathcal{G}_0(i\omega_\nu)]_{ij}^{-1} = i\omega_\nu + \mu - \Delta_{ij}(i\omega_\nu). \quad (4.18)$$

This expression can be inserted into (4.15), which we rewrite as

$$\mathcal{G}_0^{-1}(i\omega_\nu) = G_{\text{loc}}^{-1}(i\omega_\nu) + \Sigma(i\omega_\nu), \quad (4.19)$$

Eq. (4.19) is the DMFT *self-consistency condition*. To make the analogy to classical mean-field theory (e.g. for the Ising model) explicit, the local observable which should be reproduced by the single-site effective problem is the Green function (instead of the local magnetization), and the field which is adjusted

to achieve this is the hybridization function (instead of the average magnetization).

To see why (4.19) is called a self-consistency condition, observe that Σ is determined by \mathcal{G}_0 : By definition, Σ is the self-energy of (4.14), and \mathcal{G}_0 its noninteracting Green function. With the interaction fixed, \mathcal{G}_0 is sufficient to specify the model, and therefore also Σ . Thus, in practice DMFT is solved by iteration, starting with a trial self-energy (which may be $\Sigma^{(0)} = 0$) and continuing until a suitable convergence criterion is satisfied. This self-consistency cycle is summarized in Fig. 4.1 (right).

We have already remarked that DMFT becomes exact in the limit of infinite coordination $z \rightarrow \infty$ (as a mean-field approximation should). The same holds for the *non-interacting limit* $t/U \rightarrow \infty$, where $\Sigma = 0$; and the *atomic limit* $U/t \rightarrow \infty$, where $\Delta = 0$ [Geo04].

4.2.2. CTQMC as an impurity solver

The main workload in DMFT is in solving the impurity problem (4.14); in other words, mapping $\mathcal{G}_0^{(i)}$, as computed from (4.19) with the self-energy $\Sigma^{(i-1)}$ from the previous iteration, to the new self-energy $\Sigma^{(i)}$. This is a hard problem, especially so for the multiband models and complicated interactions that arise in LDA+DMFT, and different types of *impurity solvers* exist, with different advantages.

In the LDA+DMFT calculations presented in the present work, the hybridization-expansion continuous-time quantum Monte Carlo (CTQMC) algorithm [Gul+11] as implemented in the w2dynamics package [Par+12] has been used. The distinguishing feature of quantum Monte Carlo (QMC) algorithms in general is that they are free from systematic errors and in principle applicable to all input parameters of the model. Error estimates are available through statistical analysis.

For impurity models in particular, continuous-time QMC algorithms have become the standard method of solution.* In the hybridization-expansion algorithm, the hybridization term ($\sum V a^+ a$) is expanded in a perturbation

* For lattice models, discrete-time algorithms have remained the method of choice because of the unfavorable scaling $O(\beta^3)$ with inverse temperature of available continuous-time formulations, as compared to the linear scaling $O(\beta)$ of discrete-time determinant QMC [BSS81]. Recently, linear scaling has been reported for a continuous-time algorithm [IT15].

series, whose terms are summed to infinite order (at least in principle) by Monte Carlo. For a given order in the hybridization strength, the bath ($\sum \epsilon a^+ a$) and impurity ($\sum U c^+ c^+ c c$) terms of (4.14) are solved exactly.

Perhaps the main disadvantage of QMC methods is that they operate in imaginary time $\tau = it$. Frequency-dependent quantities, such as the *spectral function*

$$A(\omega) = \frac{i}{\tau}(G - G^+) \quad (4.20)$$

are therefore straightforwardly obtained only in terms of the Matsubara frequencies $i\omega_\nu$, and must be rotated back to real frequencies for interpretation. This *analytic continuation* is complicated by the fact that only a finite number of Matsubara frequencies is accessible numerically, and by the statistical QMC errors inherent in the measured quantities. It is usually performed using the maximum-entropy method (MAXENT) [JG96; Sang8].

4.2.3. Interfacing DMFT to LDA

The input needed by DMFT that should be derived from an LDA calculation is the hopping $t_{ij}^{\alpha\beta}$, and possibly the interaction U_{ijkl} and double-counting $\Delta\epsilon_i$ (if they are not treated as free parameters). The “hopping” (i.e. quadratic) term in fact contains the whole effective single-particle Hamiltonian \hat{H}_{KS} projected onto the DMFT subspace. Let us assume that this subspace is selected in terms of Wannier functions. Using translational symmetry, we can write

$$t_{ij}^{\alpha\beta} = \langle \text{w } \alpha i | \hat{H}_{\text{KS}} | \text{w } \beta j \rangle = H_{ij}^{\text{w}}(\mathbf{R}_\alpha - \mathbf{R}_\beta). \quad (4.21)$$

This matrix is provided by the Wannier projection. For DMFT, it is more natural to Fourier transform to \mathbf{k} ,

$$H_{ij}^{\text{w}}(\mathbf{k}) = t_{ij}^{\alpha\beta} e^{ik(\mathbf{R}_\alpha - \mathbf{R}_\beta)} = \sum_n \mathcal{U}_{in}^+(\mathbf{k}) \epsilon_n(\mathbf{k}) \mathcal{U}_{nj}(\mathbf{k}) \quad (4.22)$$

(the last equality holds for MLWF in the absence of disentanglement).

The flowcharts in Fig. 4.1 show simplified pictures of the LDA and DMFT self-consistency loops. The LDA+DMFT method can be seen as connecting the converged LDA calculation to the DMFT loop by means of a Wannier projection.

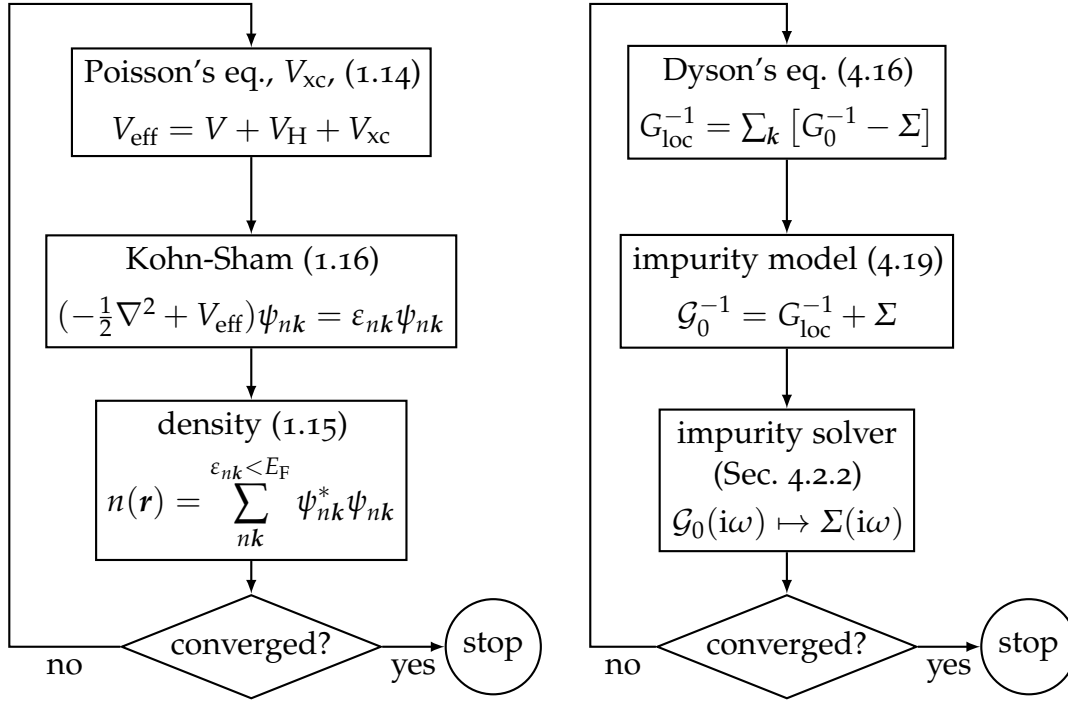


Figure 4.1.: The DFT and DMFT self-consistency cycles. In a “standard” LDA+DMFT calculation, the two are concatenated, with the input for the DMFT calculation derived from the LDA result. In charge self-consistent LDA+DMFT, the result of each DMFT iteration is fed back into the next LDA iteration in the form of a modified density.

4.2.4. LDA+DMFT charge self-consistency

When the DMFT loop is converged, the orbital occupations n_i will, in general, differ from the initial values; DMFT has produced a change $\Delta n(\mathbf{r})$ in density. But the LDA effective potential V_{eff} , which enters DMFT through the single-particle term $H^{\text{w}}(\mathbf{k})$, was determined with the LDA density—thus, density and potential will not be consistent anymore.

To address this inconsistency, we can feed the output density from DMFT back to the LDA cycle, in effect combining the two into one big loop (cf. Figs. 4.1 and 4.2). This procedure is known as *fully self-consistent* or *charge self-consistent* LDA+DMFT. Note that it is the *whole* LDA+DMFT loop which should be repeated until self-consistent, including the setup of the DMFT model (i.e., U and H^{w} have to be recomputed at every cycle).

The idea of charge self-consistency is quite natural in the LDA+DMFT frame-

work, and it goes back to the early days of the method. The first published LDA+DMFT results including charge self-consistency were for plutonium [SKA01]; two of the authors went on to provide a theoretical framework for the approach (“spectral-density functional theory”) [SK01; SK04]. Since then, while the “industry standard” is still one-shot LDA+DMFT, charge-self-consistent implementations have become more common [without claim to completeness: Ama+06; Ama12; Ani+05; APG11; Chi+03; Grå+12; HYK10; Min+05; Pou+07], recently especially so in the context of oxide heterostructures [LBG13; Lec+14; LO15].

Besides these practical implementations, the topic has received attention in various reviews [Hel+03; Hel07; Kot+06] and methodological papers (Lechermann et al. [Lec+06] in particular cover theory relevant for the MLWF approach).

The reason why charge-self-consistency is important for heterostructures in particular is their low crystal symmetry, which may lift orbital degeneracies present in the bulk (e.g. the t_{2g} orbitals in a cubic crystal). As long as the orbitals are degenerate, the charge density will remain unaffected by DMFT.

Another area where charge self-consistency can become important is the computation of LDA+DMFT total energies. In the portentous words of Savrasov and Kotliar [SK01]: “Within the DMFT technology, the implementation of this global loop is an essential new development of the present work which allows the determination of a central quantity of the solid—its total energy.”

This is because the changed density must in principle be taken into account in the LDA functional. Namely, the LDA+DMFT total energy at zero temperature is [Lec+06, Eq. (B5)]

$$E = E_{\text{LDA}}[n + \Delta n] - E_{\text{DC}}[\{n_{i\sigma}^{\alpha}\}] + \langle \hat{U} \rangle + \sum_{k ij\sigma\sigma'} H_{ij}^{\text{W}}(\mathbf{k}) [\langle c_{ki\sigma}^+ c_{kj\sigma'} \rangle - \langle c_{ki\sigma}^+ c_{kj\sigma'} \rangle_0], \quad (4.23)$$

where \hat{U} is the DMFT interaction, and $\langle \cdot \rangle$ and $\langle \cdot \rangle_0$ are the DMFT and LDA expectation values.

Nevertheless, in many cases it is possible to calculate meaningful LDA+DMFT energies without taking Δn into account: If the DMFT-induced density changes are sufficiently small, the change in E_{LDA} may be neglected. For instance, Held et al. [HMS01] successfully computed LDA+DMFT total energies for Ce without charge self-consistency.

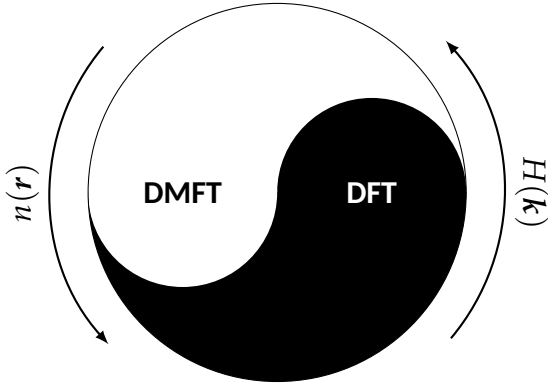


Figure 4.2.: DFT and DMFT intertwined in full self-consistency

The k -resolved change in electronic density may be computed as [Lec+06, Eq. (A6)]

$$\Delta n(\mathbf{k}) = \frac{1}{\beta} \sum_{\nu} G_0(\mathbf{k}, i\omega_{\nu}) (\Sigma(i\omega_{\nu}) - E_{\text{DC}}) G(\mathbf{k}, i\omega_{\nu}). \quad (4.24)$$

All quantities in this equation are matrices in spin-orbital space (e.g. in the Wannier basis). Note that due to the product of Green functions, the terms in this sum decay as $O(\omega^{-2})$ and no extra convergence factor is needed.

If $\Delta n(\mathbf{k})$ is given in the MLWF basis, the $\mathcal{U}(\mathbf{k})$ translate to the $\mathbf{k}\mathbf{s}$ basis (more precisely the subspace included in the MLWF construction) [Lec+06, Eq. (A9)],

$$\Delta n^{\mathbf{ks}}(\mathbf{k}) = \mathcal{U}(\mathbf{k}) \Delta n^{\mathbf{w}}(\mathbf{k}) \mathcal{U}^+(\mathbf{k}), \quad (4.25)$$

and expanding in basis functions gives the change of density in direct space [Lec+06, Eq. (A8)]

$$\Delta n(\mathbf{r}) = \sum_{k m n \sigma \sigma'} \psi_{mk}(\mathbf{r}) \Delta n_{mn}^{\mathbf{ks}}(\mathbf{k}) \psi_{nk}^*(\mathbf{r}). \quad (4.26)$$

Despite the efforts cited above, there have been few studies on the effects and practical importance of charge self-consistency. An exception is the observation by Aichhorn et al. [APG11] that self-consistency tends to reduce the difference between different DC schemes.

Part II.

Software Development

5. Wien2Wannier: MLWF from Wien2k

In Chapter 1 we discussed DFT in terms of delocalized Bloch waves $\psi_{nk}(\mathbf{r}) = e^{i\mathbf{k}\mathbf{r}}u_{nk}(\mathbf{r})$ (1.19), as implemented in the WIEN2k package [Bla+01]. In Chapter 3 we saw how these can be translated to localized orbitals $w_{n\mathbf{R}}(\mathbf{r}) = w_{n0}(\mathbf{r} - \mathbf{R})$ (3.3) using the MLWF approach; here, Wannier90 is the de facto standard implementation [Mos+08b]. In practice, there remains a gap to breach, namely computing the overlap matrices M_{mn} (3.8). Wannier90 supports this natively for the Quantum ESPRESSO (QE) code [Gia+09]. Separate interface programs exist for FLEUR [Fre+08], ABINIT [Gon+09], SIESTA [Kor+10], and VASP [Fra+12]. WIEN2WANNIER [Kun+10] implements such an interface to WIEN2k.

The difficulty of evaluating the overlap matrices depends in particular on the basis set in which the back-end code provides the Bloch waves. In a plane-wave basis (as used by QE), it is relatively straightforward to compute the matrix elements. In WIEN2k's LAPW basis (cf. Chapter 2) on the other hand, the task becomes more complex.*

Originally, WIEN2WANNIER was published as a separate package working together with WIEN2k. During the course of the present thesis, it has been integrated into the main WIEN2k distribution.† While the most computationally intensive parts of the package (i.e. the programs `w2w` and `wplot`) have changed only little in this process, much of the supporting code has been rewritten and extended. The package's release notes (in the file `NEWS`) give an overview of the changes from the user's perspective.

Perhaps the biggest single change is the implementation of initial projections with arbitrary rotations relative to the WIEN2k coordinate system. This procedure will be described in the following section. The functionality of

* The FLEUR interface also works in an LAPW basis.

† Corresponding to WIEN2WANNIER version numbers 0.96 to 1.0.2

all parts of the package is described in the WIEN2WANNIER's user's guide, which is reproduced in App. A.1. For details on the methods used in `w2w` and `wplot`, see the original publication [Kun+10].

5.1. Arbitrary orientation of initial projections

As we saw in Chapter 3, it is often necessary to guide the MLWF optimization by specifying initial projections $A_{mn}^k = \langle \psi_{mk} | f_n \rangle$ (3.9) in terms of well-chosen trial orbitals f_n . Even in cases where well-localized WF are found irrespectively of the choice of f_n , they may be useful. When several sets of maximally-localized WF exist (e.g. different spatial orientations, or atom-centered and bond-centered WF), a specific set may be chosen by specifying appropriate f_n .

Each trial orbital f_n is normally specified by (1) a center atom α and (2) the rotational part of the orbital in terms of spherical harmonics Y_ℓ^m . If we further restrict the f_n to the relevant MT sphere \mathcal{S}_α and disregard the radial part (both restrictions are usually harmless), it becomes easy to evaluate the initial projections in the LAPW basis. Since the basis functions inside \mathcal{S}_α are already proportional to spherical harmonics (cf. Eqs. (2.3) to (2.5)), the A_{mn} are simply given by a sum over the relevant coefficients [cf. Kun+10, Eqs. (6, 11, 12)]. This approach is robust, fast, and simple to implement, but leads to two noteworthy restrictions:

- (A) the spherical harmonics are oriented along the WIEN2k coordinate system, and
- (B) only trial orbitals centered on atoms are possible.

By contrast, Wannier90's native interface `pw2wannier90.x` to QE simply calculates $\psi_{nk}(\mathbf{r})$ and $f_n(\mathbf{r})$ on a set of points \mathbf{r} , and computes the projection numerically. * With this approach it is straightforward to locate trial orbitals anywhere in the unit cell as well as to rotate them away from the coordinate system used by the electronic structure code.

Restriction (A) can be relaxed while retaining the simple evaluation of A_{mn} in LAPW. In WIEN2WANNIER (specifically the program `write_inwf`), this is

* See the file `pw2wannier90.f90` included in Wannier90, in particular the subroutines `compute_amm()`, `y1m_expansion()`, `y1m_wannier()`, and `radialpart()`.

implemented using a method due to Romanowski and Krukowski [RK07]. Informally speaking, the $2\ell + 1$ functions Y_ℓ^m form a basis for the rotational part of the subspace with orbital momentum ℓ . Therefore, it is possible to expand any rotated $Y_\ell^m \circ R$ in the original Y_ℓ^m s. (Here, R is a rotation, represented by a 3×3 rotational matrix.)

In particular, if a rotational function with a well-defined angular quantum number ℓ is given as a linear combination

$$\Phi^{(\ell)} = \sum_m y_m Y_\ell^m \quad (5.1)$$

in the original coordinate system, and as

$$\Phi^{(\ell)} = \sum_m y'_m Y_\ell^m \circ R \quad (5.2)$$

in the rotated system; then there is a $(2\ell + 1) \times (2\ell + 1)$ matrix $\mathcal{R}_\ell(R)$ which maps the coefficients \mathbf{y} to \mathbf{y}' ,

$$\mathbf{y}' = \mathcal{R}_\ell \mathbf{y}, \quad (5.3)$$

and depends only on the axis and angle of rotation [RK07]. For $\ell = 0$ and 1, the relationship between R and \mathcal{R}_ℓ is trivial. In the first case, $\mathcal{R}_s = 1$ since $Y_s^0 = \text{const}$. In the latter case, if we choose the real spherical harmonics $\{Y_x, Y_y, Y_z\}$ as the basis corresponding to \mathbf{y} , we have $\mathcal{R}_p = R^{-1}$.

Romanowski and Krukowski extend this approach to the nontrivial cases $\ell = 2$ and 3, which is sufficient for our purposes. The resulting formulas for \mathcal{R}_ℓ are straightforward to implement but somewhat lengthy, and therefore not reproduced here.*

The initial projections in WIEN2WANNIER as calculated from the LAPW coefficients are relative to WIEN2k's *local* coordinate system, i.e. the *local rotation* matrices are in effect. This means that they can also be used to achieve a rotation. However, they cannot always be chosen freely; the "correct" local rotation matrices may be dictated by symmetry (cf. WIEN2k user's guide, App.A). Furthermore, after a change of local rotation matrices, the calculation must be reconverged. Therefore, it seems worthwhile to implement the rotations in the interface.

* For the sake of potential users of the method, an error in the original publication should be mentioned: In the matrix for $\ell = 2$, Eq. (35), columns 4 and 5 are interchanged [Fau+13].

5.2. Discussion and outlook

WIEN2WANNIER is a relatively mature package. It has found acceptance and application in the WIEN2k community, as evidenced by the citations to the original reference. It has been included in the main WIEN2k distribution since version 14.1 [BS14]. With BerryPI [Ahm+13], another WIEN2k module has been developed that builds upon WIEN2WANNIER. As of version 1.0 (corresponding to WIEN2k 14.2), the package can be considered more or less feature complete. That said, we conclude the chapter with some directions for future development of WIEN2WANNIER.

Parallelization The program `w2w` is at present not parallelized. A k-point-wise parallelization in a manner similar to WIEN2k should be straightforward to implement. (For the overlap matrices M_{mn}^{kb} it would in fact have to be a “k-b-wise” parallelization, but the principle remains the same.) It would be useful in particular for large WIEN2k calculations where only a few bands are included in the Wannier projection since `wannier90.x` is not parallelized and serial run times for `w2w` and `wannier90.x` are typically comparable.

A similar analysis applies to `wplot`. However, in this case a trivial parallelization is supported out of the box, namely to compute different WF in parallel. With a little care, it is also possible to partition the real-space grid and parallelize over the sub-grids; at the end, they have to be concatenated to get the WF on the whole grid.

Interstitial trial orbitals In some cases, there exist maximally localized sets of WF which are not centered on atoms; they might be centered between two atoms instead (“bond-centered”). Marzari et al. [Mar+12] give examples of both bond-centered (e.g. Si/GaAs, Fig. 2) and more general interstitial (e.g. Cu, Fig. 8; ethane and CO₂, Fig. 10) WF. To cover such cases, it is desirable to relax restriction (B) above. To allow trial orbitals f_n centered away from atoms, it would be necessary to evaluate the ψ_{nk} in real space in a manner similar to `pw2wannier90.x`.

However, interstitial f_n are not always necessary to achieve interstitial WF. For instance, in example of GaAs mentioned above, the bond-centered WF result from atom-centered sp³-hybrid initial projections. WIEN2WANNIER also allows f_n with weight on more than one atom, which may be helpful in

finding bond-centered WF.

6. Woptic: optical conductivity with MLWF

The purpose of the `woptic` package [Ass+15; Wis12] is to calculate the optical conductivity $\sigma_{\alpha\beta}(\Omega)$; its static limit, the dc conductivity $\sigma_{\alpha\beta}(\Omega \rightarrow 0)$; and the Seebeck coefficient or thermopower $S_{\alpha\beta}$ of a periodic interacting electron system. It is integrated rather tightly with `WIEN2k` (to provide the single-particle states and matrix elements between them) and `Wannier90` (to provide a localized basis); interaction effects beyond `DFT` are included via a local self-energy $\Sigma(\omega)$. The self-energy is assumed to be local under the assumption that it comes from a `DMFT` calculation, but `woptic` is not tied to any specific `DMFT` implementation.

The distinguishing features of `woptic` are an adaptive tetrahedral grid for the `BZ` integration, and the use of the full momentum matrix elements

$$V_{ab}^{\alpha}(\mathbf{k}) = \langle \psi_{a\mathbf{k}} | \hat{p}_{\alpha} | \psi_{b\mathbf{k}} \rangle \quad (6.1)$$

in place of a Peierls approximation $V(\mathbf{k}) \approx i \nabla_{\mathbf{k}} H(\mathbf{k})$ [Wis+12].

The design of the package is such that the management of the adaptive `k`-mesh is well isolated from the integration routine and other parts of the code. The `k`-mesh management code was not substantially changed in the course of this dissertation, while the integration routine and various glue and support codes were extended and to a large part rewritten with respect to the original `woptic` package presented in [Wis12]. Therefore, we will focus on these parts and refer to [Ass+15; Wis12] for a description of the adaptive `k`-mesh refinement. A practical description of `woptic` is provided in the user's guide, reproduced in App. A.2.

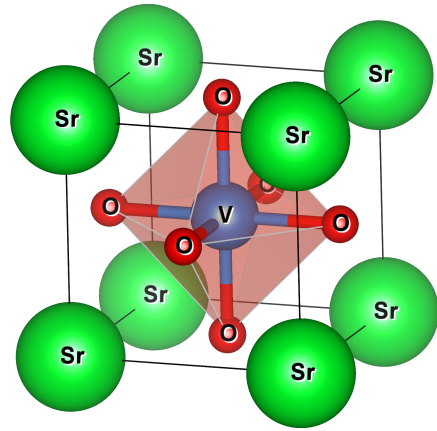


Figure 6.1.: Cubic perovskite crystal structure of SrVO_3 . The O ligands form an octahedron (shown in red) around the V site, leading to the t_{2g} - e_g splitting observed in Fig. 6.2.

6.1. Strontium vanadate, testbed material

In the following sections, strontium vanadate (SrVO_3) will be used for all numerical tests. This paramagnetic correlated metal has a cubic perovskite structure, shown in Fig. 6.1. It is a well studied material, and is often used to showcase new developments in the theory of strongly correlated materials.*

Fig. 6.2 shows the band structure and density of states of SrVO_3 as computed with WIEN2k using the PBE functional [PBE96]. The three V- t_{2g} -derived bands constitute the low-energy degrees of freedom. They are separated by finite gaps everywhere in the BZ from the O-p states below and the V- e_g states above.

For the purposes of testing *woptic*, we will use two different types of Wannier projections for SrVO_3 :

- p-3 A 3-band projection on the t_{2g} bands is straightforward. Because the t_{2g} states hybridize with O-p states, the three V-centered orbitals of the resulting “minimal model” for SrVO_3 also have a lot of weight at the O sites [Rib+14].
- p-14 A 14-band projection on the V-d and O-p bands is more delicate because at the R-point, the V- e_g bands become entangled with 3 Sr bands (as seen in Fig. 6.2). In practice, as long as the R-point is not included in the Wannierization k-mesh, this entanglement can be ignored. (For

* To give a few examples, DMFT calculations are presented in [Lieu03; Nek+05; Pav+04; Sek+04; Tar+13; Tom+12]; Wannier projections in [Kun+10; Pav+05; Sca+14], as well as [Rib+14]. The latter is reproduced in App. B.2.

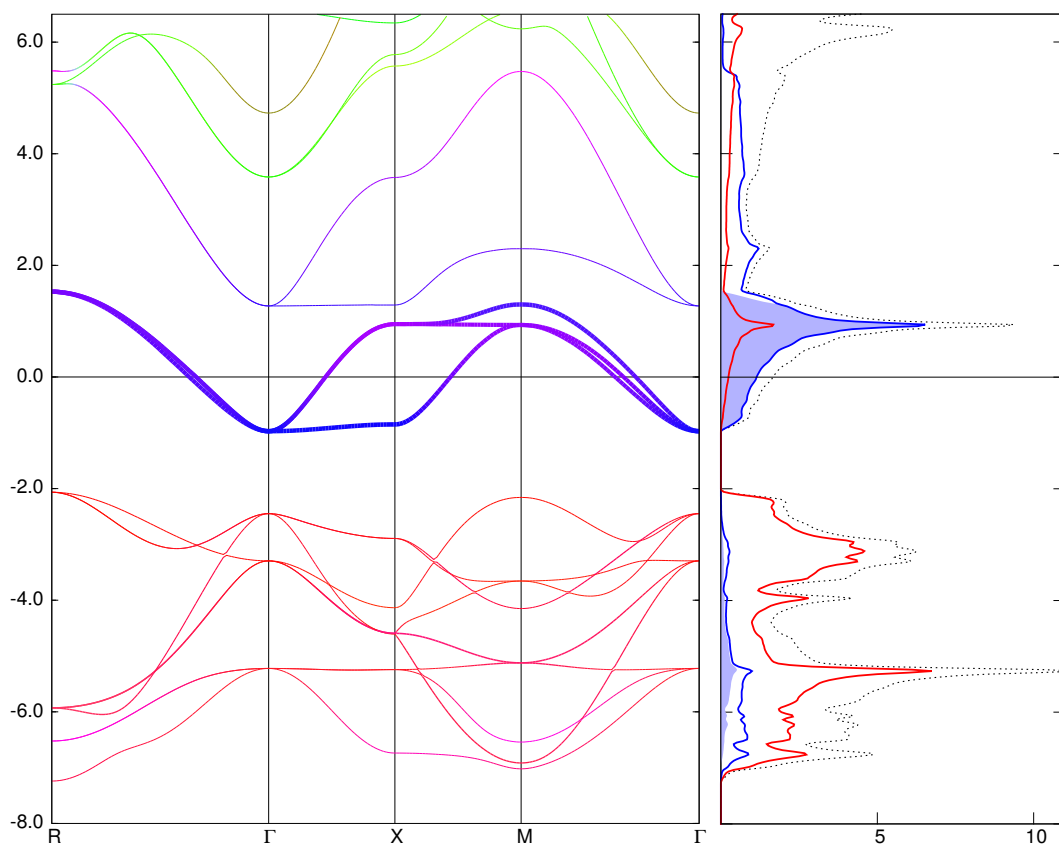


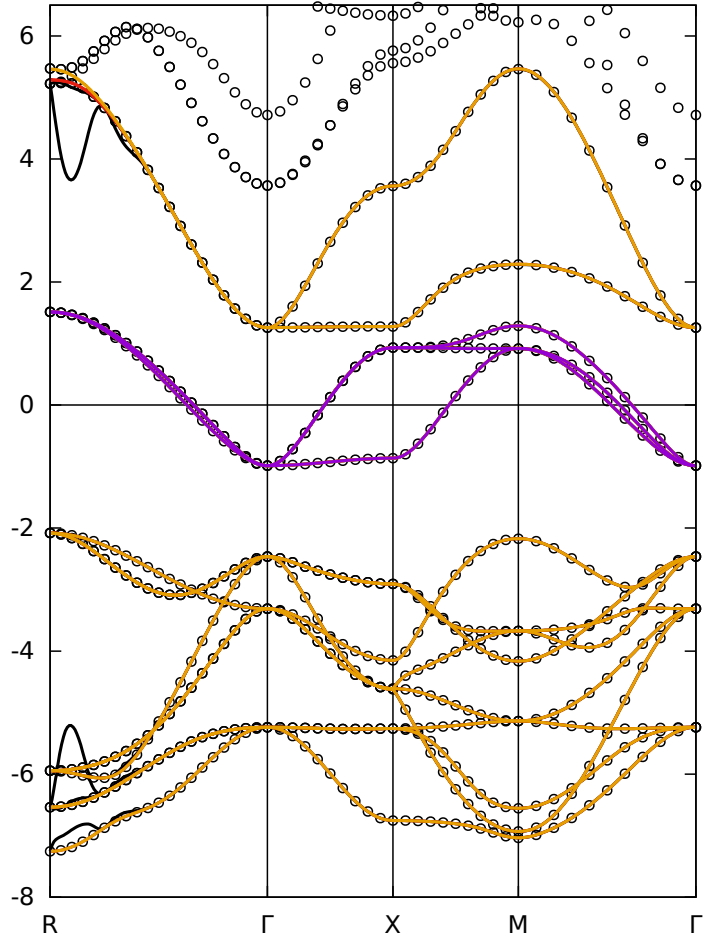
Figure 6.2.: Bandstructure (left) and dos (right; in states per eV per unit cell) of SrVO_3 . Energy (left scale) is in eV. The contributions are color-coded: red for O, blue for V, green for Sr. On the left, the V-t_{2g} bands are highlighted by thicker lines (i.e., the line width is proportional to the V-t_{2g} weight); on the right, the V-t_{2g} contribution is shaded, and the dotted line represents the total dos.

an isotropic $L \times L \times L$ mesh this is the case if L is odd.) Otherwise, disentanglement is expedient to obtain good wf. In any case, the resulting orbitals are close to the atomic case, since all relevant states are explicitly included in the Wannier projection (i.e. there is little hybridization with any other bands) [Rib+14; Sca+14].

To judge the quality of the different projections, we can compare the respective Wannier-interpolated band structures (Fig. 6.3). As described above, the $8 \times 8 \times 8$ projection without disentanglement (using the 14 lowest-

Figure 6.3.: Wannier-interpolated band structures for SrVO₃ from different projections:

- (purple) P-3,
 - (red) P-14 without disentanglement on $9 \times 9 \times 9$ k-points,
 - (black) the same on $8 \times 8 \times 8$ k-points,
 - (orange) P-14 with disentanglement;
- compared to
- (circles) the WIEN2k result.



Throughout most of the BZ, all projections follow the DFT bands closely, such that only one of the lines is visible. The discrepancies between the P-14 projections around R (i.e. the corner point of the BZ) are due to entangled Sr bands (see text).

energy bands starting from 8 eV below the Fermi level) fails to reproduce the WIEN2k bands around the R-point. Using a $9 \times 9 \times 9$ k-mesh instead, the bands are reproduced faithfully. If an additional 3 bands are included for disentanglement, the Wannier-interpolated bands follow the V character more closely, as a comparison to Fig. 6.2 reveals. To do so, it must necessarily depart from the WIEN2k bands. This is an illustration of the general rule that the MLWF transformation is no longer unitary when disentanglement is used.

6.2. Computing the integrand

The optical conductivity $\sigma^{\alpha\beta}(\Omega)$ (in the general case a tensor with $\alpha, \beta \in \{x, y, z\}$) at external frequency Ω may be written as an integral over $\mathbf{k} \in \text{BZ}$

and an internal frequency ω [Wis12],

$$\sigma^{\alpha\beta}(\Omega) = \frac{\tau}{V_{\text{UC}}} \int_{-\infty}^{+\infty} d\omega w(\omega; \Omega) \int_{\text{BZ}} d\mathbf{k} \mathcal{T}^{\alpha\beta}(\mathbf{k}, \omega; \Omega) \quad (6.2)$$

where

$$w(\omega; \Omega) := \frac{f(\omega) - f(\omega + \Omega)}{\Omega} \quad (6.3)$$

is a weight factor and the trace

$$\mathcal{T}^{\alpha\beta}(\mathbf{k}, \omega; \Omega) := \text{tr}\{A(\mathbf{k}, \omega) V^\alpha(\mathbf{k}) A(\mathbf{k}, \omega + \Omega) V^\beta(\mathbf{k})\} \quad (6.4)$$

becomes the central quantity in WOPTIC. The purpose of this section is to explain how \mathcal{T} is computed in practice.

In (6.3), $f(\omega) = (1 + \exp \beta\omega)^{-1}$ is the Fermi-Dirac distribution (setting the Fermi level to 0), $A(\mathbf{k}, \omega)$ is the spectral function matrix (4.20), $V^\alpha(\mathbf{k})$ is the momentum matrix (6.1), and the trace runs over orbitals and spin. To simplify the notation, we will usually suppress the \mathbf{k} -dependence, and adopt the following index conventions: a, b, \dots run over all Bloch states; u, v, \dots over the Wannier states; n, m, \dots over Bloch states inside and i, j, \dots over Bloch states outside of the Wannier window; α, β enumerate the Cartesian directions; and repeated indices imply summation.

The dc conductivity and thermopower can be computed from very similar expressions in the static limit, where

$$w(\omega; \Omega \rightarrow 0) = \frac{\beta/4}{(\cosh \beta\omega/2)^2}. \quad (6.5)$$

To excite an electronic transition, the photon frequency Ω must connect an empty state to a filled one, i.e. one of ω and $\omega + \Omega$ must be negative and the other positive, which is enforced by the weight factor (6.3), modulo temperature broadening. This observation can be exploited to limit the range of ω -integration. Since the external frequency $\Omega \geq 0$, the internal frequency should satisfy

$$-(\Omega + \Delta\omega) < \omega < 0 + \Delta\omega, \quad (6.6)$$

with $\Delta\omega$ chosen according to temperature and desired accuracy. To include all ω where $w > \varepsilon$, it suffices to set $\Delta\omega$ according to the static limit (6.5),

$$\cosh \beta \Delta\omega > \sqrt{\frac{\beta}{4\varepsilon}}. \quad (6.7)$$

This requirement is more stringent than $w < \varepsilon$ would be for any finite Ω , though for realistic values of the variables, the results are very similar.

For practical purposes, we will split (6.4) into parts inside the Bloch ($\psi\psi$) and Wannier ($w\psi$) subspaces, and a mixed term ($w\psi$):

$$\mathcal{T} = \mathcal{T}_{\psi\psi} + \mathcal{T}_{ww} + \mathcal{T}_{w\psi}. \quad (6.8)$$

During the adaptive k-integration, these terms must be evaluated at arbitrary k-points not necessarily contained in the k-mesh used for the Wannier projection. As we will see establishing connection between the Bloch and Wannier states at the extra k-points poses some challenges.

But first, the Bloch-only term,

$$\mathcal{T}_{\psi\psi} = A_{ii}(\omega) V_{ij}^{\alpha} A_{jj}(\omega + \Omega) V_{ji}^{\beta}, \quad (6.9)$$

simplifies because the matrix spectral function is diagonal. It can be computed using the noninteracting formula

$$A_{ii}(\mathbf{k}, \omega) = \frac{2\delta/\tau}{(\omega - \varepsilon_i(\mathbf{k}) + \mu)^2 + \delta^2}, \quad (6.10)$$

where δ is a broadening parameter (corresponding to a self-energy $\Sigma = -i\delta$ with a small $\delta > 0$). The momentum matrix elements V_{ij}^{α} are taken directly from WIEN2k's optic module [AS06].

Next, for the Wannier-only part,

$$\mathcal{T}_{ww} = A_{uv}(\omega) V_{vr}^{\alpha} A_{rs}(\omega + \Omega) V_{su}^{\beta}, \quad (6.11)$$

we have to mediate between the spectral function, which will be given in the Wannier gauge in terms of the DMFT self-energy $\Sigma(\omega)$ via the Green function

$$G(\mathbf{k}, \omega) = [\omega - H^w(\mathbf{k}) + \mu - \Sigma(\omega)]^{-1}; \quad (6.12)$$

and the momentum matrix elements, which optic computes in the ks gauge. In our index convention,

$$V_{uv}^{\alpha}(\mathbf{k}) = \langle w \mathbf{u} \mathbf{k} | \hat{p}_{\alpha} | w \mathbf{v} \mathbf{k} \rangle = \mathcal{U}_{un}^{+}(\mathbf{k}) V_{nm}^{\alpha}(\mathbf{k}) \mathcal{U}_{mv}(\mathbf{k}). \quad (6.13)$$

But if \mathbf{q} is a new k-point not included in the original Wannier mesh \mathcal{W} , $\mathcal{U}(\mathbf{q})$ is unknown. To determine \mathcal{U} for new k-points, Wannier interpolation

(cf. Sec. 3.2) can be used in the following way [Wis12]: For each new k-point $\mathbf{q} \notin \mathcal{W}$, the Wannier Hamiltonian

$$H_{uv}^{\mathbf{w}}(\mathbf{k}) = \langle \mathbf{w} \ u \mathbf{k} | \hat{H}_{\mathbf{k}\mathbf{s}} | \mathbf{w} \ v \mathbf{k} \rangle = \mathcal{U}_{un}^+(\mathbf{k}) \varepsilon_n(\mathbf{k}) \mathcal{U}_{nv}(\mathbf{k}) \quad (6.14)$$

is interpolated to $H^{\mathbf{w}}(\mathbf{q})$, and the unitary matrix $\tilde{\mathcal{U}}(\mathbf{q})$ which diagonalizes it is taken as $\mathcal{U}(\mathbf{q})$.

With $V_{nm}^{\alpha}(\mathbf{q})$ calculated by `optic` and $\Sigma(\omega)$ k-independent, all the ingredients are at hand to calculate $\mathcal{T}_{\mathbf{w}\mathbf{w}}$ at \mathbf{q} . This is the approach used in the original `woptic` implementation [Wis12]. It is straightforwardly generalized to the mixed term

$$\mathcal{T}_{\mathbf{w}\psi} = A_{uv}(\omega) V_{vi}^{\alpha} A_{ii}(\omega + \Omega) V_{iu}^{\beta} + A_{ii}(\omega) V_{iu}^{\alpha} A_{uv}(\omega + \Omega) V_{vi}^{\beta}. \quad (6.15)$$

However, there is a subtler problem. Since the $|\psi \ a \mathbf{k}\rangle$ arise from the diagonalization of $\hat{H}_{\mathbf{k}\mathbf{s}}(\mathbf{k})$, they carry complex phases $\varphi_a(\mathbf{k})$ which a priori are completely arbitrary. On the original k-points $\mathbf{k} \in \mathcal{W}$, the $\mathcal{U}(\mathbf{k})$ take into account and “cancel” these phases, yielding smooth functions $|\mathbf{w} \ v \mathbf{k}\rangle = \mathcal{U}_{iv}(\mathbf{k}) |\psi \ i \mathbf{k}\rangle$ of \mathbf{k} ; but on added k-points $\mathbf{q} \notin \mathcal{W}$, $\tilde{\mathcal{U}}(\mathbf{q})$ has no such constraint, and the phases enter into $\mathcal{T}_{\mathbf{w}\psi}$ and $\mathcal{T}_{\mathbf{w}\mathbf{w}}$ via the momentum matrix elements. (In $\mathcal{T}_{\psi\psi}$ the phases cancel because V_{ij}^{α} always appears paired with V_{ji}^{β} .)

6.2.1. Wannier-interpolating the momentum matrix elements

The solution to this “random-phase problem”^{*} explored in the present work is a direct Wannier interpolation of $V^{\alpha}(\mathbf{k})$. That is, $V_{nm}^{\alpha}(\mathbf{k})$ is computed by `optic` on $\mathbf{k} \in \mathcal{W}$ and transformed to the Wannier gauge (6.13). For all new k-points \mathbf{q} , $V_{uv}^{\alpha}(\mathbf{q})$ can be computed via Fourier interpolation (3.17). Then, $\mathcal{T}_{\mathbf{w}\mathbf{w}}$ can be computed completely in the Wannier gauge without recourse to any new $\tilde{\mathcal{U}}(\mathbf{q})$.

For this strategy to work,

$$V_{uv}^{\alpha}(\mathbf{R}) = \langle \mathbf{w} \ u \mathbf{0} | \hat{p}_{\alpha} | \mathbf{w} \ v \mathbf{R} \rangle \quad (6.16)$$

^{*} In crystal structures with inversion symmetry, it is a well-known and computationally exploited fact that the $\mathbf{k}\mathbf{s}$ vectors (more properly their basis coefficients and the necessary matrix elements) can be chosen to be real. It is tempting to conclude that there is no random-phase problem in these cases; however, the freedom to choose an arbitrary sign at each k-point, $\varphi(\mathbf{k}) \in \{0, \pi/2\}$, remains.

6. Woptic: optical conductivity with MLWF

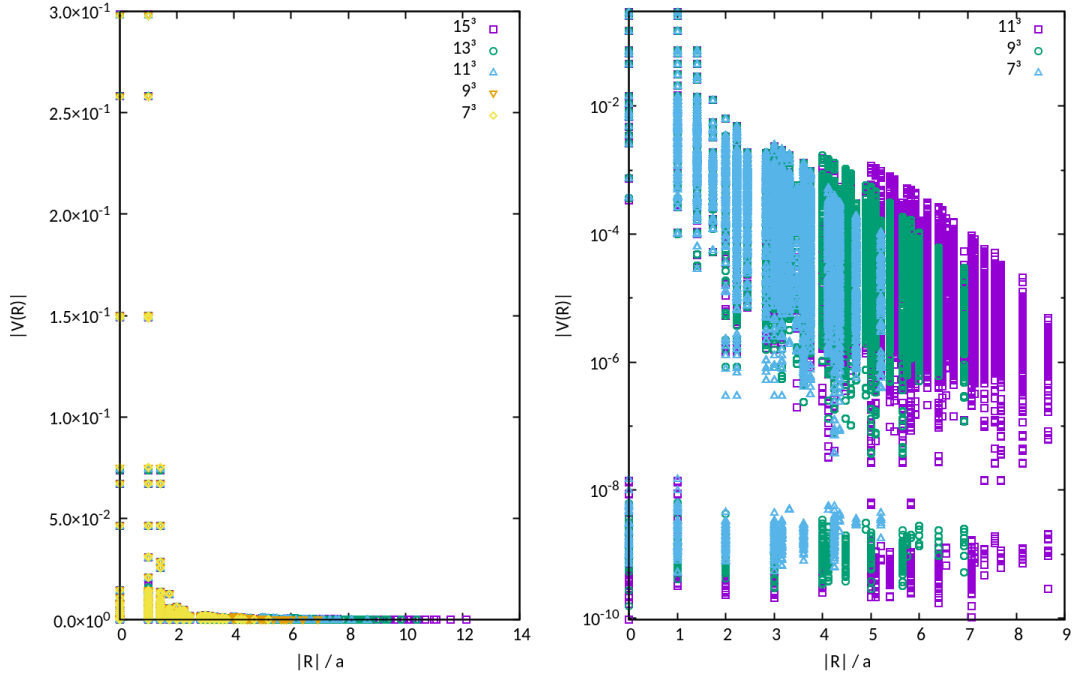


Figure 6.4.: $|V_{uv}^\alpha(\mathbf{R})|$ for SrVO_3 as a function of $|\mathbf{R}|$ in units of the lattice constant. The Wannier projection spans the O-p and V-d bands (p-14 above), and different Wannierization k-meshes are compared. For each k-mesh, all the matrix elements (for all values of u, v , and \mathbf{R}) are plotted together. Denser meshes in reciprocal space correspond to larger supercells in direct space, therefore they show a greater range and density of $|\mathbf{R}|$ values. The linear plot (left) shows that the matrix elements are well converged already at 7^3 k-points. In the semilogarithmic plot (right), the separation between signal and numeric noise becomes evident. The magnitude of the noise decreases as the k-mesh density increases. The signal roughly follows a straight line, consistent with exponential localization.

must be well-localized in direct space, which should be the case as long as well-localized wF can be found. This approach has been tested numerically for the case of SrVO_3 .

First, the rapid decay of $V_{uv}^\alpha(\mathbf{R})$ with $|\mathbf{R}|$ is seen in Fig. 6.4. With exponentially localized wF, we expect exponential decay $\sim e^{-|\mathbf{R}|}$, consistent with the apparent linear behavior in the semilogarithmic plot. Second, as long as the wF are real, $V_{uv}^\alpha = \langle w u \mathbf{k} | -i \partial_\alpha | w v \mathbf{k} \rangle$ should be purely imaginary, as confirmed numerically in Fig. 6.5. Third, the Peierls approximation suggests

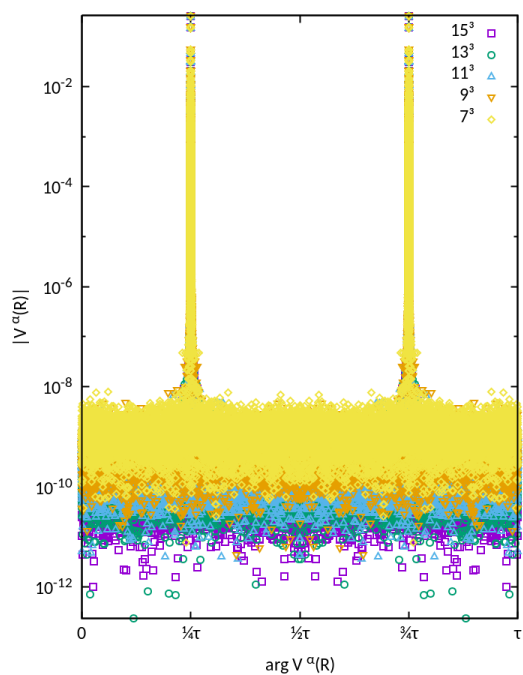


Figure 6.5.: $|V_{uv}^\alpha(\mathbf{R})|$ as a function of the complex argument $\varphi = \arg V_{uv}^\alpha(\mathbf{R})$. (Same data as Fig. 6.4.) As expected for real-valued wF, $V_{uv}^\alpha(\mathbf{R})$ is purely imaginary, except for the numerical noise which has uniformly distributed phases.

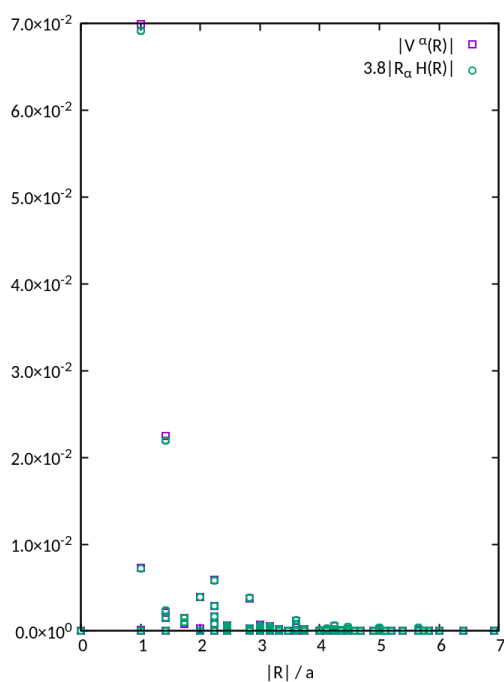


Figure 6.6.: $|V_{uv}^\alpha(\mathbf{R})|$ compared to the Peierls expression $|RH_{uv}^w(\mathbf{R})|$ (times a fitted constant) as a function of $|\mathbf{R}|$. In this case, a 3-band Wannier projection on $9 \times 9 \times 9$ k-points encompassing only the V- t_{2g} bands (P-3 above) was used, otherwise the positions of the wF within the unit cell would have to be taken into account in the Peierls approximation.

that $V(\mathbf{R}) \approx \mathbf{R}H^w(\mathbf{R})$, as shown in Fig. 6.6.

These results already make a strong case for the Wannier interpolation method as applied to \mathcal{T}_{ww} . In Sec. 6.3 we will see that this is validated also in the \mathbf{k} -integrated optical conductivity.

6.2.2. Interpolating the mixed momentum matrix elements

The mixed matrix elements $V_{vi}^\alpha = \langle w v \mathbf{k} | \hat{p}_\alpha | \psi i \mathbf{k} \rangle$ are not amenable to interpolation in the same way as $V_{uv}^\alpha(\mathbf{R})$ because $V_{vi}^\alpha(\mathbf{R})$ does not decay with $|\mathbf{R}|$ (it does not in numerical tests, and neither is there much reason to believe it should). Since the matrix elements appear in the trace in terms of the form $V_{ui}^\alpha A_{ii}(\omega) V_{iv}^\beta A_{vu}(\omega + \Omega)$, two alternative targets for interpolation present themselves:

$$S_{uiv}^{\alpha\beta}(\mathbf{k}) := V_{ui}^\alpha \cdot V_{iv}^\beta = \langle w u \mathbf{k} | \hat{p}_\alpha | \psi i \mathbf{k} \rangle \langle \psi i \mathbf{k} | \hat{p}_\beta | w v \mathbf{k} \rangle \quad (6.17)$$

(no summation implied) or

$$\begin{aligned} W_{uv}^{\alpha\beta}(\mathbf{k}, \omega) &:= V_{ui}^\alpha A_{ii}(\mathbf{k}, \omega) V_{iv}^\beta \\ &= \langle w u \mathbf{k} | \hat{p}_\alpha \left(\sum_i | \psi i \mathbf{k} \rangle A_{ii}(\mathbf{k}, \omega) \langle \psi i \mathbf{k} | \right) \hat{p}_\beta | w v \mathbf{k} \rangle; \end{aligned} \quad (6.18)$$

in each case at the cost of dealing with a larger, more complicated, object. Numerically, $S_{uiv}^{\alpha\beta}(\mathbf{R})$ does not show decay with $|\mathbf{R}|$, and we therefore discard this approach.

There is some justification to expect

$$W_{uv}^{\alpha\beta}(\mathbf{R}, \omega) = \frac{V}{\tau^3} \int_{\text{BZ}} d\mathbf{k} e^{-i\mathbf{k}\mathbf{R}} W_{uv}^{\alpha\beta}(\mathbf{k}, \omega) \quad (6.19)$$

to do better. Denoting the operator $\hat{p}_\alpha(\cdots)\hat{p}_\beta$ above as $\hat{B}(\mathbf{k})$ and suppressing the ω -dependence, we can write the Fourier transform as a convolution

$$W_{uv}^{\alpha\beta}(\mathbf{R}) = \sum_{\mathbf{R}'\mathbf{R}''} \langle w u \mathbf{R}' | \hat{B}(\mathbf{R} + \mathbf{R}' - \mathbf{R}'') | w v \mathbf{R}'' \rangle. \quad (6.20)$$

Thus, the properties of $\hat{B}(\mathbf{R})$ determine the degree of localization of $W_{uv}^{\alpha\beta}(\mathbf{R})$.

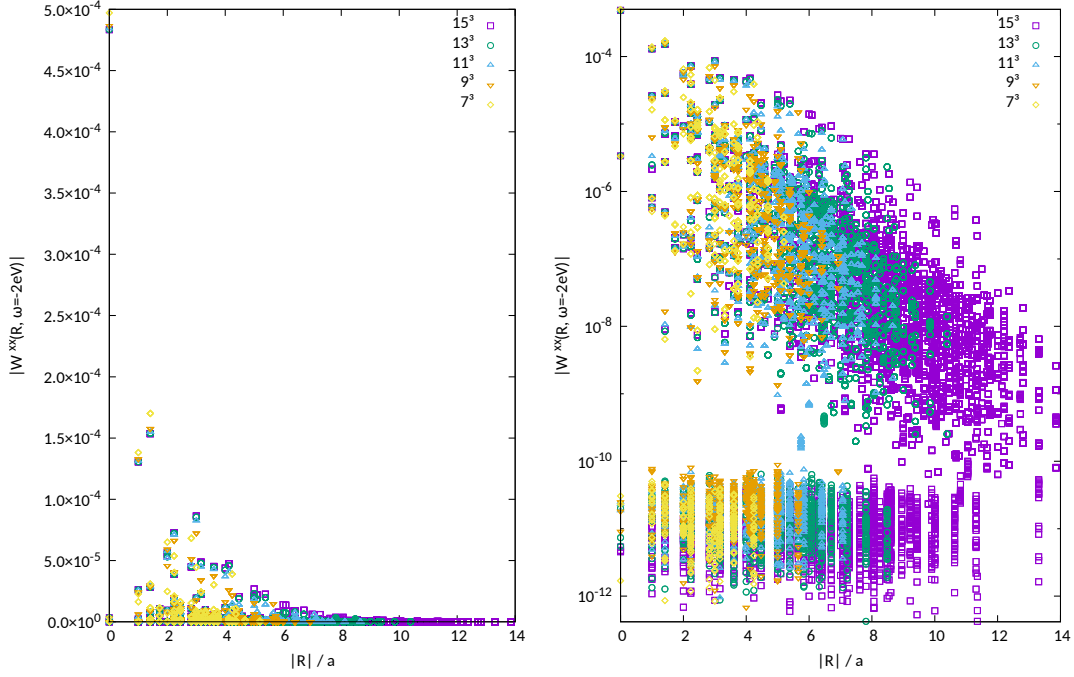


Figure 6.7.: Like Fig. 6.4, but for the mixed matrix elements $W_{uv}^{\alpha\alpha}(\mathbf{R}, \omega = -2\text{eV})$ instead of $V_{uv}^{\alpha}(\mathbf{R})$. At this frequency, a satisfactory (apparently exponential) decay with $|\mathbf{R}|$ is seen, albeit slower than for $|V^{\alpha}(\mathbf{R})|$. The Wannier projections are on the V-t_{2g} bands (p-3 above), as in Fig. 6.6, and the outer (“Bloch”) window spans the O-p and V-e_g bands.

To arrive at an expression analogous to (6.16), we must suppose that $\widehat{B}(\mathbf{k})$ is k -independent, and thus $\widehat{B}(\mathbf{R}) = \delta_{\mathbf{R},0}\widehat{B}$, which yields

$$W_{uv}^{\alpha\beta}(\mathbf{R}) = \sum_{\mathbf{R}'} \langle w u \mathbf{R}' | \widehat{B} | w v \mathbf{R} + \mathbf{R}' \rangle. \quad (6.21)$$

In this case it is clear that $W_{uv}^{\alpha\beta}$ will be localized in terms of \mathbf{R} as long as \widehat{B} is a sufficiently local operator (i.e., $\langle \mathbf{r}' | \widehat{B} | \mathbf{r}'' \rangle$ is localized in terms of $|\mathbf{r}' - \mathbf{r}''|$). If furthermore $\widehat{B}(\mathbf{R})$ is lattice-translation invariant (meaning that $\langle \mathbf{r}' - \mathbf{R} | \widehat{B}(\mathbf{R}) | \mathbf{r}'' - \mathbf{R} \rangle \equiv \langle \mathbf{r}' | \widehat{B}(\mathbf{R}) | \mathbf{r}'' \rangle$), we find, as desired,

$$W_{uv}^{\alpha\beta}(\mathbf{R}) = \langle w u \mathbf{0} | \widehat{B} | w v \mathbf{R} \rangle. \quad (6.22)$$

Considering the actual form of \widehat{B} (6.18), to get the simple case (6.22), we have to assume that (a) the Bloch states i are “nearly complete”, and (b)

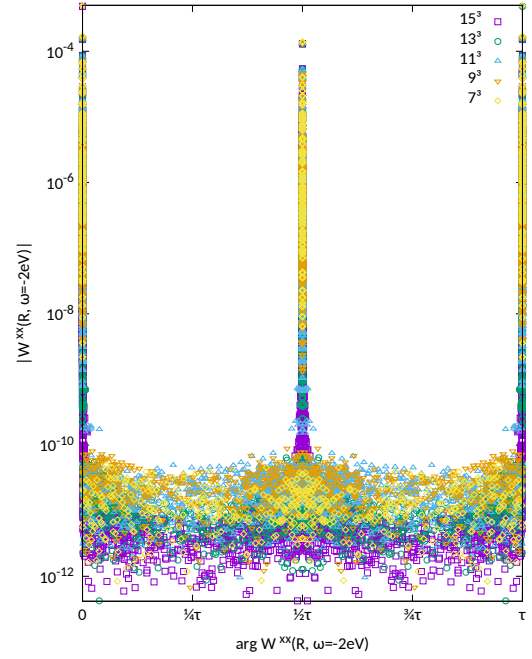


Figure 6.8.: As Fig. 6.5, but for the mixed matrix elements $W_{uv}^{\alpha\alpha}(\mathbf{R}, \omega = -2\text{eV})$ instead of $V_{uv}^{\alpha}(\mathbf{R})$. (Same data as Fig. 6.7.) A similar picture emerges for $W^{\alpha\neq\beta}$ (not shown).

$A_{ii}(\mathbf{k}, \omega) \approx A(\omega)$ is nearly constant in i and \mathbf{k} . In this case,

$$\sum_i |\psi i\mathbf{k}\rangle A_{ii}(\omega) \langle \psi i\mathbf{k}| \approx A(\omega) \hat{P}(\mathbf{k}), \quad (6.23)$$

where $\hat{P}(\mathbf{k})$ is the projector onto \mathbf{k} and can be replaced by $\hat{\mathbb{1}} = \int d\mathbf{k} \hat{P}(\mathbf{k})$ since $\langle \psi i\mathbf{k} | \hat{p}_\alpha | w u\mathbf{k}' \rangle$ enforces $\mathbf{k} = \mathbf{k}'$ anyway. This yields

$$W_{uv}^{\alpha\beta}(\mathbf{R}, \omega) \approx A(\omega) \langle w u\mathbf{0} | \hat{p}_\alpha \hat{p}_\beta | w v\mathbf{R} \rangle. \quad (6.24)$$

However, it is difficult to see how these conditions would be satisfied in a real calculation; (a) means that $\langle w u\mathbf{k} | \hat{p}_\alpha | w v\mathbf{k} \rangle \approx 0$, i.e. no w - w transitions are allowed;* and (b) is only the case in energy regions without Bloch states, where $A_{ii} = W_{uv}^{\alpha\beta} = 0$. Otherwise the noninteracting spectral function is in fact a sum over δ -peaks, $A_{ii}(\mathbf{k}) = \sum_j w_j^{(i)} \delta(\mathbf{k} - \mathbf{x}_j^{(i)})$.

Numerical tests for $W_{uv}^{\alpha\beta}(\mathbf{R}, \omega)$ analogous to those for V_{uv}^{α} conclude this section (Figs. 6.7 to 6.10). In this case the analysis is complicated by the extra dependence on ω , which turns out to be important, and the fact that

* Strictly speaking, the requirement is $\sum_{rs} \langle w u\mathbf{k} | \hat{p}_\alpha | w r\mathbf{k} \rangle \langle w s\mathbf{k} | \hat{p}_\beta | w v\mathbf{k} \rangle \approx 0$.

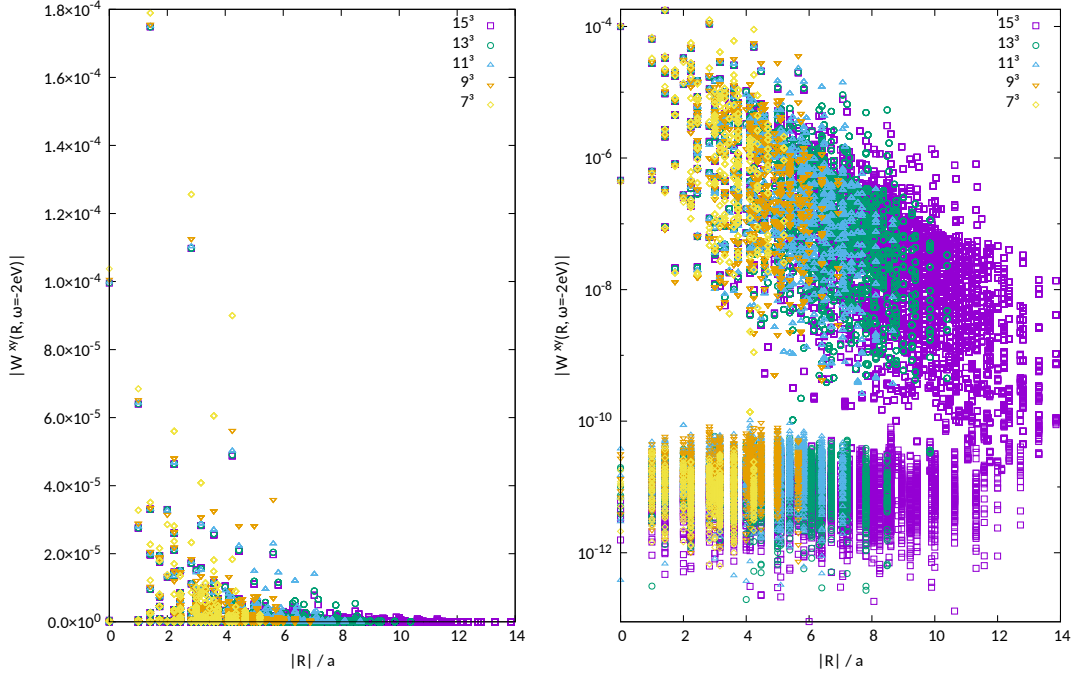


Figure 6.9.: Like Fig. 6.7, but off-diagonal in the Cartesian indices, $\alpha \neq \beta$.

$W^{\alpha\beta}$ carries two coordinate indices instead of one. Overall, $W_{uv}^{\alpha\beta}(\mathbf{R}, \omega)$ shows significant localization. Furthermore, it is essentially real, as we would expect in the simple scenario of (6.24). The latter observation holds even where $W_{uv}^{\alpha\beta}(\mathbf{R}, \omega)$ is not well localized. In the face of the considerations above, both the localization and realness of $W_{uv}^{\alpha\beta}(\mathbf{R})$ are surprising, and an explanation remains as a topic for future study. Results for the optical conductivity will be shown in Sec. 6.3. In this case as well, we will see that the interpolation works acceptably well overall.

To begin, let $\alpha = \beta$ and the internal frequency $\omega = -2$ eV, where $W_{uv}^{\alpha\alpha}(\mathbf{R}, \omega)$ is comparatively well behaved (Fig. 6.7). This corresponds to the top of the O-p bands. Fig. 6.8 shows that $W_{uv}^{\alpha\alpha}$ is essentially real. The situation is largely the same for $\alpha \neq \beta$ (the off-diagonal terms of the optical conductivity), including the magnitude of $W_{uv}^{\alpha\neq\beta}$, even though these contributions must integrate to 0 in $\sigma^{\alpha\beta}(\omega)$ for this cubic material (Fig. 6.9).

At $\omega = -4.5$ eV (Fig. 6.10), corresponding to the center of the O-p bands, there is still some decay, but it is not as pronounced. Note also that this

6. Woptic: optical conductivity with MLWF

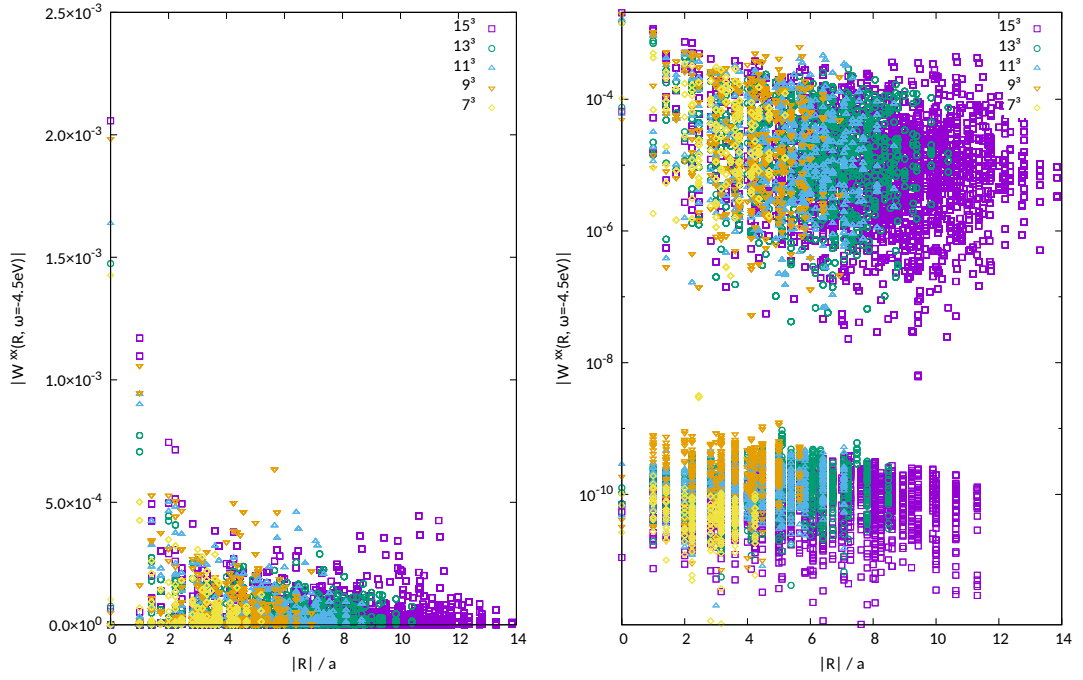


Figure 6.10.: Like Fig. 6.7, at internal frequency $\omega = -4.5$ eV. Even though the localization is lacking in this case, $W^{\alpha\beta}$ is still essentially real-valued.

coincides with larger magnitudes of $W_{uv}^{\alpha\beta}$. The realness of $W_{uv}^{\alpha\beta}(\mathbf{R})$ remains untouched by this change (the phase plot as in Fig. 6.8 is similar at both frequencies, and hence not shown for $\omega = -4.5$ eV).

6.2.3. Interpolation and disentanglement

In the above description, it was implicit that the WF were constructed without disentanglement. The basic difficulty was that we needed to mediate between the “Bloch” and “Wannier” bases at k-points \mathbf{q} where $\mathcal{U}(\mathbf{q})$ is not available. This problem is addressed in wOPTIC by interpolating either the transformation matrices $\tilde{\mathcal{U}}(\mathbf{q})$, or the momentum matrix elements $V^\alpha, W^{\alpha,\beta}$.

In the presence of disentanglement, we face a similar problem concerning the projectors $\mathcal{V}(\mathbf{q})$ (3.12) to the optimal subspace. This section will explore strategies to overcome this obstacle. However, the current version of wOPTIC supports only the simplest special case including disentanglement, namely when only w-w transitions are included, and those are treated using Wannier

interpolation.

General considerations

Disentanglement does not change the general structure of the problem. It is still useful to partition the Hilbert space into inner and outer parts. This time, the inner subspace will encompass all states that participate in the disentanglement; it is what happens inside this part that becomes more complicated. For the purposes of this discussion, upper case letters H, Σ, G, A refer to quantities in the whole ‘‘Wannier+Bloch’’ space (the physical quantities, as it were); lower case letters ε, g, a refer to their parts within or without the disentanglement window; a superscript w indicates a quantity in the Wannier basis (with the disentangled states projected out); and a superscript \star indicates the same quantity promoted to the whole disentanglement subspace (i.e., $\cdot^\star = \mathcal{V}\mathcal{U} \cdot \mathcal{U}^\dagger \mathcal{V}^\dagger$, going from a $\mathcal{J}_k \times \mathcal{J}_k$ to a $J \times J$ matrix).

Let us write the diagonal ks Hamiltonian as

$$H = \begin{pmatrix} \varepsilon' & & \\ & \varepsilon & \\ & & \varepsilon'' \end{pmatrix}, \quad (6.25)$$

where ε is the inner part of dimension $\mathcal{J}_k \times \mathcal{J}_k$, and the outer part is made up of ε' and ε'' . In order to introduce the $J \times J$ single-particle Hamiltonian used in the many-body calculation,

$$H_{uv}^w = \mathcal{U}_{un}^+ \mathcal{V}_{na}^+ \varepsilon_a \mathcal{V}_{am} \mathcal{U}_{mv}, \quad (6.26)$$

into (6.25), we use the $(\mathcal{J}_k \times \mathcal{J}_k)$ projector onto the optimal subspace and its complement within the disentanglement window,

$$P = \mathcal{V}\mathcal{V}^\dagger \quad \text{and} \quad Q = \mathbb{1} - P, \quad (6.27)$$

to write

$$\varepsilon = P\varepsilon P + Q\varepsilon Q + P\varepsilon Q + Q\varepsilon P, \quad (6.28)$$

where

$$P\varepsilon P = \mathcal{V}\mathcal{U}H^w\mathcal{U}^\dagger\mathcal{V}^\dagger = H^\star \quad (6.29)$$

corresponds to H^w promoted to $(\mathcal{J}_k \times \mathcal{J}_k)$.

We must now calculate the spectral function. The Green function

$$G = (\omega - H - \Sigma)^{-1} = \begin{pmatrix} g'_0 & & \\ & g & \\ & & g''_0 \end{pmatrix} \quad (6.30)$$

inherits the block-diagonal form of the Hamiltonian, as does the spectral function

$$A = \frac{i}{\tau}(G - G^+) = \begin{pmatrix} a'_0 & & \\ & a & \\ & & a''_0 \end{pmatrix}, \quad (6.31)$$

where g_0 and a_0 stand for the noninteracting Green function and spectral function (6.10) outside of the disentanglement window.

In constructing the Green function, the self-energy Σ^w ($J \times J$) derived from the many-body calculation should be applied only to the Wannier (P) part of the states. It must be promoted to Σ^* ($\mathcal{J}_k \times \mathcal{J}_k$). For computational purposes, a finite broadening ($\Sigma \leftarrow -i\delta$) will be imposed on all other states (Q , as well as outside the disentanglement window).

Thus, the inverse of the inner-window Green function is

$$\begin{aligned} g^{-1} &= \omega \mathbb{1}_{\mathcal{J}_k} - \varepsilon - \Sigma^* + i\delta Q \\ &= \mathcal{V} \mathcal{U} (\omega \mathbb{1}_J - H^w - \Sigma^w) \mathcal{U}^+ \mathcal{V}^+ + (\omega + i\delta)Q - (\varepsilon - P\varepsilon P) \end{aligned} \quad (6.32)$$

(since for a projector Q and a scalar c , $Qc\mathbb{1}Q = cQ$). But due to the inversion, neither the Green function itself nor the spectral function

$$a = -\frac{i}{\tau}(g - g^+) \quad (6.33)$$

admits a similar partitioning. Evidently, in the disentangled case, both $\mathcal{U}(\mathbf{q})$ and $\mathcal{V}(\mathbf{q})$ are needed on the new k-points. Wannier interpolation of the momentum matrix elements is not applicable.

Wannier-Wannier transitions only

Consider now the special case mentioned above, where we are interested only in w-w transitions but disentanglement is necessary, e.g., to remove extraneous states that interfere with the target states at the band edges, as in

the P-14 for SrVO₃. Under these circumstances, Wannier interpolation can be salvaged in the presence of disentanglement.

Namely, we can work entirely in the Wannier basis, where

$$G^w = (\omega \mathbb{1}_J - H^w - \Sigma^w)^{-1} \quad (6.34)$$

and

$$\mathcal{T} = \mathcal{T}_{ww} = \text{tr} A^w(\omega) \mathcal{V}^+ \mathcal{U}^+ V^\alpha \mathcal{U} \mathcal{V} A^w(\omega + \Omega) \mathcal{V}^+ \mathcal{U}^+ V^\beta \mathcal{U} \mathcal{V}; \quad (6.35)$$

$\mathcal{V}^+ \mathcal{U}^+ V^\alpha \mathcal{U} \mathcal{V} = (V^\alpha)^w$ can be identified as the momentum matrix elements in the Wannier basis and subjected to Wannier interpolation.

Interpolating $\mathcal{V}(k)$

The interpolation method for $\tilde{\mathcal{U}}(q)$ cannot be extended to the rectangular $\mathcal{V}(q)$ ($\mathcal{J}_q \times J$), even disregarding any random-phase problem. To obtain interpolated $\tilde{\mathcal{V}}$, it seems most promising to extend the computational definition of $\mathcal{V}(k)$. The $|\tilde{u} nk\rangle$ are computed as the eigenvectors corresponding to the J largest eigenvalues of the $\mathcal{J}_k \times \mathcal{J}_k$ matrix $Z(k)$ with elements [Mar+12, Eq. (53)]

$$Z_{mn} := \langle u mk | \sum_b g_b P_{k+b} | u nk \rangle. \quad (6.36)$$

The projector $P_k = \sum_r |\tilde{\psi} rk\rangle \langle \tilde{\psi} rk| \hat{=} \mathcal{V}(k) \mathcal{V}^+(k)$ onto the optimal subspace is the same as above and as in (3.15). In the course of the normal disentanglement routine, this equation is iterated, using the projector from the previous iteration to compute the next Z until P and Z are consistent with each other.

If the optimally smooth subspace is known on a sufficiently fine k-mesh, (6.36) can be reinterpreted to provide interpolated $\tilde{\mathcal{V}}$. Let $q \notin \mathcal{W}$ be a new k-point, and b point to its neighbors on the original k-mesh, $q + b \in \mathcal{W}$. Now we can keep P_{q+b} fixed and use it as a boundary condition to compute $Z(q)$ and hence $\tilde{\mathcal{V}}(q)$.

Recall that the sum over b and weights g_b stem from the finite-difference formulas [Mos+08b, Eqs. (8) and (9)]

$$\nabla f(k) = \sum_b g_b b [f(k+b) - f(k)] + \mathcal{O}(b^2), \quad (6.37)$$

$$|\nabla f(k)|^2 = \sum_b g_b [f(k+b) - f(k)]^2 + \mathcal{O}(b^3), \quad (6.38)$$

where b is the k-mesh spacing. These expressions are valid under the condition that [Mos+08b, Eq. (26)]

$$\sum_{\mathbf{b}} g_{\mathbf{b}} b_{\alpha} b_{\beta} = \delta_{\alpha\beta}. \quad (6.39)$$

Wannier90 ensures this in the following way: Add shells of neighbors with increasing $|\mathbf{b}|$. Compute the $N_{\mathbf{b}}$ weights by interpreting (6.39) as a linear system of equations and solving for $g_{\mathbf{b}}$. Stop when (6.39) is satisfied.*

This procedure is applicable with little or no change also for an arbitrary point \mathbf{q} , and so it should be possible to construct interpolated $\tilde{\mathcal{V}}(\mathbf{q})$; however, the random-phase problem will apply here, as well.

6.3. Numerical results for the optical conductivity

The tests on the momentum matrix elements $V^{\alpha}(\mathbf{R})$ and $W^{\alpha\beta}(\mathbf{R}, \omega)$ presented in the preceding section are insightful precisely because they address the interpolated quantities directly. However, we have yet to address the bottom line: how the observable, k-integrated, quantities are affected. The random-phase problem in the case of \mathcal{U} interpolation in particular can only be quantified in this way. In this section, optical conductivities (including the dc conductivity as the $\Omega \rightarrow 0$ limit) computed using the different approaches will be compared. SrVO_3 will be used as a testbed material throughout. A noninteracting model and other limiting cases where certain sources of error are known to be absent provide a basis for the analysis.

Unless noted otherwise, the Wannier projections were made on a $9 \times 9 \times 9$ k-mesh, consequently $V^{\alpha}(\mathbf{R})$ and $W^{\alpha\beta}(\mathbf{R}, \omega)$ were constructed on a $9 \times 9 \times 9$ supercell. This size was chosen so that the quantities in the Wannier gauge are relatively well converged, while the computational effort remains manageable. In particular, the Wannier Hamiltonian is well converged on this mesh, as is $V^{\alpha}(\mathbf{R})$ (cf. Fig. 6.6). $W^{\alpha\beta}(\mathbf{R}, \omega)$ is reasonably well converged at favorable frequencies (cf. Fig. 6.7) but perhaps less so at unfavorable ones (cf. Fig. 6.10). All results are converged with respect to the integration k-mesh.

* For the linear system of equations to be solvable, it is sufficient but not necessary to have 6 linearly independent \mathbf{b} vectors.

6.3.1. Noninteracting models

The noninteracting optical conductivity is an important test case, where “noninteracting” means that only a small imaginary self-energy is added to the WIEN2k bands for broadening, $\Sigma \leftarrow -i\delta$. On the one hand, the random-phase problem in the \mathcal{U} interpolation approach is absent (by the same argument as for the $\mathcal{T}_{\psi\psi}$ term in (6.8), i.e., that the matrix spectral function is diagonal in the Bloch basis). On the other hand, the WOPTIC results can be directly compared to WIEN2k’s `optic` module.

Adaptively integrated results

Fig. 6.11 shows a comparison of the WIEN2k result to four variants of WOPTIC, which ideally should all be identical:

- (N1) WIEN2k `optic` — black line and shaded,
- (N2) P-3 projection with interpolated $\mathcal{U}(\mathbf{k})$ and matrix elements from `optic` — purple line,
- (N3) P-14 projection with interpolated $\mathcal{U}(\mathbf{k})$ and matrix elements from `optic` — red line,
- (N4) P-3 projection with interpolated momentum matrix elements $V^\alpha, W^{\alpha\beta}$ — green line,
- (N5) P-14 projection with interpolated momentum matrix elements V^α — blue line.

Note that each WOPTIC calculation takes into account the same 14 bands (O-p and V-d); P-14 includes all of them as WF (i.e. there are only w-w transitions in (N3) and (N5)), while P-3 includes only the V- t_{2g} states as WF, and the other states in the form of ψ - ψ and w- ψ transitions.

As a first observation, there is reasonable agreement between `optic` (N1) and the WOPTIC curves (N2), (N3), and (N5). Up to frequencies ~ 4 eV, the curves match well; for larger frequencies, deviations are expected because transitions outside of the WOPTIC window become relevant. The comparison of WOPTIC to `optic` has already been addressed previously [Ass+15; Wis12]; the remaining differences can be attributed to temperature (the WOPTIC calculations were done at $\beta = 40$ eV $^{-1}$ while `optic` works in the ground

6. Woptic: optical conductivity with MLWF

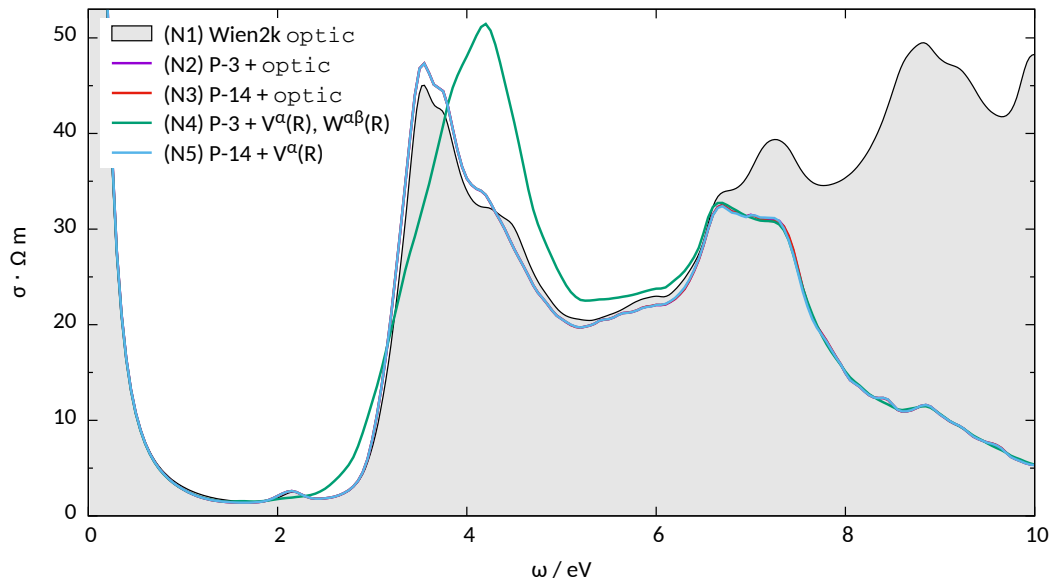


Figure 6.11.: Noninteracting optical conductivity computed by WIEN2k's optic compared with different variants of WOPTIC. See text for details.

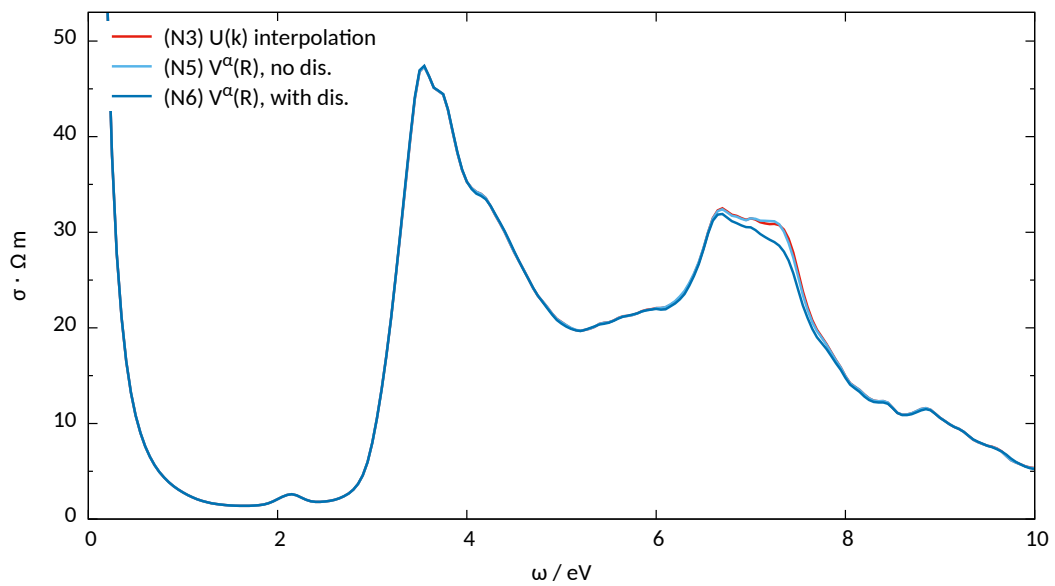


Figure 6.12.: Noninteracting optical conductivity computed from P-14 projections with and without disentanglement. See text for details.

state) and the different broadening schemes. In any case, the focus here is on the relative performance of the momentum matrix element interpolation and $\mathcal{U}(\mathbf{k})$ interpolation.

Moreover, curves (N2), (N3), and (N5) are almost identical. This shows that Wannier interpolation for the w-w transitions works well, and that the different Wannier projections introduce no change in the optical conductivity. (Recall that the *raison d'être* of the V^α and $W^{\alpha\beta}$ interpolation, the random phase problem, is absent in this noninteracting case.)

Conversely, curve (N4) clearly shows interpolation errors in the region where w- ψ transitions are important (approximately 2 to 6 eV). We will have a closer look at these errors in Fig. 6.13.

But first, to test the procedure for disentanglement taking into account w-w transitions only as outlined in Sec. 6.2.3. Fig. 6.12 adds another:

(N6) P-14 with disentanglement and interpolated momentum matrix elements V^α — dark blue line.

The agreement of this curve with the others is within reasonable expectations. The differences introduced by disentanglement are small and mostly contained in a narrow region around $\omega \approx 7$ eV, corresponding to transitions around the R-point (the only region where disentanglement is active, cf. Fig. 6.3). Since the models with and without disentanglement represent slightly different physics, they cannot be expected to yield identical results.

Contributions by subspace

The curves shown in Fig. 6.11 were calculated by converging WOPTIC on an adaptive k-mesh. This has the advantage that it corresponds to the intended usage of the code; the disadvantage is that, if there is disagreement between the different modes, the adaptively refined k-meshes will likewise be different, which could distort the intrinsic differences. Therefore, Fig. 6.13 shows the noninteracting optical conductivity obtained with uniform refinement, separated into w-w, w- ψ , and ψ - ψ contributions. For each contribution, two curves are shown, corresponding to (N2) and (N4) above. The logarithmic scale serves to show all the contributions in one plot, but since it may obscure the magnitude of disagreement between the curves, the relative errors between the two approaches are shown in a lower panel. Fig. 6.13 confirms that the divergence of (N4) from the other curves in Fig. 6.11 is due to the

6. Woptic: optical conductivity with MLWF

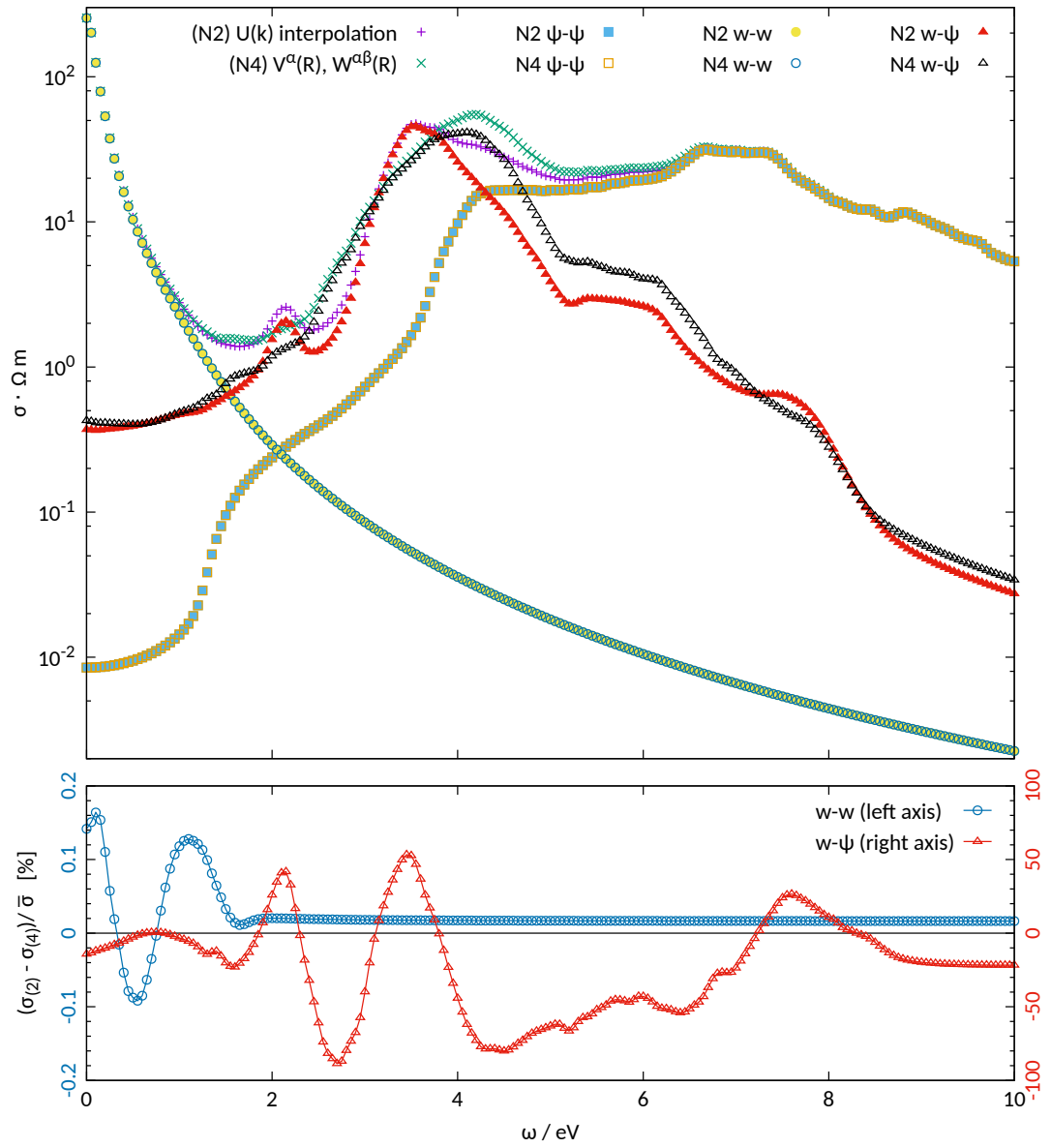


Figure 6.13.: Contributions to the noninteracting optical conductivity on a uniform k -mesh, using momentum matrix elements from `optic` (with interpolated $U(\mathbf{k})$; exact in this case), and from $V^\alpha(\mathbf{R}), W^{\alpha\beta}(\mathbf{R}, \omega)$. The lower panel shows the relative errors of the w-w and w- ψ contributions (note the different scales). The ψ - ψ contributions are identical by design.

w - ψ contribution. In particular, we see that both the peak at $\omega \approx 2$ eV which (N4) misses almost entirely, and the second, larger peak at $\omega \approx 4$ eV, which is shifted and distorted in (N4), are dominated by mixed transitions.

6.3.2. Interacting models

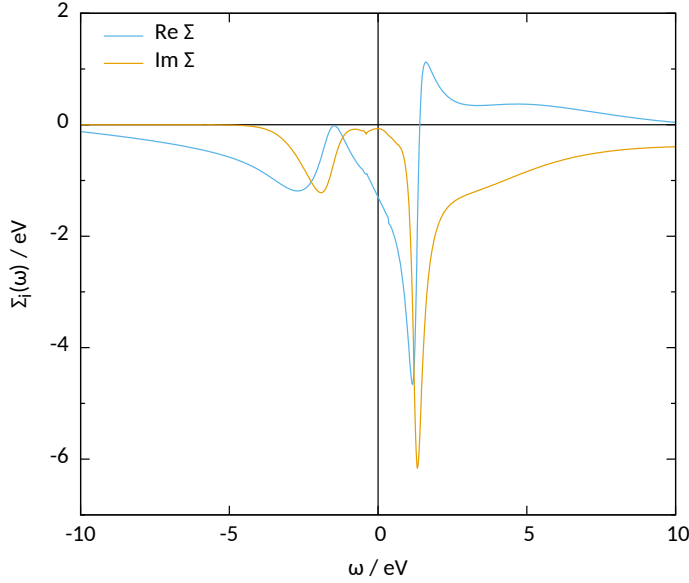


Figure 6.14.: DMFT Self-energy of SrVO_3 , Wick-rotated to the real axis using MAXENT [Ass+15; Wis12]. The model is derived from a P-3 projection. Only the self-energy for one band is shown since the other two are identical within the uncertainties of the method.

A nontrivial self-energy $\Sigma(\omega)$ will now be added. The self-energy (shown in Fig. 6.14) is taken from a DMFT calculation using a 3-band model for SrVO_3 [Ass+15; Wis12]. For testing purposes it will also be applied to the d-orbitals of the P-14 projections, even though this is unphysical. To discuss the different WOPTIC variants, let us use the following labels in analogy to the noninteracting case:

- (I2) P-3 model with interpolated $\mathcal{U}(\mathbf{k})$ and matrix elements from optic
- (I3) P-14 model with interpolated $\mathcal{U}(\mathbf{k})$ and matrix elements from optic
- (I4) P-3 model with interpolated momentum matrix elements $V^\alpha, W^{\alpha\beta}$
- (I5) P-14 model with interpolated momentum matrix elements V^α
- (I6) P-14 with disentanglement and interpolated momentum matrix elements V^α

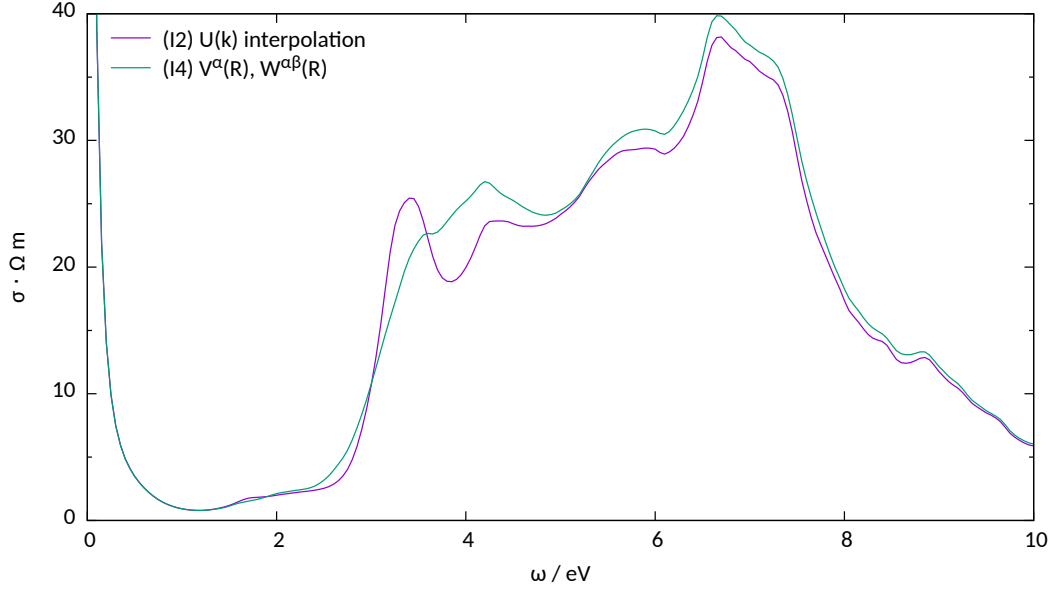


Figure 6.15.: Optical conductivity for the interacting P-3 model computed on an adaptive k-grid using matrix elements from `optic` (with interpolated $\mathcal{U}(k)$; exact in this case), and interpolated matrix elements.

But note that (I2)/(I4) can no longer be expected to agree with (I3)/(I5), since the orbitals to which the self-energy is applied have different character.

Fig. 6.15 shows the optical conductivity of the P-3 model, the exact curve (I2) compared to (I4). Again, interpolation errors are clearly visible, albeit apparently smaller than in the noninteracting case. The individual contributions, shown in Fig. 6.16, reveal that this impression is somewhat misleading. In the region where the mixed transitions are important, the error is in fact similar, but it is masked by the w - w contribution, which is larger here than in the noninteracting case. On the other hand, the small peak at $\omega \approx 2$ eV in the w - ψ contribution is reproduced better in the interacting case.

Even with the ω -dependent self-energy included, the random-phase problem has so far been absent. This is because in this cubic material, the self-energy is orbital-independent (up to numerical accuracy from the QMC and analytic continuation), and therefore the argument from the diagonal spectral function in the Bloch basis still holds. Therefore, we have been able to use the results with momentum matrix elements from `optic` as a reference against

6.3. Numerical results for the optical conductivity

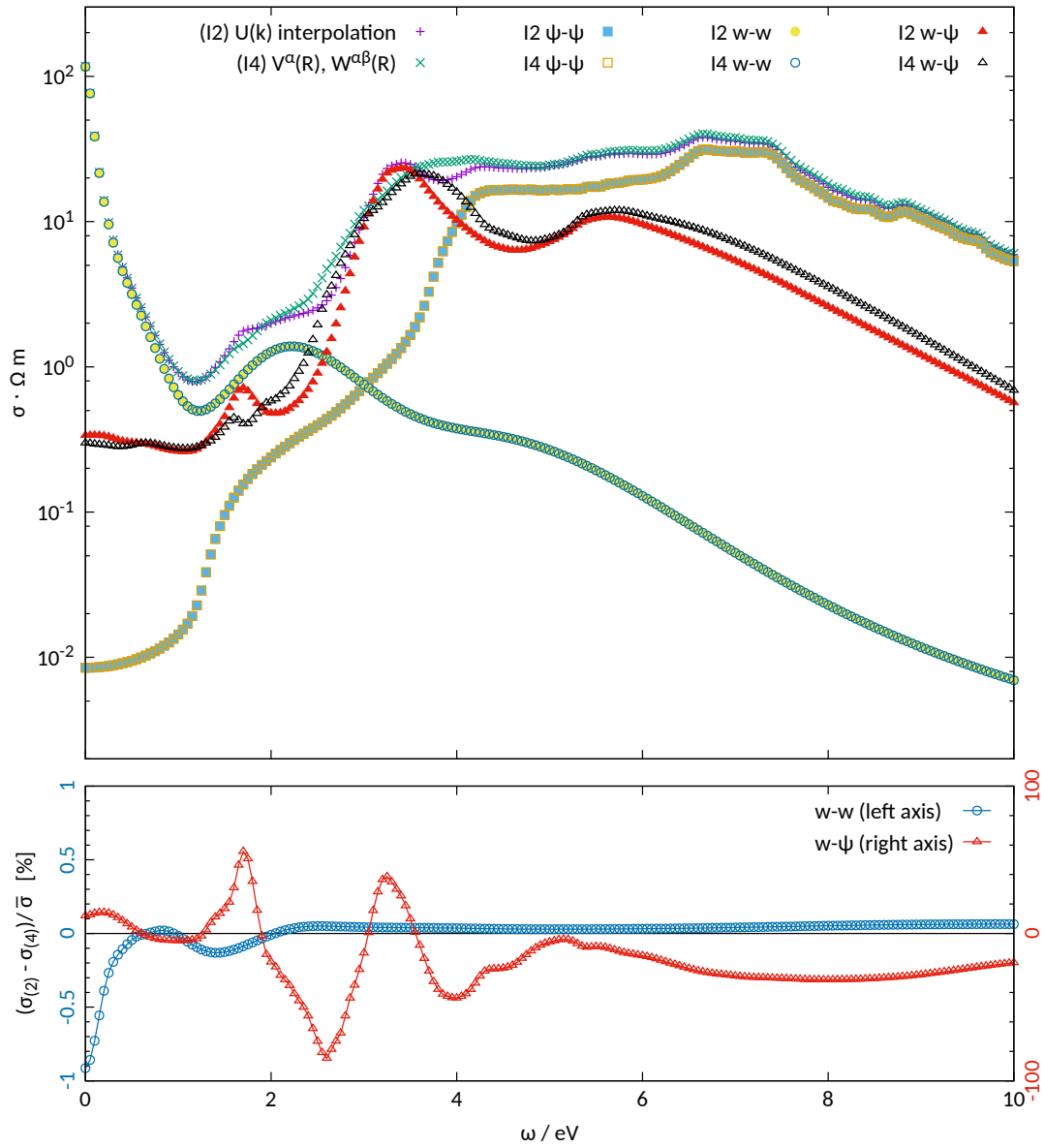


Figure 6.16.: Like Fig. 6.13, but including a nontrivial self-energy.

which the results from interpolated matrix elements could be compared.

Turning to P-14, this situation is reversed. Since we have satisfied ourselves that the Wannier interpolation for V^α is accurate, and since no mixed transitions are involved, we can rely on (15) as a reference, while (13) suffers from the random-phase problem. These results are shown in Fig. 6.17. In comparison with Fig. 6.15, the errors introduced by the random-phase problem and those introduced by the $W^{\alpha\beta}$ interpolation are similar in magnitude. The effect of disentanglement on (16) is quite similar to the noninteracting case (Fig. 6.12).

Using the original $\mathcal{U}(k)$

Up to now, the only results for the interacting P-14 model that can be considered reliable have come from matrix element interpolation (15). For independent confirmation, the original $\mathcal{U}(k)$ constructed by Wannier90 can be used together with the momentum matrix elements on the same k-mesh, thus ensuring that all the phases fit together. This approach is impractical for production usage because only the Wannier k-mesh can be used, which is a severe restriction for the optical conductivity; but as a test case, it will serve.

In Fig. 6.18, the curve

- (17) P-14 model with momentum matrix elements from `optic` and $\mathcal{U}(k)$ from Wannier90 — orange dots.

is indistinguishable from the result obtained with V^α interpolation (15). We may conclude that the differences between (13) and (15) are indeed due to the random-phase problem.

6.3. Numerical results for the optical conductivity

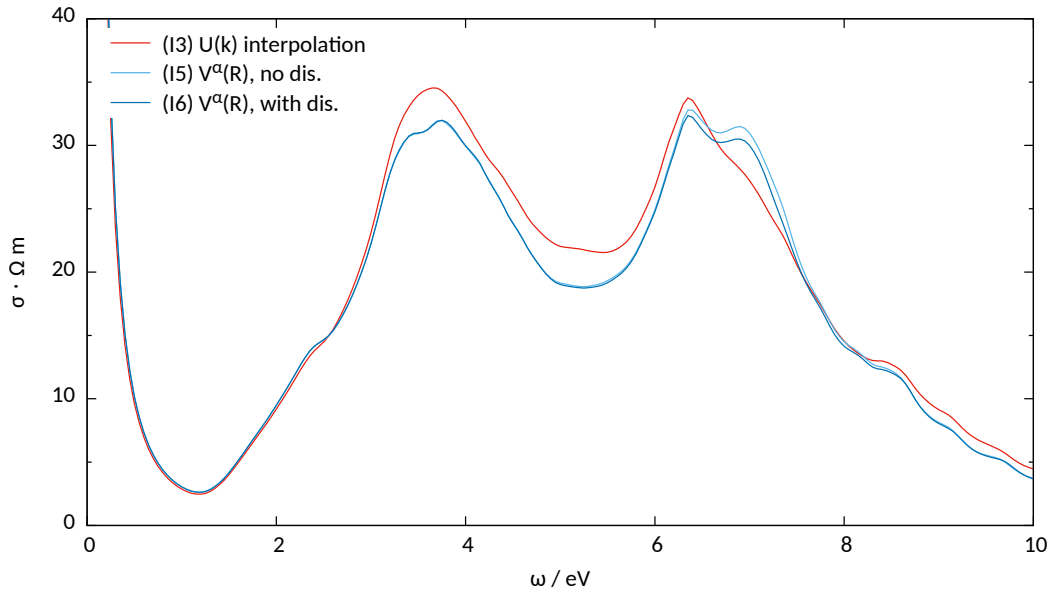


Figure 6.17.: Optical conductivity for the interacting (unphysical) P-14 model computed using matrix elements from optic (with interpolated $\mathcal{U}(k)$), and interpolated matrix elements (exact in this case), with and without disentanglement.

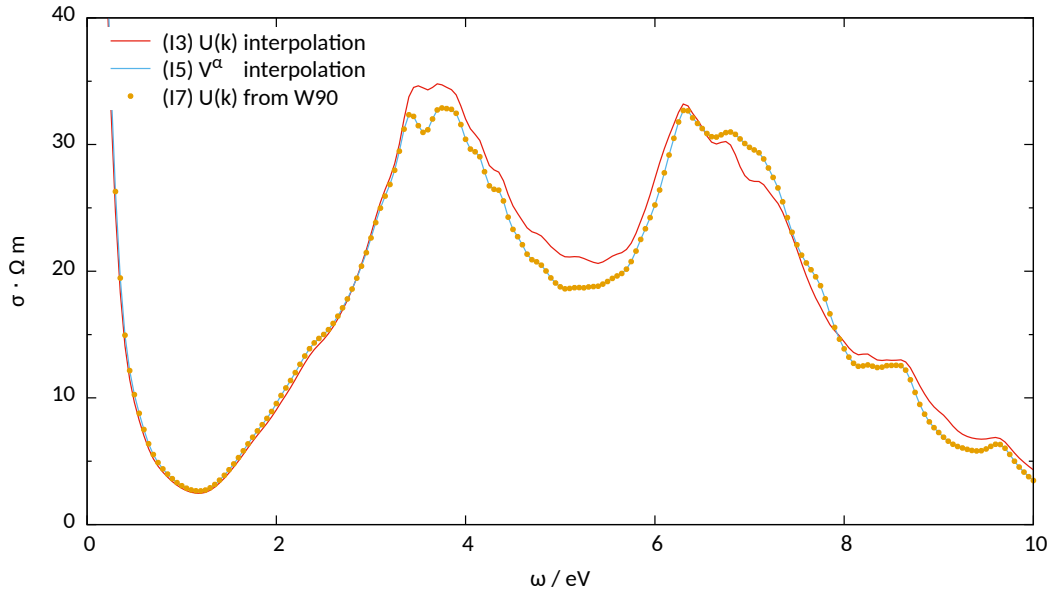


Figure 6.18.: Optical conductivity for the interacting P-14 model computed with the original $\mathcal{U}(k)$ compared to the “standard” methods on the same k-grid. This calculation was done on a $16 \times 16 \times 16$ k-grid.

6.4. Discussion and outlook

WOPTIC is an algorithm and program package to calculate optical conductivities and related quantities from WIEN2k+DMFT calculations. With the relevant theory and the adaptive k-integration already in place [Ass+15; Wis12], the remaining obstacle was the random-phase problem that appeared because of the need to interpolate the WF to k-points not included in the original Wannier k-mesh.

Wannier interpolation of the momentum matrix elements V_{uv}^α proved a reliable and practical solution as far as transitions within the Wannier subspace are concerned. However, the generalization to Wannier-Bloch transitions is somewhat problematic. In the typical case where all bands that cross the Fermi level are described by the WF, this means that the problem affects only the optical conductivity, since for the static quantities (dc conductivity and thermopower), only Wannier-Wannier transitions are relevant.

The random-phase problem is absent when the self-energy is orbital independent, either by symmetry or because there is no DMFT self-energy (i.e., correlations are treated on the DFT level). When this restriction is relaxed, the numerical tests presented here indicate that errors from the phase problem and from Wannier interpolation of the mixed transitions are comparable. In either case, the important qualitative features of the optical conductivity are preserved. In practical LDA+DMFT calculations, the errors must be seen with respect to uncertainties stemming from the impurity solver and the analytic continuation of the self-energy, which can easily be dominant.

Finally, note that the random-phase problem is not caused by the adaptive integration as such. For practical purposes, the k-mesh on which the optical conductivity is integrated has to be finer than the Wannierization k-mesh, and the matrix elements on additional k-points are required, be it on a uniform or an adaptive grid. Also, the problem is not in principle limited to the optical conductivity. Any quantity that depends on the phases of the WF (through some matrix element $O_{uv}(\mathbf{k})$ which is not paired with $O_{vu}(\mathbf{k})$) would be similarly affected.

A complete solution to the random-phase problem would likely necessitate moving away from MLWF, e.g. to projector WF [Ani+05; Ku+02], which are fast to compute on arbitrary k-points (including disentanglement), or possibly the recently proposed *optimized projection function method* [Mus+15].

Apart from that, potentially fruitful directions for future work on WOPTIC

include

- Incorporating disentanglement in the general case. Currently, cases with disentanglement are limited to Wannier-Wannier transitions as described in Sec. 6.2.3. However, given our observations in Sec. 6.2.3, it is unclear how this would be done.
- More straightforward is the generalization to a k -dependent self-energy $\Sigma(\mathbf{k}, \omega)$ (e.g. from a GW calculation). This requires no change in the WORTIC formalism, only an interpolation of the self-energy to the new k -points.
- In a more theoretical vein, it is unclear why the mixed momentum matrix elements $W^{\alpha\beta}$ are essentially real-valued and as localized as they are.

Part III.

Results on Correlated Heterostructures

7. The $\text{LaVO}_3|\text{SrTiO}_3$ heterostructure

Oxide heterostructures are artificial materials made up from oxygen anions and metal cations, combined by *stacking* different materials in various arrangements. Even in an idealized, defect-free heterostructure, there is a lot of freedom in the arrangement, for instance in the direction of stacking relative to the crystal structure, usually denoted using Miller indices $[hkl]$; in the *interface* and *surface termination* (i.e., which atomic layers lie at the interface and surface); or in the stacking sequence (e.g., *thin-films*, where a substrate is coated with a layer of another material, versus *multilayers*, where a sequence of materials is repeated). All of these distinctions can be essential for the properties of the resulting sample.

The interest in these materials comes from the flexibility with which they may be designed, coupled with the observation of phenomena in heterostructures which are absent from their constituents [Hwa+12]. An early instance was the discovery of a conducting interface layer in the polar heterostructure $\text{LaAlO}_3|\text{SrTiO}_3$ (i.e. a film of lanthanum aluminate on a strontium titanate substrate) [OHO4; Oht+02]. This effect is commonly attributed to a potential gradient that develops in the heterostructure due to the polar nature of the LaAlO_3 layers when stacked in the $[001]$ direction; it only occurs in the $\text{TiO}_2|\text{LaO}$ terminated (“n-type”) interface, but not in the alternative $\text{SrO}|\text{AlO}_2$ (“p-type”) interface.

In a first publication [Ass+13] (reproduced in App. B.4), we proposed polar oxide heterostructures in general and $\text{LaVO}_3|\text{SrTiO}_3$ in particular as novel absorber materials for high-efficiency photovoltaic (PV) cells. The first criterion for an efficient PV absorber is the band gap Δ , which must have the proper relation to the solar spectrum. On the one hand, photons with energy $\omega < \Delta$ cannot be absorbed. On the other, photo-generated electrons and holes typically relax to the band edges before they can be extracted. Therefore, each photon with $\omega \geq \Delta$ contributes only an energy Δ . A simple detailed-balance calculation based on these principles yields the *Shockley-*

7. The $\text{LaVO}_3|\text{SrTiO}_3$ heterostructure

Table 7.1: Lattice constants of bulk SrTiO_3 (cubic) [LPM07] and LaVO_3 (orthorhombic). a and b are the in-plane $\sqrt{2}$ lattice parameters, while c is the BO_2 -plane separation.

	$a/\text{\AA}$	$b/\text{\AA}$	$c/\text{\AA}$
SrTiO_3	5.523	5.523	3.905
LaVO_3	5.539	5.560	3.907

Queisser limit of conversion efficiency η as a function of the band gap, with an optimum or $\eta \approx 38\%$ at $\Delta \approx 1.4\text{ eV}$ [SQ61; Wik15c].

The character of the gap is also relevant: direct gaps (where the top of the valence band and the bottom of the conduction band occur at the same crystal momentum) are preferred. Let the Δ_d be the direct and $\Delta_i \leq \Delta_d$ the indirect gap. Because photons carry almost no momentum, only those with $\omega \geq \Delta_d$ can be absorbed,* but due to thermal relaxation, only an energy Δ_i can be harvested per electron-hole pair in a conventional pv cell.

Thus, the main motivation to choose lanthanum vanadate (LaVO_3) as an active material is its direct band gap of 1.1 eV [AT95; ATT93].[†] SrTiO_3 is a well-controlled and frequently used substrate for oxide heterostructures, and a good fit for LaVO_3 in terms of lattice constants (see Table 7.1) [Bor+93; LPM07]. Furthermore, $\text{LaVO}_3|\text{SrTiO}_3$ heterostructures have already been synthesized [He+12; HSH07; Kou+07; Rot+14a; Rot+14b]. Observations of a pv effect in related polar heterostructures [Guo+13; Lia+13; Zha+15], and in LaVO_3 thin films on an amorphous substrate [Wan+15] have appeared meanwhile.

To mitigate losses to thermal relaxation, two approaches are commonly considered: First, materials with different band gaps may be combined in a *multijunction pv cell* [Bed+78; Jac55; Jac60], such that high-energy photons may be converted efficiently by a wide-gap material on the light-facing side, while lower-energy photons may still be absorbed in subsequent layers with narrower gaps. Oxide heterostructures should provide a particularly flexible framework to construct multijunction cells; for instance, LaVO_3 might be efficiently combined with lanthanum orthoferrite (LaFeO_3) with $\Delta = 2.2\text{ eV}$ [Ass+13; AT95; ATT93].

The second approach is to make use of the carriers' excess energy before

* For a "non-vertical" excitation (i.e., with a finite momentum difference between particle and hole state), a phonon-assisted absorption process is necessary. These are, however, usually strongly suppressed.

[†] About the same value as in crystalline Si. But there, the gap is indirect, which is why Si pv cells have to be rather thick.

they thermalize. This is called *hot-carrier extraction* [KF12; RN82] and requires a very fast extraction process. The strong potential gradient in polar heterostructures, which accelerates electrons and holes in opposite directions, may support this ultrafast extraction [EW14a; EW14b]. Additionally, it has been argued that in a Mott insulator such as LaVO₃, a single incident photon may yield more than one electron-hole pair [Man10; WHE14], providing another mechanism by which energy in excess of Δ might be recovered.

Finally, metallic states emerge at the interface and possibly surface of the polar heterostructure on a thickness of about one unit cell, which provide natural contacts.

It has been argued that heterostructures involving strongly correlated materials have even greater potential for interesting physics and applications [MS10; OMO4a]. On the theoretical side, such heterostructures necessitate a more elaborate description of electronic interaction than the LDA and similar approximations can provide. Thus, LDA+DMFT has been adapted to these materials [ILO8; LBG13; Lec+14; LO15; OMO4b; Si+15; Zho+15].

The Mott insulator LaVO₃ (see next section for details) is a strongly correlated material [DPA07]. However, in [Ass+13], LaVO₃|SrTiO₃ was described only in LDA+U. A better treatment of correlations is desirable, especially so in the heterostructure, because (1) correlations may be enhanced due to the reduced symmetry, and (2) spin order must be introduced to obtain an insulating phase in LDA+U. While bulk LaVO₃ is indeed antiferromagnetic (AF) at low temperatures, it is paramagnetic (PM) at higher temperatures. In the heterostructure, spin order may be suppressed also at lower temperature.

In this chapter, DMFT results for the LaVO₃|SrTiO₃ heterostructure are presented, as well as more details on the LDA+U calculations of [Ass+13], especially with regards to lattice relaxation.

7.1. Bulk SrTiO₃ and LaVO₃

Both LaVO₃ and SrTiO₃ have a perovskite-type crystal structure, where each transition metal atom M ($M = \text{Ti}, \text{V}$) is surrounded by an octahedron of oxygen ligands; these MO_6 octahedra can be viewed as the building blocks of the crystals. While SrTiO₃ is cubic, LaVO₃ exhibits a distortion of the gadolinium-orthoferrite (GdFeO₃) type, i.e. the VO₆ octahedra are both tilted away from and rotated about the z -axis; the structure is orthorhombic at

Figure 7.1.: Crystal structures of SrTiO_3 (left) and LaVO_3 (right). On the left, the TiO_6 octahedra are shown. On the right, the red/blue lobes show the t_{2g} spin \uparrow/\downarrow electron density. Thus the lobes' colors show the AF-C spin order, their shape and orientation the AF-G orbital order. For LaVO_3 , we show the unit cell, which contains 4 V atoms; for SrTiO_3 , a matching supercell.

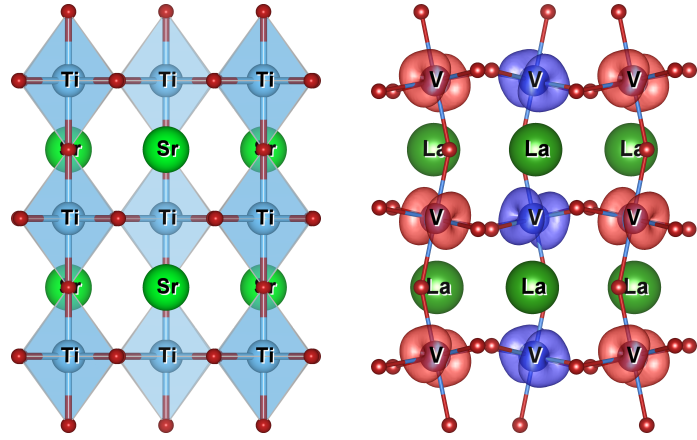
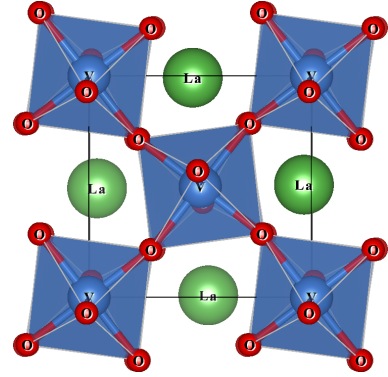


Figure 7.2.: VO_6 octahedra in bulk LaVO_3 . The rotation and tilt of the octahedra shows the GdFeO_3 -type distortion in this material.



room temperature and slightly monoclinic ($\gamma = 90.129^\circ$) below ~ 100 K. Both crystal structures are shown in Fig. 7.1; Fig. 7.2 provides a clearer view of the octahedron rotation in LaVO_3 .

This structure leads to e_g - t_{2g} splitting (exact in the cubic case, a good approximation in the distorted case). In both materials, the relevant degrees of freedom are the M - t_{2g} states. The O-p states at lower energies are full, the M - e_g states at higher energies are empty.

Both materials are insulating, but the electronic configuration is different: SrTiO_3 is a d^0 band insulator with a gap of about 3.2 eV, LaVO_3 is a d^2 Mott insulator with a gap of about 1.1 eV [ATT93]. Below ~ 140 K, LaVO_3 develops AF-C spin order (ferromagnetically stacked antiferromagnetic planes) and AF-G orbital order (alternating in all directions) channels (shown in Figs. 7.1 and 7.3) [Bor+93]. The same spin order is also used in the heterostructure LDA+U calculations.

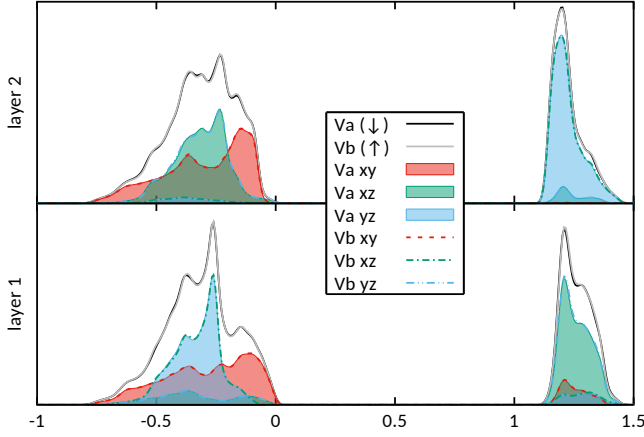


Figure 7.3.: Bulk LaVO_3 DOS computed in LDA+U, showing the C-type antiferromagnetic (AF-C) spin and G-type antiferromagnetic (AF-G) orbital order. For each of the four V atoms per unit cell, the majority spin DOS is shown (solid lines), resolved by orbital (dashed lines for one atom, shaded regions for the other). The rows correspond to the two layers in z -direction. The xy DOS is flatter than the others, and occupied on every atom, while xz and yz are narrower and alternately occupied.

7.2. Models and methods

For the DFT calculations, WIEN2k [Bla+01] and the PBESOL GGA functional [Per+08] are employed. Where LDA+U is used (more precisely, GGA+U), the interaction parameters $U_{\text{Ti}} = 9.8 \text{ eV}$ and $U_{\text{V}} = 3 \text{ eV}$ are chosen to reproduce the experimental band gaps in the bulk. This is essential for a valid description of the band alignment in the heterostructure. The large U_{Ti} is necessary because the Ti-d states are almost empty, and consequently the effect of U_{Ti} is relatively small.

To obtain a single-particle Hamiltonian for DMFT, we first converge a GGA calculation with the respective structure, including full optimization of atomic positions (see below), then construct MLWF [MV97] using WIEN2WANNIER [Kun+10] and Wannier90 [Mos+08a]. Due to the complicated band structures, disentanglement [SMV01] is essential to obtain faithful Wannier projections for the heterostructures. The resulting Wannier Hamiltonian is augmented by a Kanamori interaction operator with the parameters $U = 5 \text{ eV}$, $J = 0.7 \text{ eV}$, and $U' = U - 2J = 3.6 \text{ eV}$ on the V sites and solved at an inverse temperature of $\beta = 30 \text{ eV}^{-1}$ with 2 electrons per V site. Interactions on the Ti sites (expected to be empty) are treated in a Hartree mean-field scheme using the same parameters as for V.

For the DMFT calculations, we use the w2dynamics package [Par+12] with its CTQMC impurity solver [Gul+11] and analytic continuation from Matsubara frequencies to the real axis using MAXENT [JG96; San98].

To discuss heterostructure geometry, let us introduce a number of defini-

tions. We choose a global coordinate system such that, when a transition metal ion M is at the origin, its 6 O neighbors will lie on the coordinate axes, up to distortion from the cubic structure, with the z -axis perpendicular to the interface. We number layers of substrate and active film along the z -axis with 0 and 1 being the substrate and active-film layers adjacent to the interface. Layers always refer to transition metal atoms M ($M = \text{V}, \text{Ti}$) with the same z coordinate (up to structural relaxation), never to slabs of bulk unit cells, which might comprise more than a single layer.

In [Ass+13], we considered heterostructures in two different geometries: “multilayer” structures with periodic boundary conditions (PBC), and “thin-film” structures where the PBC in z direction are effectively broken by including a slab of vacuum between the “top” of the active layer and the “bottom” of the substrate, resulting in quasi-open boundary conditions (OBC) in z direction (technically, PBC are always in effect in WIEN2k). The DMFT calculations presented here are mostly in the thin-film setup.

Unit cell size is another crucial characteristic of models for heterostructures. At least three different extents must be taken into account: The number N of layers in the active film, the number M of substrate layers, and the number d of inequivalent M atoms per layer. To express the geometric information compactly, the notation $N|M \times d$ - b will be used, where b is “p” for PBC and “o” for OBC.

To provide a realistic model, M must be large enough for the substrate to relax to bulk-like properties. The in-plane size d should be large enough to allow for the relevant reconstruction at the interfaces as well as in-plane ordering. The film thickness N should also be “big enough”, although films can be quite thin also in experiments. In OBC structures, the vacuum should be sufficiently thick. Here, vacuum slabs of $20 a_0 \approx 10.6 \text{ \AA}$ are used, i.e., the z -extent of the heterostructure unit cell is enlarged by this amount with respect to the corresponding stack of bulk unit cells.

The distortion from the cubic perovskite structure in LaVO_3 has important consequences for the compound’s electronic structure [DPA07]; similar findings have been made for heterostructures [OMS06]. Therefore, in all heterostructure calculations, the atomic positions are optimized using the MSR1A method [Mar13] implemented in WIEN2k. In the process, OBC structures may relax into the vacuum region, whereas PBC structures are optimized in a fixed volume. Structures for the LDA+DMFT calculations were optimized in PM GGA, those used in LDA+U in the insulating, AF phase.

In LDA+U it is clear that $d \geq 2$ is necessary to allow AF spin and orbital order in LaVO_3 , which in turn is required to obtain an insulating solution within the method. On the other hand, to describe a PM insulator in LDA+DMFT, $d = 1$ is sufficient (see Fig. 7.9). However, to allow the GdFeO_3 -type distortion seen in bulk LaVO_3 , as well as orbital ordering, we use $d = 2$ with a $\sqrt{2} \times \sqrt{2}$ supercell in the xy plane in all cases.

7.3. Structural relaxation and DFT results for $\text{LaVO}_3|\text{SrTiO}_3$

All heterostructures presented in this chapter were subject to full structural relaxation within LDA+U or GGA. Let us now discuss the effects of this relaxation on the $4|6 \times 2$ structures of [Ass+13] (relaxed using LDA+U) and the $4|4 \times 2$ -o structure used in LDA+DMFT (relaxed in GGA).

Consider first the $4|6 \times 2$ -p structure in LDA+U, shown in Fig. 7.4 (top). The M -O- M bond angle as a function of layer is depicted in Fig. 7.5 (top). In the SrTiO_3 layers, it is around 170° and fairly constant, but reduces to around 155° in the LaVO_3 layers. This is close to the bulk value for that material. At the p-type interface there is an even more abrupt change back to 170° at layer 4. The deviation of these angles from 180° , and in particular the staggered pattern of the four inequivalent angles per layer, is indicative of GdFeO_3 -type distortion, which in the heterostructure develops also in the SrTiO_3 part.

On the other hand, the M - M layer distance, shown in Fig. 7.6, stays fairly constant close to the bulk value in the SrTiO_3 layers, but shows an almost linear decrease from 3.95 \AA to 3.85 \AA within the 4 V layers, as one would expect from a potential gradient.

A fairly similar picture emerges when a slab of vacuum is added ($4|6 \times 2$ -o structure, Fig. 7.4 [center]). The main changes are in the SrTiO_3 part: the GdFeO_3 distortion is weaker (see Fig. 7.5 (center)), and the layer distance (Fig. 7.6) deviates more from the bulk value (recall that while all atoms are free to move during relaxation, no volume optimization is performed, hence the total extent of the unit cell in z -direction is kept constant).

Turning now to the electronic structure, the potential gradient, conducting interfaces/surface, and AF order are clearly visible in the DOS, Fig. 7.7. In the multilayer, both interfaces support conducting V-d states on a single atomic

7. The $\text{LaVO}_3|\text{SrTiO}_3$ heterostructure

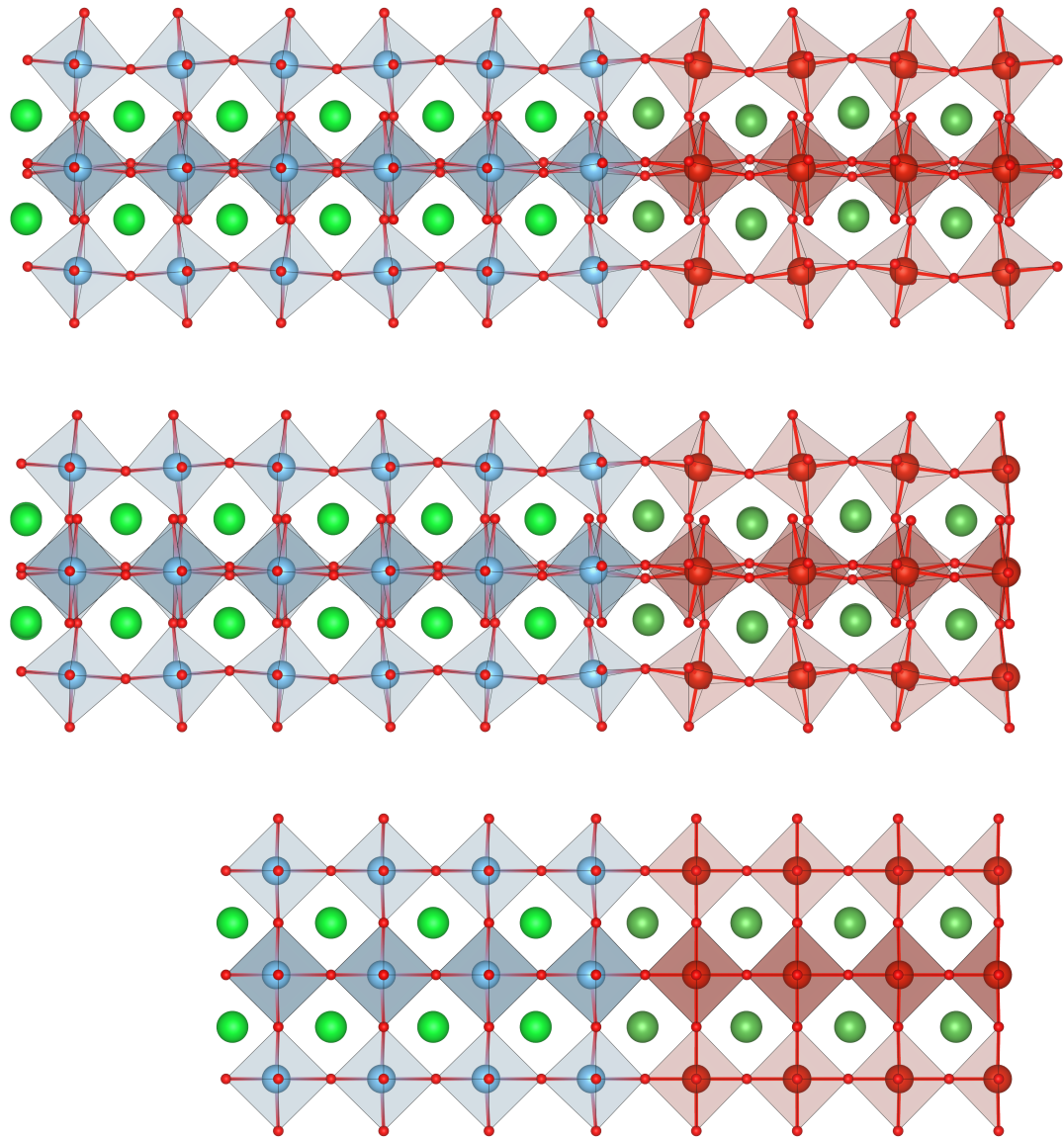


Figure 7.4.: Relaxed crystal structures of, top to bottom: $4|6 \times 2$ -p (AF), $4|6 \times 2$ -o (AF), and $4|4 \times 2$ -o (PM). Small red balls are O atoms, large red V, blue Ti, dark green La. The x and z axes lie in the plane of the picture.

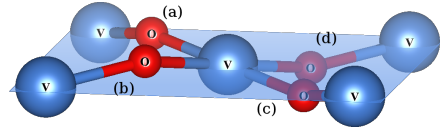
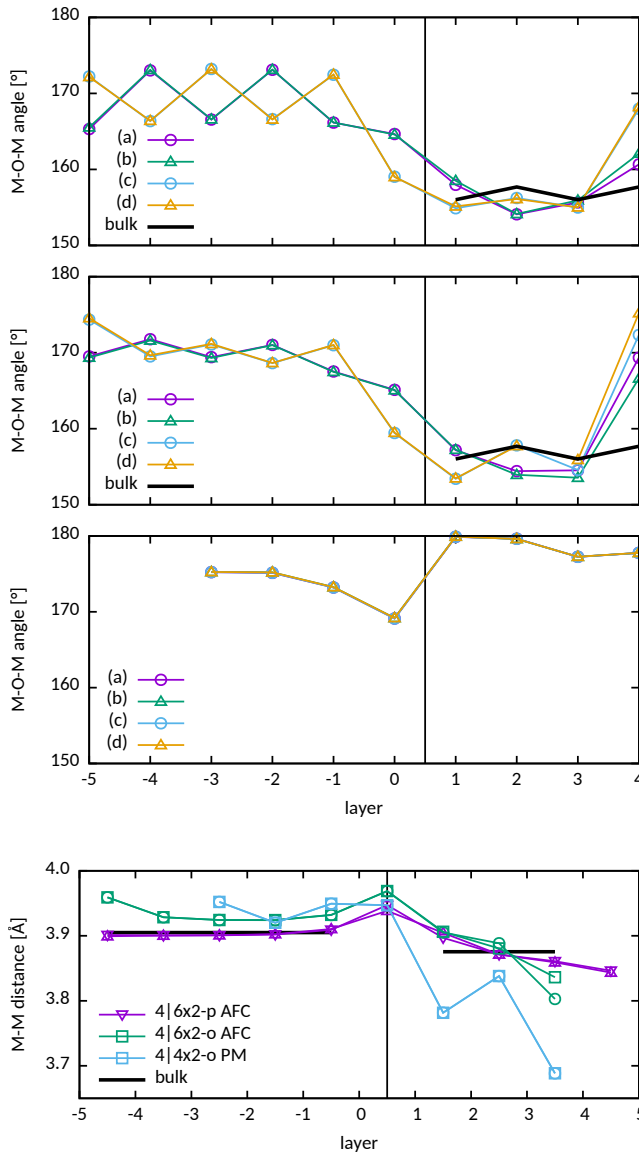


Figure 7.5.: In-plane M - O - M bond angles ($M = \text{V}$ or Ti) in different models of $\text{LaVO}_3|\text{SrTiO}_3$ and (in the top two panels) bulk LaVO_3 for comparison. There are four such angles per layer, labeled (a) through (d) as indicated above. Deviations from 180° indicate distortions away from the cubic structure; see text for further discussion. Top: $4|6 \times 2$ -p in LDA+U (AF, insulating). Center: $4|6 \times 2$ -o in LDA+U (AF, insulating). Bottom: $4|4 \times 2$ -o in GGA (PM, metallic). The vertical line marks the position of the n-type interface.

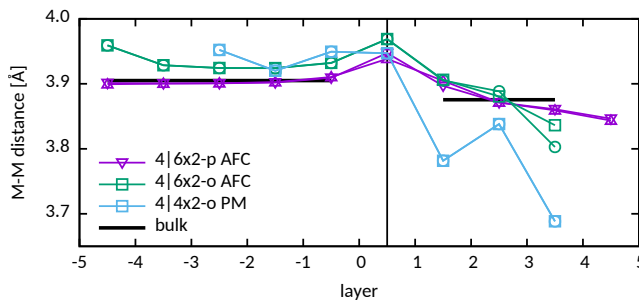


Figure 7.6.: M - M distances ($M = \text{V}$ or Ti) in different models for $\text{LaVO}_3|\text{SrTiO}_3$ compared to bulk values for SrTiO_3 and LaVO_3 . Two lines are shown for each structure, corresponding to the two atoms per layer. The vertical line marks the n-type interface.

layer. In the thin film, the interface is on the verge to metallicity (and would likely become metallic for a thicker film), but the surface has developed peaks at the Fermi energy. It is possible that these peaks are an artifact of the $\sqrt{2}$ unit cell in the xy plane, i.e., in a larger unit cell, they might be split by surface reconstruction, yielding an insulating surface at this thickness.

The GGA-relaxed structures are quite different. To begin, consider the $1|1 \times 1$ -p structure, arguably the simplest model for $\text{LaVO}_3|\text{SrTiO}_3$ within

7. The $\text{LaVO}_3|\text{SrTiO}_3$ heterostructure

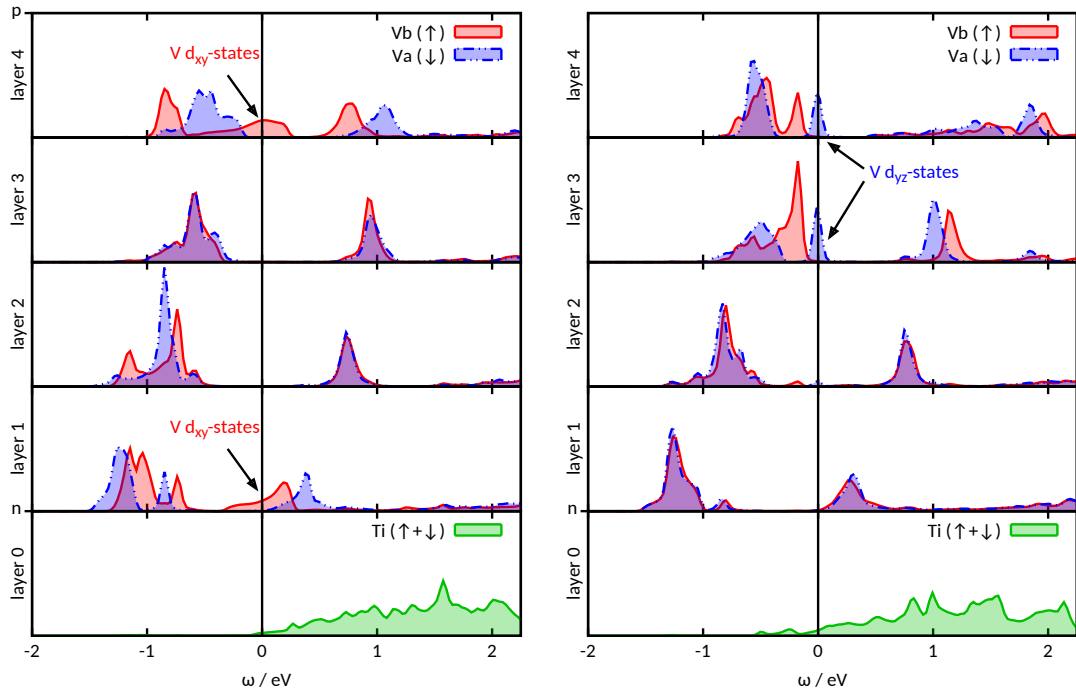


Figure 7.7.: Layer-resolved DOS of $\text{LaVO}_3|\text{SrTiO}_3$ within LDA+U. Left (reproduced from [Ass+13]): the $6|4\times 2\text{-p}$ multilayer structure, with both p- and n-type interfaces (both conducting). Right: the $4|6\times 2\text{-o}$ thin-film structure, with an n-type interface and a surface to vacuum. The models and computational details are those used in [Ass+13]. In each case, only one layer of substrate is shown.

the scheme outlined above. Its GGA band structure and relaxed crystal structure are shown in Fig. 7.8. With $d = 1$, the structure does not have the freedom to develop GdFeO_3 -type distortion. Instead, the V and Ti atoms move in opposite directions along the z-axis, resulting in an “antiferroelectric” distortion.

Next, the $4|4\times 2\text{-o}$ structure (Fig. 7.4 [bottom]) does have this freedom. However, an antiferroelectric distortion similar to $1|1\times 1\text{-p}$ is found instead. This is reflected in the staggered pattern seen in the M - M distances (Fig. 7.6). Superimposed on this, in the LaVO_3 part, we still see the linear decrease of layer distance attributed to the potential gradient, even with a larger slope than before. Correspondingly, the M - O - M angles (Fig. 7.5 (bottom)) show no GdFeO_3 distortion.

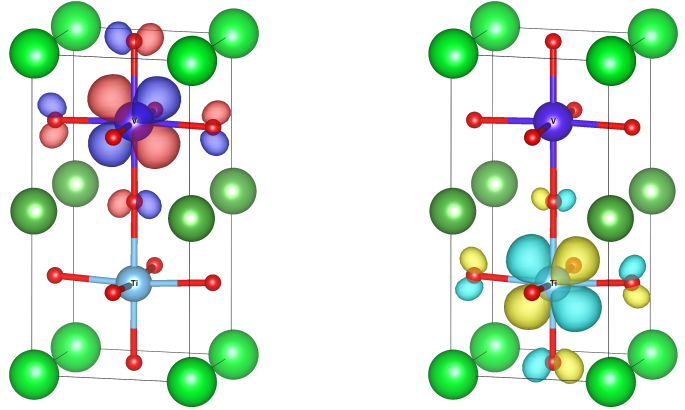
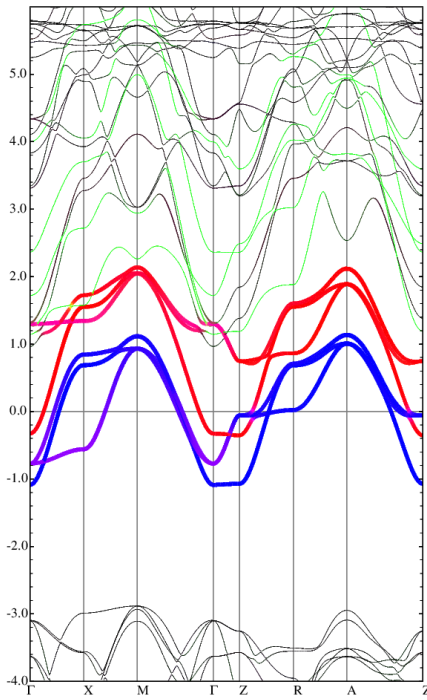


Figure 7.8.: The $1|1 \times 1$ -p heterostructure. Left: GGA band structure with band character. The six thicker lines are the V- t_{2g} (the lower three, blue) and Ti- t_{2g} (the upper three, red) derived bands. Green color corresponds to V and Ti e_g character. Center and right: relaxed crystal structure with isosurfaces of t_{2g} -like WF on V and Ti. Note the antiferroelectric distortion of the VO_6 and TiO_6 tetrahedra.

7.4. LDA+DMFT results for $\text{LaVO}_3|\text{SrTiO}_3$

7.4.1. An elementary heterostructure

The layer-dependent DMFT spectral function of the $1|1 \times 1$ -p structure is shown in Fig. 7.9. In contrast to the larger structure of the next section, in this calculation the Ti orbitals were treated in full DMFT rather than a simple Hartree approximation.

Albeit unrealistic, this model gives rise to some important observations. First, it demonstrates that DMFT can describe $\text{LaVO}_3|\text{SrTiO}_3$ in the PM insulating phase. Second, it shows the antiferroelectric distortion also seen in the larger structure. Third, it shows how the xy orbital is energetically preferred over the other t_{2g} orbitals due to the asymmetry of the heterostructure, which inhibits hopping for xz and yz in one direction within their plane of symmetry [ZZH13].

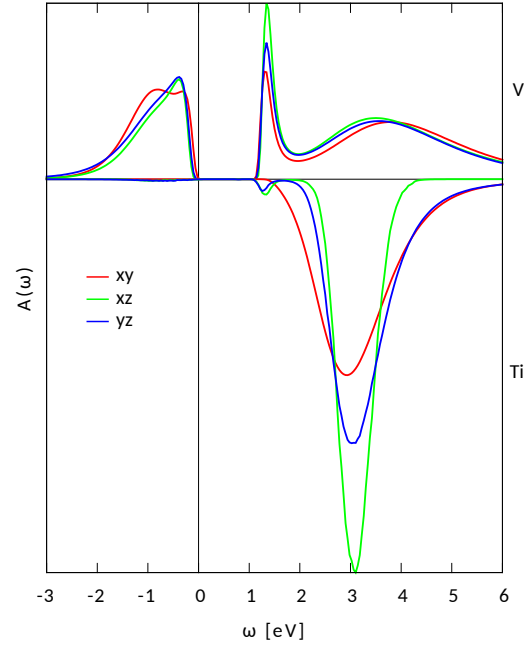
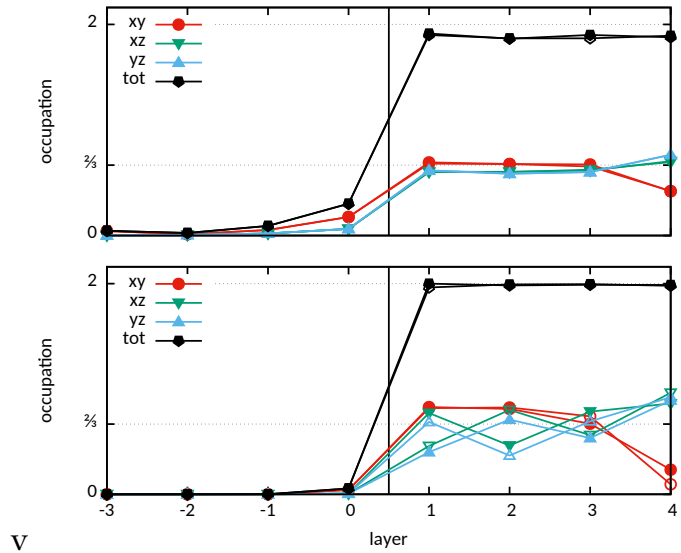


Figure 7.9.: Orbital-resolved LDA+DMFT spectral function of the V (top) and Ti (bottom) atoms in the $1|1\times 1$ -p heterostructure (cf. Fig. 7.8) in the paramagnetic phase. Note that xy and yz spectra are relatively similar while the xz spectrum is somewhat flatter and lower in energy.

Figure 7.10.: Occupation of the Ti and V d orbitals in the $4|4\times 2$ -o heterostructure within LDA+DMFT. Top: Using the standard FLL double-counting correction, the Ti sites are partially filled, and all layers of the heterostructure are metallic. Bottom: shifting the double-counting correction by 2 eV, we find empty Ti sites, and integer filling on the V sites, which are Mott insulating (cf. spectral function, Fig. 7.11). Filled and empty symbols correspond to the two atoms per layer.



7.4.2. A more realistic model

Using the standard FLL double-counting correction For a more realistic model, consider the $4|4\times 2$ -o heterostructure, enlarging the thickness of both materials, adding in-plane freedom for relaxation and orbital order, and moving to OBC.

[Ani+93] leads to Ti occupations significantly greater than 0, and hence to non-integer filling of the V sites (shown in Fig. 7.10 (top)). This in turn suppresses the Mott insulating phase in DMFT and leads to a situation where all V layers are metallic. Therefore, a larger DC was imposed on the Ti (shifted from the FLL values by 2 eV), which yields practically empty Ti and insulating V layers (see occupation in Fig. 7.10 (bottom) and spectral function in Fig. 7.11). However, no potential gradient or conducting interface/surface is observed.

Note the orbital order in these calculations. In the conducting case, all orbitals are occupied roughly equally, except for the slight preference for xy in the inner layers and for xz, yz in the surface layer. Conversely, in the insulating case, the AF-G orbital order is well developed even in the absence of spin order.

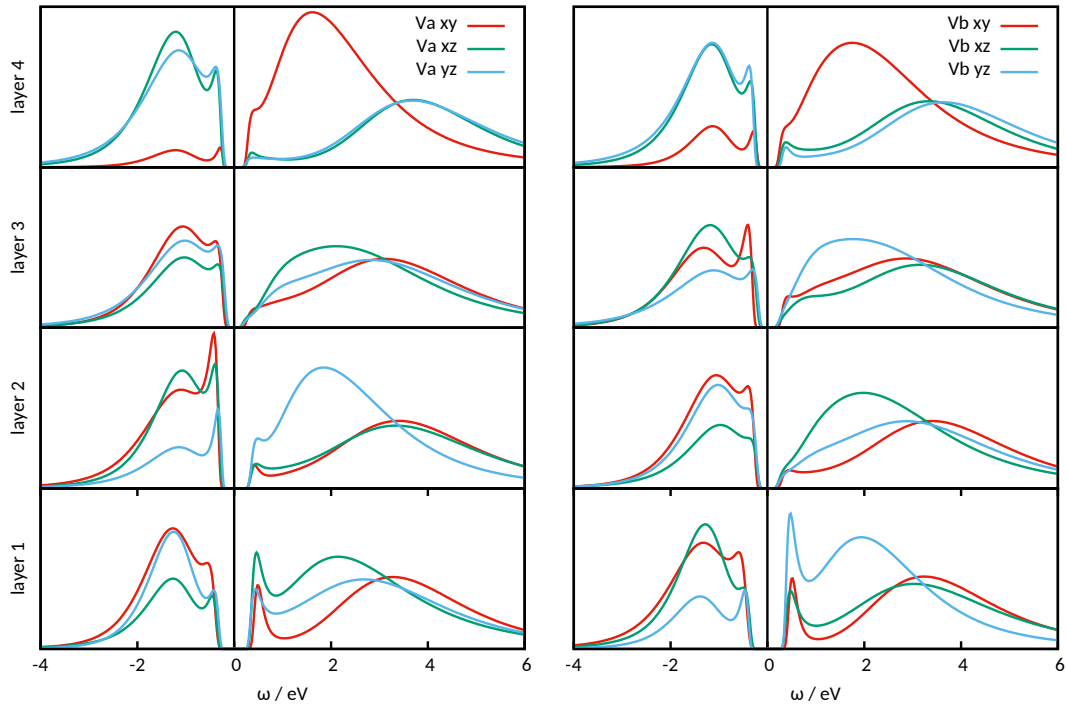


Figure 7.11.: Layer- and orbital-resolved spectral functions of the $4|4\times 2$ -o heterostructure in the paramagnetic insulating phase within LDA+DMFT (with DC shift for Ti, see text). Left and right correspond to the two V sites per layer. The orbital order seen in 7.10 is clearly visible, but no potential gradient or conductive interface/surface is seen.

7.5. Discussion and outlook

In this chapter, we have seen how the DFT+MLWF+DMFT machinery can be applied to a complex system such as the $\text{LaVO}_3|\text{SrTiO}_3$ heterostructure. A mature DFT code makes it possible to simulate the required large unit cells reliably and with a numeric effort manageable on modern computers. Building on the KS states, the MLWF construction provides a minimal basis for a many-body model. DMFT, in particular with CTQMC impurity solvers, offers a means to solve this model efficiently.

Turning to results, the most important difference to LDA+U (see Fig. 7.7 and App. B.4) is the absence of a potential gradient. At this point, let us recall the origin of the gradient: The nominal valences of the ions in LaVO_3 are

La^{3+} , V^{3+} , and O^{2-} . Along the [001] direction they form $(\text{LaO})^+$ and $(\text{VO}_2)^-$ layers. In a simple model, subsequent pairs of layers can be regarded as plate capacitors, with a homogeneous electric field between the plates, which translates to a stepwise linearly increasing potential [NHMO6]. In this model, the conducting interface/surface appears when the bands as shifted by the gradient cross the Fermi level.

However, it is clear that such a gradient can only be sustained in an insulator, where the electrons are bound to their atoms. In the GGA calculations used as basis for LDA+DMFT, the LaVO_3 layers are metallic, therefore the electrons are free to move and screen the gradient. The subsequent DMFT treatment drives them to the insulating phase, but since it is only concerned with the t_{2g} states, it cannot recover the gradient. Finally, without a gradient, there is no driving force to produce conducting interfaces or surfaces.

What, then, can be done to describe the gradient and conducting interfaces within LDA+DMFT? At least three approaches come to mind:

- Add a gradient to the model by hand, in the form of a layer-dependent on-site potential. The values for this potential could be taken e.g. from core levels of an LDA+U calculation which exhibits a gradient (cf. [Ass+13, Fig. 4 and Suppl. Fig. 1]).
- Use an LDA+U calculation as a basis for LDA+DMFT. Then, the gradient is included in the Wannier Hamiltonian. Of course, the interaction energy added by LDA+U has to be subtracted as a double-counting correction.
- Complete the LDA+DMFT charge self-consistency cycle. Through the feedback with DFT, the gradient could develop in the real part of the self energy. Only in this case could it be said that LDA+DMFT *predicts* a potential gradient.

Another point of interest is the interplay between structural relaxation and LDA+DMFT. As we have seen, the geometric differences in the structures relaxed in GGA and LDA+U are substantial. But do they translate to large differences in the electronic structure? What drives the larger distortion in LDA+U? It is interesting in this regard that the orbital order seen in the highly distorted structure within LDA+U is already quite pronounced in the insulating phase of the PM, less distorted structure.

In this case, as well, one might turn to charge self-consistency for the most complete answer. While the energy of the two structures could be compared,

7. The $\text{LaVO}_3|\text{SrTiO}_3$ heterostructure

a full lattice relaxation including DMFT is not within reach technically and computationally.

Conclusion

The focus of the present thesis has been on strongly correlated materials and theoretical methods that can adequately capture them, in particular LDA+DMFT and the construction of maximally localized Wannier functions (MLWF). The latter are used to build the single-particle part of the material-specific Hamiltonian to be solved by DMFT. After a brief review of the theory (Chapters 1 to 4), we discussed two computer codes to accomplish parts of this procedure, which were enhanced for the present thesis: WIEN2WANNIER [Kun+10] (Chapter 5) acts an interface from the WIEN2k electronic structure code to Wannier90, the standard code for constructing MLWF. In the course of the present thesis, it has seen its inclusion into the WIEN2k package along with various improvements of the user interface. WOPTIC [Ass+15] (Chapter 6) computes the optical conductivity, dc conductivity, and thermopower as a post-processing step to LDA+DMFT, or, in “noninteracting” mode, from WIEN2k without DMFT using Wannier functions and adaptive k-integration.

The adaptive integration algorithm of WOPTIC is able to sample the Brillouin zone much more efficiently than a homogeneous k-mesh, but leads to certain problems related to obtaining the momentum matrix elements in the Wannier gauge on k-points not included in the Wannier projection. Wannier interpolation was explored as a possible solution. This is one of two “matrix element modes” implemented in WOPTIC; the other is to calculate the momentum matrix elements using WIEN2k’s `optic`. The two modes are complementary in that they are accurate in different situations. Where they become inaccurate, errors have been found to be sizable but not catastrophic.

Finally, several of the methods described in the first part found application in Chapter 7, which focused on the $\text{LaVO}_3|\text{SrTiO}_3$ heterostructure, in particular with regards to its use as an absorber material for solar cells. LDA+DMFT is able to describe the heterostructure in the paramagnetic insulating phase, in contrast to LDA+U which yields an insulator only in the antiferromagnetic phase. It is found that, even in the paramagnetic insulator, staggered orbital order is well developed. However, LDA+DMFT as employed here does not

yield the expected potential gradient in the LaVO_3 film. Possibly, the gradient could be obtained using charge self-consistent LDA+DMFT.

Two appendices follow. First, the WIEN2WANNIER and WOPTIC user's guides are reproduced. Second, the journal articles related to the present thesis: [Ass+15] and [Ass+13] cover material relevant to Chapters 6 and 7, respectively; the remaining articles [Rib+14; Rub+14] cover other work carried out during the course of the thesis.

Appendix

A. Software documentation

To better document the status of the computer codes developed in conjunction with this work, the documentation of the WIEN2WANNIER (see Chapter 5) and WOPTIC (see Chapter 6) packages is reproduced in this Appendix.

WIEN2WANNIER 1.0 User's Guide

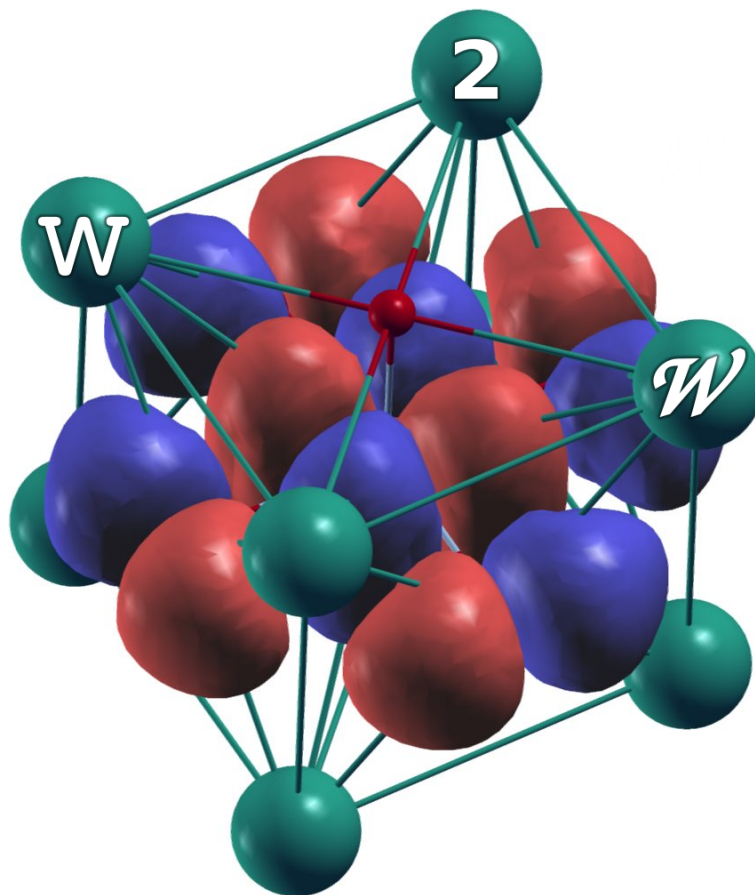
From linearized augmented plane waves to maximally localized Wannier functions..

ELIAS ASSMANN

JAN KUNEŠ

PHILIPP WISSGOTT

August 27, 2015



Introduction

In the solid state theorist's tool kit, algorithms based on density functional theory (DFT) represent the backbone applications. One of the more popular codes available is the WIEN2k package [1, 2]. It is based on dividing the real space unit cell into "muffin-tin" spheres centered on the ionic cores and an interstitial region. On the former, basis function with more or less atomic features are employed, while on the latter plain waves are used. The combined basis functions are called (linearized) augmented plane waves (LAPW).

While in WIEN2k a k-space representation of wave functions is convenient, there are many applications where a real-space picture is preferable: Determining transport properties (hopping parameters), visualization, and, especially, in codes relying on local orbital basis functions such as dynamical mean-field theory (DMFT [3]). One way to change to a real space representation is a Fourier transform of the Bloch states $\psi_{nk}(\mathbf{r})$ from the DFT calculation, yielding

$$w_{m\mathbf{R}}(\mathbf{r}) = \frac{V}{(2\pi)^3} \int_{BZ} d\mathbf{k} e^{-i\mathbf{k}\cdot\mathbf{R}} \left(\sum_n U_{nm}^{(k)} \psi_{nk}(\mathbf{r}) \right).$$

The resulting functions $w_{m\mathbf{R}}(\mathbf{r})$, parametrized by a direct lattice vector \mathbf{R} , are called Wannier functions. Due to the additional phase factors $U_{nm}^{(k)}$, which all lead to valid Wannier functions, there is considerable ambiguity in the choice of the real space basis set. This can be overcome by choosing Wannier orbitals $w_{m\mathbf{R}}(\mathbf{r})$ with minimal real-space extent (spread $\langle \Delta r^2 \rangle$). These are known as maximally localized Wannier functions (MLWF). A popular program to compute the MLWF for a given set of Bloch functions is WANNIER90 [4, 5].

Unfortunately, the application of WANNIER90 to the LAPW basis set of WIEN2k is not as straightforward as for a pure plane wave basis. In this guide, we describe the package WIEN2WANNIER which provides an interface between WIEN2k and WANNIER90. In any scientific publications arising from the use of WIEN2WANNIER, we ask that you cite Ref. [6].

J. KUNEŠ, R. ARITA, P. WISSGOTT, A. TOSCHI, H. IKEDA, and K. HELD,
Comp. Phys. Commun. **181**, 1888 (2010), arXiv:1004.3934

to acknowledge your use of our code. When using WANNIER90, you should cite Ref. [4]

A.A. MOSTOFI, J.R. YATES, Y.-S. LEE, I. SOUZA, D. VANDERBILT, and N. MARZARI,
Comput. Phys. Commun. **178**, 685 (2008), arXiv:0708.0650

independently of WIEN2WANNIER (cf. WANNIER90 user's guide [5]).

Acknowledgment Many thanks to Karsten Held, Peter Blaha, Karlheinz Schwarz, Nikolaus Frohner, Philipp Hansmann, Nico Parragh and Giorgio Sangiovanni.

Contents

1	Quickstart	1
1.1	Preparatory steps	1
1.2	Interface & Wannierization	1
1.3	Verification & Postprocessing	2
2	Detailed description	5
2.1	w2w — compute overlaps	5
2.2	wplot — Wannier function plotter	7
2.3	prepare_w2wdir — copy required files	9
2.4	init_w2w — prepare WIEN2WANNIER input files	9
2.5	findbands — get band indices inside energy interval	9
2.6	write_inwf — prepare input file for w2w	10
2.7	write_win — prepare input file for wannier90.x	10
2.8	wannier90 — wrapper for wannier90.x	10
2.9	w2waddsp — add spin directions for SOC	10
2.10	write_inwplot — prepare input file for wplot	11
2.11	wplot2xsf — convert wplot output to xsf format	11
2.12	convham — Fourier transform Wannier Hamiltonian	11
2.13	shifteig — shift energies in case.eig	12
2.14	rephase	12
2.15	joinvec — join parallel vector files	12
2.16	write_insp — write input file for spaghetti	12
3	Getting help	13
3.1	FAQ	13

1 Quickstart

Contents

1.1 Preparatory steps	1
1.2 Interface & Wannierization	1
1.3 Verification & Postprocessing	2

This section outlines the procedure for a “standard” WIEN2WANNIER calculation. A detailed description of the individual programs can be found in Section 2. For a quick reference, see the plain-text file CHEATSHEET.

1.1 Preparatory steps

Before running WIEN2WANNIER, one needs a converged WIEN2k calculation. Additionally, during the setup for WIEN2WANNIER, the bands which are to be taken into account will have to be specified, and the main character (e.g., d bands on atom 2) of these bands should be known.

To obtain this information, a combination of partial DOS and bandstructure, or a “band character” plot is often expedient (e.g. spaghetti’s “fat bands” option, or SpaghettiPrimavera and `prima.py`, available in the *unsupported software* section of the WIEN2k website).

Copy Required Files

As a “zeroth” step before a Wannier projection, it is recommended to use the script

```
prepare_w2wdir subdir
```

to create the subdirectory *subdir* where the rest of the workflow will take place. Thus, one WIEN2k calculation can be the starting point of several WIEN2WANNIER runs.

1.2 Interface & Wannierization

Write Input Files

The script `init_w2w` takes the following steps:

- x `kgen -fbz` generates the non-symmetrized k-mesh that WANNIER90 requires. The density of the mesh influences the quality of localization and visualization of the Wannier functions. Remark: The interface was only tested with unshifted k-meshes.

x findbands looks in *case.output1* for bands in a given energy range $[E_{\min}, E_{\max}]$, and outputs the corresponding band indices b_{\min}, b_{\max} . To choose the energy window of interest, consult a (p)DOS and/or band structure plot.

write_inwf writes the main input file *case.inwf* for the interface. The band indices b_{\min}, b_{\max} have to be specified, and initial projections A_{mn} may be given in terms of atomic sites and appropriate spherical harmonics.

write_win writes the input file for *wannier90.x*, *case.win*, on the basis of *case.inwf* and other files.

x wannier90 -pp reads the k-mesh in *case.win* and writes a list of nearest-neighbor k-points to *case.nnkp*.

Run Interface

After running *init_w2w*, one can proceed:

x lapw1 before the actual interface run, the eigenvectors and eigenvalues for the new (non-symmetrized) k-mesh have to be computed.

x w2w computes the overlaps M_{mn} , initial projections A_{mn} and eigenvalues E_n , and writes them to *case.mmn*, *case.amn*, and *case.eig*.

Run Wannierization

Finally,

x wannier90 computes the $U(\mathbf{k})$ by maximum localization. Output is stored in *case.wout*. The Wannier orbitals should be converged to a spread which is usually smaller than the unit cell of the structure.

1.3 Verification & Postprocessing

After a successful WANNIER90 run, one should check if the centers and spreads of the Wannier functions (printed in *case.wout*) are sensible. Another important consistency check is to compare the Wannier-interpolated bandstructure to the one computed by WIEN2k. WIEN2WANNIER also provides programs to create a real-space plot of the Wannier functions.

Compare Bandstructures

With the option *hr_plot=T*, WANNIER90 writes a bandstructure derived from the Wannier-interpolated Hamiltonian $H(\mathbf{k})$ to *case_band.dat*. To compare this to the bandstructure computed by *spaghetti*, e.g. in *gnuplot*, use the command (including a conversion from Bohr⁻¹ to Ångström⁻¹)

```
p 'case.spaghetti_ene' u ($4/0.53):5, 'case_band.dat' w l
```

Plot Wannier Functions

`write_inwplot` asks for a real-space grid on which the Wannier functions should be plotted, and writes `case.inwplot`.

`x wplot -wf m` evaluates Wannier function number m on the real-space grid, and writes the density $|w_m(\mathbf{r})|^2$ to `case_m.psink` and the phase $\arg w_m(\mathbf{r})$ to `case_m.psiarg`.

`wplot2xsf` converts all `case*.psink` plus `case*.psiarg` files in the directory to `xsf` files which can be opened by XCrySDen.

`xcrysdn -xsf case_m.xsf.gz` ; pick "Tools → Data Grid" from the menu and press OK. In the isosurface controls window choose an appropriate isovalue, e.g. 0.1, and check the "Render +/- isovalue" box.

2 Detailed description

Contents

2.1	w2w — compute overlaps	5
2.2	wplot — Wannier function plotter	7
2.3	prepare_w2wdir — copy required files	9
2.4	init_w2w — prepare wienzwannier input files	9
2.5	findbands — get band indices inside energy interval	9
2.6	write_inwf — prepare input file for w2w	10
2.7	write_win — prepare input file for wannier90.x	10
2.8	wannier90 — wrapper for wannier90.x	10
2.9	w2waddsp — add spin directions for SOC	10
2.10	write_inwplot — prepare input file for wplot	11
2.11	wplot2xsf — convert wplot output to xsf format	11
2.12	convham — Fourier transform Wannier Hamiltonian	11
2.13	shifteig — shift energies in case.eig	12
2.14	rephase	12
2.15	joinvec — join parallel vector files	12
2.16	write_insp — write input file for spaghetti	12

This section lists the programs included in WIEN2WANNIER, along with brief descriptions and usage summaries. All programs have online help (-h), which may be more complete than the material here.

Programs that are described here include: the “main” WIEN2WANNIER programs w2w and wplot; several utility programs used in a typical WIEN2WANNIER run; and some programs that are needed in special cases, or grew out of WIEN2WANNIER development and are provided here in the hope that they will be useful, even if they are not needed in the context of WIEN2WANNIER.

2.1 w2w — compute overlaps

This is the main program of the interface which provides the files *case.mmn*, *case.amn* and *case.eig* for WANNIER90 given the output of a WIEN2k run (most importantly, *case.vector*). w2w is based on lapwdm, since the main task, for the computation of the overlap matrices

$$M_{mn}^{(k,b)} = \langle \psi_{mk} | e^{-ib \cdot r} | \psi_{nk+b} \rangle \quad (2.1)$$

that are stored in `case.mmn`, is to determine the basis functions $\psi_{nk}(r)$ in the entire unit cell (using appropriate boundary conditions on the muffin-tin spheres).

In addition to standard WIEN2k files, a file `case.nnkp` is required which defines the \mathbf{b} vectors for each k in Eq. (2.1). `wannier90.x` delivers this file when called with the flag `-pp`.

Execution

The program `w2w` is executed by invoking the command:

```
x w2w [-c -up|-dn -so -p] |
w2w w2w.def [#proc] | w2wc w2w.def [#proc]
```

While `w2w` itself is not parallelized, like `x lapw2 -qt1`, it accepts a `-p` switch (or `#proc`) to read parallel vector and energy files.

With spin-orbit coupling (`-so`), `w2w` must be called separately for `-up` and `-dn`, resulting in `case.mmn{up,dn}`, `case.amn{up,dn}`, and `case.eig{up,dn}`. In a second step, the M_{mn} and A_{mn} must be added (and the eigenvalues copied) to produce `case.mmn`, `case.amn`, and `case.eig`, on which WANNIER90 may be run. This step is done by the program `w2waddsp`, which is automatically invoked by `x wannier90 -so`.

Input

A sample input file for WIEN2WANNIER is given below. It can be generated using `write_inwf`.

```

----- case.inwf -----
1 BOTH      # compute Amn | Mmn | both
2  21 23    # band-lo, band-hi
3   3  3    # max LJ in exp(ibr) expansion; #(initial projections)
4   2      # #(terms) [d-xy orbital]
5   2  2 -2  0.00000000  0.70710677  # IAT; l, m; Re(coeff), Im(coeff)
6   2  2 +2  0.00000000 -0.70710677
7   2      # [d-(x2-y2) orbital]
8   2  2 -1  0.70710678  0.00000000
9   2  2 +1  0.70710678  0.00000000
10  1      # [d-z2 orbital]
11  2  2  0  1.00000000  0.00000000
----- end of case.inwf -----

```

This file is read using Fortran list-oriented reads, i.e., items are separated by white space.

line 1 mode — what to calculate

mode	Amn	Only determine the initial orbital projections <code>case.amn</code>
	Mmn	Only determine the overlap matrices <code>case.mmn</code>
	both	Determine both the initial orbital projections and the overlap matrices

line 2 Blo, Bhi — band window

Blo, Bhi	<i>int</i>	the minimal and maximal Bloch band from the vector file to be taken into account, determining the lower edge of the (outer) energy window
----------	------------	---

2.2. WPLOT — WANNIER FUNCTION PLOTTER

7

line 3 LJmax, Nproj

LJmax *int* the number of terms which are used in the spherical harmonics expansion to approximate $\exp(-ikb)$, usually 3–4 is sufficient.
 Nproj *int* the number of target Wannier functions

line 4 Nterm — number of terms (*Nproj* times)

Nent *int* the number of Y_ℓ^m terms (lines to follow for this initial projection)

line 5 Iat, l, m, Re, Im — Y_ℓ^m term (*Nterm* times)

Iat *int* the atom where the entry is centered
 l, m *int* the orbital and magnetic quantum numbers ℓ and m for this entry
 Re, Im *real* the complex coefficient multiplying Y_ℓ^m

If initial projections are given, there must be Nproj blocks **l. 4+5**, one for each initial projection. Within each block, write Nterm lines **l. 5**, one for each Y_ℓ^m term. Otherwise, if mode is Mmn, the initial projections can be omitted.

2.2 wplot — Wannier function plotter

wplot evaluates the Wannier functions on a real-space grid. It reads the transformation matrices $U(k)$ from the file `case.chk` written by `wannier90.x` and thereby constructs the Wannier functions from the original WIEN2k Bloch states.

Execution

The program wplot is executed by invoking the command:

```
x wplot [-up|-dn -c -so -p -wf m] |
wplot def [m [#proc]] | wplotc def [m [#proc]]
```

wplot is not parallelized, but accepts a `-p` switch (or `#proc`) to read parallel vector files. Moreover, as a crude form of parallelization, one can run several wplot instances in the same directory in parallel without interference (e.g. to plot several Wannier functions on fine grids).

The input file contains the index of the Wannier orbital to be plotted; m above overrides this. Output goes to `case_m.psink` ($|w(r)|^2$) and `case_m.psiarg` ($\arg w(r)$).

Input

wplot is based on `lapw7` and shares the general structure of the input file. A sample input file for wplot is given below. It can be generated via `write_inwplot`, or adapted from the template in `$WIENROOT/SRC_templates`.

```

----- case.inwplot -----
1  3D ORTHO      # dim.; O(RTHOGONAL) | N(ON-ORTHOGONAL)
2  -1 -1 -1  1  # origin: x, y, z; idiv
3   0 -1 -1  1  # x-end: x, y, z; idiv
4  -1  0 -1  1  # y-end: x, y, z; idiv
5  -1 -1  0  1  # z-end: x, y, z; idiv
6  20 20 20    # #(grid points) in x, y, z dir.
7  NO          # DEP(HASING) | NO (POST-PROCESSING)
8  ANG  LARGE  # units: ANG|ATU; rel. comp.: LARGE|SMALL
9   1          # Wannier function index
----- end of case.inwplot -----

```

line 1 mode, switch *format(A3, A1)*

```

mode  nD      with n = 0, ..., 3, an n-dimensional grid will be specified
      ANY     read arbitrary grid from case.grid
flag  0,N     when mode = nD: check for orthogonality or not
      C,F     when mode = ANY: cartesian or fractional coordinates

```

If mode=*nD* and flag=0 or absent, grid axes will be checked for pairwise orthogonality; set flag=N for nonorthogonal axes. If mode=ANY and flag=C or absent, the grid points in *case.grid* are in cartesian coordinates (3 reals per line); if flag=F, they are in fractional coordinates (3 numbers and divisor).

line 2 ix, iy, iz, idv (*free format*) — grid origin

```

ix,iy,iz,idv  int  Coordinates of the origin of the grid, where x=ix/idv etc. in
                  units of the conventional lattice vectors

```

line 3 ix, iy, iz, idv (*free format*) — axis end-point (*n times*)

```

ix, iy, iz, idv  int  Coordinates of the end points of each grid axis

```

If mode=*nD*, **l. 3** must be given *n* times, once for each direction; if mode=ANY, it must be omitted.

line 4 nx, ny, nz (*free format*) — mesh size

```

nx,ny,nz  int  number of mesh points in each direction

```

line 5 post *format(A3)* — post-processing option

```

post  DEP    "dephasing": each wave function is multiplied by a complex phase factor
          to align it (as far as possible) to the real axis
      NO     No post-processing

```

line 6 unit, whpsi (*free format*)

```

unit  ANG    Ångström
      AU|ATU  Atomic units

```

2.3. PREPARE_W2WDIR — COPY REQUIRED FILES

9

```
whpsi  LARGE  the large relativistic component for each wave functions is evaluated
        SMALL  small relativistic component
```

line 7 `iwan` (*free format*) — Wannier function index

```
iwan  int  index of the wf to be plotted, unless overridden on command line
```

Finding the right window for plotting can be tricky. WANNIER90 often yields orbitals that are not centered in the home unit cell; `wplot2xsf` can shift them later on, but in `wplot` one has to “hit” the orbitals as given by WANNIER90 (see section “Final State” in `case.wout`). Therefore, it is recommended to start with a coarse grid (for instance $10 \times 10 \times 10$), make sure the window is correct, and only then start a calculation with a finer grid.

2.3 prepare_w2wdir — copy required files

A WIEN2k computation can be the starting point for various runs of WIEN2WANNIER. This script creates a new subfolder of a WIEN2k directory and is invoked by

```
prepare_w2wdir subdir
```

where `subdir` is the name of the subdirectory to be created.

2.4 init_w2w — prepare wien2wannier input files

This script guides the user through the initialization of WIEN2WANNIER phase as described in Section 1.2.

```
init_w2w [-up|-dn] [-b options]
```

In batch mode (`-b`), further options are available instead of interactive input.

2.5 findbands — get band indices inside energy interval

This program reads `case.output1` to identify the bands which lie within a certain energy window. The program `findbands` is executed by issuing the command:

```
x findbands window [-up|-dn -so -hf -efermi EF] |
findbands def
```

`window` may be given as `-emin e -emax E` or `-all e E`. The energies are in eV with $E_F = 0$. The Fermi energy is read from `case.fermi` (written by `prepare_w2wdir`) unless given as `-efermi` (in Ry).

The output is given in `case.outputfind` and consists of the bands in the interval at each k-point, as well as which bands are contained in the interval across all k-points, and which bands cross the interval at any k-point.

2.6 `write_inwf` — prepare input file for `w2w`

This program prepares the main input file `case.inwf` for `w2w`. It is executed by invoking the command

```
write_inwf (interactive) |
write_inwf -bands Nmin Nmax PROJ [PROJ ...] (noninteractive)
```

It will ask (in interactive mode) for a range of bands, which are all the bands to be taken into account by `w2w` (including those for disentanglement). Then, it will ask for “projection specifications” `PROJ = SITE:ORB[:ZAXIS[:XAXIS]]`, which consist of colon-separated parts naming an atomic site, an orbital, and, optionally, rotated z - and x -axes¹. Please see `write_inwf -h` and `write_inwf -H axes/sites/orbitals` for further information on these. Interactively, you can also use tab completion to discover input options and command line history to recall past inputs.

The program will keep asking for projections until it has accumulated as many projections as bands were specified. However, one can stop early by pressing `Ctrl-D` (EOF); in this case, there will be fewer Wannier functions than bands (disentanglement).

2.7 `write_win` — prepare input file for `wannier90.x`

This program reads `case.inwf`, `case.klist`, and some other files, and produces `case.win`, the input file for `wannier90.x`. It is executed by invoking the command

```
write_win [-fresh]
```

If `case.win` already exists, `write_win` updates it. Otherwise (or if `-fresh` is given), the template in `$WIENROOT/SRC_templates` is used.

2.8 `wannier90` — wrapper for `wannier90.x`

A wrapper script for `wannier90.x` is provided to take care of spin polarization and spin-orbit coupling. In the context of `WIEN2WANNIER`, `wannier90.x` is executed by invoking the command

```
x wannier90 [-up|-dn|-so|-pp] | wannier90 [-up|-dn|-so|-pp]
```

The wrapper script must be able to find the executable `wannier90.x`, i.e. you have to either have it in your `$PATH`, or edit the script `wannier90_lapw` to provide the location.

With `-pp`, `wannier90.x` will produce `case.nnkp`; with `-so`, `w2waddsp` will be called to add the spin channels together before running `wannier90.x`.

Extensive diagnostic output goes to `case.wout`, error messages to `case.werr`; the full results (in particular the $U(k)$ matrices) are stored in the binary file `case.chk`.

2.9 `w2waddsp` — add spin directions for SOC

In calculations including spin-orbit coupling (SOC), `WANNIER90` has to be invoked on `case.mmn` and `case.amn` files which contain the sum of the overlaps / projections for the two spin

¹`write_inwf` uses the method of Ref. [7] to rotate the spherical harmonics.

2.10. WRITE_INWPLOT — PREPARE INPUT FILE FOR WPLOT

11

channels. (This procedure is needed also for non-spin-polarized cases, cf. Section 2.1.) To this end, `w2waddsp` reads `case.mmn{up,dn}`, `case.amn{up,dn}` and writes `case.mmn`, `case.amn`.

There is usually no need to call this program manually, it is run by `x wannier90 -so`. If needed, it is executed by invoking the command

```
x w2waddsp | w2waddsp def
```

after running `x w2w-up` and `-dn`.

2.10 write_inwplot — prepare input file for wplot

This program may help in preparing the input file for `wplot`. (Alternatively, copy the template from `$WIENROOT/SRC_templates`.) It is executed by invoking the command

```
write_inwplot case
```

2.11 wplot2xsf — convert wplot output to xsf format

This program converts the files `case_m.psink` and `case_m.psiarg` produced by `wplot` to files `case_m.xsf` which can be opened, e.g., in XCrySDen [8] or VESTA [9].

Note that only real data can be represented in the `xsf` file. Therefore, $|w(r)|^2 \operatorname{sgn} \operatorname{Re} w(r)$ is saved by default. (In most cases the Wannier functions are real anyway.)

`wplot2xsf` has a number of options (see `wplot2xsf -h`), but usually it is executed by invoking the command

```
wplot2xsf [-up|-dn]
```

If all the required files have their standard names, this will convert all the plots in the current directory.

By default, `wplot2xsf` reads `case_centres.xyz`, and shifts the Wannier functions so that their centers have the coordinates given in that file. If `translate_home_cell` (and `write_xyz`) is set in `case.win`, this will result in a plot where the Wannier centers lie in the “home” unit cell.

2.12 convham — Fourier transform Wannier Hamiltonian

This program Fourier transforms the WANNIER90 real space Hamiltonian $H(\mathbf{R})$ (`case_hr.dat`) to its k-space representation $H(\mathbf{k})$ (`case.ham_fine`) on the k-points given by `case.klist`. In this way, if the real-space Hamiltonian is sufficiently localized, $H(\mathbf{k})$ may be interpolated to arbitrarily fine k-grids. `convham` is executed by invoking the command

```
x convham [-band] |
convham def
```

2.13 shifteig — shift energies in case.eig

to zero in *case.eig*. If needed, this program can be used to apply an additional shift by DE (in eV). *shifteig* is executed by invoking the command

```
x shifteig [-up|-dn] -efermi DE | shifteig def DE
```

2.14 rephase

program reads the *psiarg* files to determine the most probable phases of all Wannier functions. Then, the input for the interface file *case.inwf* is rewritten in a way that a subsequent run of *WIEN2WANNIER* and *WANNIER90* leads to real Wannier orbitals (this does not work in all cases). The Fortran program *rephase* is invoked by the command

```
rephase case [-w] [-up/-dn] [-wf=idx_wann]
```

where the option *-w* means that *case.inwf* is automatically updated (future *wien2wannier* runs will then have a higher probability of producing real Wannier orbitals) and the option *-w idx_wann* indicates that the action is only applied for the Wannier function *idx_wann*.

2.15 joinvec — join parallel vector files

energy files from a parallel calculation into one *case.vector* and one *case.energy*. It is executed by invoking the command

```
x joinvec [-up|-dn -c -so]
```

All *.vector_** files are merged into one *.vector* file containing the header of the first file *.vector_1* (and correspondingly for the *.energy* files).

2.16 write_insp — write input file for spaghetti

Fermi energy read from *case.scf2* in the input file for *spaghetti*, *case.insp*. It is invoked by

```
write_insp [-up/-dn]
```

3 Getting help

Online help for all programs can be requested via the option `-h`. In addition to the pointers below, the WIEN2WANNIER distribution also includes a file CHEATSHEET, which concisely summarizes the usual steps of a calculation. If this does not help, send questions relating to the usage of WIEN2WANNIER to the Wien2k mailing list at http://www.wien2k.at/reg_user/mailling_list/. For questions about WANNIER90 and the MLWF procedure, there is a mailing list at <http://www.wannier.org/forum.html>. The WIEN2WANNIER maintainer can be reached at wien2wannier@ifp.tuwien.ac.at.

3.1 FAQ

How does one choose the initial projections?

There is no general rule to choose the initial projections which have to be prepared in the `inwf` file. There are, however, some hints which usually help:

- In the energy interval of interest, identify the main atoms which contribute to the partial DOS. These atoms are usually good centers for the initial projections. The character of these atomic contributions can also be seen via the partial DOS.
- A glance at the bandstructure often helps to consider the multiplicity of equivalent `wf` and to identify certain hybridizations.

The resulting Wannier orbitals are not localized

Several possible reasons (this list is not complete)

- choosing non-optimal initial projections
- the number of k-points is too small

The bandstructure of Wien2k and wannier90 does not match

First of all, be sure to take into account the Bohr-Ångström conversion, e.g., in `gnuplot`:

```
p 'case.spaghetti_ene' u ($4/0.53):5, 'case_band.dat' w l
```

If the bands themselves differ strongly, then one might have

- non-optimal initial projections
- too few k-points
- chosen the frozen energy window in WANNIER90 in a wrong way.

When plotting a Wannier orbital in XCrySDen I can see nothing

One possible reason is that the WF centers are not necessarily in the home unit cell at [000]. The interface programs usually account for this by translating the WF to the home cell. However, the spatial mesh for `wplot` has to be defined with respect to the original centers which come out of WANNIER90. These centers can be found in `case.wout` file. Assume the WF is centered at $[-0.5 \ -0.5; -0.5]$ in the basis of conventional unit vectors. Then, appropriate mesh vectors might be

```
-1 -1 -1 1      #x, y, z, divisor of orig
 0 -1 -1 1      #x, y, z, divisor of x-end
-1  0 -1 1      #x, y, z, divisor of y-end
-1 -1  0 1      #x, y, z, divisor of z-end
```

My Wannier orbitals are not centered at the home unit cell

It happens quite frequently that a WF is not centered within the home unit cell, which is displayed by default by XCrySDen. The interface program `write_win` automatically activates the option `translate_home_cell` in the WANNIER90 input file. Then, WANNIER90 should produce a file `case_centres.xyz`, where the vectors of all WF are stored which translate the orbital to the home unit cell. If this file cannot be located by `wplot2xsf` or the option `-noshift` is activated, no translation is conducted and the WF appear centered at their original position.

Bibliography

- [1] P. BLAHA, K. SCHWARZ, G.K.H. MADSEN, D. KVASNICKA, and J. LUITZ. *WIEN2k, An Augmented Plane Wave + Local Orbitals Program for Calculating Crystal Properties*. Techn. Universität Wien, Austria, 2001. <http://www.wien2k.at>.
- [2] P. BLAHA, K. SCHWARZ, G.K.H. MADSEN, D. KVASNICKA, J. LUITZ. *WIEN2k User's Guide*. http://www.wien2k.at/reg_user/textbooks/usersguide.pdf.
- [3] K. HELD. *Electronic structure calculations using dynamical mean field theory*. *Adv. Phys.* **56**, 829-926 (2007).
- [4] A.A. MOSTOFI, J.R. YATES, Y.-S. LEE, I. SOUZA, D. VANDERBILT and N. MARZARI. *WANNIER90: A tool for obtaining maximally-localized Wannier functions*. *Comput. Phys. Commun.* **178**, 685 (2008)
- [5] A.A. MOSTOFI, J.R. YATES, Y.-S. LEE, I. SOUZA, D. VANDERBILT and N. MARZARI. *WANNIER90 User Guide*. http://wannier.org/doc/user_guide.pdf.
- [6] J. KUNEŠ, R. ARITA, P. WISSGOTT, A.TOSCHI, H. IKEDA, and K. HELD. *WIEN2WANNIER: From linearized augmented plane waves to maximally localized Wannier functions*. *Comp. Phys. Commun.* **181**, 1888 (2010).
- [7] Z. ROMANOWSKI and S. KRUKOWSKI. *Transformations of complex spherical harmonics under rotations*. *J. Phys. A: Math. Theor.* **40**, 15071 (2007).
- [8] A. KOKALJ. *Computer graphics and graphical user interfaces as tools in simulations of matter at the atomic scale*. *Comp. Mater. Sci.*, **28**, 155 (2003).; <http://www.xcrysden.org>.
- [9] K.MOMMA and F.IZUMI. *VESTA 3 for three-dimensional visualization of crystal, volumetric and morphology data*. *J. Appl. Cryst.* **44**, 1272 (2011). <http://jp-minerals.org/vesta/en/doc.html>.

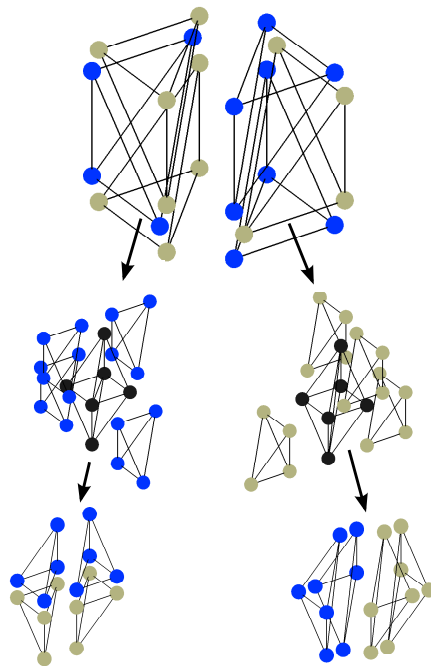
WOPTIC 1.0 User's Guide

Optical conductivity with Wannier functions.

ELIAS ASSMANN

PHILIPP WISSGOTT

August 27, 2015



Introduction

To compute the optical conductivity σ in the basis of maximally-localized Wannier orbitals the package `WOPTIC` is provided. It uses the Green function formalism, which yields

$$\sigma_{\alpha\beta}(\Omega) = \frac{2\pi e^2 \hbar}{V_{\text{uc}}} \sum_k \int d\omega \frac{f(\omega) - f(\omega + \Omega)}{\Omega} \text{tr} \left[A(\omega, k) V^\alpha(k) A(\omega, k) V^\beta(k) \right], \quad (*)$$

where $\sigma_{\alpha\beta}$ is the (α, β) element of the optical conductivity tensor ($\alpha, \beta \in \{x, y, z\}$), V_{uc} the unit cell volume, f the Fermi function, $A = \frac{i}{2\pi}(G - G^\dagger)$ the generalized spectral function [1, 2, 3], and V^α the group velocity in direction α . The numerical bottleneck in evaluating (*) is the k-summation, since usually many k-points are required to obtain converged results. For a speed-up in k-mesh convergence, `WOPTIC` therefore employs an adaptively refined tetrahedral tiling of k-space.


`WOPTIC` consists of two main programs: `woptic_main`, which calculates the optical conductivity, and `refine_tetra`, where the k-mesh is refined; as well as several smaller support programs. The individual programs are normally called by means of the driver script `woptic`. This guide provides technical documentation for `WOPTIC`. For details on the underlying formalism and algorithm, see Refs. [4, 5, 6].

Citation In any scientific publications arising from the use of `WOPTIC`, we ask that you cite Ref. [6],

P. WISSGOTT, E. ASSMANN, J. KUNEŠ, A. TOSCHI, P. BLAHA, and K. HELD,
Comp. Phys. Commun. **XXX**, YYYY (2015), arXiv:1507.04881,

to acknowledge your use of our code. This is in addition to the appropriate citations to acknowledge other codes used (such as `WIEN2k` [7], `WANNIER90` [8], and `WIEN2WANNIER` [9]).

Contact Comments, patches, and the like can be sent to `wien2wannier@ifp.tuwien.ac.at`.

Caution Following the many recent changes in `WIEN2WANNIER` and `WOPTIC`, some parts of the older version of `WOPTIC` have not yet been adapted. As such, they must be considered experimental. We keep such untested (or even known to be broken) features in the code and in this guide, where they are marked with the sign .

Common options and other resources This guide attempts to document the features most relevant to the `WOPTIC` user; it will not list every option or every file used by every command. Most commands honor the option `--help`, which should provide a definitive list of

iv

options for that command. The wOPTIC distribution also includes a terse instruction sheet as doc/WOPTICHEAT.

Contents

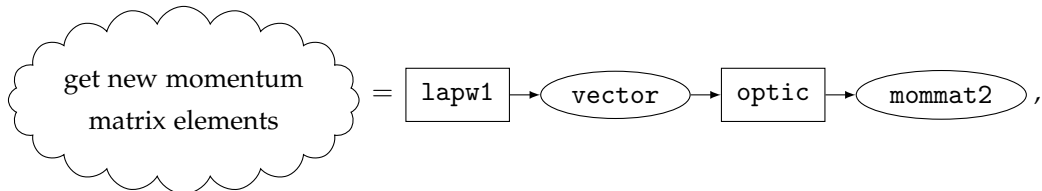
1	The driver script woptic	1
1.1	Synopsis	5
1.2	Options	5
1.3	The input file <i>case.inwop</i>	5
1.4	Output files	7
2	Support Programs	9
2.1	wopticlean — remove left-over files from WOPTIC runs	9
2.2	compute_vr — compute $V^w(R)$	9
⊕	2.3 kanalysis — $\sigma(k, \omega)$ on a BZ path	10
⊕	2.4 obtain_dist — intra-UC hopping for Peierls	10
2.5	inwopcheck — parse inwop file	11
2.6	woptic_main — k-integration	11
2.7	refine_tetra — k-mesh refinement	12
2.8	joinham — combine hk / mommat2 / vk α / vvka β files	13
2.9	convert_vr — Fourier-interpolate $V^w(k)$	13

1 The driver script woptic

This is the main user-callable program. It runs the other programs as necessary until a set number of iterations is completed (or an error occurs) — convergence has to be checked manually. If you include an outer window in your `interp` calculation, you should check the localization of $W^{\alpha\beta}(R, \omega)$ and/or the interpolation errors in the optical conductivity.

Since the procedure is a little involved, we provide Fig. 1.1 to give an overview of the files and programs involved in one iteration (but note that not all files that might be involved are shown). The computation of the group velocities $V^\alpha(k)$ for the new k-points varies according to the option `matelmode`. `WOPTIC` implements two modes using the full momentum matrix elements $V_{ab}^\alpha(k) = \langle \psi ak | \hat{p}_\alpha | \psi bk \rangle$ as group velocities:

`optic mode` takes the matrix elements from `WIEN2k`'s `optic` module,

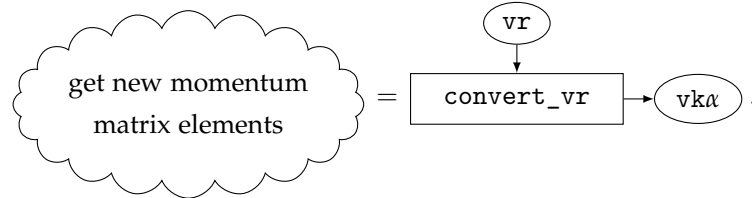


and transforms them to the Wannier basis using the matrices $U(k)$ which diagonalize the Wannier-interpolated Hamiltonian, $U_{nu}(k)H_{uv}^w(k)U_{vm}^\dagger(k) = \delta_{nm}\epsilon_n(k)$. But the diagonalization fixes the eigenvectors only up to a phase, which leads to a *random-phase problem* in (*) and associated uncertainties in the optical conductivity. The problem is absent whenever the self-energy is orbital-independent (by symmetry, or in a noninteracting model). In such a case, `optic mode` should be dependable. Otherwise, the results should be checked for the influence of the random-phase problem.

`interp mode` applies Wannier interpolation to the matrix elements directly in order to overcome the random-phase problem. `compute_vr` calculates the Wannier momentum matrix elements in direct space

$$V_{uv}^{w,\alpha}(R) = \frac{1}{N_k} \sum_k e^{-ik \cdot R} U_{un}^\dagger(k) V_{nm}^\alpha(k) U_{mv}(k) = \langle w u0 | \hat{p}_\alpha | w vR \rangle,$$

and `convert_vr` interpolates them to the new k-points,¹



The interpolation works well for the Wannier-Wannier transitions ($V^{W,\alpha}$), but interpolation errors may become large for the mixed transitions governed by $W^{\alpha\beta}(R,\omega)$, where

$$W_{uv}^{\alpha\beta}(k,\omega) = \sum_i V_{ui}^\alpha(k) A_{ii}(\omega) V_{iv}^\beta(k)$$

with the index i running over the non-Wannier states (i.e. the outer window) and the matrix elements are transformed into the Wannier basis on one side only. Note that the interpolation errors typically only affect the interband optical conductivity; as long as the low-energy degrees of freedom are described by the Wannier functions, the static quantities (dc conductivity and thermopower) should be reliable.



In addition, Peierls mode uses the Peierls approximation $V(k) \approx i \nabla_k H(k)$ instead of the momentum matrix elements. It is currently unsupported.

Further reading. See [4] for the original description of `woptic` in the `optic` and `Peierls` modes. See [5] for a detailed description of `interp` mode and a numerical comparison to `optic` mode including an analysis of the errors committed in each of them. Ref. [10] tests the Peierls approximation against the full momentum matrix elements.



Disentanglement is supported only in `interp` mode in the case where only Wannier-Wannier transitions are included. This may be useful when the Wannier model is expected to describe all the salient features of a system, but disentanglement is necessary, e.g., to remove extraneous states at the band edges.

¹In the interest of full disclosure, the diagram is accurate in the case where only Wannier-Wannier transitions are taken into account. With mixed transitions, `vr` is supplemented by `vvr` and `vkα` by `vkαβ`, and `optic` is also called for the mixed [Wannier-Bloch] matrix elements.

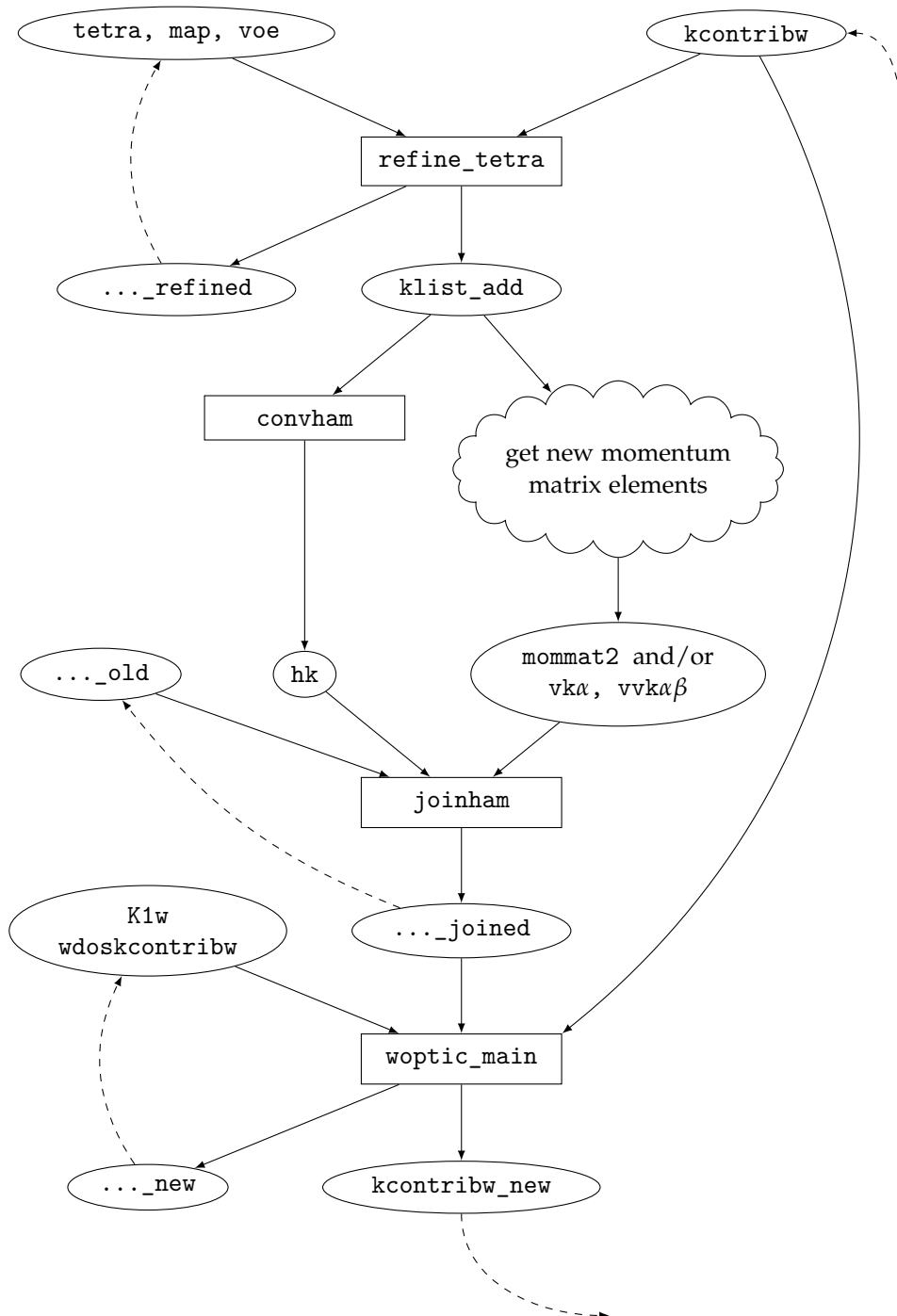


Figure 1.1: Flow of control and information in the main WOPTIC loop: programs (rectangles) and selected files (ellipses). Dashed lines indicate a file is taken from the previous iteration.

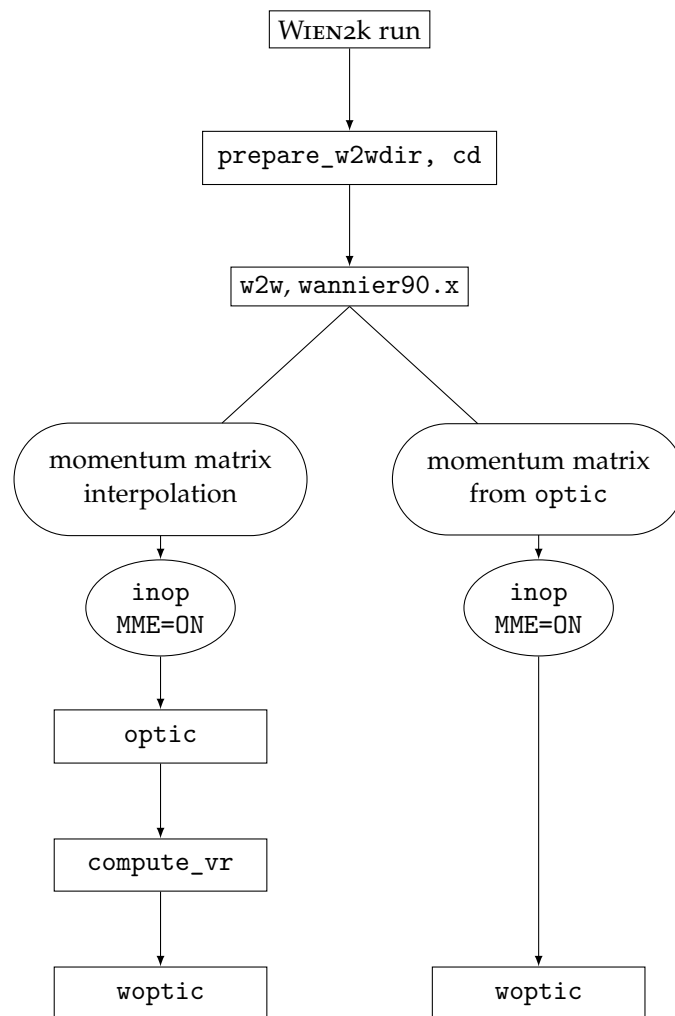


Figure 1.2: Flow of control and information in WOPTIC initialization.


1.1. SYNOPSIS

5

1.1 Synopsis

```
woptic [-i  $N_{\text{tot}}$  ] [--restart  $I$ ] [more options]
```

1.2 Options

```
-i  $N_{\text{tot}}$  stop after iteration  $N_{\text{tot}}$  (default: 5)
--restart  $I$  restart from case.wophist.zip at the beginning of iteration  $I$  (default: 1)
--restore  $I$  restore iteration  $I$  from case.wophist.zip without continuing
--theta  $\Theta$  refinement harshness ( $\Theta = 0$ : uniform mesh,  $\Theta = 1$ : most adaptive; default: 0.5)
--inter focus refinement on larger  $\Omega$ 
--init  $N_i$  initial uniform refinement steps (default: 3)
 --band compute optical conductivity contributions along case.klist_band to be processed by kanalysis
```

The iterations in `-i`, `--restart`, and `--restore` are “absolute” in the sense that iteration 1 always corresponds to the initial k-mesh. Thus, `woptic --restart 3 -i 5` does three iterations: nos. 3, 4, and 5. Iteration no. 1 starts with a uniform k-mesh whose density is determined by N_i . The starting mesh corresponds to $(2^{N_i+1})^3$ k-points in the full `BZ`.

Let T be a tetrahedron and $\epsilon(T)$ its associated integration error estimate. The precise meaning of the “harshness” $\Theta \in [0, 1]$ is: T will be refined if

$$\epsilon(T) \geq \Theta \max_T \epsilon(T) \quad (\text{--theta})$$

(but may also be refined due to other rules) [4, 6]. The `--inter` option scales the contributions to the error estimates by the frequency,

$$\epsilon(T; \Omega) \leftarrow \Omega \cdot \epsilon(T, \Omega), \quad (\text{--inter})$$

for the purposes of refinement.

1.3 The input file `case.inwop`


The main input file for WOPTIC is

```
----- case.inwop -----
1 OPT  interp  F      # mode;      matemode;      intra-uc hop? (Peierls)
2 10 0.05 0.05  3 1e-5 # Emax, dE, delta (eV);  omega-div, tol-cutoff
3 21 23 12 25   # inner window (= WFs); [outer window]
4 40.0 0.00     # inv. temp. (eV^-1);   chemical potential (eV)
5 1.0  F        # Drude-sumrule sep. [eV]; compute orb.resolv.?
6 T 0          # read self-energy?     #bands
7 21 22 23     # bands with self-energy (if #b=0: inner window)
8 F F 1.23 0   # rotate WFs?;         scissors?, shift (eV), #bands
9 24 25       # bands to shift
----- end of case.inwop -----
```

This file is read using Fortran list-oriented reads, i.e., items are separated by white space.

line 1 mode, matemode, intrahop — modes of operation

mode	OPT	compute the optical conductivity
	JOINT	compute the joint density of states (noninteracting only)
matemode	1 Peierls	use dH^w/dk as momentum matrix elements
	2 interp	Wannier-interpolated momentum matrix elements
	3 optic	matrix elements computed by WIEN2k's optic
	4 Bloch	for testing (noninteracting only)
	5 LDA	for testing (noninteracting only; should be similar to optic-joint-kram)
intrahop	<i>logical</i>	whether to use intra-UC hopping in Peierls mode [2, 3] (needs <code>case.intrahop</code>)

 Only modes `interp` and `optic` are thoroughly tested; `Peierls`, `Bloch`, and `LDA` must be considered experimental.

line 2 Ω_{\max} , $\Delta\Omega$, δ , $N_{\omega/\Omega}$, ϵ — frequency grids and broadening

Ω_{\max}	eV	maximum external frequency for which $\sigma(\Omega = \Omega_{\max})$ is computed
$\Delta\Omega$	eV	Ω grid spacing
δ	eV	broadening parameter for noninteracting bands (where $\Sigma \leftarrow i\delta$)
$N_{\omega/\Omega}$	<i>int</i>	internal frequency density ($N_{\omega/\Omega}$ internal ω per external Ω)
ϵ	<i>real</i>	tolerance for ω -integration limits ($-\Omega_{\max} \lesssim \omega \lesssim 0$)

line 3 W_{lo} , W_{hi} , [B_{lo} , B_{hi}] — band windows

W_{lo} , W_{hi}	<i>int</i>	band indices corresponding to WFs
B_{lo} , B_{hi}	<i>int</i>	the outer (“Bloch”) window (<i>optional, default: W_{lo}, W_{hi}</i>)

line 4 β , μ — grand-canonical ensemble parameters

β	eV^{-1}	the inverse temperature (<i>To convert to temperature in Kelvin: $T \cong 11604/\beta$.</i>)
μ	eV	the chemical potential (<i>applied only to the interacting bands [see <code>iself</code>], use the DMFT value; for noninteracting calculations, set $\mu = 0$</i>)

line 5 $Drudeseq$, $orbresolv$

$Drudeseq$	eV	cutoff for Drude sumrule integration
$orbresolv$	<i>logical</i>	whether to compute observables per-orbital

line 6 $selfE$, $Nself$ — self-energy specification

$selfE$	<i>logical</i>	whether to read self-energy $\Sigma_i(\omega)$ from <code>case.selfE</code>
$Nself$	<i>int</i>	number of bands with self-energy, or 0 (<i>in this case, $W_{hi} - W_{lo} + 1$</i>)

line 7 $iself$ — interacting bands (*ignored if `selfE=.false.` or `Nself=0`*)

$iself$	<i>int</i> ($Nself$)	indices of interacting bands (<i>if <code>Nself=0</code>: inner window</i>)
---------	------------------------	---

line 8 $wfrot$, $shift$, $Eshift$, $Nshift$ — WF rotation and scissors operator

$wfrot$	<i>logical</i>	whether to apply unitary matrix from <code>case.wfrot</code> to WF basis
---------	----------------	--

1.4. OUTPUT FILES

7

<code>shift</code>	<i>logical</i>	whether to apply rigid "scissors" shift
<code>Eshift</code>	<i>eV</i>	shift value
<code>Nshift</code>	<i>int</i>	number of bands to shift

line 9 `ishift` — scissor bands

<code>ishift</code>	<i>int(Nshift)</i>	indices of bands to shift
---------------------	--------------------	---------------------------

1.4 Output files

Over the course of the iterations, `woptic` writes diagnostic information to standard output and lists the executed commands in `:log`. In particular, the current values of the quantities `thermopower`, `dc conductivity`, and `sumrules` are extracted from `woptic_main`'s output file `case.outputwop`, as well as the integration error estimator from `refine_tetra`'s `case.outputref`. The latter is given in arbitrary units and should decrease over the iterations.

The optical conductivity is written to `case.optcondw`. For comparison with `WIEN2k`'s standard `optic` module, note that there is a factor ≈ 1112.65 between `optic`'s output (given in Gaussian CGS units of 10^{15} s^{-1} in `case.sigmak`) and `WOPTIC`'s (in SI units of S cm^{-1}). Expressed in the SI, the conversion is $\text{optic} = \text{WOPTIC} \cdot 4\pi \epsilon_0 10^{15} \text{ Hz } \Omega \text{ cm}$.

The density of states is written to `case.wdos`. The files `case.optcondw` and `case.wdos` always correspond to the latest iteration. Together with certain other files, they are archived in `case.wophist.zip` with a suffix `.I` for iteration `I`.

2 Support Programs

In this section, the sub-programs called by `woptic` are documented, roughly in order of decreasing user-callability.

2.1 `wopticlean` — remove left-over files from woptic runs

`wopticlean` preserves files which serve as input to `woptic` and its sub-programs, as well as the archive file `case.wophist.zip`. The number of files considered for deletion is substantial; to check which ones are, use the `--recon` option or the source.

Synopsis

```
wopticlean [--recursive] [--mrproper] [--recon] [directory ...]
```

Options and arguments

- `-r|--recursive` Operate recursively on *all* directories below
- `-A|--mrproper` delete also files whose basename does not match the containing directory
- `-n|--recon` dry-run; print file names that would be deleted

The arguments specify *directories* to operate on (*default: .*). Before a big cleanup (especially when using `-A` or `-r`), you are advised to do a dry-run.

2.2 `compute_vr` — compute $V^w(R)$

`compute_vr` computes the dipole matrix elements $V^{W,\alpha}(R)$ and $W^{\alpha\beta}(R,\omega)$ in direct space by applying the matrices $U(k)$ and a Fourier transform for use with the `interp` mode. You should check these matrix elements (especially $W^{\alpha\beta}$) for decay in R when using this mode.

Synopsis

```
compute_vr [--text] case
```

Option

`--text` output `case.vvr` in plain text

Files read

`case.inwop` input file
`case.chk` WANNIER90 checkpoint file
`case_hr.dat` Hamiltonian in direct space
`case.mommat2` momentum matrix elements
`case.struct` WIEN2k master input file (*mixed transitions*)
`case.energy` energies from `lapw1` (*mixed transitions*)
`case.fermi` Fermi energy (*mixed transitions*)
`case.inwf` `w2w` input file (*disentanglement*)

Files written

`case.outputvr` log file
`case.vr` $V^{W,\alpha}(R)$
`case.vvr` $W^{\alpha\beta}(R, \omega)$ (*mixed transitions*)

2.3 kanalysis — $\sigma(k, \omega)$ on a BZ path

This program generates files that can be used for analysis of the contributions to the optical conductivity in `WOPTIC`. Required is a run of `woptic` with the `--band` option, such that it computes the contributions to the optical conductivity along `case.klist_band` and stores them in `case.kcontribw_band`. `kanalysis` reads this file and generates 2D data in ω - and k -space readable e.g. by `gnuplot`.

Synopsis

`kanalysis` n_{Ω}^{\min} `case` [`mode`]

Arguments

n_{Ω}^{\min} minimum frequency index for output
`mode` (*optional*) by default, the output includes extra newlines for convenient plotting with `gnuplot` (`splot "case.optanalysis_band" with pm3d`); if `mode = 1`, these newlines are omitted

2.4 obtain_dist — intra-UC hopping for Peierls

In `WOPTIC`, for the generalized Peierls approximation [2], the distances between the Wannier centers are required. This program reads `case_centres.xyz` which is produced by `WANNIER90` and generates `case.intrahop` which can then be used by `WOPTIC`.

2.5. INWOPCHECK — PARSE INWOP FILE

11

Synopsis

```
obtain_dist case
```

2.5 inwopcheck — parse inwop file

A helper program for woptic. Reads an inwop file and outputs information suitable for reading in a shell script or for inspection.

Synopsis

```
inwopcheck case.inwop
```

2.6 woptic_main — k-integration

woptic_main computes the optical conductivity contributions $\sigma(k, \omega)$ on the k-mesh constructed by refine_tetra and performs the k- and ω -integration. It is normally called by woptic, but it may be useful to call it manually after a woptic run.

Synopsis

```
woptic_main [--band] case
```

Option

--band compute optical conductivity contributions along `case.klist_band` to be processed by `kanalysis`

Files used by woptic_main are listed below. *Updated* files are written with a suffix `_new`. Which files precisely are used depends on the options in effect, this dependence is partially indicated below.

Files read

```
case.inwop  woptic main input file (always)
case.struct Wien2k master input file (always)
case.symop  symmetry operations from optic (always)
case.klist  symmetrized k-points (always)
case.tetra  symmetrized tetrahedra (always)
case.energy energies from lapw1
case.fermi  Fermi energy
case.mommat2 matrix elements from optic
case.chk    WANNIER90 checkpoint file (testing mode)
case.vk $\alpha$  Wannier-interpolated matrix elements (interp)
```

`case.vvk $\alpha\beta$` Wannier-interpolated mixed matrix elements (*interp*)
`case.hk` Wannier Hamiltonian $H^w(R)$
`case.selfE` self-energy $\Sigma(\omega)$ (*selfE*)
`case.wfrot` Wannier function rotation matrix (*wfrot*)
`case.klist_full` unsymmetrized k-points (*Peierls*)
`case.tetra_full` unsymmetrized tetrahedra (*Peierls*)
`case.map` mapping of `klist_full` to `klist` (*Peierls*)
`case.intrahop` WF center distance matrix (*Peierls & intrahop*)

Files written

`case.outputwop` diagnostic output (*always*)
`case.optcondw` optical conductivity (*always*)
`case.wdos` (joint) density of states (*always*)
`case.optcondw_orb $\alpha\beta$` orbitally resolved optical conductivity (*orbresolv*)

Files updated

`case.kcontribw` optical conductivity contributions
`case.K1w` thermopower contributions
`case.wdoskcontribw` DOS contributions

2.7 refine_tetra — k-mesh refinement

`refine_tetra` uses the optical conductivity contributions $\sigma(k, \omega)$ to compute integration error estimates and refine the k-mesh. It is normally called by `woptic`.

Synopsis

```
refine_tetra [options] case
```

Options

`--theta` Θ $0 \leq \Theta \leq 1$ defines the “harshness” of refinement (see corresponding option of `woptic`)
`--init` N_i initial refinement with N_i steps (see corresponding option of `woptic`)
`-inter` give larger weight to higher-energy contributions (see corresponding option of `woptic`)

Files used by `refine_tetra` are listed below. Updated files are written with a suffix `_refined`.

2.8. JOINHAM — COMBINE HK / MOMMAT2 / VK α / VVK $\alpha\beta$ FILES

13

Files read

`case.inwop` woptic main input file
`case.struct` Wienzk master input file

Files written

`case.kcontribw` function values for estimator on `case.klist`
`case.outputref` log file

Files updated

`case.klist` symmetrized k-points
`case.klist_full` unsymmetrized k-points
`case.tetra` symmetrized tetrahedra
`case.tetra_full` unsymmetrized tetrahedra
`case.voe` list of k-points on tetrahedral edges
`case.map` internal mapping of `case.klist_full` to `case.klist`

2.8 joinham — combine hk / mommat2 / vk α / vvk $\alpha\beta$ files

joinham combines `_old` files from the previous iteration with new files corresponding to added k-points. It is normally called by woptic.

Synopsis

```
joinham case |
joinham hk mommat |
joinham hk1 hk2 hkout |
joinham hk1 hk2 hkout mom1 mom2 momout
```

Arguments

hk* a file of type `case.hk`, `case.vk α` , or `case.vvk $\alpha\beta$`
mom* a file of type `case.mommat2`

In the first form, `case.hk_old` is joined with `case.hk`, and, if they exist, `case.mommat2_old` with `case.mommat`. In the second form, `hk_old` is joined with `hk` and `mom_old` with `mom`. In both cases, output file names are suffixed with `_joined`. Unformatted `mom` files are handled automatically and result in unformatted output.

2.9 convert_vr — Fourier-interpolate $V^w(k)$

`convert_vr` computes `case.vk α` and `case.vvk $\alpha\beta$` from `case.vr` and `case.vvr` by Fourier transform. The procedure is analogous to `convham`, `case.hk`, and `case_hr.dat`.

Synopsis

```
convert_vr [--text] case
```

Option

-t, --text write *case.vvka β* in plain text instead of unformatted (*case.vk α* is always plain text)

Files read

case.struct WIEN2k master input file

case.klist target k-points

case.inwop woptic input file

case.vr direct-space matrix elements $V^{W,\alpha}(R)$

case.vvr direct-space mixed matrix elements $W^{\alpha\beta}(R,\omega)$ (*mixed transitions*)

Files written

case.outputvk log file

case.vk{x,y,z} k-space matrix elements $V^{W,\alpha}(k)$

case.vvk{xx,xy,xz,yy,yz,zz} k-space mixed matrix elements $W^{\alpha\beta}(R,\omega)$ (*mixed transitions*)

Bibliography

- [1] P. WISSGOTT, J. KUNEŠ, A. TOSCHI, and K. HELD. *Dipole matrix element approach versus Peierls approximation for optical conductivity*. Phys. Rev. B **85**, 205133 (2012).
- [2] J.M. TOMCZAK and S. BIERMANN. *Optical properties of correlated materials: Generalized Peierls approach and its application to VO₂*. Phys. Rev. B **80**, 085117 (2009).
- [3] J.M. TOMCZAK. *Spectral and optical properties of correlated materials*. PhD Thesis, École Polytechnique, Paris (2007).
- [4] P. WISSGOTT. *Transport properties of correlated materials from first principles*. PhD Thesis, TU Wien, Vienna (2012).
- [5] E. ASSMANN. *Spectral properties of strongly correlated materials*. PhD Thesis, TU Wien, Vienna (2015).
- [6] P. WISSGOTT, E. ASSMANN, J. KUNEŠ, A. TOSCHI, P. BLAHA, and K. HELD. *woptic: optical conductivity with Wannier functions and adaptive k-mesh refinement*. Comp. Phys. Commun. **XXX**, YYY (2015), arXiv:15UU.WWWW.
- [7] P. BLAHA, K. SCHWARZ, G.K.H. MADSEN, D. KVASNICKA, and J. LUITZ. *Wien2k, An Augmented Plane Wave + Local Orbitals Program for Calculating Crystal Properties*. Techn. Universität Wien, Vienna, (2001). <http://www.wien2k.at>.
- [8] J. KUNEŠ, R. ARITA, P. WISSGOTT, A. TOSCHI, H. IKEDA, and K. HELD. *Wien2wannier: From linearized augmented plane waves to maximally localized Wannier functions*. Comp. Phys. Commun. **181**, 1888 (2010), arXiv:1004.3934.
- [9] A.A. MOSTOFI, J.R. YATES, Y.-S. LEE, I. SOUZA, D. VANDERBILT, and N. MARZARI. *Wannier90: A tool for obtaining maximally-localized Wannier functions*. Comput. Phys. Commun. **178**, 685 (2008).
- [10] P. WISSGOTT, J. KUNEŠ, A. TOSCHI, and K. HELD. *Dipole matrix element approach versus Peierls approximation for optical conductivity*. Phys. Rev. B **85**, 205133 (2012).

B. Reproduced journal articles

In this appendix, the journal articles published during the course of this thesis are reproduced in reverse chronological order. To wit:

B1 [Ass+15]. The article on WOPTIC (Chapter 6), submitted but not yet published at the time of writing. It comprises an outline of the calculation of the k-dependent contributions to the optical conductivity, a description of the adaptive integration algorithm, as well as applications to fcc-Al in a “noninteracting” (i.e. DFT-only) model and SrVO₃ (cf. Sec. 6.1) in DMFT.

B2 [Rib+14]. In LDA+DMFT and similar methods, when multiple orbitals are included, the local electron-electron interaction is a complicated object. In a single-orbital model, it is completely specified by a single parameter U ; a priori, this generalizes to a full tensor $U_{ijkl}^{\sigma\tau}$, whose upper indices refer to spins, and lower indices to orbitals (cf. Chapter 4).

In practice, the structure of this tensor is often simplified by symmetry or approximation. For t_{2g} models in a cubic environment, a commonly used form is given by the Kanamori Hamiltonian (4.2), normally in conjunction with the rule $U = U' + 2J$ (4.3). Eq. (4.2) is accurate in cubic symmetry, but (4.3) is only valid in spherical symmetry. This article explores the physical origins and, using MLWF, the magnitude of the deviations in real cubic materials, specifically, SrVO₃ (3d) and BaOsO₃ (5d).

B3 [Rub+14]. In supercell calculations, for example to model disorder or impurities, the BZ shrinks with respect to the ideal crystal, in proportion to the size of the supercell. This effect is known as *Brillouin-zone folding*, and results in energy bands being “folded back” into the smaller BZ. It can seriously hamper the interpretation of the band structure, necessitating a procedure to “unfold” the band structure.

B. Reproduced journal articles

This article presents *band-structure unfolding* in the context of WIEN2k as implemented in the FOLD2BLOCH package, together with applications to the group III-V and II-VI semiconductor solid solutions GaP:N, GaAs:Bi and (HgCd)Te.

- B4 [Ass+13]. The article proposing $\text{LaVO}_3|\text{SrTiO}_3$ solar cells, which forms the basis of Chapter 7.

woptic: optical conductivity with Wannier functions and adaptive k-mesh refinement

E. Assmann^{a,b,*}, P. Wissgott^a, J. Kuneš^c, A. Toschi^a, P. Blaha^d, K. Held^a

^aInstitute of Solid State Physics, Vienna University of Technology, 1040 Vienna, Austria

^bInstitute of Theoretical and Computational Physics, Graz University of Technology, 8010 Graz, Austria

^cInstitute of Physics, Academy of Sciences of the Czech Republic, 18221 Praha 8, Czechia

^dInstitute of Materials Chemistry, Vienna University of Technology, 1060 Vienna, Austria

Abstract

We present an algorithm for the adaptive tetrahedral integration over the Brillouin zone of crystalline materials, and apply it to compute the optical conductivity, dc conductivity, and thermopower. For these quantities, whose contributions are often localized in small portions of the Brillouin zone, adaptive integration is especially relevant. Our implementation, the *woptic* package, is tied into the WIEN2WANNIER framework and allows including a many-body self energy, e.g. from dynamical mean-field theory (DMFT). Wannier functions and dipole matrix elements are computed with the DFT package WIEN2k and Wannier90. For illustration, we show DFT results for fcc-Al and DMFT results for the correlated metal SrVO₃.

Keywords: optical conductivity, adaptive algorithm, electronic structure, density functional theory, Wannier functions, augmented plane waves

1. Introduction

The theoretical description of crystalline solids is greatly simplified by their periodicity. The Bloch theorem for non-interacting electrons allows one to replace a sum over infinitely many discrete lattice vectors by an integral over a continuous k-vector restricted to the Brillouin zone (BZ). A similar simplification is possible in interacting systems where the crystal momentum \mathbf{k} is a conserved quantity for a variety of excitations. This makes BZ-integration an indispensable part of any numerical technique for periodic solids. To evaluate the integral numerically, we must discretize the BZ in some way. The usual methods used in band-structure calculations rely on an *a priori* choice of the k-mesh which covers the BZ uniformly; e.g. using a straightforward summation [1–3], or the more sophisticated *tetrahedron method* [4]. This is a natural choice for the calculation of quantities such as the charge density, to which all k-points contribute. On the other hand, the transport or low-energy spectral properties are usually dominated by certain regions of the BZ, e.g. the vicinity of the Fermi surface. To compute such quantities, an inhomogeneous k-mesh adapted to a particular material may be a better choice.

In the present article, we describe a technique to recursively generate an inhomogeneous k-mesh for periodic solids in three dimensions. Our implementation, the *woptic* package, is designed to calculate the optical conductivity, dc conductivity, and thermopower of interacting electrons. However, the adaptive k-mesh management is encapsulated in a subprogram (`refine_tetra`) which may easily be adapted to other quantities.

Woptic operates in the context of dynamical mean-field theory (DMFT) [5, 6] for real materials. This “DFT+DMFT” approach [7, 8] uses the band structure from density-functional theory (DFT) in the local-density or generalized gradient approximations (GGA) to construct an effective multiband Hubbard model, which is analyzed using the DMFT technique.¹ Calculation of the optical conductivity represents a post-processing step in this scheme. In the present implementation, we use inputs generated by the WIEN2k [10], WIEN2WANNIER [11], and Wannier90 [12] codes and a self energy (on the real- ω axis) from any DMFT solver. So far, only local self energies $\Sigma(\omega)$ are implemented, but the approach is very general and allows including any self energy on top of WIEN2k. In particular, extension to a non-local $\Sigma(\mathbf{k}, \omega)$ (e.g. from GW [13, 14], or from extensions of DMFT [15–17]) is simple as long as $\Sigma(\mathbf{k}, \omega)$ may be obtained at any \mathbf{k} .

When vertex corrections are neglected (they are strongly suppressed in DMFT, see below), the optical conductivity involves a BZ sum of contributions obtained from the k-resolved one-particle spectral functions and dipole matrix elements between the corresponding wave functions. We start by evaluating the optical conductivity on a uniform tetrahedral k-mesh. Next, we offer a refinement, test the sensitivity of the studied quantity and decide whether the refinement should be accepted. Accepting a refinement leads to the recursive generation of additional k-points in a way that ensures the numerical stability of the algorithm.

While the band structure part of the calculation uses augmented plane waves, the Hubbard model is naturally formulated in terms of localized orbitals. The transformation between

*Corresponding author

Email address: elias.assmann@tugraz.at (E. Assmann)

¹The calculations reported in this article use the GGA in the form of the PBE functional [9].

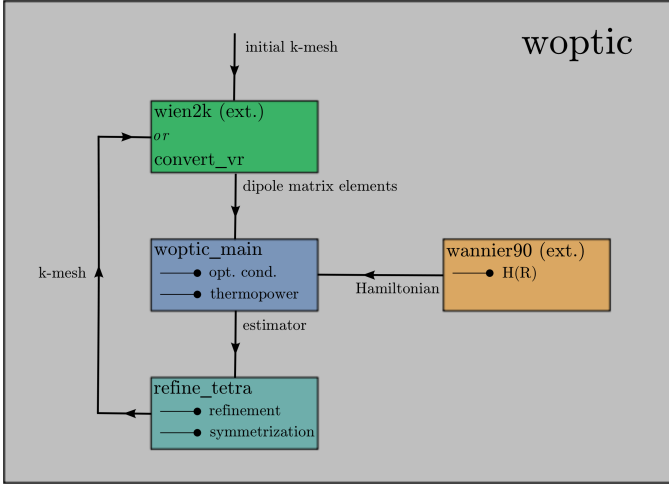


Figure 1: Schematic work flow of the woptic algorithm to compute the optical conductivity with an adaptive tetrahedral refinement for the BZ-integration. The algorithm is implemented in two new programs `woptic_main` (evaluates the optical conductivity for a given k-mesh) and `refine_tetra` (adaptively refines the k-mesh) which are called by the driver script `woptic`, together with several support programs. Wannier90 provides the real space hopping matrix $H(\mathbf{R})$, whereas the dipole matrix elements are computed either by the WIEN2k programs `lapw1` and `optic`, or by the woptic program `convert_vr`. See woptic user's guide for more detailed work flow diagrams.

the two bases is accomplished by the Wannier construction [11, 18, 19].

An overview of the work flow of the adaptive refinement program called `woptic` can be found in Fig. 1. The work flow can be summarized as

0. Choose an initial k-mesh and set iteration $\ell = 0$ (see Sec. 3.1 for the formal definition of the mesh).
1. Compute the dipole matrix elements $v^{(\ell)}(\mathbf{k})$ of Eq. (2) (see Sec. 4 for details).
2. Compute the optical conductivity $\sigma^{(\ell)}$ for a given k-mesh (see Sec. 2 for the formula used to obtain $\sigma^{(\ell)}$). Extract the information which regions of k-space have a large contribution to the integration error (see Sec. 3.2 for details on the numerical quadrature and how the error is estimated).
3. Stop if the change of the optical conductivity with respect to the previous iteration $\sigma^{(\ell-1)}$ is below a given tolerance,² otherwise refine the k-mesh where necessary, thus obtaining a new k-mesh, and return to step 1 with $\ell \leftarrow \ell + 1$ (see Sec. 3.1 for information on the refinement process).

A more detailed version of the work flow, with a description of available modes, can be found in Sec. 4.2.

This paper is structured as follows: First, in Sec. 2, we give a description of the specific numerical problem to compute the optical conductivity. In Sec. 3, we specify the tetrahedral mesh and the refinement strategy. Furthermore, we survey the estimation of the integration error necessary to mark tetrahedra for refinement in Sec. 3.2 and depict methods to increase the numerical performance in Sec. 3.3. In Sec. 4, we focus on practical

considerations such as the available modes in the program and more details of the work flow and show numerical tests. Finally, in Sec. 5 we present two applications, elementary aluminum and the vanadate SrVO_3 .

2. Problem statement

The Kohn-Sham Hamiltonian H of DFT is diagonal in the Bloch-wave basis. Hence, the corresponding optical conductivity σ can be written in terms of the dipole matrix elements and δ -functions [20]

$$\sigma_{\alpha\beta}(\Omega) = -\frac{2\pi e^2}{V} \int_{\text{BZ}} d\mathbf{k} \sum_{c,v} \frac{\delta(\varepsilon_c(\mathbf{k}) - \varepsilon_v(\mathbf{k}) - \Omega)}{\Omega} \cdot v_{v,c}^\alpha(\mathbf{k}) v_{v,c}^\beta(\mathbf{k}). \quad (1)$$

Here, Ω is the external frequency, e is the electronic charge, V the volume of the unit cell, the sum is over conduction (c) and valence (v) electrons with energy ε_{nk} , while

$$v_{nm}^\alpha(\mathbf{k}) = -\frac{i}{m_e} \langle \psi_{nk} | \partial_\alpha | \psi_{mk} \rangle \quad (2)$$

are the dipole matrix elements with the Bloch states ψ_{nk} (we set $\hbar = 1$), and m_e denotes the electron mass. In general, the resulting value for σ depends on the number of k-points used in the integration as well as the applied quadrature rule. However, the evaluation of the integrand in Eq. (1) is numerically cheap and one usually proceeds to uniformly refine a given k-mesh until convergence.

In the following we assume that we have constructed a mapping $U(\mathbf{k})$ from N Bloch states computed by WIEN2k [21] to N maximally localized Wannier functions (WFs) with Wannier90 [12]; thus we have the Hamiltonian in Wannier space

$$H(\mathbf{k}) = U^\dagger(\mathbf{k}) E(\mathbf{k}) U(\mathbf{k}) \quad \text{with} \quad E_{nm}(\mathbf{k}) = \delta_{nm} \varepsilon_{nk}. \quad (3)$$

This means that the electronic structure is not described in terms of bands ε_{nk} , $1 \leq n \leq N$, but by a Hamiltonian matrix $H(\mathbf{k}) \in \mathbb{C}^{N \times N}$. This is appropriate, for example, when a set of WF's is required as an input for many-body calculations such as DFT+DMFT. Also in light of possible DFT+DMFT applications of the algorithm, we will not consider the effects of vertex corrections. In fact, while they can significantly affect the DMFT results for other response functions like the spin/charge susceptibilities [22, 23], their contribution to the DMFT optical conductivity is strongly suppressed (and vanishes exactly in the single-band case) due to the k-structure of the electronic current operator [24, 25]. On the basis of these considerations, the following general expression for the optical conductivity [25, 26] can be written

$$\sigma_{\alpha\beta}(\Omega) = -\frac{2\pi e^2}{V} \int_{\text{BZ}} d\mathbf{k} \int_{-\infty}^{+\infty} d\omega \frac{f(\omega + \Omega) - f(\omega)}{\Omega} \cdot \text{Tr} \left[v^{\text{w}\alpha}(\mathbf{k}) A(\mathbf{k}, \omega + \Omega) v^{\text{w}\beta}(\mathbf{k}) A(\mathbf{k}, \omega) \right]. \quad (4)$$

²In the current version of the code, convergence has to be checked manually.

Here, N_ω is the number of frequencies, f the Fermi function at a given temperature,

$$v_{rs}^{w\alpha}(\mathbf{k}) = U_m^\dagger(\mathbf{k}) v_{nm}^\alpha(\mathbf{k}) U_{ms}(\mathbf{k}) = -\frac{i}{m_e} \langle w_{rk} | \partial_\alpha | w_{sk} \rangle \quad (5)$$

the dipole matrix rotated to the basis of k-space WFs $w_{rk}(\mathbf{r})$, and A the matrix spectral function

$$A_{mn}(\mathbf{k}, \omega) = \frac{i}{2\pi} [G_{nm}^{ret}(\mathbf{k}, \omega) - G_{nm}^{ret,*}(\mathbf{k}, \omega)] \quad (6)$$

defined via the Green's function

$$G(\mathbf{k}, \omega) = [\omega - H(\mathbf{k}) - \Sigma(\mathbf{k}, \omega)]^{-1} \quad (7)$$

and the corresponding electronic self energy $\Sigma(\mathbf{k}, \omega)$, all of which are also taken to be in the Wannier basis. Whereas in DFT, Eq. (1) scales linearly with the number of included bands, the general version, i.e., Eq. (4), scales quadratically with the number of orbitals. Thus, for a basis set in which $H(\mathbf{k})$ is not diagonal, such as WFs, it is useful to reduce the number of k-space evaluations, while keeping the level of accuracy as close to the DFT formalism as possible.

In the specific case of DFT+DMFT calculations, the (\mathbf{k}, ω) -resolution required to resolve all features of the integrand of Eq. (4) depends in particular on the imaginary part of the self energy $\Im\Sigma(\mathbf{k}, \omega) = \Im\Sigma(\omega)$ contained in the DMFT Green's function $G(\mathbf{k}, \omega)$. For small $\Im\Sigma(\omega)$, a fine (\mathbf{k}, ω) -mesh is needed, since

$$\text{Tr} [v^w(\mathbf{k}) A(\mathbf{k}, \omega + \Omega) v^w(\mathbf{k}) A(\mathbf{k}, \omega)] \quad (8)$$

becomes sharply peaked. In many systems, the values of $\Im\Sigma(\omega)$ vary significantly between the different orbital manifolds, in particular when considering transitions between localized orbitals (which have been treated, e.g., with DMFT) and itinerant orbitals (whose description usually remains at the DFT or at the Hartree approximation level). Hence, a useful approach is to adapt the k-mesh to the problem under consideration and use a finer resolution only where it provides a substantial increase of accuracy. Though the present implementation assumes local self energies $\Sigma(\omega)$, generalization to a k-dependent $\Sigma(\mathbf{k}, \omega)$ is straightforward as long as $\Sigma(\mathbf{k}, \omega)$ can be obtained for any k-point in reciprocal space.

3. Algorithmic details

3.1. Tetrahedral mesh

The non-uniform triangulation of a three-dimensional domain represents a formidable numerical task. The concepts surveyed in this section are not new but combine various well-known methods, and below, we will concentrate on the definitions necessary for the rest of this paper. For a more formal and complete introduction to tetrahedral triangulation see for example Ref. [27].

We denote the set of k-points of a certain tetrahedral triangulation by \mathcal{K} and the corresponding set of tetrahedra by \mathcal{T} . Then,

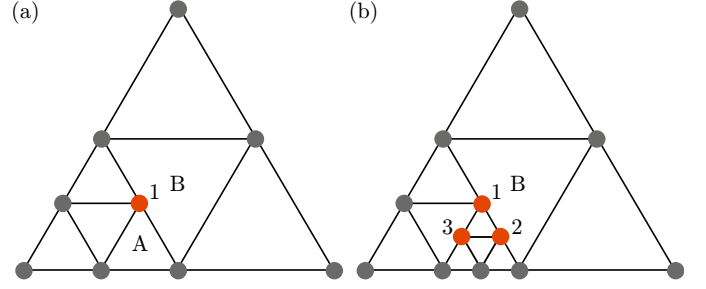


Figure 2: An example of a 2D triangulation with a hanging node (a) shown in red and marked 1 (in this example we only discuss the nodes interior to the picture). Upon refinement of element A shown in (a), one arrives at the triangulation (b) with two additional hanging nodes 2, 3. This triangulation violates the regularity condition, since there are two hanging nodes 1, 2 on the same edge. To make (b) regular we must also refine element B; this is the mesh closure for this triangulation.

$N_k = |\mathcal{K}|$ is the total number of k-points, and \mathcal{K} contains as elements or nodes the 3D coordinates

$$n_m = [k_x \quad k_y \quad k_z], \quad 1 \leq m \leq N_k. \quad (9)$$

Furthermore, \mathcal{T} stores a list of vertices

$$T_m = [v_1 \quad v_2 \quad v_3 \quad v_4], \quad 1 \leq m \leq N_T \quad (10)$$

where $v_1, \dots, v_4 \in \mathcal{K}$ and $N_T = |\mathcal{T}|$ is the total number of tetrahedra (in practice, we store more information for each tetrahedron than just the vertices, see below). Thus, the four vertices v_1, \dots, v_4 are nodes that define a tetrahedron $T_m \in \mathcal{T}$ and are themselves elements of \mathcal{K} . We will use the term *vertex* only in connection to a specific tetrahedron, while a node is a general element of the set of k-points. A special type of node is a so-called

hanging node: $n_h \in \mathcal{K}$ is a hanging node if it lies on an edge of an element $T \in \mathcal{T}$ without being a vertex of T .

In the 2D visualization Fig. 2(a), node 1 is not a vertex of the central triangle B and hence a hanging node. Of course, a hanging node is a vertex of other triangles (here, A).

We require \mathcal{T} to fulfill the following two conditions:

regularity: No element $T \in \mathcal{T}$ has an edge with more than one hanging node (see Fig. 2; otherwise, perform mesh closure, see below).

shape stability: For all tetrahedra $T \in \mathcal{T}$, there is a predefined constant c_S such that the radius of the circumscribed sphere r_T satisfies $r_T^3/|T| \leq c_S$ where $|T|$ is the volume of T .

A large amount of the algorithmic effort in woptic is focused on keeping \mathcal{T} shape stable and regular on refinement. If the ratio $r_T^3/|T|$ becomes large this indicates a highly distorted (also called a degenerate element) and the numerical error of the integration rules may become large. A highly non-regular mesh, on the other hand, means that nearby regions of k-space are resolved very differently, see e.g. Fig. 2(b). This often leads to unstable

convergence rates since some features of the integrand may not be fully resolved.

In contrast to the 2D case of triangles, the refinement of a tetrahedron into 8 sub-tetrahedra of equal size is not unique and, in general, the resulting elements cannot all be similar to the original tetrahedron. In the following, we will depict Ong's idea [28] for a refinement strategy where the shape of the element is at least confined to two classes, and shape stability is thus guaranteed. This strategy is based on the triangulation of the parallelepiped defined by the three reciprocal unit vectors of the BZ into six tetrahedra of equal volume [Kuhn triangulation, Fig. 3(a)]. The resulting tetrahedra fall into two classes, in the following denoted by class 1 and 2. Specifically, it can be proven [28, 29] that for the refinements shown in Fig. 3, the resulting 8 new elements of a tetrahedron will again belong to one of the two classes. Of the 8 new elements, 4 will share a vertex with the original tetrahedron and the other 4 will form a central octahedron. The difference between the two refinement methods shown in Fig. 3 is how the central octahedron is split into tetrahedra. Since the triangulation of the central octahedron is not unique there are other strategies to ensure shape stability, e.g. based on the numbering of the vertices [27]. In practice, ensuring shape stability of the mesh \mathcal{T} amounts to book-keeping of the classes of the tetrahedra upon refinement.

In order to satisfy the *regularity* of the mesh \mathcal{T} upon refinement, we add an additional step after the standard refinement of elements: *mesh closure* [30]. This procedure refines the elements with edges where regularity is violated (see Fig. 2(b) for a 2D example of a case where mesh closure is required). This leads to neighboring tetrahedra that will only differ by one level of refinement, since any tetrahedron which is refined twice while all of its neighbors remain in the initial state will automatically produce two hanging nodes on an edge. In this case the second refinement would trigger a refinement of the neighboring tetrahedra as well. Thus, when moving through k -space, the refinement level changes “smoothly”, i.e., regions with very fine resolution will not adjoin regions with very coarse resolution. These additional refinements lead to a higher number of total tetrahedra with respect to runs without mesh closure. Experience shows however that the price paid in performance is acceptable, since mesh closure helps avoid unstable runs of the algorithm.

Summarizing, we obtain the following refinement strategy, assuming we have a regular mesh $\mathcal{T}^{(\ell)}$ from the ℓ -th iteration of woptic (see Fig. 1) and a list of tetrahedra marked for refinement (see Section 3.2).

1. Refine all marked elements of $\mathcal{T}^{(\ell)}$ according to Fig. 3(c) and (e) for class 1 tetrahedra, and according to Fig. 3(b) and (d) for class 2 tetrahedra to obtain a refined mesh $\mathcal{T}_{\text{ref}}^{(\ell)}$.
2. Scan $\mathcal{T}_{\text{ref}}^{(\ell)}$ for hanging nodes.
3. Mark all elements of $\mathcal{T}_{\text{ref}}^{(\ell)}$ for refinement whose edges violate the regularity condition, i.e., have multiple hanging nodes.
4. If there are marked elements return to 1 with $\mathcal{T}_{\text{ref}}^{(\ell)} \rightarrow \mathcal{T}^{(\ell)}$, otherwise continue with $\mathcal{T}^{(\ell+1)} = \mathcal{T}_{\text{ref}}^{(\ell)}$.

This procedure gives a tree-like nested algorithm of refinement steps, which allows us to store the hanging nodes of $\mathcal{T}_{\text{ref}}^{(\ell)}$ and

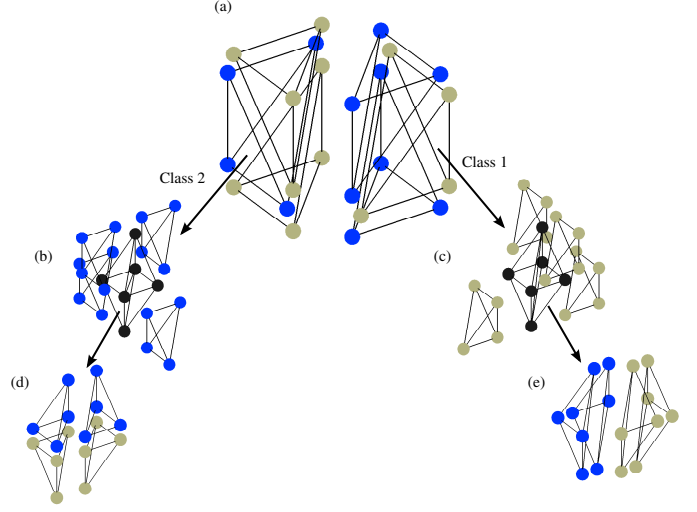


Figure 3: (a) Kuhn's refinement of a parallelepiped into eight tetrahedra as used by the woptic program. Class 1 tetrahedra are marked by beige vertices while class 2 tetrahedra are marked in blue. Note that every element of class 1 is mapped onto an element of class 2 and vice versa if mirrored along the main diagonal plane of the cube. The tetrahedra are first refined in 4 tetrahedra similar to the original one (having therefore the same class) and in a central octahedron denoted with black vertices, see panel (b) and (c). Depending on the class, the central octahedron is further split into 4 tetrahedra where 2 elements fall into the same class as the original tetrahedron and 2 in the respective other class, see panel (d) and (e).

pass them on to the next iteration of woptic. In woptic, the refinement strategy described above is implemented by the program `refine_tetra` (see Fig. 1).

3.2. Integration error estimation and refinement

Having outlined the salient points of mesh management, let us now discuss how elements of a mesh \mathcal{T} are chosen for refinement in the first place. Since we aim at minimizing the numerical integration error, we have to estimate the error ϵ_T which an element $T \in \mathcal{T}$ contributes to the overall error

$$\epsilon_{\text{tot}} = \left| \int_{\text{BZ}} d\mathbf{k} g(\mathbf{k}) - \sum_{T \in \mathcal{T}} g_T \right|, \quad (11)$$

where $g(\mathbf{k})$ denotes the integrand of the optical conductivity

$$\sigma_{\alpha\beta}(\Omega) = \int_{\text{BZ}} d\mathbf{k} \left(-\frac{2\pi e^2}{V} \right) \int_{-\infty}^{+\infty} d\omega \frac{f(\omega + \Omega) - f(\omega)}{\Omega} \text{Tr} [v^\omega(\mathbf{k})A(\mathbf{k}, \omega + \Omega)v^\omega(\mathbf{k})A(\mathbf{k}, \omega)] := \int_{\text{BZ}} d\mathbf{k} g(\mathbf{k}) \quad (12)$$

and g_T denotes an adequate tetrahedral quadrature rule (in $g(\mathbf{k})$ we omitted the dependence on the external frequency Ω for the moment, see below). For the integration over the internal frequency ω , we use a straightforward summation, exploiting only the weight factor $f(\omega + \Omega) - f(\omega)$ to limit the range of

integration. For the k -integration we use two different rules: First, a linear 4-point rule

$$g_T^{4p} = \frac{1}{4} \sum_{i=1}^4 g(v_i) \quad (13)$$

with v_1, \dots, v_4 being the vertices of T . Second, rule (13) can also be applied to the refined elements as

$$g_T^{4pr} = \frac{1}{32} \sum_{j=1}^8 \sum_{i=1}^4 g(v_{ji}), \quad (14)$$

where v_{ji} is the i -th vertex of the tetrahedron T_j ($j = 1, \dots, 8$) obtained from a refinement of T as introduced in the previous section. In the implementation, we evaluate the function $g(\mathbf{k})$ on the 10 points required to apply both rules Eq. (13) and (14). The 4 vertices of T required for the rule 4p are also included in T_1, \dots, T_8 . The latter additionally have 6 midpoints on the edges of T . Thus, $T_m \in \mathcal{T}$ is represented by the 10 nodes plus the class of the tetrahedron (which is required for the refinement strategy, see previous section),

$$T_m = [v_1 \ v_2 \ v_3 \ v_4; \ n_{12} \ n_{13} \ n_{23} \ n_{14} \ n_{23} \ n_{34}; \ 1 \ \text{or} \ 2], \quad (15)$$

where n_{ij} is the midpoint between the vertices v_i and v_j . Note that the nested nature of our quadrature rules allows us to re-use values of $g(\mathbf{k})$ in following iterations of the algorithm.

To estimate the contribution which T adds to the total error ϵ_{tot} , we compare the results of Eqs. (13) and (14), which means that the same rule is compared for two different levels of refinement [31]. Thus, our error estimator is

$$\epsilon_T = \left| \int_T d\mathbf{k} g(\mathbf{k}) - g_T^{4p} \right| \sim \left| g_T^{4p} - g_T^{4pr} \right|. \quad (16)$$

Since the rule (14) is obtained by applying the rule (13) to the sub-elements T_1, \dots, T_8 which would be new elements if T was refined, the error estimate ϵ_T provides a measure of how much a refinement of T would improve the numerical integration.

The dependence of the optical conductivity $\sigma_{\alpha\beta}(\Omega)$ on the external frequency Ω and the directional dependence ($\alpha\beta$) have been neglected so far. To take these dependencies into account, all error estimates of an element are averaged,

$$\bar{\epsilon}_T = \frac{1}{6} \frac{1}{N_\Omega} \sum_{\Omega\alpha\beta} \epsilon_T^{\alpha\beta}(\Omega), \quad \alpha\beta \in \{xx, xy, xz, yy, yz, zz\}. \quad (17)$$

To mark certain elements for refinement, we apply a standard procedure for adaptive mesh algorithms [30]: an element T is marked if

$$\bar{\epsilon}_T \geq \Theta \max_{T' \in \mathcal{T}} \bar{\epsilon}_{T'}, \quad (18)$$

where $\Theta \in [0, 1]$ is a parameter determining the *harshness* of the refinement. A value of $\Theta = 0$ means that all elements satisfy (18), i.e. uniform refinement, whereas large values of Θ lead to highly adaptive meshes. In *woptic*, the error estimation is

partly performed by *woptic_main* and partly by *refine_tetra* (see Fig. 1). The former computes the integrand, the latter calculates the error estimators $\bar{\epsilon}_T$ and marks the elements for refinement according to Eq. (18).

In metallic cases, the optical conductivity $\sigma(\Omega)$ for $\Omega \rightarrow 0$ has a Drude contribution corresponding to a Lorentzian at $\Omega = 0$ which is broadened by $\Im\Sigma(0)$. Thus, if $\Im\Sigma(0)$ is small, the error estimator (17) is often dominated by the values around the Fermi level $\Omega = 0$ and the algorithm mainly resolves the Fermi surface. This behavior may be adequate when one is interested in the dc-conductivity or the thermopower, but for the optical inter-orbital transitions at higher energies one might favor a better description in that region. In this case, another error estimator instead of Eq. (17) is more appropriate:

$$\bar{\epsilon}'_T = \frac{1}{6N_\Omega} \sum_{\Omega\alpha\beta} \Omega \epsilon_T^{\alpha\beta}(\Omega) \quad \alpha\beta \in \{xx, xy, xz, yy, yz, zz\}, \quad (19)$$

where the additional factor Ω attributes a larger weight to the error at higher frequencies.

3.3. Performance and symmetry considerations

Given that one evaluation of the function $g(\mathbf{k})$ from Eq. (12) is numerically expensive, the number of total evaluations should be kept as small as possible. For this reason, we use two techniques: (i) re-using the data from previous iterations and (ii) taking into account the symmetries of the crystal. The first point is the main reason for choosing the two nested quadrature rules (13 & 14), since, as mentioned above, a refinement of an element $T \in \mathcal{T}$ yields at most 6 new nodes. Moreover, neighboring elements with similar refinement level share nodes with T . Thus, though our integration rules are of low order, they represent an efficient choice in terms of the number of total evaluation points.

To understand (ii), i.e. how to increase the performance by symmetry, let us define matrices $\mathcal{S} \subset \mathbb{R}^{3 \times 3}$ describing the symmetry operations of the crystal in a Cartesian coordinate system. Furthermore, $\mathcal{K}_s \subseteq \mathcal{K}$ denotes the symmetrized k -mesh, i.e. the reduced mesh when the symmetry operations of \mathcal{S} are exploited, with the corresponding mapping $m_s : n \mapsto n_s$ such that $n \in \mathcal{K}$ and $n_s \in \mathcal{K}_s$. If one replaces each vertex v of each element of \mathcal{T} by its reduced vertex $m_s(v)$, one formally obtains a new tetrahedral mesh \mathcal{T}_s . Note that \mathcal{T}_s might include elements that do not correspond to real tetrahedra but have e.g. equal nodes when multiple vertices of an element of \mathcal{T} have been mapped onto the same k -point in the reduced set \mathcal{K}_s . After the mapping $\mathcal{T} \rightarrow \mathcal{T}_s$ there are in general multiple occurrences of an element T_s . For simplicity, \mathcal{T}_s in the following denotes the reduced symmetrized mesh, i.e. all elements $T_s \in \mathcal{T}_s$ are only considered once and carry a weight w_{T_s} , which accounts for the volume and multiplicity of T_s .

The numerical quadrature to yield the optical conductivity according to Eq. (11) is given by

$$\sigma = \sum_{T \in \mathcal{T}} g_T. \quad (20)$$

It is important to stress here that one cannot simply replace $n \in \mathcal{K}$ within the rule g_T by $m_s(n) \in \mathcal{K}_s$, since σ and g_T are

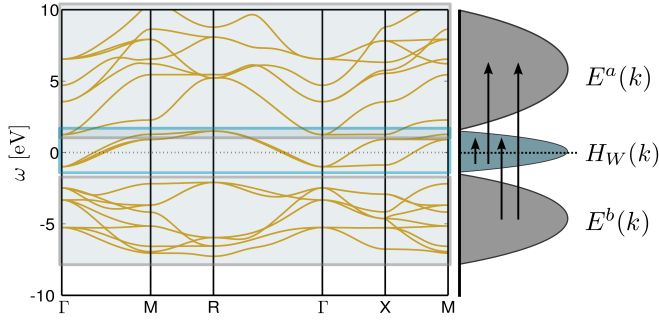


Figure 4: Possible optical transitions and corresponding Hamiltonians according to Eq. (26) for various manifolds in a low energy model for SrVO₃. In the schematic visualization of the spectrum, the t_{2g} manifold where the Wannier projection is performed is shown in blue and all other parts of the spectrum in gray.

tensors. Hence, rotated quantities have to be used:

$$\sigma = \frac{1}{|S|} \sum_{W_s \in S} \sum_{T_s \in \mathcal{T}_s} w_{T_s} W_s^+ g_{T_s} W_s. \quad (21)$$

In this approach it is sufficient to compute $g(n_s)$ for $n_s \in \mathcal{K}_s$ and this, depending on the symmetry of the problem, may yield a considerable speed-up.

4. Practical usage

After the general description of the algorithm in the previous section, let us now turn to the connections of woptic to the program packages WIEN2k and Wannier90, the available modes of operation and a more detailed work flow. As a prerequisite to start a woptic calculation, three other programs are needed: WIEN2k [21], WIEN2WANNIER [11] and Wannier90 [12]. This set of programs allows constructing maximally localized WFs from WIEN2k (see Refs. [11, 32] for a detailed description).

To employ the adaptive integration described in the previous section, we have to be able to generate the dipole matrix $v^w(\mathbf{k})$ and the Hamiltonian $H(\mathbf{k})$ at arbitrary, *a priori* unknown, \mathbf{k} -points. Two approaches are implemented in woptic: (1) matrix elements between WFs can be obtained by Fourier transformation from direct space — this is called `interp` mode in the program; or (2) these matrix elements can be recomputed by WIEN2k every iteration — `optic` mode.

Two issues are central in the following:

Gauge invariance of the optical conductivity (4) and other observables, i.e. the independence of the random gauge of the Bloch states. While the trace in Eq. (4) is gauge invariant, its building blocks $v^w(\mathbf{k})$ and $A(\mathbf{k}, \omega)$ are not. It is therefore essential that they be expressed in the same gauge.

Mixed transitions, dipole transitions between Wannier states on the one hand, and Bloch states that are *not* included in the initial Wannier projection on the other.

Gauge invariance is easily ensured if approach 1 (`interp` mode) is available. The Wannier construction consists in finding a \mathbf{k} -smooth gauge on the initial \mathbf{k} -mesh \mathcal{K}_w . This amounts to finding a set of unitary matrices $U(\mathbf{k})$ which represent the transformation from the initial, “random” gauge³ to the new gauge [19]. One then expresses the Kohn-Sham Hamiltonian and the dipole matrix elements in the new gauge using Eqs. (3) and (5), to repeat:

$$H(\mathbf{k}) = U^+(\mathbf{k}) E(\mathbf{k}) U(\mathbf{k}) \quad \text{with } E_{nm}(\mathbf{k}) = \delta_{nm} \varepsilon_{nk}, \\ v^w(\mathbf{k}) = U^+(\mathbf{k}) v(\mathbf{k}) U(\mathbf{k}).$$

The smoothness of the the Wannier gauge guarantees that the corresponding basis functions (i.e. the WFs) are exponentially localized, and hence that the Fourier transforms of the Hamiltonian

$$H_{rs}(\mathbf{R}) = \frac{1}{N_k} \sum_{\mathbf{k} \in \mathcal{K}_w} H(\mathbf{k}) e^{-i\mathbf{k} \cdot \mathbf{R}} = \langle w_{r0} | \hat{H} | w_{sR} \rangle \quad (22)$$

and dipole matrix elements

$$v_{rs}^w(\mathbf{R}) = \frac{1}{N_k} \sum_{\mathbf{k} \in \mathcal{K}_w} v^w(\mathbf{k}) e^{-i\mathbf{k} \cdot \mathbf{R}} = -\frac{i}{m_e} \langle w_{r0} | \partial_\alpha | w_{sR} \rangle \quad (23)$$

converge rapidly with the mesh spacing of \mathcal{K}_w . (Here and below, $w_{rR}(\mathbf{r})$ is a direct-space WF.)

Thus we obtain direct space hopping and dipole parameters for all the significant neighbor shells (exponentially small contributions of the tails of the WFs are neglected). Having the direct space representation allows us to compute the matrix elements at an arbitrary \mathbf{k} -point \mathbf{q} outside \mathcal{K}_w via

$$H(\mathbf{q}) = \frac{1}{N_R} \sum_{\mathbf{R} \in \mathcal{R}_w} H(\mathbf{R}) e^{i\mathbf{q} \cdot \mathbf{R}}, \quad (24)$$

$$v^w(\mathbf{q}) = \frac{1}{N_R} \sum_{\mathbf{R} \in \mathcal{R}_w} v^w(\mathbf{R}) e^{i\mathbf{q} \cdot \mathbf{R}}. \quad (25)$$

To emphasize, the \mathbf{R} -sums run over \mathcal{R}_w , the set of lattice vectors dual to \mathcal{K}_w , but the localization of the WFs allows us to apply the reverse Fourier transform for $\mathbf{q} \notin \mathcal{K}_w$ with excellent accuracy. This procedure is known as *Wannier interpolation* [33, 34].

Mixed transitions arise when we want to extend the optical conductivity, which we have written in Eq. (4) in terms of a trace over the WFs (*inner* or *Wannier window*), to include states not covered by the Wannier projection (*outer* or *Bloch window*). The motivation for the outer window is normally to compute the optical conductivity over a larger frequency range (see Fig. 4 for a visualization of the model and the possible transitions).

For a DFT+DMFT calculation, the self energy $\Sigma(\omega)$, describing correlation effects beyond GGA, has to be provided on the real axis. In the following, this situation is referred to as *interacting*. Woptic also provides the option to set the self energy to

³More precisely, the gauge determined by diagonalization of $H(\mathbf{k})$ in the electronic structure code.

a small imaginary constant $\Sigma(\omega) \equiv -i\delta$ to mimic broadening, e.g. from impurity scattering.⁴ We will refer to bands treated in this way as *non-interacting*. By supposition, the Bloch states in the outer window are adequately described in DFT and thus non-interacting in this sense.

When an outer window is included, we split the Hamiltonian, Wannier transformation, and dipole matrices into Wannier, Bloch, and mixed parts. Likewise, the trace in the optical conductivity (4) splits into Wannier–Wannier, Wannier–Bloch, and Bloch–Bloch terms. Denoting the diagonal energy matrix connected to the states above (below) the WFs in energy by $E^{a(b)}(\mathbf{k})$, we can write the “large” Hamiltonian, which is block-diagonal,

$$\mathcal{H}(\mathbf{k}) = \begin{pmatrix} E^b(\mathbf{k}) & & \\ & H(\mathbf{k}) & \\ & & E^a(\mathbf{k}) \end{pmatrix}. \quad (26)$$

Analogously, the large Wannier transformation matrix is

$$\mathcal{U}(\mathbf{k}) = \begin{pmatrix} \mathbb{1} & & \\ & U(\mathbf{k}) & \\ & & \mathbb{1} \end{pmatrix}. \quad (27)$$

It affects only the inner window and leaves the outer window unchanged. Additionally, we have the large dipole matrix $\mathcal{V}_{mn}^\alpha(\mathbf{k}) = -\frac{i}{m_e} \langle \psi_{mk} | \partial_\alpha | \psi_{nk} \rangle$ with the indices n, m running now over all bands in the outer window instead of only the inner window. Inserting $\mathcal{H}(\mathbf{k})$ into Eqs. (7) and (6) yields the block-diagonal matrix spectral function $\mathcal{A}(\mathbf{k}, \omega)$ of the large system. Together with the large dipole matrix in the Wannier basis

$$\begin{aligned} \mathcal{V}^w(\mathbf{k}) &= \mathcal{U}^\dagger(\mathbf{k}) \mathcal{V}(\mathbf{k}) \mathcal{U}(\mathbf{k}) \\ &= \begin{pmatrix} (v_{ij}^\alpha) & (v_{rj}^u) & (v_{kj}^\alpha) \\ (v_{is}^u) & (v_{rs}^w) & (v_{ks}^u) \\ (v_{il}^\alpha) & (v_{rl}^u) & (v_{kl}^\alpha) \end{pmatrix}, \end{aligned} \quad (28)$$

this spectral function can be used in Eq. (4) to give a more complete description of optical transitions in the system.

Approach 1 (*interp*) is straightforward for the Wannier–Wannier transitions, but not directly applicable to the mixed dipole matrix elements

$$v_{ri}^u(\mathbf{k}) = \sum_n U_{rn}^\dagger(\mathbf{k}) v_{ni}^\alpha(\mathbf{k}) = -\frac{i}{m_e} \langle w_{rk} | \partial_\alpha | \psi_{ik} \rangle \quad (29)$$

because their Fourier transform $v_{ri}^u(\mathbf{R})$ does not decay with $|\mathbf{R}|$. To salvage Wannier interpolation in the presence of an outer window, we define the quantity

$$w_{rs}^{\alpha\beta}(\mathbf{k}, \omega) = \sum_i v_{ri}^{\alpha} A_{ii}^{a,b}(\mathbf{k}, \omega) v_{is}^{\beta} \quad (30)$$

where the index i runs over all non-Wannier states (which are non-interacting, hence their matrix spectral function $A^{a,b}$ is diagonal). Its Fourier transform $w^{\alpha\beta}(\mathbf{R}, \omega)$ decays with $|\mathbf{R}|$, albeit more slowly than $v^w(\mathbf{R})$ [35].

With these two interpolated quantities, and using the WIEN2k programs *lapw1* and *optic* [20] to compute the Bloch energies $E^{a,b}(\mathbf{q})$ and Bloch–Bloch dipole matrix elements $v_{ij}^\alpha(\mathbf{q})$, we can evaluate the trace (8) at any new k-point. On the other hand, the interpolation errors from $w^{\alpha\beta}(\mathbf{q}, \omega)$ may get large, see next section and Ref. [35] for tests. (Interpolation errors from $v^w(\mathbf{q})$ are insignificant so long as properly localized WFs are found.)

As an alternative in the mixed case, we turn to approach 2 (*optic* mode): computing $\mathcal{V}(\mathbf{q})$ and $E^{a,b}(\mathbf{q})$ at new k-points using *lapw1* and *optic*. (The Hamiltonian $H(\mathbf{q})$ is still computed using Eq. (24).) Because the (inner-window) spectral function $A(\mathbf{q}, \omega)$ is computed in the Wannier basis, but *optic* yields the dipole matrix elements in the Bloch basis, we need the Wannier transformation $U(\mathbf{q})$ on the new k-points to mediate between them. Since the Bloch basis is the one in which the Hamiltonian is diagonal, we can obtain $U(\mathbf{q})$ by diagonalizing $H(\mathbf{k})$ (inverting Eq. (3)).

The problem with approach 2 (*optic*) lies in the arbitrariness of the Bloch gauge. Since the $U(\mathbf{q})$ obtained via Wannier interpolation are computed by diagonalization, they are determined only up to the phases of the respective eigenvectors. In the non-interacting case, where the matrix spectral functions are diagonal, these phases evidently cancel in the trace (8); in fact, this reasoning can be extended to the interacting case as long as the Wannier self energy is a scalar (diagonal in and independent of the orbital index), e.g., because of crystal symmetry.

From a different point of view, the Bloch states ψ_{nk} , obtained as solutions of independent eigenproblems at each k-point, carry “random” phases. The original $U(\mathbf{k})$ from Wannier90 take these phases into account in constructing smooth functions $w_{rk}(\mathbf{r}) = \sum_n U_{nr}(\mathbf{k}) \psi_{nk}(\mathbf{r})$ of \mathbf{k} . These phases are included both in $U(\mathbf{k})$ and $v^\alpha(\mathbf{k})$ and hence cancel when calculating the dipole matrix elements in Wannier space using Eq. (28).

However, if the adaptive k-mesh algorithm now selects a new point \mathbf{q} , the phase of ψ_{nq} is included in the recalculated $v^\alpha(\mathbf{q})$ but not in $U(\mathbf{q})$ obtained as explained above. Hence, the “random” phase may enter into the trace (8) both through the Wannier–Wannier and the mixed transitions (for the Bloch–Bloch transitions it cancels). The resulting *random-gauge problem* leads to errors in the results whose magnitude is *a priori* unknown.

So far we have assumed that the transformation between the Bloch and Wannier states at each k-point is accomplished by a unitary matrix $U(\mathbf{k})$. This excludes the *disentanglement* procedure [36] implemented in Wannier90, where additionally a rectangular matrix $V(\mathbf{k})$ intervenes. In fact, woptic supports disentanglement only in *interp* mode without an outer window (Wannier–Wannier transitions only). It is not clear how the method may be extended to the general disentangled case [35].

4.1. Benchmarks of interpolation and random-gauge errors

In Fig. 5, we compare the optical conductivity of SrVO₃ from the *optic* and *interp* modes, including a self energy from DMFT on the V-t_{2g} states (see Sec. 5.2 for details on the DMFT calculation). Since in this material the self energy is orbital independent by symmetry, there is no random-gauge problem, and this case can be regarded as a test for the Wannier interpolation of v^w and $w^{\alpha\beta}$.

⁴This means that in the non-interacting case, the lifetime broadening (resulting also in a finite width of the Drude peak) is added “by hand”, while in the interacting case, it arises naturally from DMFT.

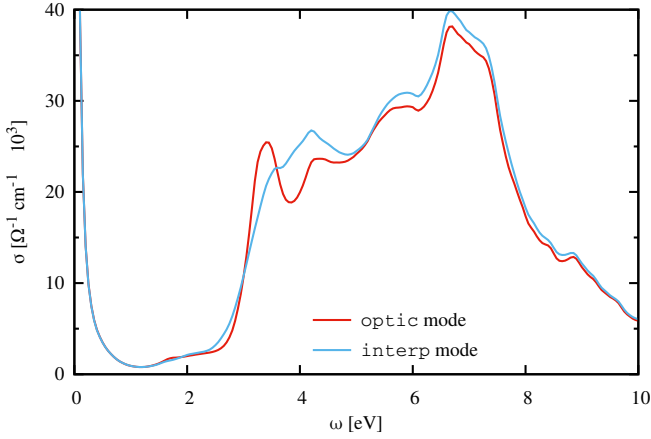


Figure 5: Optical conductivity of SrVO₃ computed in the `optic` (red curve) and `interp` (blue curve) modes. For this model, whose self energy is orbital-independent due to the cubic symmetry, `optic` mode can be considered exact. Thus the difference between the curves reflects the interpolation errors afflicting the Wannier–non-Wannier transitions in `interp` mode. Note that the outer window of included bands is smaller here than in Fig. 9, which is why the optical conductivity starts to drop off above $\omega \approx 7$ eV. Here, 14 bands are included, corresponding to O-p and V-d states.

In order to quantify the random-gauge errors, we require a test case which is complementary to the one of Fig. 5, i.e., where interpolation is reliable, but the gauge problem is in effect. To this end, we construct a Wannier projection covering all the bands of SrVO₃ included in Fig. 5, and apply the V- t_{2g} self-energy from Fig. 5 to the t_{2g} -derived orbitals of this larger projection.⁵ Since all included transitions are now between WFs, we need to interpolate only v^w , and can rely on `interp` mode as a reference; but since we apply a non-trivial self energy only to the t_{2g} orbitals, $\Sigma_i(\omega)$ is now strongly orbital-dependent and `optic` mode suffers from the gauge problem. The results are shown in Fig. 6.

Comparing Figs. 5 and 6, we find that the errors from $w^{\alpha\beta}$ interpolation and from the random-gauge problem are similar in magnitude. In both cases, the qualitative features are preserved. The quantitative differences must be viewed in relation to other sources of uncertainty in these calculations. Most importantly, in DMFT the self energy on the real- ω axis is typically obtained through analytic continuation from the imaginary- ω axis. This leads to uncertainties which can easily be comparable to the errors observed in Figs. 5 and 6. It also bears mentioning that the orbital symmetry which protects `optic` mode from the random-gauge problem is broken especially sharply in the 14-band model used above (nontrivial $\Sigma(\omega)$ on the t_{2g} orbitals, $\Sigma_i = -i\delta$ on the others).

Fig. 6 contains a third curve, which corresponds to `interp` mode on a model constructed with disentanglement. At the R point near the top of the V- e_g bands, they are entangled with Sr-s bands, as seen in the band structure of Fig. 4. These unwanted bands can be removed using disentanglement [36]. The corresponding curve in Fig. 6 is practically identical to the one with-

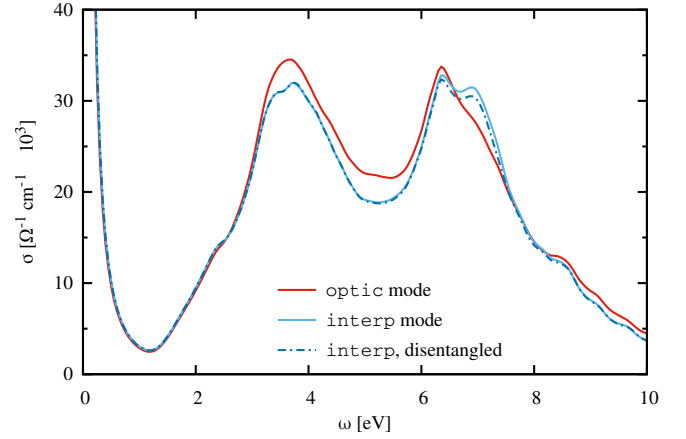


Figure 6: Optical conductivity of a model derived from SrVO₃ by imposing the self energy from the 3-band model on the t_{2g} -like orbitals in a 14-band Wannier projection, which includes the same bands as in Fig. 5: O-p, V- t_{2g} , and V- e_g . The red curve corresponds to `optic` mode, the light blue to `interp` mode. For this model without mixed transitions, `interp` mode can be considered exact, thus the difference reflects the random-gauge errors in `optic` mode. The dark blue curve is from `interp` mode using a Wannier projection with disentanglement of the Sr-s bands crossing the V- e_g bands at the R point [35]. Since this corresponds to a somewhat different model, complete agreement with the light blue curve cannot be expected.

out disentanglement, except for the region around 7 eV, where transitions involving the entangled states are relevant.

For details on the issues discussed in the preceding paragraphs (to wit: the random-gauge problem in `optic` mode, interpolation of v^w and $w^{\alpha\beta}$, and disentanglement in relation to `woptic`), we refer to Ref. [35].

4.2. Program details

To summarize, `woptic` offers two main choices for the *matrix element mode* (corresponding to the program parameter `matelmode`). This choice determines the method to compute the dipole matrix elements $v(\mathbf{k})$. The modes and corresponding keywords in the `woptic` input file are:

Wannier interpolated dipole matrix elements (`interp`):

Apply Wannier interpolation (25) to the dipole matrix elements $v_{rs}^{w\alpha}(\mathbf{k})$ in the Wannier gauge (5), as well as to the Hamiltonian (3). In the presence of an outer window, the mixed transitions are calculated from the quantity $w_{rs}(\mathbf{k}, \omega)$ (30), which is likewise interpolated [35].

Ab initio dipole matrix elements (`optic`):

Obtain the dipole matrix elements $v_{ij}^\alpha(\mathbf{q})$ in the Bloch gauge (2) from the WIEN2k programs `lapw1` and `optic`; the Hamiltonian $H(\mathbf{q})$ from Wannier interpolation; and the transformation $U(\mathbf{q})$ to the Wannier gauge by diagonalization of $H(\mathbf{q})$.

`interp` mode is reliable for the Wannier–Wannier and Bloch–Bloch transitions, but the Wannier–Bloch terms acquire interpolation errors. `optic` mode is reliable whenever the self-energy in the Wannier gauge is diagonal and orbital independent (by symmetry, or in the non-interacting case), but the Wannier–Wannier

⁵This is unphysical but yields a convenient test case.

and Wannier–Bloch terms acquire errors due to the random-gauge problem when it is not. In our tests, the errors from these two issues are comparable.

We conclude this section with a summary of the detailed work flow of *woptic*.

0. A preliminary run of `refine_tetra` prepares the initial k-mesh $\mathcal{K}^{(0)}$ and the initial set of tetrahedra $\mathcal{T}^{(0)}$. In `interp` mode, run `compute_vr` to obtain $v^w(\mathbf{R})$ and $w^{\alpha\beta}(\mathbf{R}, \omega)$ (if mixed transitions are requested). Set $\ell = 0$.
1. Determine which k-points of $\mathcal{K}^{(\ell)}$ were not in $\mathcal{K}^{(\ell-1)}$, i.e., find $\mathcal{K}^{(\ell)} \setminus \mathcal{K}^{(\ell-1)}$.
2. Obtain the Hamiltonian $H(\mathbf{k})$ for all k-points in $\mathcal{K}^{(\ell)} \setminus \mathcal{K}^{(\ell-1)}$ via Eq. (24).
3. Obtain the dipole matrix $v_{mn}(\mathbf{k})$ for all k-points in $\mathcal{K}^{(\ell)} \setminus \mathcal{K}^{(\ell-1)}$, from the WIEN2k programs `lapw1` and `optic` or from Eq. (25).
4. Call `woptic_main`
 - (a) Rotate $v(\mathbf{k})$ to the Wannier basis.
 - (b) Load the self energy $\Sigma(\omega)$ and determine the Green's function $G(\mathbf{k}, \omega)$ according to Eq. (7) for all k-points in $\mathcal{K}^{(\ell)} \setminus \mathcal{K}^{(\ell-1)}$.
 - (c) Evaluate the contributions to the optical conductivity $g(\mathbf{k})$ from Eq. (12) for all k-points in $\mathcal{K}^{(\ell)} \setminus \mathcal{K}^{(\ell-1)}$ and load the old data $g(\mathbf{k})$ for $\mathcal{K}^{(\ell-1)}$.
 - (d) Perform tetrahedral integration for $\mathcal{T}^{(\ell)}$ using Eq. (21) and obtain the optical conductivity $\sigma^{(\ell)}(\omega)$.
5. Call `refine_tetra`
 - (a) Determine the error estimators $\bar{\epsilon}_T$ for $T \in \mathcal{T}^{(\ell)}$ via Eqs. (13 & 14) and (16 & 17), respectively.
 - (b) Mark the elements of $\mathcal{T}^{(\ell)}$ for refinement if they satisfy the criterion (18), obtaining $\mathcal{T}_m^{(\ell)} \subseteq \mathcal{T}^{(\ell)}$.
 - (c) If $\mathcal{T}_m^{(\ell)}$ is empty, i.e. no elements have been marked, set $\mathcal{T}^{(\ell+1)} = \mathcal{T}^{(\ell)}$ (and $\mathcal{K}^{(\ell+1)} = \mathcal{K}^{(\ell)}$) and exit from `refine_tetra`.
 - (d) Refine the marked tetrahedra $\mathcal{T}_m^{(\ell)}$ according to their class and the rules shown in Fig. 3, leading to the refined mesh $\mathcal{T}_{\text{ref}}^{(\ell)}$ of $\mathcal{T}^{(\ell)}$ and a new set of k-points $\mathcal{K}_{\text{ref}}^{(\ell)}$.
 - (e) Perform mesh closure: Mark the non-refined tetrahedra of $\mathcal{T}_{\text{ref}}^{(\ell)}$ for refinement if they violate the regularity condition, i.e. if they have more than one hanging node on an edge, and obtain $\tilde{\mathcal{T}}_m^{(\ell)}$. If $\tilde{\mathcal{T}}_m^{(\ell)}$ is empty, the mesh is regular: set $\mathcal{T}^{(\ell+1)} = \mathcal{T}_{\text{ref}}^{(\ell)}$, $\mathcal{K}^{(\ell+1)} = \mathcal{K}_{\text{ref}}^{(\ell)}$ and exit. Otherwise set $\mathcal{T}_m^{(\ell)} = \tilde{\mathcal{T}}_m^{(\ell)}$, $\mathcal{T}^{(\ell)} = \mathcal{T}_{\text{ref}}^{(\ell)}$, $\mathcal{K}^{(\ell)} = \mathcal{K}_{\text{ref}}^{(\ell)}$ and return to step 5d.
6. If $\ell < \ell_{\text{max}}$ return to step 1; otherwise, exit.

The key difference between the modes is in step 3, where the matrix elements for the new k-points are computed.

5. Applications

5.1. Aluminum

As a simple example to show that our adaptive procedure can reproduce standard WIEN2k results at much lower computational

cost we have chosen fcc-Al. As shown before [20, 38], there is a strong dependency of the optical properties on the quality of the BZ integration. Using a regular grid and the tetrahedron method as implemented in WIEN2k's `optic` module, up to 20 000 k-points in the irreducible wedge of the BZ are necessary to obtain converged results for the optical conductivity. With our adaptive mesh the number of k-points can be greatly reduced. Note that $\sigma(\omega)$ also depends crucially on the applied broadening scheme, and small differences may appear between the two methods, because they are somewhat different in the way the broadening is introduced. The `optic` module in WIEN2k first calculates the imaginary part of the unbroadened dielectric function $\epsilon_2(\omega)$ due to interband transitions and the plasma frequency due to intraband transitions, and adds smearing later (using Lorentzian broadening). On the other hand, the Green's function method uses a related broadening constant δ for the self energy $\Sigma(\omega) \equiv -i\delta$ which enters into the Green's function (7).

The reason for the slow convergence of σ with the number of k-points is quite obvious when one inspects the band structure. Consider the first interband peak at $\omega \approx 1.5$ eV. In the relevant energy range, only a narrow region of the BZ around W contributes, as seen in the k-resolved contributions to $\sigma(\omega)$ (Fig. 7(b)). Comparison with the bandstructure (Fig. 7(c)) shows that these contributions stem from four bands near the Fermi level at W (two particle and two hole bands). A regular mesh must be quite dense to properly sample these small portions of the BZ, while our adaptive scheme is much more efficient. This is illustrated in Fig. 8, where one can see that the regions around the W -point are refined most and have the smallest tetrahedra.

5.2. Strontium vanadate

As a second application of the method, we present in this section calculations for SrVO₃. Its low-energy electronic structure is dominated by the degenerate 3d-t_{2g} orbitals of vanadium and it constitutes a textbook example of a strongly correlated metal, perfectly suited for illustrating the intermediate steps and the final results of the *woptic* package. Specific details about the crystal and electronic structures of SrVO₃ can be found, e.g., in Refs. [26, 32]. In fact, SrVO₃ is a good example of a situation where DFT cannot accurately describe the low-energy optical response of the system,⁶ necessitating the inclusion of local correlation effects, e.g. by means of DMFT. In this work, we focus on the workings of the adaptive algorithm rather than physical implications of our results; see Ref. [26] for a discussion about the latter.

In Fig. 9, the intermediate ($\ell = 1$) and final ($\ell = 5$) results for the optical conductivity of SrVO₃ are reported, in each case for an interacting and a non-interacting calculation. Experimental results from Ref. [39] are reproduced for comparison. Here, the DMFT calculations have been performed using a Kanamori interaction [42] with parameters $U = 5.05$ eV, $U' = 3.55$ eV and $J = 0.75$ eV, consistent with the setup used in Ref. [26].

⁶Another prototypical situation is the analysis of the optical spectroscopy experiments in V₂O₃ [26, 32, 40, 41], where the corrections generated by the inclusion of electronic correlation in DFT+DMFT are even larger than for the SrVO₃ case.

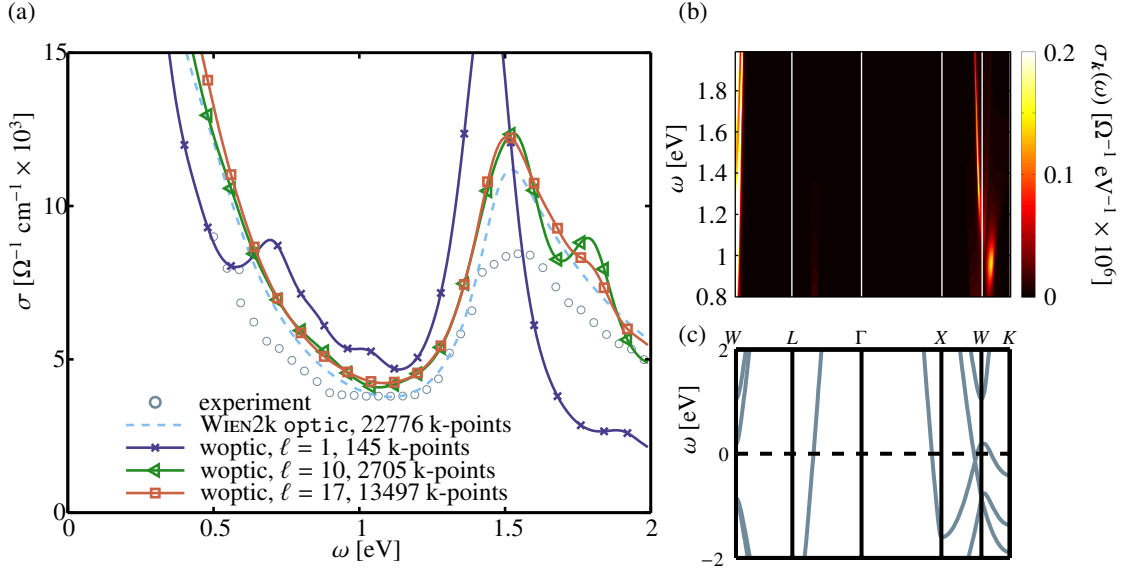


Figure 7: The non-interacting optical conductivity of Al computed by woptic compared to corresponding results from the WIEN2k optic package and experimental data [37] in panel (a). For convergence of the uniform WIEN2k calculation a large number of (symmetrized) k-points is required, while due to the adaptivity, woptic converges for a much smaller number of k-points. After convergence both programs yield similar results, in particular the experimental peak position is reproduced. (An arbitrary scaling has been applied to the experimental results.) The contributions to the optical conductivity σ resolved in (\mathbf{k}, ω) -space (b). Only a small part of k-space around W contributes to σ and the contributions can be understood by identifying possible transitions in the band structure (c).

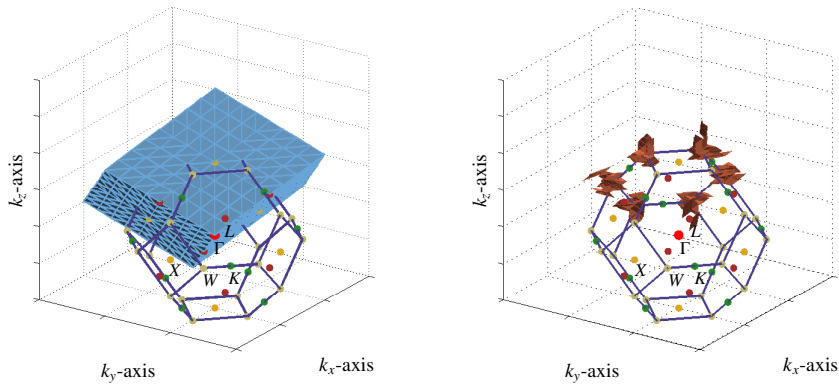


Figure 8: The unsymmetrized initial tetrahedral mesh $\mathcal{T}^{(0)}$ used in the calculations for elementary Al with 3072 tetrahedra and 4913 k-points (left). The highly adaptive mesh after 6 iterations $\mathcal{T}^{(6)}$ with 13152 tetrahedra and 24667 k-points (right). For the sake of visualization only the smallest tetrahedra are shown. The region yielding the largest contribution to the estimator (17) is located close to the W -point around $[0.7500 \ 0.5000 \ 0.2812]$ in terms of the primitive vectors of the reciprocal unit cell.

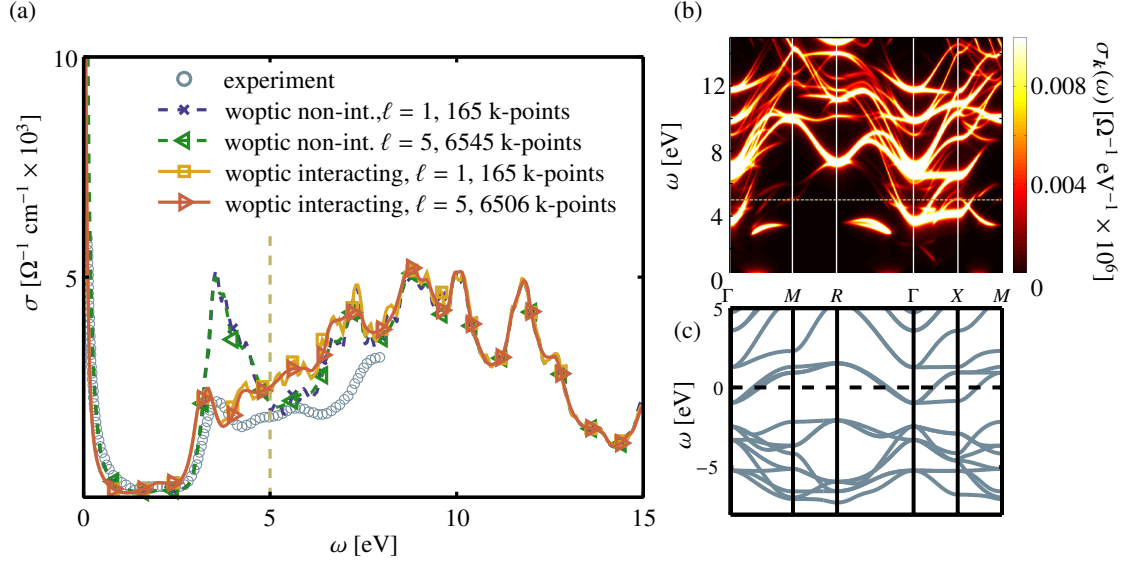


Figure 9: The interacting and non-interacting optical conductivity of SrVO_3 computed by the adaptive algorithm woptic compared to experiment [39] in panel (a). While the interacting result is much closer to experiment, the convergence of the algorithm requires far fewer iterations than for AI both in the interacting and in the non-interacting case. This indicates that larger regions of k -space contribute to the optical conductivity, as also suggested by the contributions to σ resolved in (k, ω) -space (b). (Note also the different scales of the contributions here and in Fig. 10.) A significant part of the optical conductivity in the energy window under investigation stems from $O-p \rightarrow V-d$ transitions, which can be understood by inspection of the band structure (c). In panels (a) and (b), the dashed line indicates the restricted frequency window (0 to 5 eV), which has been considered for the illustration of the evolution of the tetrahedral mesh in Fig. 10. In the non-interacting case, the broadening, in particular the finite width of the Drude peak, arises solely from the small imaginary self energy $\Sigma = -i\delta$ which is added for this purpose. By contrast, in the interacting case, it is a direct result of DMFT.

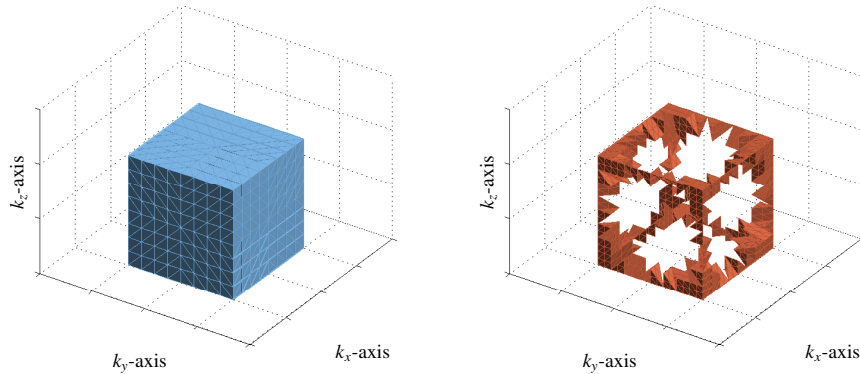


Figure 10: The unsymmetrized initial tetrahedral mesh $\mathcal{T}^{(0)}$ used in the non-interacting calculations for SrVO_3 with 3072 tetrahedra and 4913 k -points (left). After 5 iterations, in the highly adaptive mesh regime ($\theta = 0.9$), the mesh $\mathcal{T}^{(5)}$ has 4920 elements and 9533 k -points (right); for the sake of visualization only the smallest tetrahedra are shown)

Since the random-gauge problem is absent in this case due to the cubic symmetry (see Sec. 4), we use `woptic` mode for the interacting optical conductivity. One immediately notes the role of the electronic correlations, as evidenced by a significant shift of optical spectral weight from the Drude peak and the frequency window between 3 and 5 eV to higher energies as compared to the non-interacting calculations. Such many-body effects are expected due to the correlated nature of the 3d- t_{2g} orbitals of SrVO_3 , and they significantly improve the match between theory and experiment.

A more detailed analysis of the `woptic` results in Fig. 9 shows that the convergence of the adaptive algorithm is much faster than for the AI case of the previous section. This can be understood by plotting the k-resolved contributions to $\sigma(\omega)$ (i.e., the integrand of the k-summation of Eq. 4), as shown in Fig. 9(b): In the wide energy range considered (i.e., up to 5 eV), the contributions to the optical conductivity are spread over all of k-space. As a consequence, the adaptivity of the `woptic` algorithm becomes less important and the final adaptive mesh (not shown) essentially coincides with one obtained in a uniform calculation. This would be different when focusing on the low-energy region (e.g., up to 5 eV as marked by the dashed lines in Fig. 9) – as is usual when comparing with optical spectroscopic experiments. In that case, the predominant contribution to $\sigma(\omega)$ below 5 eV (apart from the Drude peak) is from around the Γ point, and between Γ and X. This corresponds to the peak in $\sigma(\omega)$ located at about 4 eV in the non-interacting spectrum, which originates not from optical transitions between the V- t_{2g} orbitals, but rather from transitions between the O- $2p$ and the V- e_g bands.

This situation is well reflected in the evolution of the tetrahedral mesh, reported in Fig. 10 for a calculation in the window up to 5 eV, and performed with a highly adaptive mesh ($\theta = 0.9$) for the sake of illustration. In the right panel of Fig. 10 the resulting tetrahedral mesh after 5 iterations is visualized, showing refinements essentially from $\Gamma \rightarrow X$, which is exactly the region we identified in Fig. 9(b) and (c). Moreover, especially along this k-path, the p and the e_g orbitals mainly responsible for the optical transitions are relatively flat and hence difficult to resolve in (\mathbf{k}, ω) -space, which explains `woptic`'s behavior in this case.

6. Summary

We have developed a flexible and efficient adaptive BZ integration algorithm based on a recursively generated tetrahedral k-mesh. In regions where the numerical error would otherwise be large, the k-mesh becomes fine, whereas it remains coarser elsewhere. We apply this approach to the optical conductivity in a Wannier basis, with the possibility to include a many-body self energy $\Sigma(\omega)$ on top of the DFT band structure. The peakedness of the contributions in k-space is determined mainly by the band structure and by the imaginary part of the self energy, which broadens the peaks. Thus, weakly interacting materials, where $\Im\Sigma$ is small, tend to have more sharply peaked contributions.

Results for AI and SrVO_3 illustrate the algorithm and its performance. These calculations would require much more computational effort using uniform k-grids.

The `woptic` package, our implementation of the adaptive k-mesh algorithm in the framework of WIEN2k, Wannier90, and DMFT, is available at <http://www.ifp.tuwien.ac.at/forschung/arbeitsgruppen/cms/software-download/woptic>. In addition to the ready-made computation of the optical conductivity, dc conductivity, and thermopower, the k-mesh management code may easily be adapted to other quantities, in particular where a conventional tetrahedron integration is impossible or impractical.

In the optical conductivity, in order to include transitions involving bands beyond the Wannier projection, an *outer band window* may be defined, although this leads to certain numerical problems in some cases (see Sec. 4). The outer bands will be described at the DFT level, i.e. without a self energy. Apart from the physical, k-integrated quantities, `woptic` also provides tools to examine the k-dependent contributions (as in Figs. 7 and 9 (b)), which often provide valuable physical insight.

Acknowledgments

We acknowledge financial support from the Austrian science fund FWF through SFB ViCoM F41 (P.W., P.B., K.H.) and START project Y746 (E.A.); Vienna University of Technology through an *innovative project* grant (E.A.); research unit FOR 1346 of the German science foundation DFG (J.K.) and its Austrian subproject FWF ID I597-N16 (A.T.); and the European Research Council under the European Union's Seventh Framework Program (FP/2007-2013)/ERC through grant agreement n. 306447 (E.A., K.H.). Calculations have been done on the Vienna Scientific Cluster (VSC).

- [1] H. J. Monkhorst, J. D. Pack, *Special points for Brillouin-zone integrations*, Phys. Rev. B 13 (12) (1976) 5188–5192. doi:10.1103/PhysRevB.13.5188. URL <http://link.aps.org/doi/10.1103/PhysRevB.13.5188>
- [2] D. J. Chadi, M. L. Cohen, *Special Points in the Brillouin Zone*, Phys. Rev. B 8 (12) (1973) 5747–5753. doi:10.1103/PhysRevB.8.5747. URL <http://link.aps.org/doi/10.1103/PhysRevB.8.5747>
- [3] D. J. Chadi, *Special points for Brillouin-zone integrations*, Phys. Rev. B 16 (4) (1977) 1746–1747. doi:10.1103/PhysRevB.16.1746. URL <http://link.aps.org/doi/10.1103/PhysRevB.16.1746>
- [4] P. E. Blöchl, O. Jepsen, O. K. Andersen, *Improved tetrahedron method for Brillouin-zone integrations*, Phys. Rev. B 49 (23) (1994) 16223–16233. doi:10.1103/PhysRevB.49.16223. URL <http://link.aps.org/doi/10.1103/PhysRevB.49.16223>
- [5] W. Metzner, D. Vollhardt, *Correlated Lattice Fermions in $d = \infty$ Dimensions*, Phys. Rev. Lett. 62 (3) (1989) 324–327. doi:10.1103/PhysRevLett.62.324. URL <http://link.aps.org/doi/10.1103/PhysRevLett.62.324>
- [6] A. Georges, G. Kotliar, *Hubbard model in infinite dimensions*, Phys. Rev. B 45 (12) (1992) 6479–6483. doi:10.1103/PhysRevB.45.6479. URL <http://link.aps.org/doi/10.1103/PhysRevB.45.6479>
- [7] G. Kotliar, S. Y. Savrasov, K. Haule, V. S. Oudovenko, O. Parcollet, C. A. Marianetti, *Electronic structure calculations with dynamical mean-field theory*, Rev. Mod. Phys. 78 (3) (2006) 865–951. doi:10.1103/RevModPhys.78.865. URL <http://link.aps.org/doi/10.1103/RevModPhys.78.865>
- [8] K. Held, *Electronic structure calculations using dynamical mean field theory*, Adv. Phys. 56 (6) (2007) 829–926. URL <http://arxiv.org/abs/cond-mat/0511293>
- [9] J. P. Perdew, K. Burke, M. Ernzerhof, *Generalized Gradient Approximation Made Simple*, Phys. Rev. Lett. 77 (18) (1996) 3865–3868. doi:10.1103/PhysRevLett.77.3865. URL <http://link.aps.org/doi/10.1103/PhysRevLett.77.3865>

- [10] P. Blaha, K. Schwarz, P. Sorantin, S. Trickey, Full-potential, linearized augmented plane wave programs for crystalline systems, *Computer Physics Communications* 59 (2) (1990) 399–415. doi:10.1016/0010-4655(90)90187-6. URL <http://www.sciencedirect.com/science/article/pii/S0010465590901876>
- [11] J. Kuneš, R. Arita, P. Wissgott, A. Toschi, H. Ikeda, K. Held, Wien2wannier: From linearized augmented plane waves to maximally localized Wannier functions, *Computer Physics Communications* 181 (11) (2010) 1888–1895. doi:10.1016/j.cpc.2010.08.005. URL <http://www.sciencedirect.com/science/article/pii/S0010465510002948>
- [12] A. A. Mostofi, J. R. Yates, Y.-S. Lee, I. Souza, D. Vanderbilt, N. Marzari, wannier90: A tool for obtaining maximally-localised Wannier functions, *Computer Physics Communications* 178 (9) (2008) 685–699. doi:10.1016/j.cpc.2007.11.016. URL <http://www.sciencedirect.com/science/article/pii/S0010465507004936>
- [13] L. Hedin, New Method for Calculating the One-Particle Green's Function with Application to the Electron-Gas Problem, *Phys. Rev.* 139 (3A) (1965) A796–A823. doi:10.1103/PhysRev.139.A796. URL <http://link.aps.org/doi/10.1103/PhysRev.139.A796>
- [14] J. M. Tomczak, M. Casula, T. Miyake, F. Aryasetiawan, S. Biermann, Combined GW and dynamical mean-field theory: Dynamical screening effects in transition metal oxides, *EPL (Europhysics Letters)* 100 (6) (2012) 67001. doi:10.1209/0295-5075/100/i=6/a=67001?key=crossref.6924fb4a403bf2fbd800c92cb62524db. URL <http://stacks.iop.org/0295-5075/100/i=6/a=67001?key=crossref.6924fb4a403bf2fbd800c92cb62524db>
- [15] A. Toschi, A. A. Katanin, K. Held, Dynamical vertex approximation: A step beyond dynamical mean-field theory, *Phys. Rev. B* 75 (4) (2007) 045118. doi:10.1103/PhysRevB.75.045118. URL <http://link.aps.org/doi/10.1103/PhysRevB.75.045118>
- [16] A. N. Rubtsov, M. I. Katsnelson, A. I. Lichtenstein, Dual fermion approach to nonlocal correlations in the Hubbard model, *Phys. Rev. B* 77 (3) (2008) 033101. doi:10.1103/PhysRevB.77.033101. URL <http://link.aps.org/doi/10.1103/PhysRevB.77.033101>
- [17] T. Maier, M. Jarrell, T. Pruschke, M. H. Hettler, Quantum cluster theories, *Rev. Mod. Phys.* 77 (3) (2005) 1027–1080. doi:10.1103/RevModPhys.77.1027. URL <http://link.aps.org/doi/10.1103/RevModPhys.77.1027>
- [18] G. H. Wannier, The Structure of Electronic Excitation Levels in Insulating Crystals, *Phys. Rev.* 52 (3) (1937) 191–197. doi:10.1103/PhysRev.52.191. URL <http://link.aps.org/doi/10.1103/PhysRev.52.191>
- [19] N. Marzari, D. Vanderbilt, Maximally localized generalized Wannier functions for composite energy bands, *Phys. Rev. B* 56 (20) (1997) 12847–12865. doi:10.1103/PhysRevB.56.12847. URL <http://link.aps.org/doi/10.1103/PhysRevB.56.12847>
- [20] C. Ambrosch-Draxl, J. O. Sofo, Linear optical properties of solids within the full-potential linearized augmented plane-wave method, *Computer Physics Communications* 175 (1) (2006) 1–14. doi:10.1016/j.cpc.2006.03.005. URL <http://www.sciencedirect.com/science/article/pii/S0010465506001299>
- [21] G. K. H. Madsen, P. Blaha, K. Schwarz, E. Sjöstedt, L. Nordström, Efficient linearization of the augmented plane-wave method, *Phys. Rev. B* 64 (19) (2001) 195134. doi:10.1103/PhysRevB.64.195134. URL <http://link.aps.org/doi/10.1103/PhysRevB.64.195134>
- [22] G. Rohringer, A. Valli, A. Toschi, Local electronic correlation at the two-particle level, *Phys. Rev. B* 86 (12) (2012) 125114. doi:10.1103/PhysRevB.86.125114. URL <http://link.aps.org/doi/10.1103/PhysRevB.86.125114>
- [23] A. Toschi, R. Arita, P. Hansmann, G. Sangiovanni, K. Held, Quantum dynamical screening of the local magnetic moment in Fe-based superconductors, *Phys. Rev. B* 86 (6) (2012) 064411. doi:10.1103/PhysRevB.86.064411. URL <http://link.aps.org/doi/10.1103/PhysRevB.86.064411>
- [24] A. Georges, G. Kotliar, W. Krauth, M. J. Rozenberg, Dynamical mean-field theory of strongly correlated fermion systems and the limit of infinite dimensions, *Rev. Mod. Phys.* 68 (1) (1996) 13. doi:10.1103/RevModPhys.68.13. URL <http://link.aps.org/doi/10.1103/RevModPhys.68.13>
- [25] J. M. Tomczak, S. Biermann, Optical properties of correlated materials: Generalized Peierls approach and its application to VO₂, *Phys. Rev. B* 80 (8) (2009) 085117. doi:10.1103/PhysRevB.80.085117. URL <http://link.aps.org/doi/10.1103/PhysRevB.80.085117>
- [26] P. Wissgott, J. Kuneš, A. Toschi, K. Held, Dipole matrix element approach versus Peierls approximation for optical conductivity, *Phys. Rev. B* 85 (20) (2012) 205133. doi:10.1103/PhysRevB.85.205133. URL <http://link.aps.org/doi/10.1103/PhysRevB.85.205133>
- [27] J. Bey, Tetrahedral grid refinement, *Computing* 55 (4) (1995) 355–378. doi:10.1007/BF02238487. URL <http://link.springer.com/article/10.1007/BF02238487>
- [28] M. Ong, Uniform Refinement of a Tetrahedron, *SIAM J. Sci. Comput.* 15 (5) (1994) 1134–1144. doi:10.1137/0915070. URL <http://epubs.siam.org/doi/abs/10.1137/0915070>
- [29] L. Endres, P. Krysl, Octasection-based refinement of finite element approximations of tetrahedral meshes that guarantees shape quality, *Int. J. Numer. Meth. Engng.* 59 (1) (2004) 69–82. doi:10.1002/nme.863. URL <http://onlinelibrary.wiley.com/doi/10.1002/nme.863/abstract>
- [30] P. Wissgott, A space-time adaptive algorithm for linear parabolic problems, Master's Thesis, Technische Universität Wien, Vienna, Austria (2007).
- [31] P. Deuffhard, A. Hohmann, *Numerical Analysis in Modern Scientific Computing*, Vol. 43 of Texts in Applied Mathematics, Springer New York, New York, NY, 2003. URL <http://link.springer.com/10.1007/978-0-387-21584-6>
- [32] P. Wissgott, Transport Properties of Correlated Materials from First Principles, PhD thesis, Technische Universität Wien, Vienna, Austria (2012).
- [33] J. R. Yates, X. Wang, D. Vanderbilt, I. Souza, Spectral and Fermi surface properties from Wannier interpolation, *Phys. Rev. B* 75 (19) (2007) 195121. doi:10.1103/PhysRevB.75.195121. URL <http://link.aps.org/doi/10.1103/PhysRevB.75.195121>
- [34] X. Wang, J. R. Yates, I. Souza, D. Vanderbilt, Ab initio calculation of the anomalous Hall conductivity by Wannier interpolation, *Phys. Rev. B* 74 (19) (2006) 195118. doi:10.1103/PhysRevB.74.195118. URL <http://link.aps.org/doi/10.1103/PhysRevB.74.195118>
- [35] E. Assmann, Spectral properties of strongly correlated materials, PhD thesis, Technische Universität Wien, Vienna, Austria (2015), the chapter relevant for woptic is available at <http://www.ifp.tuwien.ac.at/forschung/arbeitsgruppen/cms/software-download/woptic>
- [36] I. Souza, N. Marzari, D. Vanderbilt, Maximally localized Wannier functions for entangled energy bands, *Phys. Rev. B* 65 (3) (2001) 035109. doi:10.1103/PhysRevB.65.035109. URL <http://link.aps.org/doi/10.1103/PhysRevB.65.035109>
- [37] H. Ehrenreich, H. R. Philipp, B. Segall, Optical Properties of Aluminum, *Phys. Rev.* 132 (5) (1963) 1918–1928. doi:10.1103/PhysRev.132.1918. URL <http://link.aps.org/doi/10.1103/PhysRev.132.1918>
- [38] K.-H. Lee, K. J. Chang, First-principles study of the optical properties and the dielectric response of Al, *Phys. Rev. B* 49 (4) (1994) 2362–2367. doi:10.1103/PhysRevB.49.2362. URL <http://link.aps.org/doi/10.1103/PhysRevB.49.2362>
- [39] H. Makino, I. H. Inoue, M. J. Rozenberg, I. Hase, Y. Aiura, S. Onari, Bandwidth control in a perovskite-type 3d¹-correlated metal Ca_{1-x}Sr_xVO₃. II. Optical spectroscopy, *Phys. Rev. B* 58 (8) (1998) 4384–4393. doi:10.1103/PhysRevB.58.4384. URL <http://link.aps.org/doi/10.1103/PhysRevB.58.4384>
- [40] S. Lupi, L. Baldassarre, B. Mansart, A. Perucchi, A. Barinov, P. Dudin, E. Papalazarou, F. Rodolakis, J.-P. Rueff, J.-P. Itié, S. Ravy, D. Nicoletti, P. Postorino, P. Hansmann, N. Parragh, A. Toschi, T. Saha-Dasgupta, O. K. Andersen, G. Sangiovanni, K. Held, M. Marsi, A microscopic view on the Mott transition in chromium-doped V₂O₃, *Nat Commun* 1 (2010) 105. doi:10.1038/ncomms1109. URL <http://www.nature.com/ncomms/journal/v1/n8/full/ncomms1109.html>
- [41] L. Baldassarre, A. Perucchi, D. Nicoletti, A. Toschi, G. Sangiovanni, K. Held, M. Capone, M. Ortolani, L. Malavasi, M. Marsi, P. Metcalf, P. Postorino, S. Lupi, Quasiparticle evolution and pseudogap formation in V₂O₃: An infrared spectroscopy study, *Phys. Rev. B* 77 (11) (2008) 113107. doi:10.1103/PhysRevB.77.113107.

URL <http://link.aps.org/doi/10.1103/PhysRevB.77.113107>

- [42] J. Kanamori, *Electron Correlation and Ferromagnetism of Transition Metals*, *Prog. Theor. Phys.* 30 (3) (1963) 275–289. doi:10.1143/PTP.30.275.

URL <http://ptp.oxfordjournals.org/content/30/3/275>

PHYSICAL REVIEW B **90**, 165105 (2014)

Cubic interaction parameters for t_{2g} Wannier orbitals

T. Ribic, E. Assmann, A. Tóth, and K. Held

Institute of Solid State Physics, Vienna University of Technology, A-1040 Vienna, Austria

(Received 28 May 2014; revised manuscript received 10 September 2014; published 7 October 2014)

Many-body calculations for multi-orbital systems at present typically employ Slater or Kanamori interactions which implicitly assume a full rotational invariance of the orbitals, whereas the real crystal has a lower symmetry. In cubic symmetry, the low-energy t_{2g} orbitals have an on-site Kanamori interaction, albeit without the constraint $U = U' + 2J$ implied by spherical symmetry (U is the intra-orbital interaction, U' is the interorbital interaction, J is Hund's exchange). Using maximally localized Wannier functions we show that deviations from the standard, spherically symmetric interactions are indeed significant for $5d$ orbitals ($\sim 25\%$ for BaOsO_3 ; $\sim 12\%$ if screening is included) but are less important for $3d$ orbitals ($\sim 6\%$ for SrVO_3 ; $\sim 1\%$ if screened).

 DOI: [10.1103/PhysRevB.90.165105](https://doi.org/10.1103/PhysRevB.90.165105)

PACS number(s): 71.27.+a, 71.10.Fd

I. INTRODUCTION

Strongly correlated electron systems show a rich variety of unconventional phenomena such as high temperature superconductivity [1] and quantum criticality [2]—and their theoretical description and understanding constitutes a particular challenge. The origin of these correlations is the strong Coulomb interaction, as particularly found in materials with partially filled d or f bands, such as transition metals, their oxides, and rare-earth and lanthanide compounds.

The Coulomb interaction between two electrons, which scatter from orbitals α , β to α' , β' in the course of the interaction, is simply given by

$$U_{\alpha'\beta'\beta\alpha} = \int d^3r d^3r' \psi_{\alpha'}^*(\mathbf{r}) \psi_{\beta'}^*(\mathbf{r}') V(|\mathbf{r}' - \mathbf{r}|) \psi_{\beta}(\mathbf{r}) \psi_{\alpha}(\mathbf{r}). \quad (1)$$

Here, $V(|\mathbf{r}' - \mathbf{r}|) = e^2/(4\pi\epsilon_0|\mathbf{r}' - \mathbf{r}|)$ is the Coulomb interaction with electron charge e and vacuum permittivity ϵ_0 ; $\psi_{\alpha}(\mathbf{r})$ is the electron wave function for orbital α ; no screening by further electrons has been included in this bare interaction $U_{\alpha'\beta'\beta\alpha}$. We do not consider relativistic corrections such as the spin-orbit coupling here so that the one-electron eigenstates simply need to be multiplied with a spinor and the integrals $U_{\alpha'\beta'\beta\alpha}$ are independent of spin; however, the α' and α one-electron eigenstates (as well as β' and β) need to have the same spin.

For practical calculations, it is essential to reduce the number of interaction parameters. Often, e.g., in DFT + U (density-functional theory augmented by a Hubbard- U interaction in a static mean-field approximation) [3] and DFT + DMFT (dynamical mean-field theory) [4], one considers only the *local* interaction. That is, all orbitals α, β in Eq. (1) are on the same site; they might correspond to Wannier orbitals [5] localized around the same lattice site. This is justified not only because this on-site interaction is by far the largest interaction parameter, but also since nonlocal interactions between orbitals on different sites can be treated in simple (Hartree) mean-field theory in the limit of a large number of neighbors [6]. Certainly there are situations where such nonlocal interactions can be of importance, particularly in one and two dimensions, or also between transition-metal d and oxygen p orbitals [7].

A further reduction of parameters can be achieved by using the so-called Slater integrals [8]

$$F_l = \int dr dr' R(r)^2 R(r')^2 \frac{\min(r, r')^l}{\max(r, r')^{l+1}} r^2 r'^2. \quad (2)$$

Here, the underlying assumption is spherical symmetry, which allows for an analytical angular integration so that eventually only the integrals (2) over the radial part $R(r)$ of the wave functions remain; see the appendix. These Slater integrals, the simpler Kanamori [9] interaction, and or even just a single U parameter, are commonly used in DFT + U [10], DFT + DMFT [4, 11–13], or full-multiplet configuration-interaction calculations [14–16]. However, a crystal lattice is not spherically symmetric. It has a lower, e.g., cubic, symmetry.

The aim of our paper is hence to analyze the nature and magnitude of the deviations from spherical interaction parameters. To this end, we study the specific and arguably most relevant case of transition-metal oxides with a cubic perovskite (ABO_3) structure. In Sec. II, we study analytically the structure of the Coulomb matrix elements for a BO_6 octahedron. For the low-energy t_{2g} orbitals, the cubic Coulomb interaction requires three parameters instead of the two parameters for spherical symmetry. We explicitly derive the most relevant integrals that deviate from the Slater integrals (2).

In Sec. III, we calculate the quantitative deviations from spherical symmetry by means of maximally localized Wannier orbitals. While the bare interaction in $3d^1$ SrVO_3 is still described reasonably well by spherically symmetric interaction parameters, the stronger p - d hybridization in $5d^4$ BaOsO_3 results in larger deviations ($\sim 25\%$). In a Wannier basis which includes both the transition-metal t_{2g} and oxygen p orbitals, working with spherically symmetric interactions is justified. Even for BaOsO_3 , deviations between cubic and spherical symmetric interactions are only 3% in this case.

The effect of screening within the Thomas–Fermi approximation is considered in Sec. III C. For short screening lengths, deviations from spherical symmetry are even larger than in the unscreened case; for realistic screening lengths, deviations are reduced but still significant for BaOsO_3 in a three-orbital Wannier basis ($\sim 12\%$).

II. CUBIC INTERACTION PARAMETERS

We consider the typical situation for transition-metal oxides with an octahedron of oxygens surrounding each transition-metal atom, as shown in Fig. 1. While an isolated transition-metal atom would be spherically symmetric and the parametrization in terms of Slater integrals exact, the oxygen octahedron reduces the symmetry to cubic point group symmetry [17] around the transition-metal atom. Therefore, the fivefold degeneracy of the atomic d level is partially lifted, leaving a threefold degenerate t_{2g} and a twofold degenerate e_g level in the cubic environment. In the cases we consider, the octahedron vertices are occupied by negatively charged O^{2-} ions. In this case, the e_g states, which have a lot of weight along the B -O lines, are higher in energy than the t_{2g} states, whose weight resides predominantly in the space between the O ions; see Fig. 1(right).

The effective t_{2g} orbitals are a combination of predominantly transition-metal d orbitals admixed with oxygen p orbitals. For many transition-metal oxides, these t_{2g} orbitals constitute the low-energy degrees of freedom for excitations around the Fermi energy [18]. For an analytical description we consider an atomic transition-metal t_{2g} orbital, denoted d_α with $\alpha \in \{xy, yz, xz\}$ in the following. This d_α orbital mixes with a linear combination of oxygen p orbitals of the same symmetry; see, e.g., Ref. [15]. It is convenient to define this linear combination as o_α : e.g.,

$$o_{xy} = (p_x^{+y} + p_y^{+x} - p_x^{-y} - p_y^{-x})/2, \quad (3)$$

where p_x^{+y} is the p_x orbital centered around the oxygen atom in the the positive y direction; see Fig. 1. The orbitals o_{xz} and o_{yz} follow from Eq. (3) by cubic symmetry, i.e., $x \leftrightarrow z$ and $y \leftrightarrow z$, respectively.

Symmetry ensures that the orbital o_α is orthogonal to $d_{\alpha'}$, except when $\alpha = \alpha'$. Thus to orthogonalize the set of orbitals $\{o_\alpha, d_{\alpha'}\}$, one has only to orthonormalize o_α with respect to its associated d_α . The orthonormalized orbitals are

$$o'_{\alpha=ij} = \frac{o_{ij} - d_{ij}\langle d_{ij}|o_{ij}\rangle}{\sqrt{1 - \langle d_{ij}|o_{ij}\rangle^2}}. \quad (4)$$

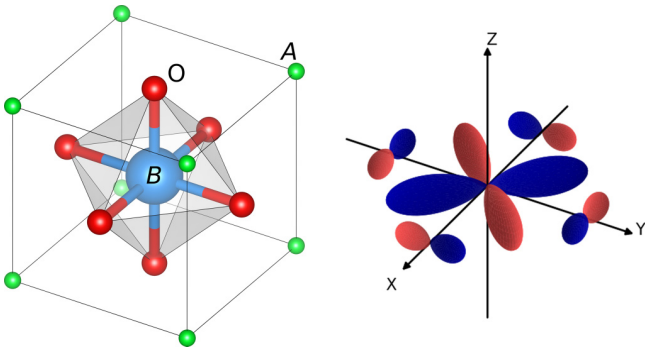


FIG. 1. (Color online) (left) In the perovskite (ABO_3) structure, the oxygen octahedron around the central transition-metal ion breaks spherical symmetry down to cubic. The B ion (large sphere) occupies the center of a cube with A at the corners and O at the face centers. (right) Schematic representation of the low-energy d'_{xy} orbital of Eq. (5) [light and dark shading indicates opposite signs of the wave function].

The mixing of transition-metal d orbitals and oxygen p orbitals stems from hybridization; by symmetry, there is a hybridization only between d_α and o'_α with the same α . Hence we obtain the tight-binding Hamiltonian

$$\begin{pmatrix} E_d & t \\ t & E_p \end{pmatrix},$$

where E_d and E_p are the d and p (more precisely the orthogonalized o') energy levels; $E_d - E_p$ is the charge transfer energy. The predominantly d eigenfunctions of this tight-binding Hamiltonian, d'_{ij} , are the effective low-energy t_{2g} orbitals

$$d'_{ij} = ad_{ij} + bo'_{ij}, \quad (5)$$

with $\eta = (E_d - E_p)/(2t)$, $a = [2(\eta^2 - \eta\sqrt{\eta^2 + 1} + 1)]^{-1/2}$, and $b = [2(\eta^2 + \eta\sqrt{\eta^2 + 1} + 1)]^{-1/2}$.

After defining the low-energy t_{2g} orbitals, we need to calculate the Coulomb interaction between these one-particle eigenstates, i.e.,

$$U_{\alpha'\beta'\beta\alpha} = \langle d'_{\alpha'=ij} | \langle d'_{\beta'=kl} | V | d'_{\beta=mn} \rangle | d'_{\alpha=op} \rangle. \quad (6)$$

This is the relevant site-local Coulomb interaction for the low-energy degrees of freedom. Note that, in this context, $U_{\alpha'\beta'\beta\alpha}$ is defined as the matrix element between direct products of single-particle states denoted as $|d'_{\beta=mn}\rangle |d'_{\alpha=op}\rangle$, not between antisymmetrized Fock states.

Since often $b \ll 1$ in transition-metal oxides, we consider in the following only the leading terms in the limit of large distance between transition-metal and oxygen sites. In this limit, the direct overlap $\langle d_{ij}|o_{ij}\rangle$, b (which is the overlap with respect to the one-particle Hamiltonian, $b \sim t$), and Coulomb integrals between orbitals on different sites are small. In the following we hence restrict ourselves to all terms up to second order in (any) of the above off-site overlaps and obtain the following three contributions:

Directly from the ad_{ij} terms in Eq. (5) and from the orthogonalization of the o'_{ij} we get a contribution

$$\left(\alpha^4 - 4\alpha^3 b \frac{\langle d_{uv}|o_{uv}\rangle}{N} \right) \langle d_{ij} | \langle d_{kl} | V | d_{mn} \rangle | d_{op} \rangle. \quad (7)$$

This term is centered around the transition-metal ion and can be expressed in terms of the Slater integrals F_l for the d_{ij} orbitals. Hence, this term can still be parametrized with Kanamori interaction parameters.

From two bo'_{ij} s in Eq. (5) we get a contribution

$$\left(2\alpha^2 b^2 \frac{1}{N^2} \right) \langle d_{ij} | \langle o_{kl} | V | o_{mn} \rangle | d_{op} \rangle. \quad (8)$$

Note that o_{kl} and o_{mn} have a contribution from the same oxygen site, so that the r and r' integrals both include on-site overlaps. Since for large oxygen–transition-metal distances the intersite overlap decays exponentially while the Coulomb interaction decays like $1/r$, we keep the term Eq. (8).

Finally, there is a contribution involving only one bo'_{ij} in Eq. (5) and a Coulomb integral overlap between transition-metal and oxygen sites:

$$\left(2\alpha^3 b \frac{1}{N} \right) \langle d_{ij} | \langle d_{kl} | V | o_{mn} \rangle | d_{op} \rangle. \quad (9)$$

All other terms are of higher order in b or the off-center overlap integrals.

Equations (8) and (9) involve Coulomb integrals with two distinct sites, oxygen and transition metal. Hence, they cannot be expressed in terms of Slater integrals any longer. One can also envisage this from the orbital in Fig. 1(right). While the spherical rotations around the x or y axis of the central d_{xy} part of the d'_{xy} orbital in Fig. 1(right) map the d_{xy} orbital onto a linear combination of the three d_α orbitals, this is not possible any longer with the oxygen admixture o'_{xy} in d'_{xy} except for 90 degree rotations. Noncubic rotations will put the rotated orbitals into positions where there is actually no oxygen site.

Employing the cubic symmetry, we can further reduce the number of integrals needed in Eqs. (7)–(9); or (1); cf. Ref. [19]. Any integral involving an orbital index $\alpha = ij$ once or thrice is odd in one cubic direction and hence vanishes. This leaves us with integrals where all orbitals are the same, i.e., the intra-orbital Hubbard interaction $U = U_{\alpha\alpha\alpha}$ and integrals where we have two distinct orbitals $\alpha \neq \beta$ twice. For the latter we have three possibilities: the interorbital interaction $U' = U_{\alpha\beta\beta\alpha}$, the Hund's exchange $J = U_{\alpha\beta\alpha\beta}$, the pair hopping term and $U_{\alpha\alpha\beta\beta}$ which, for real-valued wave functions, has the same amplitude as J . These symmetry considerations actually hold in general, but without spherical symmetry $U \neq U' + 2J$ because of the terms (8) and (9). For spherical symmetry, the connection to the Slater integrals is as follows (cf. Ref. [19]): $U = F_0 + \frac{4}{49}(F_2 + F_4)$, $U' = F_0 - \frac{2}{49}F_2 - \frac{4}{441}F_4$, $J = \frac{3}{49}F_2 + \frac{20}{441}F_4$, so that $U = U' + 2J$ holds [20]. If we have instead only cubic symmetry, we can still parametrize the interaction in terms of U , U' , and J , but now with $U \neq U' + 2J$ and no expression in terms of Slater integrals.

In second quantization, this Kanamori Hamiltonian [9], which is obtained from Eq. (1) by including all valid spin combinations in Eq. (1), reads

$$\begin{aligned}
 H_U &= \frac{1}{2} \sum_{\substack{\alpha, \beta \\ \alpha', \beta'}} U_{\alpha'\beta'\beta\alpha} \sum_{\sigma, \sigma'} c_{\alpha'\sigma}^\dagger c_{\beta'\sigma'}^\dagger c_{\beta\sigma} c_{\alpha\sigma} \\
 &= U \sum_{\alpha} n_{\alpha, \uparrow} n_{\alpha, \downarrow} + \sum_{\substack{\alpha > \beta \\ \sigma, \sigma'}} [(U' - \delta_{\sigma\sigma'} J) n_{\alpha, \sigma} n_{\beta, \sigma'}] \\
 &\quad - \sum_{\alpha \neq \beta} J (c_{\alpha, \downarrow}^\dagger c_{\beta, \uparrow}^\dagger c_{\beta, \downarrow} c_{\alpha, \uparrow} + c_{\beta, \uparrow}^\dagger c_{\beta, \downarrow}^\dagger c_{\alpha, \uparrow} c_{\alpha, \downarrow} + \text{H.c.}).
 \end{aligned} \tag{10}$$

Here, $c_{\alpha, \sigma}^\dagger$ ($c_{\alpha, \sigma}$) creates (annihilates) an electron with spin σ in orbital α ; $n_{\alpha, \sigma} = c_{\alpha, \sigma}^\dagger c_{\alpha, \sigma}$.

In contrast, for the e_g orbitals, which are proportional to $3z^2 - r^2$ and $\sqrt{3}(x^2 - y^2)$, the relation $U = U' + 2J$ still holds for cubic symmetry: Again because of cubic symmetry ($x \leftrightarrow y$) any term involving one or three $x^2 - y^2$ orbitals vanishes; only the terms $U = U_{\alpha\alpha\alpha}$, $U' = U_{\alpha\beta\beta\alpha}$, $J = U_{\alpha\beta\alpha\beta} = U_{\alpha\alpha\beta\beta}$ remain. However, now, instead of interchanging the orbitals, cubic symmetry operations such as ($x \rightarrow x$, $y \rightarrow z$, $z \rightarrow -y$), lead to mixed orbitals: $3z^2 - r^2 \rightarrow -1/2(3z^2 - r^2) - \sqrt{3}/2\sqrt{3}(x^2 - y^2)$. Hence, the intra-orbital Hubbard interaction U for the e_g orbitals is not a cubic invariant, and

U has to depend on the other parameters U' and J through $U = U' + 2J$.

III. QUANTITATIVE DEVIATIONS FOR SrVO₃ AND BaOsO₃

A. Construction of Wannier functions

We now aim to validate our analytical results and quantify the deviation from the spherical-symmetry relationship (1) in real materials. To this end, we perform DFT calculations [21] by using a generalized-gradient approximation to the exchange-correlation functional [22] for two cubic perovskite materials and construct low-energy effective models using maximally localized Wannier functions (MLWFs) [23,24].

In terms of the formalism of Sec. II, the role of the Wannier functions is to provide the radial dependence of the orbitals which was irrelevant for our arguments from symmetry, but which must be provided to compute numerical values for the interaction parameters. The main difference is that we considered a local octahedron before, while Wannier functions $|w_{\alpha\mathbf{R}}\rangle$ properly belong to a periodic crystal: they have finite hopping amplitudes $t_{\alpha\mathbf{R}\alpha'\mathbf{R}'}$ also for $\mathbf{R} \neq \mathbf{R}'$ (or equivalently, they show a \mathbf{k} dispersion) and form an orthonormal set $\langle w_{\alpha\mathbf{R}} | w_{\alpha'\mathbf{R}'} \rangle = \delta_{\alpha\alpha'} \delta_{\mathbf{R}\mathbf{R}'}$ with respect to sites \mathbf{R} and orbitals α .

Our first example is SrVO₃, which is often used as a “test bed” strongly correlated material. (For DFT + DMFT calculations; see, e.g., Ref. [25]. Detailed discussions of Wannier projections in this and related materials are given in Refs. [24,26,27].) The cubic perovskite SrVO₃ is a paramagnetic, correlated metal with electronic configuration $3d^1$, i.e., one of the t_{2g} -derived states will be filled.

Second, we consider the recently synthesized compound BaOsO₃ [28]. With a low-spin $5d^4$ configuration, this is another paramagnetic metal. Since the $5d$ states are more extended than the $3d$ states of V, we expect to find greater p - d hybridization and, in turn, greater deviation from $U = U' + 2J$ in this case.

For each material, we construct two sets of Wannier functions:

- (1) three “ d -only” Wannier functions corresponding to the d'_{ij} of Eq. (5), and
- (2) twelve “ $d + p$ ” Wannier functions corresponding to the atomic d_{ij} and p_i states.

It is instructive to compare these two approaches: The first set of Wannier functions translates the three t_{2g} -derived bands to three orbitals $|w'_{\alpha\mathbf{0}}\rangle$ centered on the B ion. Direct and O-mediated hopping processes are subsumed in an effective B - B hopping $t_{d'd'}$. To account for this, $|w'\rangle$ must have substantial weight not only at B but also at O atoms. (In a band picture, the reason is the significant O- p contribution to the t_{2g} -derived bands.) Which combinations of O- p and B - d orbitals mix is determined by symmetry, as discussed in Sec. II; cf. Fig. 2. Going beyond an effective single-particle description, the Coulomb interaction is expected to be well represented by a site local “multiband Hubbard” term $U_{\alpha'\beta'\beta\alpha}$ which can be parametrized by three independent quantities U , U' , and J , as we saw in the previous section.

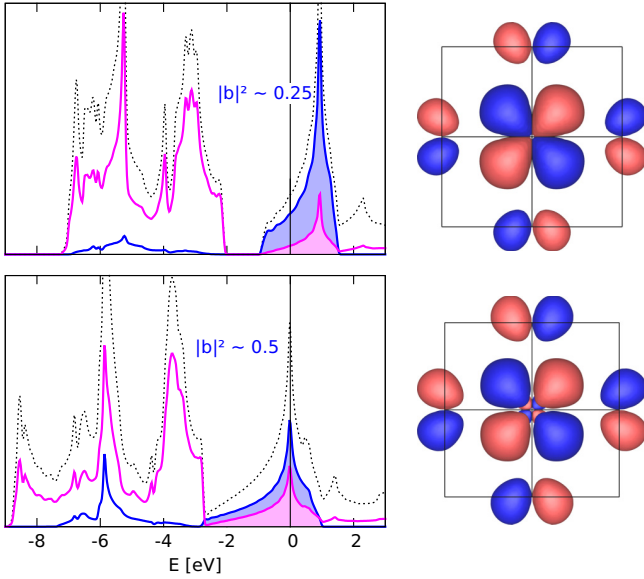


FIG. 2. (Color online) Densities of states and Wannier functions for the d -only Wannier orbitals for SrVO₃ (top) and BaOsO₃ (bottom). On the left, we show the total DOS (dotted line) and the projections on transition-metal t_{2g} (dark) and O (light) states. The shaded area marks the region of integration used to estimate the O- p weight [corresponding to $|b|^2$ in Eq. (5)], see text. On the right, the light (dark) lobes are isosurfaces for the positive (negative) parts of the real-valued Wannier functions. The strong p - t_{2g} hybridization and the antibonding character are plainly visible.

The second set of Wannier functions spans nine additional bands: three p -derived bands per O. With the p states explicitly included, the d -like MLWFs are free to become more localized; the weight at the O sites will be carried by the p -like orbitals (cf. Fig. 3). The downside is that the resulting model becomes significantly more complex, since a correct treatment of such a $d + p$ model must take into account not only the intra-atomic interactions on the B (U_{dd}) and on the O (U_{pp}) sites, but also the interatomic (U_{pd}) interactions [7,29]. This added complexity will increase the computational cost to solve the model in any numerical method, but it will also make the physical interpretation of the results more involved.

Before we turn to the results, note that the heavy ($Z = 76$) element Os leads to an appreciable spin-orbit splitting in BaOsO₃. Because it would invalidate the symmetry analysis of Sec. II, we neglect this effect in the construction of the Wannier functions. While our analysis could be extended to include spin-orbit coupling, a spin-orbit interaction term can also be added afterwards to the tight-binding model in any case [30].

B. Results

Figure 2 shows the densities of states (DOS) of SrVO₃ and BaOsO₃, and the Wannier orbitals corresponding to the three-band case. The DOS around the Fermi level is derived from the π -antibonding combinations of O- p and B - t_{2g} states; correspondingly, the three-band orbitals are composed of a d -like contribution at the B site and p -like contributions at the O sites sharing a plane with the d -like part, akin to the o'_α

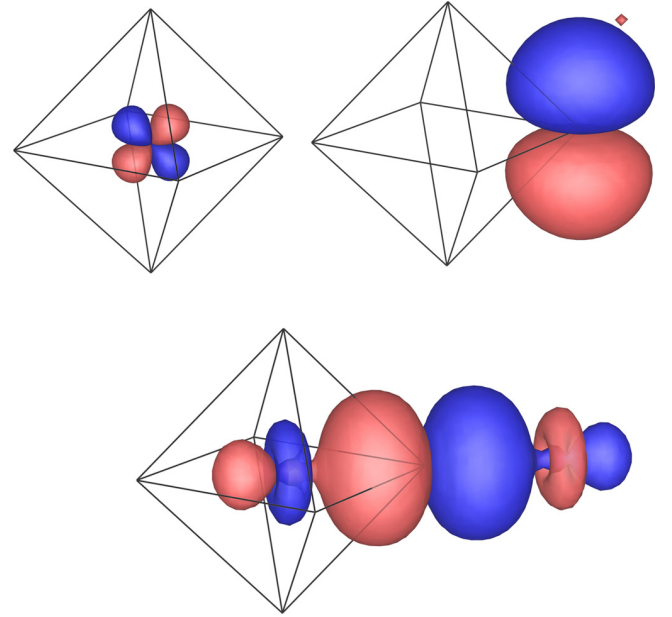


FIG. 3. (Color online) Twelve-orbital Wannier functions for SrVO₃ [plotted as in Fig. 2(right)]. (top left) By symmetry, the twelve orbitals are grouped into three equivalent d -like orbitals; and two types of p -like orbitals, (bottom) three “ p_σ ” whose symmetry axes point toward their B neighbors, and (top right) six “ p_π ” pointing away from the B sites. With the O- p states explicitly included, no p - t_{2g} hybridization is seen in these orbitals. Correspondingly, the d and p_π orbitals are close to their atomic counterparts. Conversely, the p_σ orbitals, which mediate the σ bonding between O- p and B - e_g states, are elongated along their symmetry axis and have large contributions at their B neighbors [26,27].

orbitals in Sec. II. These Wannier orbitals are also referred to as d only, where the quotation marks hint that these orbitals are actually not pure d orbitals. The Wannier functions are equivalent to each other under cubic symmetry.

As expected, the p - d hybridization is stronger in BaOsO₃ than in SrVO₃. This is seen both in the DOS (more O weight around the Fermi energy $E_F = 0$) and in the orbitals (bigger lobes at the O sites). We can quantify this observation by integrating over the shaded areas in the DOS; this yields an O admixture of $|b_{\text{SrVO}_3}|^2 \sim 0.25$ and $|b_{\text{BaOsO}_3}|^2 \sim 0.5$, respectively. In this sense, the “ d bands” of BaOsO₃ consist in fact of almost equal parts O and Os contributions. These values agree qualitatively with Eq. (5), which yields $|b_{\text{SrVO}_3}|^2 \sim 0.20$ and $|b_{\text{BaOsO}_3}|^2 \sim 0.33$ using the parameters from Table VI [31]. Quantitative differences have to be expected because (i) Eq. (5) holds for an isolated octahedron instead of the periodic crystal, (ii) there are further hopping integrals that would have to be considered, and (iii) the partial DOS of Fig. 2 are only projections within the muffin-tin spheres [21].

For these d -only Wannier orbitals, we calculated the Coulomb interaction by spatial integration of Eq. (1) [32]. Table I summarizes the results obtained for the bare interaction. For the $3d^1$ perovskite SrVO₃, deviations from the spherical symmetric relation $U - U' = 2J$ are 6%. That is, calculations employing this relation can still be expected to yield quite reliable results. For the $5d^4$ perovskite BaOsO₃, on the other

TABLE I. Coulomb interactions (unscreened) for d -only Wannier functions of SrVO₃ and BaOsO₃; $(U - U')/2 = J$ holds for spherical but not for cubic symmetry, for BaOsO₃ deviations are indeed substantial.

Interaction	SrVO ₃	BaOsO ₃
U	16.30 eV	10.54 eV
U'	15.14 eV	9.67 eV
J	0.55 eV	0.33 eV
$(U - U')/2$	0.58 eV	0.44 eV

hand, deviations are 25%. The reason for this is the larger admixture of oxygen p contributions, which according to Sec. II yield larger off-center Coulomb integral overlaps and hence a larger deviation from spherical symmetry.

Recently, transition-metal oxides with heavy $4d$ or $5d$ elements have attracted more and more attention. Indeed, in such systems electronic correlations are stronger than expected—due to Hund's rule coupling [19,33,34]. All the more important is a correct Hamiltonian and multiplet structure with Hund's exchange. In this respect, our finding highlights the substantial difference between $(U - U')/2$ and J . A Kanamori Hamiltonian with three independent Coulomb interactions needs to be considered for obtaining the correct multiplet structure.

Next, we turn to the twelve-orbital $d + p$ Wannier functions. This is an alternative description of the low-energy physics, where the oxygen p orbitals are explicitly taken into account. The corresponding Wannier functions for SrVO₃ are shown in Fig. 3. The d -like orbitals are again equivalent up to symmetry, but two inequivalent types of p -like orbitals appear. Symmetry also greatly restricts the possible hopping processes between these states. The hopping amplitudes within the octahedron as well as selected longer-ranged ones for all four Wannier projections are reported in Appendix B.

We list the Coulomb interaction parameters between the twelve-band orbitals for SrVO₃ and BaOsO₃ in Tables II and III, respectively. For the d -like orbitals, $U = U' + 2J$ is fulfilled with a reasonable accuracy of 3% even in BaOsO₃. Having the additional degree of freedom regarding oxygen- p Wannier orbitals, the t_{2g} orbitals are now localized around the transition-metal ion and have the spherically symmetric form; cf. Fig. 3. In this case, two parameters are sufficient for the d - d Kanamori interaction.

TABLE II. Left: Same as Table I but for $d + p$ SrVO₃ Wannier functions. Right: the different d - p density-density Coulomb interactions for these Wannier functions; see main text for the notation.

Interaction	SrVO ₃	Interaction	SrVO ₃
U	19.99 eV	$U_{p\pi d}$	7.24 eV
U'	18.52 eV	$U'_{p\pi d}$	7.18 eV
J	0.74 eV	$U_{p\sigma d}$	8.52 eV
		$U_{p\sigma d}^\perp$	6.87 eV
$(U - U')/2$	0.74 eV	$U_{p\pi d}^\perp$	8.06 eV

TABLE III. Same as Table II but for $d + p$ BaOsO₃ Wannier functions.

Interaction	BaOsO ₃	Interaction	BaOsO ₃
U	14.90 eV	$U_{p\pi d}$	6.94 eV
U'	13.65 eV	$U'_{p\pi d}$	6.80 eV
J	0.64 eV	$U_{p\sigma d}$	7.85 eV
		$U_{p\sigma d}^\perp$	7.23 eV
$(U - U')/2$	0.62 eV	$U_{p\pi d}^\perp$	6.38 eV

As a side note, observe that in the twelve-band case $U - U' < 2J$, while in the three-band case $U - U' > 2J$. This is because U' and J are more strongly reduced than U by the shift of t_{2g} weight to the oxygens which occurs in the three-band case, as U' and J are *interorbital* interactions that include more nonoverlapping oxygens in the interaction integral.

Let us emphasize that the d - p interaction also plays an important role [29]. The d - p interactions of density-density type are listed in Tables II and III (right). There are two types of p orbitals, denoted p_π and p_σ (see Fig. 3). Interactions with p orbitals centered on an oxygen atom outside the plane of the d orbital lobes are denoted by \perp . The d - p_σ interactions $U_{p\sigma d}$ and $U_{p\sigma d}^\perp$ with the p_σ orbitals oriented toward the transition-metal site is considerably stronger than that with the more regular p_π orbitals. There is only one $U_{p\pi d}^\perp$, while two parameters arise from density-density interaction between d and p_π orbitals with the p_π orbitals being centered around oxygen sites within the plane defined by the d orbitals. We denote these as $U_{p\pi d}$ if the p_π orbital lies within the same plane and $U'_{p\pi d}$ if it is oriented perpendicular to it. The considerable differences in the d - p Coulomb interaction can be understood from the very different p_π and p_σ orbitals in Fig. 3. These differences are of relevance for $d + p$ DFT + DMFT calculations that include U_{pd} [29].

C. Effect of screening

The values reported above were calculated for a bare, unscreened Coulomb interaction. In this section we include screening, within Thomas–Fermi theory. That is, we replace the bare interaction in Eq. (1) by

$$V(|\mathbf{r}' - \mathbf{r}|) = \frac{e^2}{4\pi\epsilon_0} \frac{1}{|\mathbf{r}' - \mathbf{r}|} e^{-|\mathbf{r}' - \mathbf{r}|/\lambda_{\text{TF}}}, \quad (11)$$

where λ_{TF} is the Thomas–Fermi screening length. Let us emphasize that, for a cubic crystal, the screened interaction $V(\mathbf{r}, \mathbf{r}')$ itself will be of cubic symmetry and hence deviate from spherical symmetry. This effect is not taken into account in the following; it will on its own generate further deviations of the Kanamori interaction parameters from the spherical relation $U = U' + 2J$.

In the following, we adjust the parameter λ_{TF} to yield a screened Coulomb interaction $U' \sim 3.5$ eV for $3d$ SrVO₃, as calculated using the constrained local density approximation [25]. This corresponds to a screening length $\lambda_{\text{TF}} = 0.43$ Å (the lattice parameters are $a_{\text{SrVO}_3} = 3.8425$ Å [35] and $a_{\text{BaOsO}_3} = 4.025$ Å [28]). We employ the same screening length

TABLE IV. Same as Table I but for screened interaction with screening length $\lambda_{\text{TF}} = 0.43 \text{ \AA}$.

Interaction	SrVO ₃	BaOsO ₃
U	4.40 eV	2.44 eV
U'	3.47 eV	1.80 eV
J	0.46 eV	0.28 eV
$(U - U')/2$	0.47 eV	0.32 eV

also for BaOsO₃ because this yields an interaction parameter $U' \sim 1.8 \text{ eV}$, which is in the expected range for the $5d$ BaOsO₃.

Table IV shows the results obtained for the d -only models. In the case of $3d$ orbitals, as exemplified by SrVO₃, deviations from spherically symmetric interaction parameters are already small without screening and become negligible if screening is included. By contrast, for $5d$ BaOsO₃, $U - U' = 2J$ is significantly violated even when screened. Let us note that the degree of deviation is quite robust over a large range of screening lengths. For example with $\lambda_{\text{TF}} = 0.61 \text{ \AA}$ we obtain a similar deviation of 14% ($U = 2.55 \text{ eV}$, $U' = 1.90 \text{ eV}$, and $J = 0.28 \text{ eV}$).

Interestingly, for weak screening (large λ) J can even be enhanced whereas U and U' are always reduced. The reason for this is that the exchange integral J includes positive and negative contributions; and for large λ_{TF} , the negative contributions are more strongly reduced than the positive ones. For example, at $\lambda_{\text{TF}} = 21.13 \text{ \AA}$ we obtain $J = 0.5465 \text{ eV}$ for SrVO₃, which is larger than the unscreened $J = 0.5464 \text{ eV}$. As the increase is very small, the results are given to a higher precision than elsewhere in the paper. With $U = 15.67 \text{ eV}$ and $U' = 12.50 \text{ eV}$, deviations are 6.2% for this screening strength.

In the limit of infinite screening, i.e., $\lambda_{\text{TF}} \rightarrow 0$, one can show that $U' = J$. That is, one can describe this limit by one Kanamori interaction parameter $U = 3U' = 3J$ for spherical symmetry, and two (U and $U' = J$) for cubic symmetry. Numerically, we get, however, also for cubic d -only Wannier functions, $U/J \sim 3$ for both SrVO₃ and BaOsO₃. The limits of strong and weak screening show that the idea that screening strongly reduces U' and hardly reduces J is not true in general. For strong screening, J is reduced as much as U' , since they are equal, while for weak screening J is even enhanced.

IV. CONCLUSION

We analyzed the physical origin and the magnitude of the difference between a spherically symmetric and a cubic interaction for t_{2g} orbitals. Deviations are quite large for $5d$ orbitals of heavy transition metals. Since for these systems Hund's exchange is paramount for electronic correlations [12,19,34,36], we conclude that a Kanamori interaction with three instead of two independent parameters is necessary. Unfortunately, this requires the calculation of one additional interaction parameter and hence a more thorough analysis of the interaction in DFT + DMFT calculations than was customary hitherto. Only if the oxygen degrees of freedom are included in the Wannier projection is this not necessary. In this case, however, the (different) d - p Coulomb interactions should be taken into account. For e_g orbitals there is no such difference between spherical and cubic interaction.

Depending on the screening length, screening enhances or reduces the difference between spherically symmetric and cubic interaction parameters. Screening can even enhance J whereas U and U' are always reduced. For Thomas–Fermi screening, $U = U' + 2J$ is still significantly violated for $5d$ BaOsO₃. Let us note that the simple Thomas–Fermi screening employed here is spherically symmetric, whereas the physical screening function obeys the cubic, not the spherical symmetry. This effect is an additional source of deviations from spherically symmetric interaction parameters.

For both e_g -only and t_{2g} -only low-energy effective models, we have a Kanamori interaction for cubic symmetry. This makes continuous-time quantum Monte Carlo simulations [37] very efficient because of an additional local symmetry; see Ref. [38].

ACKNOWLEDGMENTS

This work was supported by the European Research Council under the European Union's Seventh Framework Programme (FP/2007-2013)/ERC through Grant Agreement No. 306447 and by an *Innovative Project* Grant from Vienna University of Technology (E.A.).

APPENDIX A: COULOMB INTERACTION AND SLATER INTEGRALS

For the sake of completeness, let us briefly add the representation of the Coulomb interaction (1) by Slater integrals. Expressing

$$1/|\mathbf{r} - \mathbf{r}'| = \sum_{l,m} \frac{\min(r,r')^l}{\max(r,r')^{l+1}} \frac{4\pi}{2l+1} Y_{l,m}(\theta,\varphi) Y_{l,m}^*(\theta',\varphi')$$

in terms of spherical harmonics $Y_{l,m}$ and with $\psi_\alpha(\mathbf{r}) = R(r)Y_\alpha$ where $R(r)$ is independent of l (or α), the Coulomb interaction Eq. (1) becomes

$$U_{\alpha'\beta'\beta\alpha} = \frac{e^2}{4\pi\epsilon_0} \int dr d\Omega dr' d\Omega' R(r) Y_{\alpha'}(\theta,\varphi) R(r') Y_{\beta'}(\theta',\varphi') \times \sum_{l,m} \left[\frac{\min(r,r')^l}{\max(r,r')^{l+1}} \frac{4\pi}{2l+1} Y_{l,m}(\theta,\varphi) Y_{l,m}(\theta',\varphi') \right] \times R(r') Y_{\beta}(\theta',\varphi') R(r) Y_{\alpha}(\theta,\varphi) r'^2 r^2. \quad (\text{A1})$$

This integral can be decomposed into a radial part ($dr dr'$) and an angular part ($d\Omega d\Omega'$), and the latter can be expressed in terms of Clebsch–Gordan coefficients. Thus, only the radial integrals (also known as Slater parameters) F_l of Eq. (2) need to be calculated.

 TABLE V. Hopping amplitudes t between the three t_{2g} Wannier functions at various distances and their on-site energies E relative to the Fermi level. Values are in eV.

	$t_\pi^{(1)}$	$t_\delta^{(1)}$	$t_\sigma^{(2)}$	$t_\perp^{(2)}$	$t_\parallel^{(2)}$	E
SrVO ₃	-0.263	-0.027	-0.084	0.009	0.006	0.580
BaOsO ₃	-0.394	-0.043	-0.112	-0.012	0.013	-0.453

TABLE VI. Selected hopping amplitudes t between twelve-band Wannier functions and their on-site energies E relative to the Fermi level. Where the sign of the hopping alternates due to the signs of the p -type orbitals, we give the modulus. Values are in eV.

	$t_{dd\pi}^{(1)}$	$t_{dd\delta}^{(1)}$	$ t_{dp\pi} $	$ t_{p\pi p\pi} $	$ t_{p\pi p'_\pi} $	$ t_{p\pi p\sigma} $	$t_{p\sigma p\sigma}$	$t_{p\pi p\pi}^{(1)}$	$t_{p\sigma p\sigma}^{(1)}$	E_d	$E_{p\pi}$	$E_{p\sigma}$
SrVO ₃	-0.128	-0.005	1.099	0.064	0.369	0.258	-0.044	-0.078	0.671	-0.407	-3.780	-5.520
BaOsO ₃	-0.187	-0.002	1.240	0.007	0.204	0.195	-0.024	-0.107	0.903	-2.063	-3.896	-6.887

APPENDIX B: HOPPING MATRICES

In this appendix, we report the numerical values of selected hopping amplitudes in our Wannier projections [39]. The values for SrVO₃ may be compared with Refs. [24,26]. Note that this is not an enumeration of the largest hopping amplitudes; rather, the selection is meant to be illustrative.

For the three-band Wannier functions (values in Table V), no hopping is possible within the unit cell. Two nearest-neighbor hoppings are allowed, a π -type hopping $t_{\pi}^{(1)}$ when the displacement is in the same plane as the orbital lobes [e.g., xy orbitals with displacement (1 0 0)], and a smaller $t_{\delta}^{(1)}$ of δ type where the displacement is perpendicular [e.g., xy and (0 0 1)]. Interorbital nearest-neighbor hopping is forbidden by cubic symmetry. There are three second-nearest-neighbor hopping parameters: $t_{\sigma}^{(2)}$ when both orbitals and the displacement share a plane [e.g., xy and (1 1 0)]; $t_{\parallel}^{(2)}$ when the orbitals' planes are parallel [e.g., $xz \leftrightarrow xz$ and (1 1 0)]; and $t_{\perp}^{(2)}$ when the planes are perpendicular [e.g., $xz \leftrightarrow yz$ and (1 1 0)].

For the twelve-band case (Table VI), we report the nearest-neighbor $d \leftrightarrow d$ hopping parameters $t_{dd}^{(1)}$ analogous to those of the three-band case, but not those to further neighbors. In any case, O-mediated hopping, which was subsumed in the hoppings of the three-band orbitals, now has to be taken into account explicitly.

Within the octahedron, the following hopping processes are possible: $t_{dp\pi}$ when the p_{π} orbital resides in the plane defined by the d (e.g., $d_{xy} \leftrightarrow p_y^{+x}$); $t_{p\pi p\pi}$ between nearest-O neighbors, i.e., along an edge of the octahedron (e.g., $p_y^{+x} \leftrightarrow p_y^{+z}$); $t_{p\pi p'_\pi}$ which is the same as the last, but between orbitals of different orientation (e.g., $p_y^{+x} \leftrightarrow p_x^{+y}$); $t_{p\pi p\sigma}$ along an edge (e.g., $p_y^{+x} \leftrightarrow p_y^{+y}$); $t_{p\sigma p\sigma}$ along an edge (e.g., $p_x^{+x} \leftrightarrow p_y^{+y}$); $t_{p\pi p\pi}^{(1)}$ across the octahedron (e.g., $p_y^{+x} \leftrightarrow p_y^{-x}$); and $t_{p\sigma p\sigma}^{(1)}$ across the octahedron (e.g., $p_x^{+x} \leftrightarrow p_x^{-x}$).

Comparing the sequences of values for the two materials, the same trends are observed (with the exceptions of $t_{\perp}^{(2)} \geq t_{\parallel}^{(2)}$ and $|t_{p\pi p\pi}| \geq |t_{p\sigma p\sigma}|$). However, the values for the d -only orbitals, and for dd and pd processes in the twelve-band orbitals, are in general larger for BaOsO₃ than for SrVO₃, the larger lattice constant of BaOsO₃ notwithstanding (4.03 Å versus 3.84 Å for SrVO₃). This is reflective of the greater p - d hybridization and spatial extent of the $5d$ states.

Contrariwise, the twelve-band pp hopping processes have larger amplitude in SrVO₃. Our interpretation is that, in this case, the larger spatial distance prevails; indeed, the difference in Wannier-function spread ($\langle r^2 \rangle$) between SrVO₃ and BaOsO₃ is much more pronounced for the d than for the p orbitals. The exceptions to this rule, $t_{p\pi p\pi}^{(1)}$ and $t_{p\sigma p\sigma}^{(1)}$ (hopping across the octahedron), may be explained by the stronger p - d hybridization in BaOsO₃.

- [1] J. G. Bednorz and K. A. Müller, *Z. Phys. B: Condens. Matter* **64**, 189 (1986); Y. Kamihara, T. Watanabe, M. Hirano, and H. Hosono, *J. Am. Chem. Soc.* **130**, 3296 (2008).
- [2] P. Coleman and A. J. Schofield, *Nature* **433**, 226 (2005).
- [3] V. I. Anisimov, J. Zaanen, and O. K. Andersen, *Phys. Rev. B* **44**, 943 (1991).
- [4] V. I. Anisimov, A. I. Poteryaev, M. A. Korotin, A. O. Anokhin, and G. Kotliar, *J. Phys.: Condens. Matter* **9**, 7359 (1997); A. I. Lichtenstein and M. I. Katsnelson, *Phys. Rev. B* **57**, 6884 (1998); K. Held, I. A. Nekrasov, G. Keller, V. Eyert, N. Blümer, A. McMahan, R. Scalettar, T. Pruschke, V. I. Anisimov, and D. Vollhardt, *Phys. Status Solidi B* **243**, 2599 (2006); G. Kotliar, S. Y. Savrasov, K. Haule, V. S. Oudovenko, O. Parcollet, and C. A. Marianetti, *Rev. Mod. Phys.* **78**, 865 (2006); K. Held, *Adv. Phys.* **56**, 829 (2007).
- [5] G. H. Wannier, *Phys. Rev.* **52**, 191 (1937).
- [6] E. Müller-Hartmann, *Z. Phys. B: Condens. Matter* **74**, 507 (1989).
- [7] N. Parragh, G. Sangiovanni, P. Hansmann, S. Hummel, K. Held, and A. Toschi, *Phys. Rev. B* **88**, 195116 (2013).
- [8] J. C. Slater, *Quantum Theory of Atomic Structure* (McGraw-Hill, New York, 1960); J. S. Griffith, *The Theory of Transition-Metal Ions* (Cambridge University Press, Cambridge, 1971).
- [9] J. Kanamori, *Prog. Theor. Phys.* **30**, 275 (1963).
- [10] See, among others, [3]; P. Blaha, K. Schwarz, G. Madsen, D. Kvasnicka, J. Luitz, User's Guide, Wien2K_13.1 [www.wien2k.at/reg_user/textbooks]; Jan Kunes, Alexey V. Lukoyanov, Vladimir I. Anisimov, Richard T. Scalettar, and Warren E. Pickett, *Nat. Mater.* **7**, 198 (2008); E. Assmann, P. Blaha, R. Laskowski, K. Held, S. Okamoto, and Giorgio Sangiovanni, *Phys. Rev. Lett.* **110**, 078701 (2013); C. Franchini, R. Kovacik, M. Marsman, S. Sathyanarayana Murthy, J. He, C. Ederer, and G. Kresse, *J. Phys.: Condens. Matter* **24**, 235602 (2012); A. A. Tsirlin, O. Janson, and H. Rosner, *Phys. Rev. B* **84**, 144429 (2011); E. R. Ylvisaker, W. E. Pickett, and K. Koepnik, *ibid.* **79**, 035103 (2009).
- [11] In DFT + DMFT usually Kanamori interaction parameters are used; see, among others, K. Haule, C.-H. Yee, and K. Kim, *Phys. Rev. B* **81**, 195107 (2010); I. Di Marco, P. Thunström, M. I. Katsnelson, J. Sadowski, K. Karlsson, S. Lebègue, J. Kanski, and O. Eriksson, *Nat. Commun.* **4**, 2645 (2013); P. Hansmann, A. Toschi, G. Sangiovanni, T. Saha-Dasgupta, S. Lupi, M. Marsi, and K. Held, *Phys. Status Solidi B* **250**, 1251 (2013); S. Backes, D. Guterding, H. O. Jeschke, and R. Valenti, *New J. Phys.* **16**, 083025 (2014); Z. Zhong, M. Wallerberger, J. M. Tomczak, C. Taranto,

- N. Parragh, A. Toschi, G. Sangiovanni, and K. Held, [arXiv:1312.5989](#); G. Giovannetti, M. Aichhorn, and M. Capone, [arXiv:1402.0901](#); H. T. Dang, X. Ai, A. J. Millis, and C. A. Marianetti, *Phys. Rev. B* **90**, 125114 (2014).
- [12] L. de'Medici, J. Mravlje, and A. Georges, *Phys. Rev. Lett.* **107**, 256401 (2011).
- [13] For DFT + DMFT calculations with Slater integrals see, e.g., P. Thunström, I. Di Marco, O. Eriksson, *Phys. Rev. Lett.* **109**, 186401 (2012); R. Arita, J. Kunes, A. V. Kozhevnikov, A. G. Eguiluz, and M. Imada, *ibid.* **108**, 086403 (2012).
- [14] C. J. Ballhausen, *Introduction to Ligand Field Theory* (McGraw-Hill, New York, 1962).
- [15] M. W. Haverkort, M. Zwierzycki, and O. K. Andersen, *Phys. Rev. B* **85**, 165113 (2012); N. Rezaei, P. Hansmann, M. S. Bahramy, and R. Arita, *ibid.* **89**, 125125 (2014).
- [16] Note that, in the constrained random phase approximation [40], one can in principle and sometimes does calculate the full Coulomb interaction matrix. However, usually the subsequent DMFT calculation only employs Slater or Kanamori parameters; if not, a Kanamori parametrization is assumed from the very beginning [41].
- [17] See, e.g., G. F. Koster, J. O. Dimmock, R. G. Wheeler, and H. Statz, *Properties of the Thirty-Two Point Groups* (MIT Press, Cambridge, 1963).
- [18] M. Imada, A. Fujimori, and Y. Tokura, *Rev. Mod. Phys.* **70**, 1039 (1998).
- [19] A. Georges, L. de'Medici, and J. Mravlje, *Annu. Rev. Condens. Matter Phys.* **4**, 137 (2013); S. Sugano, Y. Tanabe, and H. Kamimura, *Multiplets of Transition-Metal Ions in Crystals* (Academic Press, New York, 1970).
- [20] Note that, without the e_g orbitals, the Hamiltonian itself is actually not spherically symmetric. Rotation of, e.g., the d_{xy} orbital around the z axis maps it onto a linear combination involving (missing) e_g orbitals; rotating it around the x or y axis maps it onto a linear combination of the (included) t_{2g} . The Hamiltonian is invariant under the latter rotations if $U = U' + 2J$.
- [21] P. Blaha, K. Schwarz, G. K. H. Madsen, D. Kvasnicka, and J. Luitz, *WIEN2k, An Augmented Plane Wave + Local Orbitals Program for Calculating Crystal Properties* (Techn. Universität Wien, Vienna, Austria, 2001).
- [22] J. P. Perdew, K. Burke, and M. Ernzerhof, *Phys. Rev. Lett.* **77**, 3865 (1996).
- [23] A. A. Mostofi, J. R. Yates, Y.-S. Lee, I. Souza, D. Vanderbilt, and N. Marzari, *Comput. Phys. Commun.* **178**, 685 (2008); N. Marzari, A. A. Mostofi, J. R. Yates, I. Souza, and D. Vanderbilt, *Rev. Mod. Phys.* **84**, 1419 (2012).
- [24] J. Kuneš, R. Arita, P. Wissgott, A. Toschi, H. Ikeda, and K. Held, *Comput. Phys. Commun.* **181**, 1888 (2010).
- [25] A. Sekiyama, H. Fujiwara, S. Imada, S. Suga, H. Eisaki, S. I. Uchida, K. Takegahara, H. Harima, Y. Saitoh, I. A. Nekrasov, G. Keller, D. E. Kondakov, A. V. Kozhevnikov, Th. Pruschke, K. Held, D. Vollhardt, and V. I. Anisimov, *Phys. Rev. Lett.* **93**, 156402 (2004); E. Pavarini, S. Biermann, A. Poteryaev, A. I. Lichtenstein, A. Georges, and O. K. Andersen, *ibid.* **92**, 176403 (2004); A. Liebsch, *ibid.* **90**, 096401 (2003); I. A. Nekrasov, G. Keller, D. E. Kondakov, A. V. Kozhevnikov, T. Pruschke, K. Held, D. Vollhardt, and V. I. Anisimov, *Phys. Rev. B* **72**, 155106 (2005).
- [26] E. Pavarini, A. Yamasaki, J. Nuss, and O. K. Andersen, *New J. Phys.* **7**, 188 (2005).
- [27] A. Scaramucci, J. Ammann, N. A. Spaldin, and C. Ederer, [arXiv:1405.3804](#).
- [28] Y. Shi, Y. Guo, Y. Shirako, W. Yi, X. Wang, A. A. Belik, Y. Matsushita, H. L. Feng, and Y. Tsujimoto, M. Arai *et al.*, *J. Am. Chem. Soc.* **135**, 16507 (2013).
- [29] P. Hansmann, N. Parragh, A. Toschi, G. Sangiovanni, and K. Held, *New J. Phys.* **16**, 033009 (2014).
- [30] Z. Zhong, A. Toth, and K. Held, *Phys. Rev. B* **87**, 161102(R) (2013).
- [31] Note that t in Eq. (5) is $|t| \sim 2|t_{dpp}|$ since the former denotes the hopping between d and O orbitals, and the latter between d and p .
- [32] We checked for convergence and errors with respect to the number of Wannierization k points, the size of the real-space cell, the number of real-space support points, and shifts of these support points. The accuracy of integrals is $\lesssim 0.2\%$.
- [33] J. Mravlje, M. Aichhorn, T. Miyake, K. Haule, G. Kotliar, and A. Georges, *Phys. Rev. Lett.* **106**, 096401 (2011).
- [34] L. Vaugier, H. Jiang, and Silke Biermann, *Phys. Rev. B* **86**, 165105 (2012).
- [35] Y. C. Lan, X. L. Chen, and A. He, *J. Alloys Compd.* **354**, 95 (2003).
- [36] K. Haule and G. Kotliar, *New J. Phys.* **11**, 025021 (2011).
- [37] A. N. Rubtsov and A. I. Lichtenstein, *JETP Lett.* **80**, 61 (2004); P. Werner, A. Comanac, L. de'Medici, M. Troyer, and A. J. Millis, *Phys. Rev. Lett.* **97**, 076405 (2006); E. Gull, P. Werner, O. Parcollet, and M. Troyer, *Europhys. Lett.* **82**, 57003 (2008); E. Gull, A. J. Mills, A. I. Lichtenstein, A. N. Rubtsov, M. Troyer, and P. Werner, *Rev. Mod. Phys.* **83**, 349 (2011).
- [38] N. Parragh, A. Toschi, K. Held, and G. Sangiovanni, *Phys. Rev. B* **86**, 155158 (2012).
- [39] The signs of the hopping amplitudes reported here are as they would appear in a Hamiltonian matrix, i.e., without the extra sign of “ $-t$.”
- [40] F. Aryasetiawan, M. Imada, A. Georges, G. Kotliar, S. Biermann, and A. I. Lichtenstein, *Phys. Rev. B* **70**, 195104 (2004); T. Miyake, F. Aryasetiawan, and M. Imada, *ibid.* **80**, 155134 (2009); M. Hirayama, T. Miyake, and M. Imada, *ibid.* **87**, 195144 (2013); M. Imada and T. Miyake, *J. Phys. Soc. Jpn.* **79**, 112001 (2010).
- [41] J. M. Tomczak, M. Casula, T. Miyake, F. Aryasetiawan, and S. Biermann, *Europhys. Lett.* **100**, 67001 (2012); C. Taranto, M. Kaltak, N. Parragh, G. Sangiovanni, G. Kresse, A. Toschi, and K. Held, *Phys. Rev. B* **88**, 165119 (2013); M. Hirayama, T. Miyake, and M. Imada, *ibid.* **87**, 195144 (2013).

Unfolding the band structure of disordered solids: From bound states to high-mobility Kane fermions

O. Rubel,^{1,2,*} A. Bokhanchuk,¹ S. J. Ahmed,³ and E. Assmann⁴

¹Thunder Bay Regional Research Institute, 980 Oliver Road, Thunder Bay, Ontario, Canada P7B 6V4

²Department of Physics, Lakehead University, 955 Oliver Road, Thunder Bay, Ontario, Canada P7B 5E1

³Department of Materials Science and Engineering, McMaster University, Hamilton, Ontario, Canada L8S 4L8

⁴Institute for Solid State Physics, Vienna University of Technology, Wiedner Hauptstraße 8-10, 1040 Vienna, Austria

(Received 16 May 2014; revised manuscript received 14 August 2014; published 4 September 2014)

Supercells are often used in *ab initio* calculations to model compound alloys, surfaces, and defects. One of the main challenges of supercell electronic structure calculations is to recover the Bloch character of electronic eigenstates perturbed by disorder. Here we apply the spectral weight approach to unfolding the electronic structure of group III-V and II-VI semiconductor solid solutions. The illustrative examples include formation of donorlike states in dilute Ga(PN) and associated enhancement of its optical activity, direct observation of the valence band anticrossing in dilute GaAs:Bi, and a topological band crossover in ternary (HgCd)Te alloy accompanied by emergence of high-mobility Kane fermions. The analysis facilitates interpretation of optical and transport characteristics of alloys that are otherwise ambiguous in traditional first-principles supercell calculations.

DOI: [10.1103/PhysRevB.90.115202](https://doi.org/10.1103/PhysRevB.90.115202)

PACS number(s): 71.15.Mb, 71.20.Nr, 71.23.-k, 71.55.Eq

I. INTRODUCTION

Electronic energy eigenstates of periodic solids are traditionally represented by Bloch waves $\psi_{n,\mathbf{k}}(\mathbf{r})$ with a wave vector \mathbf{k} describing the translational periodicity of a given state. Existence of the well defined wave vector in periodic structures has important consequences for their optical and transport properties imposed in the form of selection rules for inter- and intraband transitions. Therefore, the vast majority of existing theoretical studies that focus on the electronic band structure of solids use a primitive basis (or Bloch) representation.

In reality, the ideal translational periodicity of solids is disturbed by disorder in the form of structural defects, fluctuations of the chemical composition in compound alloys, magnetic disorder, or even the lack of long-range order in noncrystalline solids. The disorder can significantly alter electronic structure of solids resulting in the emergence of properties that are strikingly different from their nominal constituencies [1]. For example, electronic states associated with substitutional impurities can facilitate optical transitions in otherwise indirect semiconductors [2]. Modeling of disordered structures requires construction of supercells that greatly exceed the size of a primitive basis. Since the Brillouin zone (BZ) shrinks as a result of the zone folding, the recovery of a dispersion relation $\epsilon(\mathbf{k})$ in the momentum-energy space becomes nontrivial.

The most successful approach that links the supercell band structure with the primitive basis representation is based on a Bloch spectral density [3,4], which is also known as a “spectral weight” [5–7]. The spectral weight $w_n(\mathbf{k})$ amounts to a Bloch \mathbf{k} character of the n th energy eigenstates ϵ_n and fulfills the normalization $\sum_{\mathbf{k}} w_n(\mathbf{k}) = 1$. For symmetric structures, the Bloch wave vector \mathbf{k}_B is unambiguously defined, i.e., $w_n(\mathbf{k}) = \delta(\mathbf{k} - \mathbf{k}_B)$. In supercells with a broken symmetry, the energy eigenstate is characterized by broadening of $w_n(\mathbf{k})$. In the ultimate extreme of spatially localized states, the uncertainty

approaches its fundamental limit of $\Delta k \sim r_B^{-1}$, where r_B is the localization radius.

The spectral weight can be obtained by a Fourier transformation of local basis functions, such as atomic orbitals [6,8,9], Wannier functions [10–17], or projected local orbitals [18]. In the case of a nonlocal basis set, such as plane waves, the spectral weight can be constructed from the Fourier expansion coefficients by gathering them in groups associated with a particular Bloch wave vector [2,7,19–21]. The latter approach is the most straightforward for implementation in solid-state *ab initio* electronic structure codes, since the plane wave (PW) expansion coefficients are readily available in pseudopotential or full-potential packages.

Here we apply the spectral weight approach to unfolding of the electronic structure of group III-V and II-VI semiconductor solid solutions obtained in the framework of density functional theory with the all-electron WIEN2K package [22]. For illustration, we investigate (i) formation of donorlike states in dilute GaP:N and associated enhancement of its optical activity, (ii) direct observation of the valence band anticrossing in dilute GaAs:Bi, and (iii) a topological band crossover in a bulk (HgCd)Te compound alloy and related formation of high-mobility Kane fermions. These features, which would have been difficult to identify in standard band structure calculations, become apparent in the unfolded band structures produced by our method.

II. UNFOLDING PROCEDURE

Our approach to the calculation of the spectral weight is based on remapping the supercell reciprocal space with a mesh that is compatible with the translational symmetry of a primitive cell [2,19,23]. Here we briefly review the basics of this method.

The PW expansion alone

$$\Psi_{n,\mathbf{k}}(\mathbf{r}) = \sum_{\mathbf{G}} C_{n,\mathbf{K}}(\mathbf{G}) e^{i(\mathbf{K}+\mathbf{G})\cdot\mathbf{r}} \quad (1)$$

*rubelo@tbh.net

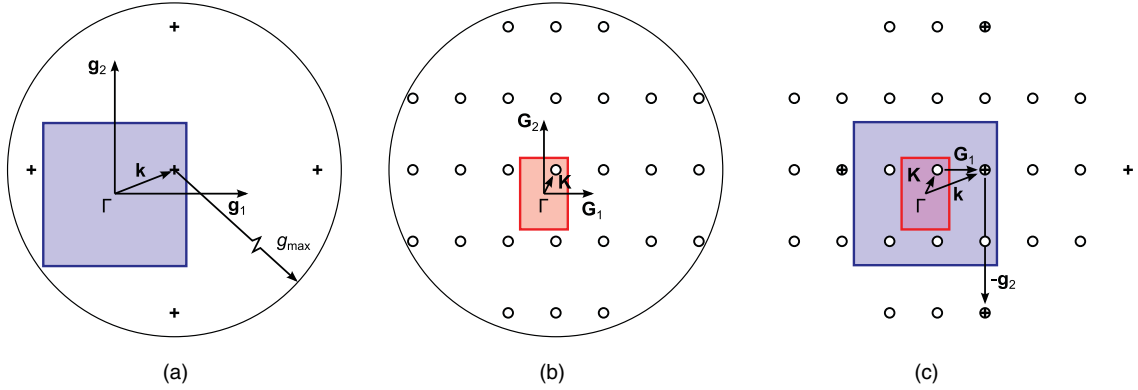


FIG. 1. (Color online) Relation between k mesh in the reciprocal space for a square primitive lattice (a) and that for a 3×2 supercell (b). The first BZ is outlined on both panels. The overlay of both patterns is shown on the panel (c). The overlapped points form a subgroup of \mathbf{K} that represents the Bloch wave vector \mathbf{k} . There is a total of six subgroups (3×2), which indicates that each K point in the supercell bears information about six k points of the primitive basis.

or its combination with a local basis set (such as augmented plane waves) is a popular choice for representing wave functions in periodic solids. Here n refers to a particular eigenstate (band index), \mathbf{K} is the wave vector within the first BZ, and C are expansion coefficients. The summation runs over a set of K points repeated with periodicity of the reciprocal lattice vectors \mathbf{G}_1 , \mathbf{G}_2 , and \mathbf{G}_3 . The plane wave cutoff G_{\max} determines the range of the summation and, therefore, the completeness of the basis set. The general form of expansion (1) is identical irrespective of whether a supercell or a primitive cell basis is used. We will employ upper-case and lower-case notations in order to distinguish between these two cases, respectively.

Figures 1(a) and 1(b) illustrate the reciprocal space mesh in two dimensions for a primitive cubic lattice and its supercell of the size 3×2 . Each point on this mesh is associated with an individual PW, and can be assigned a relative “weight” of $|C_{n,\mathbf{K}}(\mathbf{G})|^2$. When the two meshes corresponding to the primitive cell and supercell overlay as shown in Fig. 1(c), it is possible to match the supercell \mathbf{K} and the primitive Bloch wave \mathbf{k} PW expansion coefficients

$$C_{n,\mathbf{K}}(\mathbf{G}) \rightarrow c_{n,\mathbf{k}}(\mathbf{g}) \quad (2)$$

at the points which fulfill

$$\mathbf{K} + \mathbf{G} = \mathbf{k} + \mathbf{g}. \quad (3)$$

As can be seen in Fig. 1(c), any K point transforms into $N_1 N_2 N_3$ k points in the first primitive BZ under the translation

$$\mathbf{k} = \mathbf{K} + m_1 \mathbf{G}_1 + m_2 \mathbf{G}_2 + m_3 \mathbf{G}_3, \quad (4)$$

with $m_i = 0, 1, \dots, N_i - 1$ that extends up to the scaling factor N_i used when constructing the supercell along i 's axis. This generates a multitude of “unfolded” Bloch wave vectors, each with its own subgroup of the PW expansion coefficients $C_{n,\mathbf{K}}(\mathbf{k} + \mathbf{g})$. Thus the individual weights of unfolded k points are expressed in terms of the PW coefficients which belong to the subgroup of \mathbf{k} ,

$$w_n(\mathbf{k}) = \sum_{\mathbf{g}} |C_{n,\mathbf{K}}(\mathbf{k} + \mathbf{g})|^2. \quad (5)$$

Note that the subgroups are formed by the translation vectors \mathbf{g} , not \mathbf{G} . In order to facilitate the mapping, the supercell needs to be generated by translation of the *primitive cell* along its lattice vectors in real space, which implies a simple relation between the reciprocal lattice vectors $\mathbf{g}_i = m_i \mathbf{G}_i$. If the latter is not the case, an additional coordinate transformation ($m_i \mathbf{G}_i \rightarrow \mathbf{g}_i$) is required for the resultant wave vectors \mathbf{k} given by Eq. (4).

III. APPLICATIONS

A. Dilute GaP:N

Group III-V dilute nitride semiconductors continue to be in the focus since the 1990s as a material system for long-wavelength telecommunication and photovoltaic applications [24,25]. In spite of the fact that nitrides (GaN and AlN) are wideband-gap semiconductors, addition of a small fraction of nitrogen (a few percent) in the host III-V semiconductors, e.g., GaAs, results in a drastic reduction of their energy gap. This narrowing of the band gap is attributed to an anticrossing between extended states of the host conduction band and the localized nitrogen resonant states [26].

Ga(NP) was a progenitor of modern dilute nitrides [27]. It was shown that nitrogen and its complexes behave in GaP as isoelectronic traps by creating a tail of localized states in the vicinity of the conduction band edge [28]. The nitrogen-related states facilitate radiative recombination of optical excitations, which is otherwise suppressed due to the indirect band structure of GaP [29]. However, it should be noted that disorder also introduces nonradiative channels that have an adverse effect on the internal quantum efficiency of light-emitting devices [30,31]. These are the main features of Ga(NP), which will be used as a benchmark in order to prove the validity of the proposed method.

The band structure of GaP is presented in Fig. 2(a). (Computational details are provided in the Appendix.) The calculated band structure reproduces experimental features of the GaP band structure, namely, the indirect band gap with the conduction band minimum along Δ path near X point followed by L and Γ valleys in the direction of increasing the electron energy (see Ref. [32], pp. 198–199). Our calculations do not purport to reproduce an experimental value of the band gap in

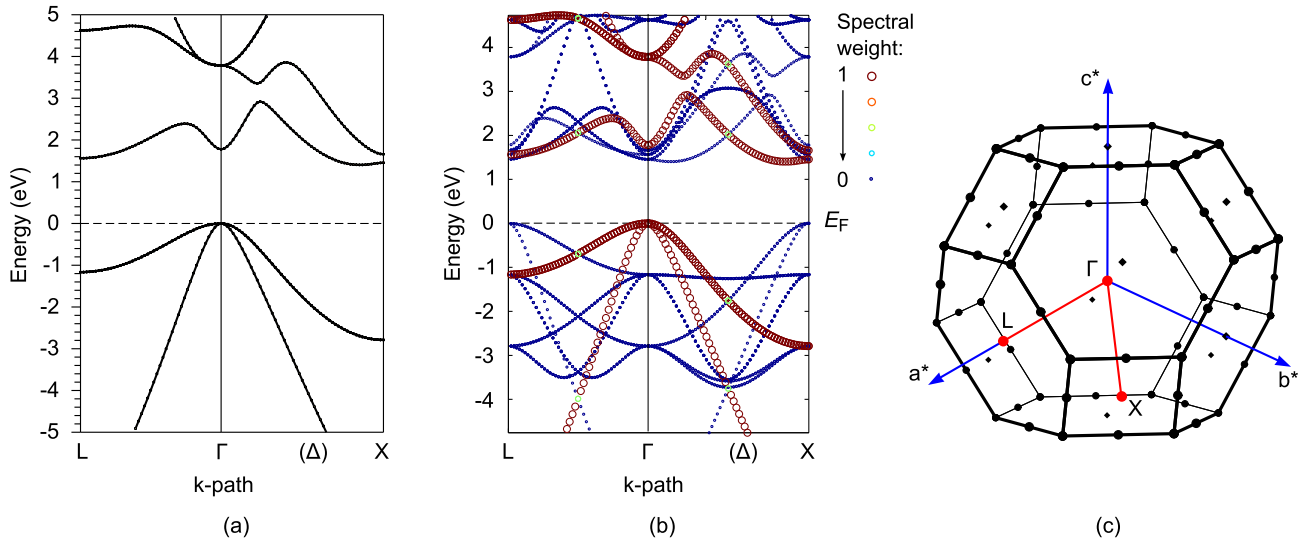


FIG. 2. (Color online) Band structure of GaP: 2-atom primitive unit cell (a) and 16-atom $2 \times 2 \times 2$ supercell (b). The supercell band structure is “obfuscated” due to the zone folding. Fat bands on panel (b) illustrate the unfolded band structure where the symbols size and color represent the Bloch spectral weight. Both cells have the Brillouin zone shown on panel (c). Here and in all figures hereafter the Fermi energy is set to zero.

GaP. The calculated energy gap of GaP is only about 60% of its experimental value, which is due to a shortcoming of the density functional theory (DFT) in its Kohn-Sham formulation [33]. This drawback is not critical for the purpose of our study since qualitative prediction of the optical emission spectrum is beyond the scope of our work. Next, we repeat the band structure calculation for a 16-atom supercell of GaP. Results are presented in Fig. 2(b), which exemplifies a zone folding

that hinders analysis of the band structure of supercells. Even for such a comparatively small supercell ($2 \times 2 \times 2$), the direct or indirect character of the band gap is obscured.

Now we apply the procedure described in Sec. II in the attempt to recover the GaP band structure in its conventional Bloch representation from a 128-atom supercell. The unfolded band structure is shown in Fig. 3(a) and can be directly compared to that in Fig. 2(a), including the indirect band gap

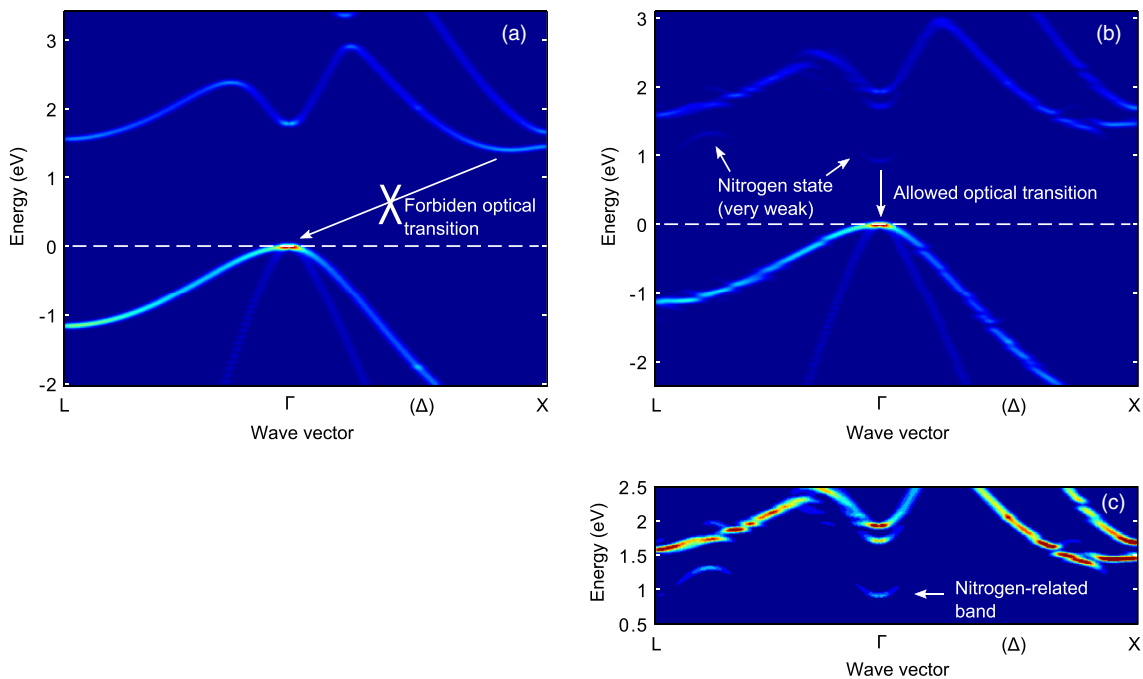


FIG. 3. (Color online) Band structure of $\text{Ga}_{64}\text{P}_{64}$ (a) and $\text{Ga}_{64}\text{N}_1\text{P}_{63}$ (b),(c) supercell unfolded to the primitive Bloch representation. A very weak signature of a nitrogen-related conduction band can be seen within the GaP energy gap (b). Panel (c) shows a snapshot of $\text{Ga}_{64}\text{N}_1\text{P}_{63}$ conduction band with the contrast artificially enhanced by using a nonlinear (square root) intensity scale. The nitrogen band introduces a direct optical transition (b) thereby stimulating radiative optical transitions in Ga(NP) [29].

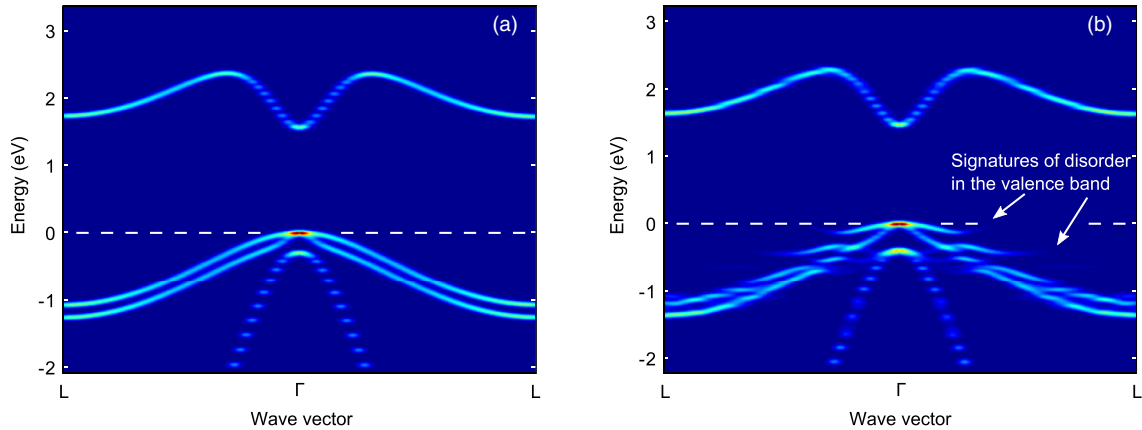


FIG. 4. (Color online) Band structure of $\text{Ga}_{64}\text{As}_{64}$ (a) and $\text{Ga}_{64}\text{As}_{63}\text{Bi}_1$ (b) supercells unfolded to the primitive Bloch representation. Bismuth incorporation leads to perturbations in the valence band, reduction of the band gap, and enhanced spin-orbit splitting.

and ordering of valleys in the conduction band. It is important to note that all points are sharp within the limit of a Gaussian smearing applied. This feature is inherent to Bloch states with a well defined wave vector \mathbf{k} , as anticipated for a structure in the absence of a disorder. The brightness of the spots is determined by the magnitude of the corresponding Bloch character as well as by the degeneracy. The distinct brightness of the valence and conduction bands in Fig. 3(a) is due to a degeneracy of the corresponding eigenvalues. This band structure will be used as a reference when studying effects of disorder.

The symmetry of GaP supercell is then disturbed by introducing nitrogen as an isoelectronic substitutional impurity. The unfolded band structure of $\text{Ga}_{64}\text{N}_1\text{P}_{63}$ is shown in Fig. 3(b). Nitrogen incorporation results in the emergence of a new band beneath the host conduction band of GaP. At the same time, the valence band remains almost unperturbed. The nitrogen-related states are better seen in Fig. 3(c) where the conduction band region is shown with enhanced contrast. Contrary to the extended states of GaP, the nitrogen states do not have a well defined \mathbf{k} and they are only weakly present at the Γ point. These results are consistent with the localized nature of nitrogen states in GaP and confirm their role as recombination centers for optical excitations, albeit slow and inefficient [28,34].

The intrinsic limitations of dilute Ga(NP) stimulated exploration of alternative materials for room-temperature optical emitters. Ga(NAsP) is one of the recent developments in the family of dilute nitrides that holds promise for the realization of monolithic optoelectronic integrated circuits on silicon substrates [35,36].

It is important to acknowledge that study of random alloys using small supercells without proper configurational averaging may result in artifacts observed in the unfolded band structure due to a periodic ordering [18]. This indicates a need to test convergence of the resultant band structure with respect to the size of the supercell as well as the number of random configurations. At this point, the simulation scale may become computationally prohibitive for DFT. Development of an effective Hamiltonian, which incorporates effects of compositional disorder, based on first-principles Wannier functions

[13] is an efficient technique that enables one to overcome this limitation. Furthermore, the configurational averaging can be expedited by constructing special quasirandom structures with relevant radial correlation functions tailored to match a perfectly random structure [37].

B. Dilute GaAs:Bi

The above example of Ga(NP) shows that incorporation of nitrogen is responsible for the modulation of the conduction band in the host semiconductor. Alloying of GaAs with bismuth has been proposed as a complementary approach for engineering of the valence band [38]. Reduction of the band gap in Ga(AsBi) is explained using a semiempirical valence band anticrossing model [39]. The model is similar in spirit to the band anticrossing of dilute nitrides [26]. Recent electronic structure calculations of $\text{GaAs}_{1-x}\text{Bi}_x$ [40] performed beyond the popular band anticrossing model provide important insight to the structure of the valence band. However, the valuable link between electronic eigenstates of the alloy and their dispersion characteristics is overlooked in this analysis. This relation can be recovered using the unfolding procedure.

The band structures of GaAs and $\text{Ga}_{64}\text{As}_{63}\text{Bi}_1$ are shown in Fig. 4. Their comparison allows us to draw the following conclusions: (i) incorporation of Bi in GaAs mostly affects the valence band, (ii) no bound states are found above the valence band edge of the host GaAs, and (iii) the energy gap shrinks along with enhancement of the spin-orbit splitting. These features are consistent with the experimental trends [39] and prediction from first principles of bismuth-related signatures of localization *beneath* the host valence band maximum [40].

Finally, we would like to emphasize a fundamental difference between $\text{GaAs}_{1-x}\text{Bi}_x$ and the majority of other group III-V ternary semiconductors, including $\text{GaAs}_{1-x}\text{Sb}_x$ alloy. GaBi is a metal with an anomalous order of bands [41], which is reminiscent of the better known α -Sn with a band inversion or negative band gap caused by spin-orbit effects [42]. Thus the electronic structures of GaAs and GaBi have different topology, which is not the case in GaAs-GaSb,

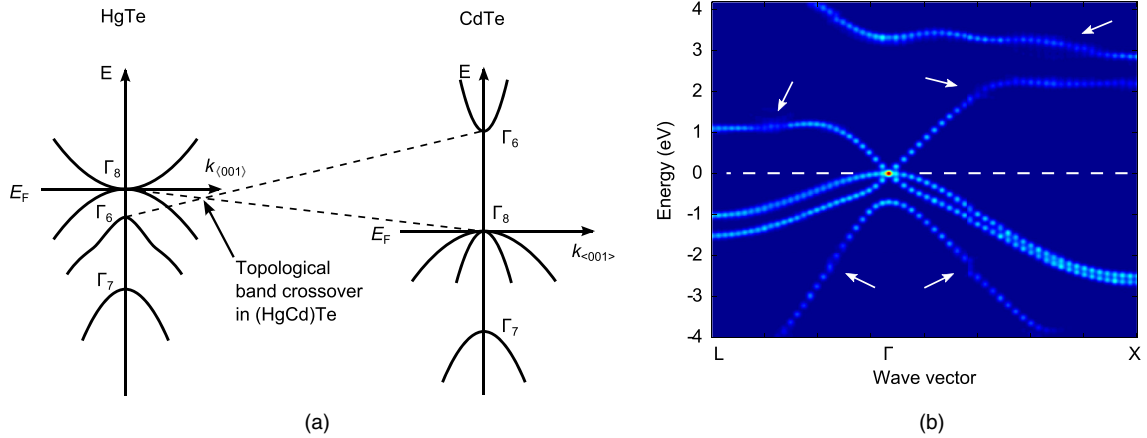


FIG. 5. (Color online) Band order and symmetry labels for HgTe and CdTe compounds (a). These two compounds exhibit a band inversion ($\Gamma_6 \leftrightarrow \Gamma_8$) and, thus, have different “topology.” As the composition $\text{Hg}_{1-x}\text{Cd}_x\text{Te}$ varies between two binary compounds, a topological band crossover occurs. The crossover takes place near $x_c \approx 0.19$ and is accompanied by emergence of massless Kane fermions at the Γ point (b). Regions of the band structure perturbed by disorder are labeled with arrows. The disorder affects only the electronic states located 1–3 eV above and below the Fermi energy.

for instance. The electronic structure of $\text{GaAs}_{1-x}\text{Bi}_x$ cannot evolve “smoothly” in the range $0 < x < 1$ and must undergo a topological phase transition. This transition is accompanied by a gradual transformation of the host GaAs parabolic conduction band to a graphenelike cone with increasing x ; electrons ultimately become massless fermions as it will be shown later. Verification of this prediction would require electron transport measurements in $\text{GaAs}_{1-x}\text{Bi}_x$ for a wide range of x . So far, the successful incorporation of Bi in GaAs under 12% has been reported [43]. The lattice mismatch of 12% between GaAs and GaBi is one of the main factors that limits their solubility.

C. (HgCd)Te alloy

$\text{Hg}_{1-x}\text{Cd}_x\text{Te}$ (HCT) is an example of a material system with the topological band inversion [44], which is similar to $\text{GaAs}_{1-x}\text{Bi}_x$ discussed in the preceding Sec. III B. The

arrangement of bands in binary HgTe and CdTe as well as their symmetry are shown at Fig. 5(a). The conduction band minimum and the valence band maximum of CdTe have Γ_6 and Γ_8 symmetries, respectively. In HgTe, the order of bands is inverted due to a strong spin-orbit interaction [45]. The crossover between the Γ_6 and Γ_8 bands is inevitable in the course of a gradual change in the composition of ternary $\text{Hg}_{1-x}\text{Cd}_x\text{Te}$ alloy as illustrated by dashed lines in Fig. 5(a). The prominent feature of HCT is the presence of massless Kane fermions [46] at the crossover composition [Fig. 5(b)], whose experimental observation was recently reported by Orlita *et al.* [47].

The evolution of the $\text{Hg}_{1-x}\text{Cd}_x\text{Te}$ band structure as a function of composition is shown in Fig. 6. The composition range was chosen to cover the transition from a semimetal with a negative band gap to an insulator. The negative gap gradually shrinks with increasing the Cd content [Fig. 6(a)] until threefold degeneracy is established at a critical composition

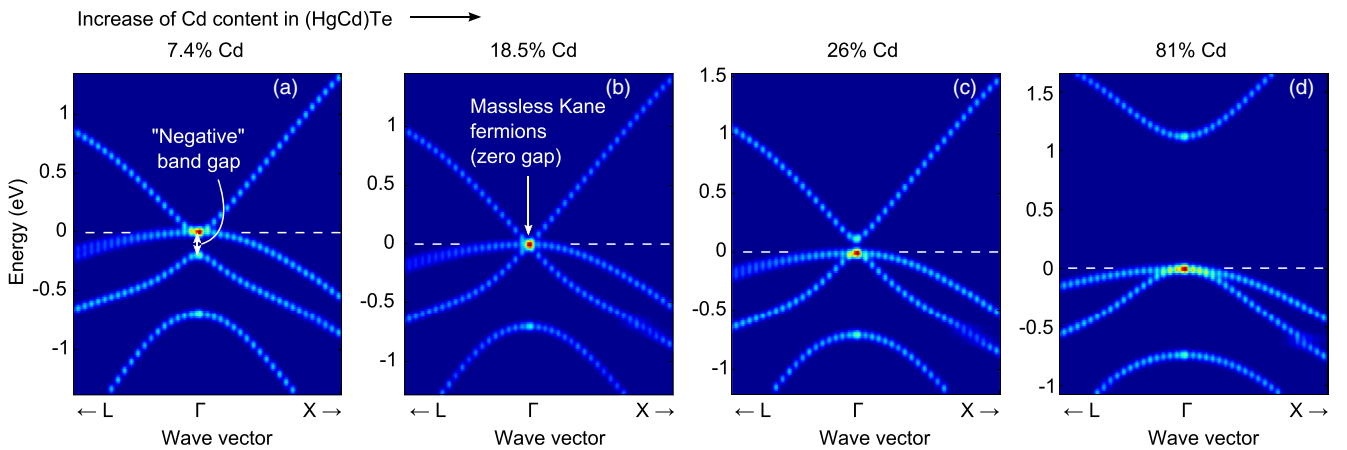


FIG. 6. (Color online) Evolution of the band structure in ternary (HgCd)Te alloy near the Γ point as a function of the chemical composition: $\text{Hg}_{25}\text{Cd}_2\text{Te}_{27}$ (a), $\text{Hg}_{22}\text{Cd}_5\text{Te}_{27}$ (b), $\text{Hg}_{20}\text{Cd}_7\text{Te}_{27}$ (c), and $\text{Hg}_5\text{Cd}_{22}\text{Te}_{27}$ (d). The transition from a semimetal (a) to an insulator (c),(d) occurs by passing through a Kane point (b). The nearly linear dispersion $E \propto |\mathbf{k}|$, which is characteristic of the Kane point, persists in the conduction band after opening of the band gap (c).

[Fig. 6(b)]. At this composition, the light hole and electron masses vanish near Γ as it is evident from the conical shape of their dispersion. Orlita *et al.* [47] stressed that Kane fermions are not protected by symmetry, unlike Dirac fermions. The emergence of Kane fermions corresponds to a critical chemical composition x_c . The critical composition is sensitive to extrinsic factors, such as temperature and pressure.

The band structure calculations yield the critical cadmium content of $x_c \approx 0.19 \pm 0.04$ vs $0.15\text{--}0.17$ observed experimentally [48]. The modest level of discrepancy is largely due to success of the Tran-Blaha modified Becke and Johnson (mBJ) exchange potential [49] in correcting the energy gap error introduced in regular LDA (local density approximation) calculations. The LDA-mBJ values of the band gap in binary CdTe and HgTe are 1.56 and -0.25 eV, respectively, compared to their experimental values of 1.65 and -0.3 eV [48]. It is interesting that LDA-mBJ accurately reproduces not only the energy gap for insulators, but also performs well for semimetals. Without mBJ potential, the LDA results for the band gap in CdTe and HgTe are 0.3 and -0.8 eV. The Kane fermions can still be observed, but the critical concentration is heavily shifted towards Cd-rich composition $x_c \approx 0.8$.

Further increase of the cadmium content beyond x_c leads to a narrow-gap semiconductor with a highly non-parabolic conduction band [compare Figs. 6(c) and 6(d)]. Apparently, there is no ambiguity in the Bloch character for all states near the Fermi energy irrespective of the $\text{Hg}_{1-x}\text{Cd}_x\text{Te}$ composition (Fig. 6). This result indicates that charge transport characteristics of HCT do not degrade as a result of the alloy scattering as dramatically as in dilute nitride semiconductors [50]. Our results explain the previously established experimental facts for HCT, such as the exceptional electron mobility exceeding $10^5 \text{ cm}^2 \text{ V}^{-1} \text{ s}^{-1}$ at low temperature [51] with its maximum value of $\sim 10^6 \text{ cm}^2 \text{ V}^{-1} \text{ s}^{-1}$ at the composition that corresponds to the topological band crossover [52].

There are two arguments why the disorder has such a mild effect on the band structure of $\text{Hg}_{1-x}\text{Cd}_x\text{Te}$. First, Hg and Cd have almost identical atomic radii that results in no local lattice distortions when one element is interchanged by the other. Second, both elements have almost identical energy levels of their valence s and p electrons which leads to comparable electronegativity of the two elements. None of these conditions apply to Ga(PN) or Ga(AsBi) alloys. As a result, their band structure is heavily perturbed by the disorder.

IV. CONCLUSIONS

Effects of alloying on the electronic structure of Ga(NP), Ga(AsBi), and (HgCd)Te were studied from first principles. Particular emphasis was placed on the Bloch character of the energy bands, which is evaluated using a Bloch spectral function technique specially tailored to the density functional full-potential package WIEN2K. The success of the theory in predicting chemical trends is validated by reproducing well-known properties of dilute GaP:N. The calculations yield a nitrogen-related band near the bottom of the host

GaP conduction band. A simultaneous enhancement of the optical activity observed in GaP:N is attributed to a weak Γ character of nitrogen-related states within the band gap of GaP.

In contrast to the role of nitrogen, incorporation of bismuth in GaAs leads to perturbations in the valence band without any noticeable degradation of the conduction band. The valence band dispersion in the energy range of $0\text{--}0.6$ eV below the Fermi energy is significantly affected by disorder. Uncertainties in the Bloch character of those states indicate the lost approximate translational symmetry of the host GaAs. Based on the analogy between GaAs-GaBi and CdTe-HgTe material systems, it is anticipated that the electron effective mass will be reduced as the bismuth content grows. This trend is common to all compound alloys that combine a semiconductor and a semimetal with the topological band inversion.

A topological band crossover was illustrated by the example of a bulk ternary (HgCd)Te alloy, which manifests in the formation of high-mobility Kane fermions previously reported experimentally. The massless dispersion develops at the composition that corresponds to the semimetal-insulator transition. In contrary to Ga(NP) and Ga(AsBi), the compositional disorder practically does not disturb the bottom of the conduction band and the top of the valence band in (HgCd)Te, which translates to its exceptional charge transport characteristics.

ACKNOWLEDGMENTS

The authors are indebted to Professor Marek Niewczas and Professor Peter Blaha for stimulating discussions and critical reading of the manuscript. O.R. and S.J.A. would like to acknowledge funding provided by the Natural Sciences and Engineering Research Council of Canada under the Discovery Grant Program No. 386018-2010; E.A. acknowledges the support from a “Vienna University of Technology innovative project grant.”

APPENDIX: COMPUTATIONAL DETAILS

The first-principles calculations were carried out using density functional theory and the linear augmented plane wave method implemented in the WIEN2K package [22]. The local density approximation [53] has been used for the exchange correlation functional. The Tran-Blaha modified Becke and Johnson (mBJ) potential [49] was applied to GaAs:Bi and (HgCd)Te compounds in order to improve their band gaps. Sampling of the Brillouin zone, muffin tin radii $R_{\text{min}}^{\text{MT}}$, the product $R_{\text{min}}^{\text{MT}} K_{\text{max}}$, which determines the accuracy of a plane wave expansion of the wave function, and other parameters are summarized in Table I.

The supercells were built on the basis of primitive cells instead of conventional ones. The self-consistent lattice constants a_0 of binary hosts were used in the calculations (Table I). Where indicated, the internal degrees of freedom were relaxed by minimizing Hellmann-Feynman forces acting on atoms below 2 mRy/bohrs. Calculations of the spectral weight were performed using FOLD2BLOCH package, which is available from GitHub.

TABLE I. Calculation parameters for the compounds studied.

Parameters	GaP:N	GaAs:Bi	Hg _{27-x} Cd _x Te ₂₇
a_0 (Å)	5.41	5.61	6.41 ^a
Supercell size	4×4×4	4×4×4	3×3×3
Number of atoms	128	128	54
Muffin tin radii R^{MT} (bohr)	1.93 (Ga)	2.17 (Ga)	2.50 (Hg)
	1.93 (P)	2.06 (As)	2.50 (Cd)
	1.60 (N)	2.28 (Bi)	2.49 (Te)
Valence electrons	3d ¹⁰ 4s ² 4p ¹ (Ga)	3d ¹⁰ 4s ² 4p ¹ (Ga)	5p ⁶ 5d ¹⁰ 6s ² (Hg)
	3s ² 3p ³ (P)	3d ¹⁰ 4s ² 4p ³ (As)	4p ⁶ 4d ¹⁰ 5s ² (Cd)
	2s ² 2p ³ (N)	5d ¹⁰ 6s ² 6p ³ (Bi)	4d ¹⁰ 5s ² 5p ⁴ (Te)
Optimization of atomic positions	Yes	Yes	No ^b
Reciprocal k mesh	2×2×2	2×2×2	3×3×3
$R_{\text{min}}^{\text{MT}} K_{\text{max}}$	7	7	6
Spin-orbit coupling	No	Yes	Yes
Direction of magnetization	–	[001]	[001]
mBJ potential	No	Yes	Yes

^aThe binary average value of a_0 is used throughout the calculations due to a minor difference (less than 1%) in the unit cell volume between HgTe and CdTe.

^bForces did not exceed 2 mRy/bohrs.

- [1] C. Freysoldt, B. Grabowski, T. Hickel, J. Neugebauer, G. Kresse, A. Janotti, and C. G. Van de Walle, *Rev. Mod. Phys.* **86**, 253 (2014).
- [2] V. Popescu and A. Zunger, *Phys. Rev. Lett.* **104**, 236403 (2010).
- [3] J. S. Faulkner and G. M. Stocks, *Phys. Rev. B* **21**, 3222 (1980).
- [4] P. J. Durham, *J. Phys. F: Met. Phys.* **11**, 2475 (1981).
- [5] S. Baroni, S. de Gironcoli, and P. Giannozzi, *Phys. Rev. Lett.* **65**, 84 (1990).
- [6] T. G. Dargam, R. B. Capaz, and B. Koiller, *Phys. Rev. B* **56**, 9625 (1997).
- [7] L.-W. Wang, L. Bellaiche, S.-H. Wei, and A. Zunger, *Phys. Rev. Lett.* **80**, 4725 (1998).
- [8] T. B. Boykin and G. Klimeck, *Phys. Rev. B* **71**, 115215 (2005).
- [9] C.-C. Lee, Y. Yamada-Takamura, and T. Ozaki, *J. Phys.: Condens. Matter* **25**, 345501 (2013).
- [10] F. Giustino, J. R. Yates, I. Souza, M. L. Cohen, and G. Louie, *Phys. Rev. Lett.* **98**, 047005 (2007).
- [11] W. Ku, T. Berlijn, and C.-C. Lee, *Phys. Rev. Lett.* **104**, 216401 (2010).
- [12] S. Konbu, K. Nakamura, H. Ikeda, and R. Arita, *J. Phys. Soc. Jpn.* **80**, 123701 (2011).
- [13] T. Berlijn, D. Volja, and W. Ku, *Phys. Rev. Lett.* **106**, 077005 (2011).
- [14] T. Berlijn, C.-H. Lin, W. Garber, and W. Ku, *Phys. Rev. Lett.* **108**, 207003 (2012).
- [15] T. Berlijn, P. J. Hirschfeld, and W. Ku, *Phys. Rev. Lett.* **109**, 147003 (2012).
- [16] S. Konbu, K. Nakamura, H. Ikeda, and R. Arita, *Solid State Commun.* **152**, 728 (2012).
- [17] T. Berlijn, H.-P. Cheng, P. J. Hirschfeld, and W. Ku, *Phys. Rev. B* **89**, 020501 (2014).
- [18] M. W. Haverkort, I. S. Elfimov, and G. A. Sawatzky, [arXiv:1109.4036](https://arxiv.org/abs/1109.4036) [cond-mat.mtrl-sci].
- [19] V. Popescu and A. Zunger, *Phys. Rev. B* **85**, 085201 (2012).
- [20] P. B. Allen, T. Berlijn, D. A. Casavant, and J. M. Soler, *Phys. Rev. B* **87**, 085322 (2013).
- [21] P. V. C. Medeiros, S. Stafström, and J. Björk, *Phys. Rev. B* **89**, 041407 (2014).
- [22] P. Blaha, K. Schwarz, G. K. H. Madsen, D. Kvasnicka, and J. Luitz, WIEN2K: An Augmented Plane Wave + Local Orbitals Program for Calculating Crystal Properties, Karlheinz Schwarz, Techn. Universität Wien, Austria, 2001.
- [23] M. Chen and M. Weinert, *Nano Lett.*, doi:10.1021/nl502107v.
- [24] M. Kondow, K. Uomi, T. Kitatani, S. Watahiki, and Y. Yazawa, *J. Cryst. Growth* **164**, 175 (1996).
- [25] M. Kondow, K. Uomi, A. Niwa, T. Kitatani, S. Watahiki, and Y. Yazawa, *Jpn. J. Appl. Phys.* **35**, 1273 (1996).
- [26] W. Shan, W. Walukiewicz, J. W. Ager, E. E. Haller, J. F. Geisz, D. J. Friedman, J. M. Olson, and S. R. Kurtz, *Phys. Rev. Lett.* **82**, 1221 (1999).
- [27] D. G. Thomas and J. J. Hopfield, *Phys. Rev.* **150**, 680 (1966).
- [28] P. R. C. Kent and A. Zunger, *Phys. Rev. B* **64**, 115208 (2001).
- [29] W. O. Groves, A. H. Herzog, and M. G. Craford, US Patent No. 3,725,749 (1973).
- [30] I. A. Buyanova and W. M. Chen, *Physics and Applications of Dilute Nitrides* (Taylor & Francis, London, 2004), Chap. Recombination processes in dilute nitrides, pp. 255–280.
- [31] O. Rubel, S. D. Baranovskii, K. Hantke, B. Kunert, W. W. Ruhle, P. Thomas, K. Volz, and W. Stolz, *Phys. Rev. B* **73**, 233201 (2006).
- [32] S. Adachi, *Optical Constants of Crystalline and Amorphous Semiconductors: Numerical Data and Graphical Information* (Springer, New York, 1999).
- [33] W. Kohn and L. J. Sham, *Phys. Rev.* **140**, A1133 (1965).
- [34] T. Niebling, O. Rubel, W. Heimbrodt, W. Stolz, S. D. Baranovskii, P. J. Klar, and J. F. Geisz, *J. Phys.: Condens. Matter* **20**, 015217 (2008).

O. RUBEL, A. BOKHANCHUK, S. J. AHMED, AND E. ASSMANN

PHYSICAL REVIEW B **90**, 115202 (2014)

- [35] B. Kunert, K. Volz, J. Koch, and W. Stolz, *Appl. Phys. Lett.* **88**, 182108 (2006).
- [36] K. M. Yu, W. Walukiewicz, J. W. Ager, D. Bour, R. Farshchi, O. D. Dubon, S. X. Li, I. D. Sharp, and E. E. Haller, *Appl. Phys. Lett.* **88**, 092110 (2006).
- [37] A. Zunger, S.-H. Wei, L. G. Ferreira, and J. E. Bernard, *Phys. Rev. Lett.* **65**, 353 (1990).
- [38] S. Francoeur, M.-J. Seong, A. Mascarenhas, S. Tixier, M. Adamcyk, and T. Tiedje, *Appl. Phys. Lett.* **82**, 3874 (2003).
- [39] K. Alberi, O. D. Dubon, W. Walukiewicz, K. M. Yu, K. Bertulis, and A. Krotkus, *Appl. Phys. Lett.* **91**, 051909 (2007).
- [40] H.-X. Deng, J. Li, S.-S. Li, H. Peng, J.-B. Xia, L.-W. Wang, and S.-H. Wei, *Phys. Rev. B* **82**, 193204 (2010).
- [41] A. Janotti, S.-H. Wei, and S. B. Zhang, *Phys. Rev. B* **65**, 115203 (2002).
- [42] S. Kűfner, J. Furthműller, L. Matthes, and F. Bechstedt, *Nanotechnology* **24**, 405702 (2013).
- [43] Z. Batool, S. Chatterjee, A. Chernikov, A. Duzik, R. Fritz, C. Gogineni, K. Hild, T. J. C. Hosea, S. Imhof, S. R. Johnson *et al.*, *Molecular Beam Epitaxy: From Research to Mass Production* (Elsevier, Amsterdam, 2013), Chap. Bismuth-containing IIIeV semiconductors: Epitaxial growth and physical properties, pp. 139–158.
- [44] M. Z. Hasan and C. L. Kane, *Rev. Mod. Phys.* **82**, 3045 (2010).
- [45] W. Zawadzki, *Adv. Phys.* **23**, 435 (1974).
- [46] E. O. Kane, *J. Phys. Chem. Solids* **1**, 249 (1957).
- [47] M. Orlita, D. M. Basko, M. S. Zholudev, F. Teppe, W. Knap, V. I. Gavrilenko, N. N. Mikhailov, S. A. Dvoretiskii, P. Neugebauer, C. Faugeras *et al.*, *Nat. Phys.* **10**, 233 (2014).
- [48] A. Rogalski, *Rep. Prog. Phys.* **68**, 2267 (2005).
- [49] F. Tran and P. Blaha, *Phys. Rev. Lett.* **102**, 226401 (2009).
- [50] S. Fahy and E. P. O'Reilly, *Appl. Phys. Lett.* **83**, 3731 (2003).
- [51] D. D. Edwall, M. Zandian, A. C. Chen, and J. M. Arias, *J. Electron. Mater.* **26**, 493 (1997).
- [52] S. D. Yoo and K. D. Kwack, *J. Appl. Phys.* **81**, 719 (1997).
- [53] J. P. Perdew and Y. Wang, *Phys. Rev. B* **45**, 13244 (1992).

Oxide Heterostructures for Efficient Solar Cells

Elias Assmann,¹ Peter Blaha,² Robert Laskowski,² Karsten Held,¹ Satoshi Okamoto,^{3,*} and Giorgio Sangiovanni^{1,4}¹*Institute of Solid State Physics, Vienna University of Technology, 1040 Vienna, Austria*²*Institute of Materials Chemistry, Vienna University of Technology, 1040 Vienna, Austria*³*Materials Science and Technology Division, Oak Ridge National Laboratory, Oak Ridge, Tennessee 37831, USA*⁴*Institut für Theoretische Physik und Astrophysik, Universität Würzburg, 97074 Würzburg, Germany*

(Received 5 November 2012; published 11 February 2013)

We propose an unexplored class of absorbing materials for high-efficiency solar cells: heterostructures of transition-metal oxides. In particular, LaVO_3 grown on SrTiO_3 has a direct band gap ~ 1.1 eV in the optimal range as well as an internal potential gradient, which can greatly help to separate the photo-generated electron-hole pairs. Furthermore, oxide heterostructures afford the flexibility to combine LaVO_3 with other materials such as LaFeO_3 in order to achieve even higher efficiencies with band-gap graded solar cells. We use density-functional theory to demonstrate these features.

DOI: [10.1103/PhysRevLett.110.078701](https://doi.org/10.1103/PhysRevLett.110.078701)

PACS numbers: 88.40.fh, 73.20.At, 78.20.Bh

The stunning discovery by Ohtomo and Hwang [1,2] that the interface between the band insulators SrTiO_3 and LaAlO_3 (or LaTiO_3) can become conductive above a critical thickness of the latter opened the research field of layered oxide heterostructures. The interest comes not only from novel physical effects that are absent in the constituent bulk materials, but also from the perspective of designing and tuning specific properties to achieve desired functionalities. This flexibility becomes even more pronounced when materials with partially filled d shells, and hence strong electronic correlations, are involved [3,4]. In particular, these novel oxide heterostructures raise hope to surpass state-of-the-art semiconductors for specific applications. In this Letter, we propose high-efficiency solar cells as such an application.

The performance of photovoltaic systems is characterized by the efficiency η of conversion of the incident photon energy to electrical power. A natural limit for η is set by the optical gap Δ of the absorbing material: photons with energy $\hbar\omega < \Delta$ are not absorbed at all; those with $\hbar\omega > \Delta$ may be absorbed but each only contributes an amount of energy equal to Δ , with the difference being lost to relaxation processes, i.e., heat generation. This consideration, combined with further loss channels, leads to the famous Shockley-Queisser limit [5], which gives an upper bound for η as a function of Δ with $\eta \lesssim 34\%$ in the optimum range $\Delta = 1\text{--}1.5$ eV. In the case of semiconductors, a great effort now concentrates on the reduction of so-called Shockley-Read-Hall electron-hole recombination caused by defect-induced “trap” states and, in general, any intrinsic recombination mechanism. Even small improvements on the final efficiency of a solar cell have an immense economical and environmental impact, and are intensively pursued by industry [6,7].

Why oxide heterostructures?—There are four properties that make layered oxide heterostructures, and in particular $\text{LaVO}_3|\text{SrTiO}_3$, a promising candidate for efficient solar

cells (cf. Fig. 1): (i) an intrinsic electric field emerges in the photoabsorbing region, which may efficiently separate photoexcited electrons and holes; (ii) the band gap of 1.1 eV is direct and in the ideal energy range for harvesting the sunlight reaching the Earth’s surface; (iii) interfaces and surfaces can become metallic on a thickness of about

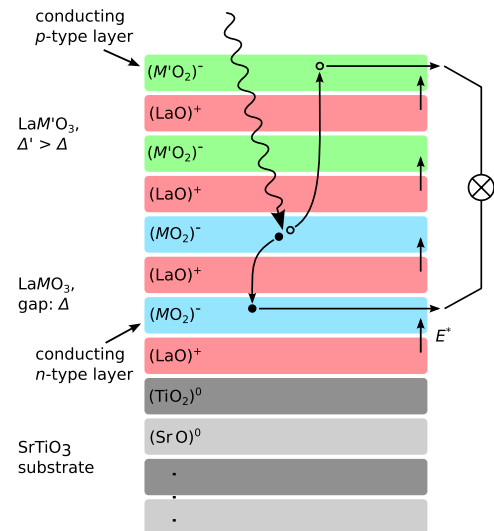


FIG. 1 (color online). Schematic of a gap-graded oxide-heterostructure solar cell. The cell shown here combines two absorber materials, generically, $\text{LaM}'\text{O}_3$ and LaMO_3 (M and M' being different transition metals); the compound with the larger band gap $\Delta' > \Delta$ should face the sun. Incoming photons with energy $\hbar\omega > \Delta'$ can be absorbed in the top material and contribute an energy Δ' , whereas those with $\Delta < \hbar\omega < \Delta'$ traverse the first part, which is transparent to them, and can be absorbed in the lower material, contributing an energy Δ . Once an electron-hole pair is dissociated, the built-in effective electric field E^* will drive the carriers to their respective contacts, which are naturally provided in the form of conducting surface and interface layers.

one unit cell, and those layers naturally allow for extracting the charge carriers; and (iv) one can flexibly combine different materials [8–12] and grow heterostructures with multiple band gaps, e.g., alternate LaVO_3 with LaFeO_3 in order to realize a so-called *band-gap graded* design [13]. By means of density-functional theory (DFT) calculations we establish these properties of $\text{LaVO}_3|\text{SrTiO}_3$ and, given the enormous flexibility offered by oxide heterostructures, we suggest them as a new candidate for efficient photovoltaic devices.

$\text{LaAlO}_3|\text{SrTiO}_3$ can be considered the prototype for the kind of heterostructure we consider here, and has attracted by far the most attention [14–18]. However, for our purposes $\text{LaVO}_3|\text{SrTiO}_3$ is more suitable since $\text{LaAlO}_3|\text{SrTiO}_3$ has a band gap of several electron volts, much too large for photovoltaics. Both heterostructures share a feature which is most interesting in relation to the electron-hole recombination problem: a polar interface with an intrinsic electric field. In LaVO_3 both La and V have nominal valence +3 such that the LaO planes are positively charged and the VO_2 planes are negatively charged, inducing an electric field between these layers (depicted schematically in Fig. 1; for quantitative results see Fig. 4 below). In the substrate SrTiO_3 , on the other hand, Sr has nominal valence +2 and Ti has +4, such that the SrO and TiO_2 planes are both charge neutral. Based on these simple considerations one expects a potential gradient induced by the polar discontinuity between LaVO_3 (or LaAlO_3) and SrTiO_3 [19]. DFT calculations for $\text{LaAlO}_3|\text{SrTiO}_3$ show that, in order to avoid this so-called *polarization catastrophe*, the polar discontinuity is partially compensated by electrons transferred from the top of the heterostructure to the interface, whereas a substantial gradient persists. Recently, a finite potential gradient has also been measured experimentally [20]. That said, such measurements are challenging, in particular because of the difficulty of controlling oxygen vacancies in LaAlO_3 (or, equally, LaVO_3), which may greatly influence the gradient.

The built-in electric field will support the separation of photogenerated electron-hole pairs and will drive the dissociated charge carriers selectively to the respective contacts for extraction. $\text{LaVO}_3|\text{SrTiO}_3$ combines this feature with a near-optimum direct band gap of 1.1 eV. Therefore, we concentrate on this structure in the present Letter.

Another advantage of the proposed oxide heterostructures for solar-cell applications is that electrical contacts to collect the photogenerated charge carriers are naturally provided. The (“*n*-type”; see below) $\text{LaVO}_3|\text{SrTiO}_3$ interface itself is metallic; in fact, it would be difficult to contact it otherwise. Our DFT calculations show that the surface layer is also metallic and, hence, suitable to extract the holes. However, surface defects and edges might localize the holes. Hence, careful surface preparation or even an additional metallic layer such as SrVO_3 or other metallic contacts will be necessary on the surface side.

Ab initio simulations of oxide solar cells.—We study structures with different numbers of LaO and VO_2 layers grown on the (001) surface of SrTiO_3 , considering both (i) periodically repeated arrangements containing one “*n*-type” ($\text{TiO}_2|[\text{LaO}]^+$) and one “*p*-type” ($\text{SrO}|[\text{VO}_2]^-$) interface and (ii) an *n*-type ($\text{TiO}_2|\text{LaO}$) interface with a slab of vacuum on top of the LaVO_3 part to break periodicity. These setups are termed (i) “multilayer” and (ii) “thin-film” geometries.

The DFT + U calculations were performed using the full-potential linearized augmented plane-wave code WIEN2K [21], with the PBEsol [22] and modified Becke-Johnson [23] exchange-correlation potential and a local Coulomb interaction term U on Ti, V, and Fe. The absorption coefficients in Fig. 5 were calculated using the optic code for WIEN2K [24]. See Supplemental Material [25] for technical details, including a discussion of excitonic effects.

We begin by showing one representative $\text{LaVO}_3|\text{SrTiO}_3$ structure, including the results from structural optimization and electronic self-consistency, in Fig. 2. As in the bulk [26,27], the $V-d$ electrons show staggered spin and orbital order. The spin order is of the *C* type (ferromagnetically coupled antiferromagnetic planes), while the orbital order is of the *G* type (alternating in all directions) [28]. The V and Ti contributions to the density of states for this case are shown in Fig. 3, in the energy range of the $V-d$ bands. These bands shift layer by layer, a first sign of the potential gradient. The gradient can be evidenced more clearly by tracking the energy of a core level throughout all layers, as shown in Fig. 4.

We estimate the potential slope in the LaVO_3 region to be $0.08 \text{ eV}/\text{\AA}$ (see Fig. 4). A similar potential slope is observed in the LaVO_3 region of thin-film structures (see Supplemental Material, Fig. 1 [25]). As the photocarrier excitation takes place in the LaVO_3 region, such a potential gradient inside LaVO_3 regions helps to efficiently separate photoexcited electrons and holes.

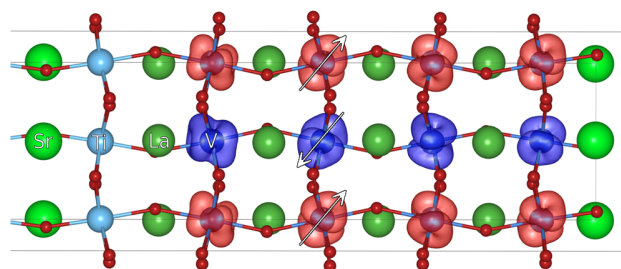


FIG. 2 (color online). Multilayer $\text{LaVO}_3|\text{SrTiO}_3$ heterostructure with 4 VO_2 planes. Superimposed on the relaxed structure, the red or blue (light or dark gray) lobes show isosurfaces of the positive or negative part of the spin-density $n_\uparrow - n_\downarrow$. Owing to the periodic repetition of the cell, both an *n*-type (left) and a *p*-type (right) interface appear. The substrate is only partly shown; altogether there are six Ti layers. As in bulk LaVO_3 , the $V-d$ electrons show AF-*C* spin order; for the central V layers, the AF-*G* orbital order is similarly preserved.

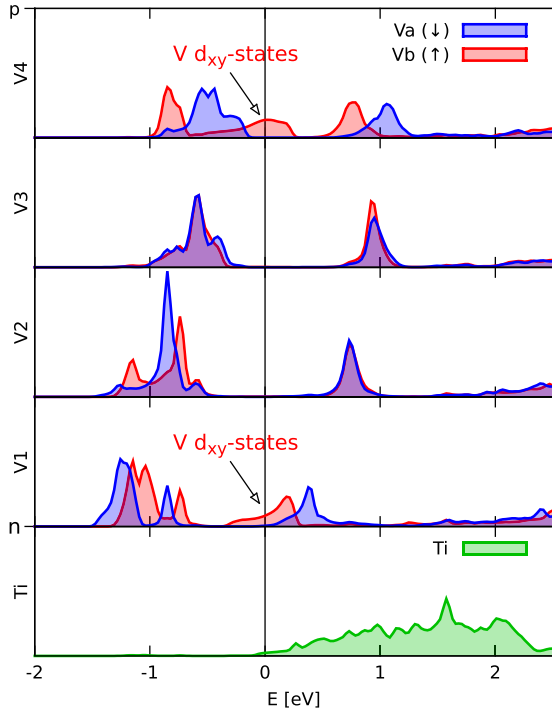


FIG. 3 (color online). Density of states of a multilayer $\text{LaVO}_3|\text{SrTiO}_3$ heterostructure. Each of the four VO_2 layers (V1-V4) contains two inequivalent V atoms [Va (darker shade) and Vb (lighter shade)] carrying opposite spin; the majority-spin V contribution is shown for each atom. For the Ti contribution (we show only the interfacial layer), the two spins as well as the two sites are essentially identical. These are the only relevant contributions around the Fermi level. Note the layer-by-layer shift of the bands which indicates the potential gradient, and the appearance of conducting states (of d_{xy} character, only in one spin channel) on the interfacial V.

For the multilayer heterostructure with four V layers, we observe the appearance of states at the Fermi level at the interfaces between LaVO_3 and SrTiO_3 . This confirms the scenario of metallic interfaces due to the electronic reconstruction found also in $\text{LaAlO}_3|\text{SrTiO}_3$ within DFT. Yet, contrary to $\text{LaAlO}_3|\text{SrTiO}_3$, the carriers reside not only on the Ti, but also on the V in accordance with recent experimental results [29]. The critical thickness that we find for multilayer $\text{LaVO}_3|\text{SrTiO}_3$ heterostructures at the DFT + U level is four. This result compares well with what has been reported in one experiment [30] and it is smaller than what was found in another experiment [29]. While any solar cell must have a band gap in order to generate electrical energy, conducting states that stay confined to the interface may in fact prove useful in extracting the photogenerated charge carriers.

Let us now turn to a central quantity for solar cell applications, the optical absorption (i.e., α in the Beer-Lambert law $I(r) \sim e^{-\alpha r}$, see Supplemental Material for details [25]), shown in Fig. 5. A major advantage of $\text{LaVO}_3|\text{SrTiO}_3$ heterostructures over the current standard absorber material is that, contrary to Si, the band gap in LaVO_3 is direct, such that photons carrying the band-gap energy can create electron-hole pairs without the aid of phonons or another indirect scattering processes. Furthermore, across most of the solar spectrum, bulk LaVO_3 compares favorably with CdTe, a direct-gap material currently used for high-efficiency, thin-film solar cells.

The validity of the absorption coefficient computed within DFT is confirmed by a comparison to experimental data on bulk LaVO_3 from Ref. [27]. Note that the first sharp peak in the theoretical curve is very sensitive to details of the crystal structure (in the limit of a cubic unit cell, it vanishes by symmetry). This might explain why it is

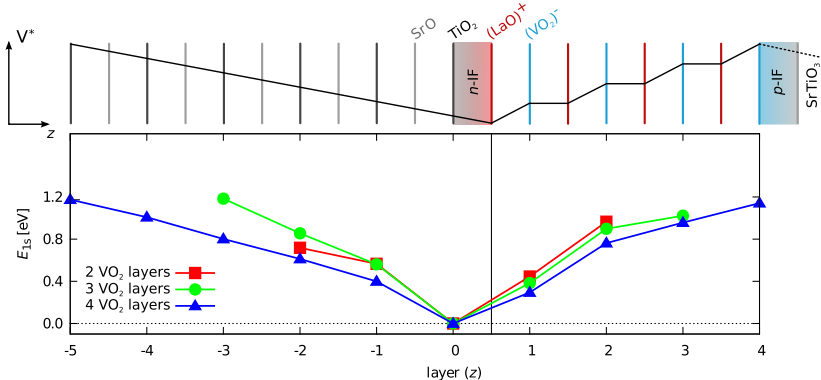


FIG. 4 (color online). Potential gradient in multilayer $\text{LaVO}_3|\text{SrTiO}_3$ heterostructures. The curves (squares, circles, and triangles distinguish structure size) track the energy of an O-1s state through the TiO_2 (layer ≤ 0) and VO_2 (layer > 0) layers, providing a measure of the potential gradient. Above the data, the layers, interfaces (IF), and effective electron potential V^* are shown schematically. Periodicity forces the potential to return to zero in the SrTiO_3 part after it has ramped up in the LaVO_3 part.

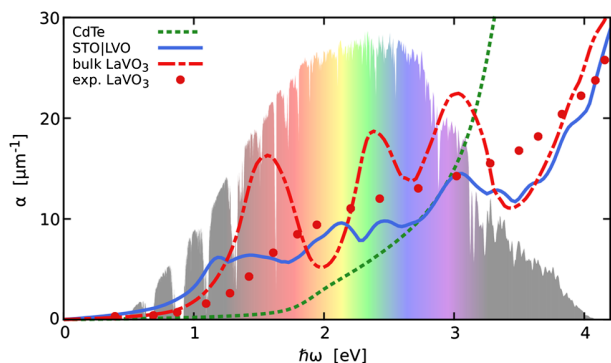


FIG. 5 (color online). Absorption coefficients and solar spectrum. The lines show the absorption coefficients of bulk LaVO_3 and $\text{LaVO}_3|\text{SrTiO}_3$ (for a multilayer structure with 2 V layers) compared to experimental data on bulk LaVO_3 [27] and a calculation for CdTe, which is widely used in current high-efficiency solar cells. In the background, the solar spectrum as measured on the Earth's surface is shown (standard global air mass 1.5, in arbitrary units).

absent in the experiment and in the heterostructure calculation.

$\text{LaVO}_3|\text{SrTiO}_3$ heterostructures have similar optical properties as bulk LaVO_3 , with the additional freedom that individual layers can have different band gaps owing to layer-dependent distortion and resulting crystal-field splittings. Another advantage of oxide heterostructures is that we can flexibly combine LaVO_3 with a second transition metal oxide with a somewhat larger band gap, such as LaFeO_3 , improving the conversion efficiency in the high-energy region of the solar spectrum. Thus one can construct gap-graded structures, in which the layers facing the sun have larger gaps than the layers underneath. The SrTiO_3 substrate can be on either side because it is transparent to visible light. This scheme efficiently reduces the losses due to the magnitude of the band gap and provides the primary means to exceed the Shockley-Queisser limit. We perform DFT + U calculations for such a $\text{LaFeO}_3|\text{LaVO}_3|\text{SrTiO}_3$ heterostructure and find a layer-dependent gap of 2.2 eV for the LaFeO_3 and 1.1 eV for the LaVO_3 part, in close agreement with the bulk values. See Supplemental Material, Fig. 3, for details [25].

We thank Ralph Claessen, Ho-Nyung Lee, Margherita Marsili, David Parker, Andrei Pimenov, Jens Pflaum, and Zhicheng Zhong for fruitful discussions, and we acknowledge financial support from a Vienna University of Technology innovative project grant (E. A. and G. S.), SFB ViCoM [FWF project ID F4103] (P. B. and K. H.), and the Laboratory Directed Research and Development Program of ORNL (S. O.).

Note added in proof.—Manousakis [Phys. Rev. B **82**, 125109 (2010)] reports that, in a Mott insulator, a single photon may create multiple electron-hole pairs by impact ionization. This effect could further increase the efficiency of the $\text{LaVO}_3|\text{SrTiO}_3$ solar cell proposed here.

*okapon@ornl.gov

- [1] A. Ohtomo, D. A. Muller, J. L. Grazul, and H. Y. Hwang, *Nature (London)* **419**, 378 (2002).
- [2] A. Ohtomo and H. Y. Hwang, *Nature (London)* **427**, 423 (2004).
- [3] S. Okamoto and A. J. Millis, *Nature (London)* **428**, 630 (2004).
- [4] A. J. Millis and D. G. Schlom, *Phys. Rev. B* **82**, 073101 (2010).
- [5] W. Shockley and H. J. Queisser, *J. Appl. Phys.* **32**, 510 (1961).
- [6] A. Polman and H. A. Atwater, *Nat. Mater.* **11**, 174 (2012).
- [7] EPIA, Global Market Outlook for Photovoltaics until 2016, <http://epia.org>.
- [8] T. Koida, M. Lippmaa, T. Fukumura, K. Itaka, Y. Matsumoto, M. Kawasaki, and H. Koinuma, *Phys. Rev. B* **66**, 144418 (2002).
- [9] I. Bozovic, G. Logvenov, M. A. J. Verhoeven, P. Caputo, E. Goldobin, and T. H. Geballe, *Nature (London)* **422**, 873 (2003).
- [10] Z. Sefrioui, D. Arias, V. Peña, J. E. Villegas, M. Varela, P. Prieto, C. Leon, J. L. Martinez, and J. Santamaria, *Phys. Rev. B* **67**, 214511 (2003).
- [11] P. Yu, J. S. Lee, S. Okamoto, M. D. Rossell, M. Huijben, C.-H. Yang, Q. He, J. X. Zhang, S. Y. Yang, M. J. Lee, Q.-M. Ramasse, R. Erni, Y.-H. Chu, D. A. Arena, C.-C. Kao, L. W. Martin, and R. Ramesh, *Phys. Rev. Lett.* **105**, 027201 (2010).
- [12] H. N. Lee, H. M. Christen, M. F. Chisholm, C. M. Rouleau, and D. H. Lowndes, *Nature (London)* **433**, 395 (2005).
- [13] G. Sassi, *J. Appl. Phys.* **54**, 5421 (1983); M. Konagai and K. Takahashi, *J. Appl. Phys.* **46**, 3542 (1975).
- [14] S. Thiel, G. Hammerl, A. Schmehl, C. W. Schneider, and J. Mannhart, *Science* **313**, 1942 (2006).
- [15] A. Brinkman, M. Huijben, M. van Zalk, J. Huijben, U. Zeitler, J. C. Maan, W. G. van der Wiel, G. Rijnders, D. H. A. Blank, and H. Hilgenkamp, *Nat. Mater.* **6**, 493 (2007).
- [16] N. Reyren, S. Thiel, A. D. Caviglia, L. F. Kourkoutis, G. Hammerl, C. Richter, C. W. Schneider, T. Kopp, A.-S. Ruetschi, D. Jaccard, M. Gabay, D. A. Muller, J.-M. Triscone, and J. Mannhart, *Science* **317**, 1196 (2007).
- [17] A. D. Caviglia, S. Gariglio, N. Reyren, D. Jaccard, T. Schneider, M. Gabay, S. Thiel, G. Hammerl, J. Mannhart, and J.-M. Triscone, *Nature (London)* **456**, 624 (2008).
- [18] C. Cen, S. Thiel, G. Hammerl, C. W. Schneider, K. E. Andersen, C. S. Hellberg, J. Mannhart, and J. Levy, *Nat. Mater.* **7**, 298 (2008).
- [19] N. Nakagawa, H. Y. Hwang, and D. A. Muller, *Nat. Mater.* **5**, 204 (2006).
- [20] G. Singh-Bhalla, C. Bell, J. Ravichandran, W. Siemons, Y. Hikita, S. Salahuddin, A. F. Hebard, H. Y. Hwang, and R. Ramesh, *Nat. Phys.* **7**, 80 (2011).
- [21] P. Blaha, K. Schwarz, G. K. H. Madsen, D. Kvasnicka, and J. Luitz, *WIEN2k, An Augmented Plane Wave + Local Orbitals Program for Calculating Crystal Properties* (Technische Universität Wien, Vienna, Austria, 2001), ISBN 3-9501031-1-2.

- [22] J. P. Perdew, A. Ruzsinszky, G. I. Csonka, O. A. Vydrov, G. E. Scuseria, L. A. Constantin, X. Zhou, and K. Burke, *Phys. Rev. Lett.* **100**, 136406 (2008).
- [23] F. Tran and P. Blaha, *Phys. Rev. Lett.* **102**, 226401 (2009).
- [24] C. Ambrosch-Draxl and J. Sofo, *Comput. Phys. Commun.* **175**, 1 (2006).
- [25] See Supplemental Material at <http://link.aps.org/supplemental/10.1103/PhysRevLett.110.078701> for technical details on the DFT calculations including a discussion of excitonic effects, as well as additional results on the gap-graded $\text{LaFeO}_3|\text{LaVO}_3|\text{SrTiO}_3$ structure and potential gradient in $\text{LaVO}_3|\text{SrTiO}_3$.
- [26] M. De Raychaudhury, E. Pavarini, and O. K. Andersen, *Phys. Rev. Lett.* **99**, 126402 (2007).
- [27] T.-H. Arima, Y. Tokura, and J. B. Torrance, *Phys. Rev. B* **48**, 17006 (1993); T.-H. Arima and Y. Tokura, *J. Phys. Soc. Jpn.* **64**, 2488 (1995); We calculated the absorption coefficient from the reported reflectivity using Kramers-Kronig relations following Ref. [31].
- [28] H. Weng and K. Terakura, *Phys. Rev. B* **82**, 115105 (2010).
- [29] R. Claessen (private communication).
- [30] Y. Hotta, T. Susaki, and H. Y. Hwang, *Phys. Rev. Lett.* **99**, 236805 (2007).
- [31] Data analysis package *datan* by C. Porter and D. Tanner, <http://www.phys.ufl.edu/~tanner/datan.html>.

Oxide heterostructures for efficient solar cells — Supplementary Information

Elias Assmann,¹ Peter Blaha,² Robert Laskowski,² Karsten Held,¹ Satoshi Okamoto,³ and Giorgio Sangiovanni⁴¹*Institute of Solid State Physics, Vienna University of Technology, 1040 Vienna, Austria*²*Institute of Materials Chemistry, Vienna University of Technology, 1040 Vienna, Austria*³*Materials Science and Technology Division, Oak Ridge National Laboratory, Oak Ridge, Tennessee 37831, USA*⁴*Institut für Theoretische Physik und Astrophysik, Universität Würzburg, 97074 Würzburg, Germany*

(Dated: April 9, 2013)

The DFT calculations were performed using the full-potential linearized augmented plane-wave code WIEN2k [21], with the PBESol exchange-correlation potential [22] and a local Coulomb interaction term U on Ti, V and Fe ($U_{\text{Ti}} = 9.8$ eV, $U_{\text{V}} = 3$ eV, $U_{\text{Fe}} = 5$ eV, i.e. a GGA+ U scheme. The U values have been selected to reproduce the experimental band gaps in the bulk, which is essential in this case since the heterostructures would become conducting too soon (i.e. the critical thickness would be too small) if the gaps were smaller.

This is also the rationale for the large U_{Ti} : It is necessary to shift the Ti- d states up far enough; but because they are almost empty, this drastic value is needed to achieve the desired effect. This is analogous to the case of LaTiO₃, where a large U on the empty La- f states is necessary to shift them away from Ti- d .

An independent verification of the results achieved with this U_{Ti} comes in the form of a calculation using the parameter-free *modified Becke-Johnson* (mBJ) exchange-correlation potential [31], which we find to qualitatively agree with the corresponding DFT+ U calculation.

Formally, periodic boundary conditions are in force in all our calculations; however, in the thin-film case the vacuum acts to separate LaVO₃ and SrTiO₃, effectively imposing open boundary conditions.

The lattice constants of SrTiO₃, LaVO₃, and LaFeO₃ are quite similar when one takes into account that the unit cells of the latter two are enlarged with respect to the primitive cubic perovskite cell due to the reduced symmetry; they are doubled in the z -direction, and form a $\sqrt{2}$ -cell in the xy -plane. We take this $\sqrt{2}$ setting for the heterostructure unit cell in the xy -plane, thus there are two Ti/V/Fe atoms per plane. We fix the in-plane lattice parameter to the value in the SrTiO₃ substrate (this corresponds to the experimental situation), while the extent in z -direction for the multi-layer structures corresponds to the sum of the bulk layer separations. For the corresponding thin-film structure, this value is enlarged by 20 Bohr ≈ 10.6 Å. Within this volume, all atomic positions are relaxed. For the numerical values, see Supplemental Table I.

In the bulk, both LaVO₃ and LaFeO₃ show antiferromagnetic (AF) spin and orbital order at low temperatures: LaVO₃ has AF-C spin and AF-G orbital order while LaFeO₃ has AF-G order in both channels; DFT predicts this in accordance with experiment. This raises

Supplemental Table I: Lattice constants of bulk SrTiO₃ (cubic), LaVO₃ (orthorhombic), and LaFeO₃ (orthorhombic). a and b are the in-plane $\sqrt{2}$ lattice parameters, while c is the BO_2 -plane separation.

	$a/\text{Å}$	$b/\text{Å}$	$c/\text{Å}$
SrTiO ₃	5.523	5.523	3.905
LaVO ₃	5.539	5.560	3.907
LaFeO ₃	5.554	5.568	3.928

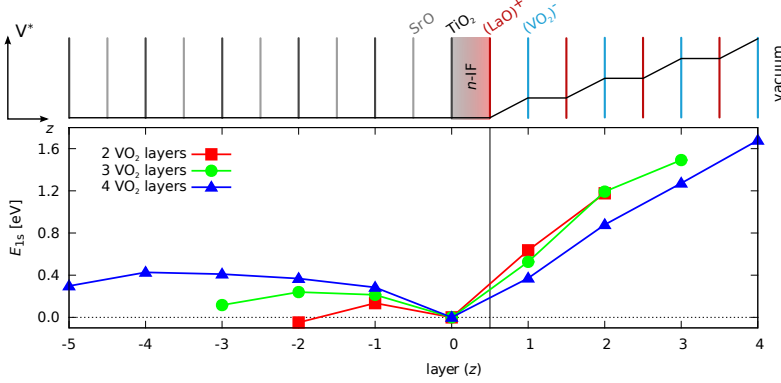
the question which spin order prevails in the heterostructures. For LaVO₃|SrTiO₃, we focus on AF-C both in analogy to the bulk, and because it has the lowest energy in DFT (among AF-A, AF-C, AF-G and FM) in two test cases.

When a second magnetic material comes into play with LaFeO₃, the situation becomes more complicated and three different spin orders have to be considered in general: within LaVO₃, within LaFeO₃ and at the interface. In the LaFeO₃|LaVO₃|SrTiO₃ calculation presented here, there is only one layer of each material, therefore we need to consider only the coupling between LaFeO₃ and LaVO₃, which we choose antiferromagnetic in the interest of comparability with the LaVO₃-only calculations, resulting in “AF-C” spin order across V and Fe.

The absorption coefficient for LaVO₃ was calculated within GGA+ U as described above, using the program of Ref. 23 while for the semiconductors the mBJ potential was used [31], which yields band gaps in good agreement with the experimental values in these cases. The calculated absorption coefficients have been checked regarding convergence with respect to the density of k -points used to sample the Brillouin zone. For the heterostructure, up to $10 \times 10 \times 1$ k -points were used.

The electron-hole interaction, which we investigated by solving the Bethe-Salpeter equation for bulk LaVO₃, introduces a sizable (~ 0.6 eV) but rigid shift of the spectrum to lower energies. However, since the shape of the optical absorption is hardly changed, a somewhat larger value of U_{V} could easily compensate this shift, reproducing once again the experimental value for the optical gap as in Fig. 5 in the main paper. Thus we conclude that electron-hole interactions do not change our predictions significantly.

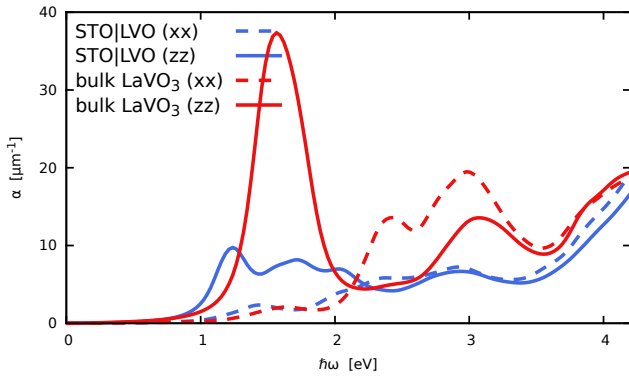
The experimental absorption coefficient for LaVO₃ was



Supplemental Figure 1: Potential gradient in thin-film $\text{LaVO}_3|\text{SrTiO}_3$ heterostructures. The curves ($\blacksquare/\bullet/\blacktriangle$ distinguish structure size) track the energy of an O-1s state through the TiO_2 (layer ≤ 0) and VO_2 (layer > 0) layers, which provides a measure of the potential gradient. Above the data, the layers, interfaces (IF), and effective electron potential V^* are shown schematically. The potential in the SrTiO_3 part is almost flat, showing only a slight buckling which we attribute to band bending at the interface.

calculated from the reflectivity measured in Ref. 26 using Kramers-Kronig relations, employing the *datan* program package [32].

Gradient in the thin-film case. In analogy to Fig. 4 in the main paper, we show the behavior of the O-1s level in thin-film heterostructures in Supplemental Fig. 1.

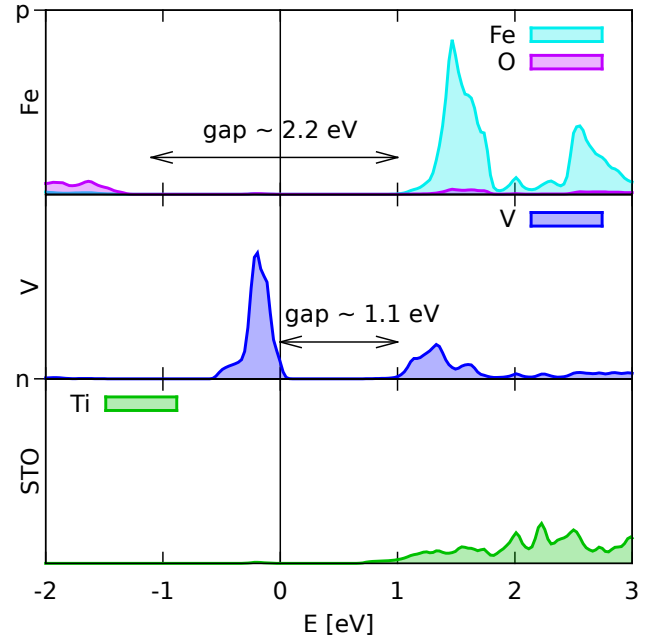


Supplemental Figure 2: Contributions to absorption coefficients. Both in bulk LaVO_3 and the heterostructure, a significant asymmetry is seen between the xx and the zz components, while yy is similar to xx . The off-diagonal components are rather small in comparison with the diagonal ones.

Absorption coefficients. As stated in the main text, the absorption coefficient $\alpha(\omega)$ is defined via the exponential dampening of the light intensity as a function of distance travelled through the material. However, in addition to the frequency dependency, the absorption also depends on the light's polarization, leading to a matrix α_{ij} analogous to the dielectric tensor. In cubic crystals (such as CdTe and GaAs), symmetry reduces the tensor to only one independent component, α_{ii} , and this is what is plotted for these materials in Fig. 5 in the main paper.

On the contrary, in LaVO_3 and $\text{LaVO}_3|\text{SrTiO}_3$, the reduced symmetry allows six independent entries. Which of these may contribute to the actual absorption depends of course on the light's angle of incidence with respect to the crystal. Since the heterostructure is grown along the z -direction, in the first approximation the polarization will

be in the xy plane. However, because some of the light will come from other directions due to scattering, and because heterostructures are often grown on a stepped substrate, some z -component will also be present, and all α_{ij} may contribute. Therefore, we plotted a suitably averaged quantity $\bar{\alpha} := \frac{1}{3}(\sum_i \alpha_{ii} + \sum_{ij} \alpha_{ij})$ in Fig. 5. Supplemental Fig. 2 shows some of the individual contributions. The optical absorption for the heterostructure was calculated in the multi-layer geometry with two VO_2 layers.



Supplemental Figure 3: The relevant contributions to the density of states around the Fermi level for the “gap-graded” $\text{LaFeO}_3|\text{LaVO}_3|\text{SrTiO}_3$ structure. In this case, the two V/Fe sites give almost identical contributions (in opposite spin channels). A p - and an n -type interface appear, as marked, due to periodic boundary conditions.

Band-gap grading with LaFeO_3 . In this section, we give details on the calculation combining LaVO_3 and LaFeO_3 referenced in the main text. The structure con-

tains 3 Ti, 1 V and 1 Fe layer, with two metal atoms per layer. The projected density of states for Fe, V and the Ti layer at the *n*-type interface is shown in Supplemental Fig. 3. The differing magnitudes of the Fe–O and V–V gaps are clearly seen.

It should be emphasized that $\text{LaVO}_3 + \text{LaFeO}_3$ is only one example for many different combinations that may be envisaged within the flexible framework provided by oxide heterostructures.

Acknowledgments. We thank Andrei Pimenov for the calculation of the experimental LaVO_3 absorption.

[21] P. Blaha, K. Schwarz, G. K. H. Madsen, D. Kvasnicka, and J. Luitz, *WIEN2k, An Augmented Plane Wave + Lo-*

cal Orbitals Program for Calculating Crystal Properties (Techn. Universität Wien, Vienna, Austria, 2001). ISBN 3-9501031-1-2

[22] J. P. Perdew, A. Ruzsinszky, G. I. Csonka, O. A. Vydrov, G. E. Scuseria, L. A. Constantin, X. Zhou and K. Burke, *Phys. Rev. Lett.* **100**, 136406 (2008)

[23] C. Ambrosch-Draxl and J. Sofo, *Comp. Phys. Comm.* **175**, 1 (2006).

[26] T.-H. Arima and Y. Tokura, *Journ. Phys. Soc. Japan* **64**, 2488 (1995).

[31] F. Tran and P. Blaha, *Phys. Rev. Lett.* **102**, 226401 (2009).

[32] Data analysis package *Datan* by C. Porter and D. Tanner, <http://www.phys.ufl.edu/~tanner/datan.html>

References

- [AAL97] V. I. Anisimov, F. Aryasetiawan, and A. I. Lichtenstein. "First-principles calculations of the electronic structure and spectra of strongly correlated systems: the LDA+U method." *J. Phys.: Condens. Matter* 9, 767 (1997). (Cit. on p. 21).
- [AB85] C.-O. Almbladh and U. von Barth. "Exact results for the charge and spin densities, exchange-correlation potentials, and density-functional eigenvalues." *Phys. Rev. B* 31, 3231 (1985). (Cit. on p. 7).
- [AG91] V. I. Anisimov and O. Gunnarsson. "Density-functional calculation of effective Coulomb interactions in metals." *Phys. Rev. B* 43, 7570 (1991). (Cit. on p. 21).
- [Ahm+13] S. J. Ahmed, J. Kivinen, B. Zaporzan, L. Curiel, S. Pichardo, and O. Rubel. "BerryPI: A software for studying polarization of crystalline solids with WIEN2k density functional all-electron package." *Comput. Phys. Commun.* 184, 647 (2013). (Cit. on p. 36).
- [Ama+06] B. Amadon, S. Biermann, A. Georges, and F. Aryasetiawan. "The α - γ Transition of Cerium Is Entropy Driven." *Phys. Rev. Lett.* 96, 066402 (2006). (Cit. on p. 28).
- [Ama12] B. Amadon. "A self-consistent DFT+DMFT scheme in the projector augmented wave method: applications to cerium, Ce_2O_3 and Pu_2O_3 with the Hubbard I solver and comparison to DFT+U." *J. Phys.: Condens. Matter* 24, 075604 (2012). (Cit. on p. 28).
- [And72] P. W. Anderson. "More Is Different." *Science* 177, 393 (1972). (Cit. on p. viii).
- [And75] O. K. Andersen. "Linear methods in band theory." *Phys. Rev. B* 12, 3060 (1975). (Cit. on p. 10).
- [Ani+05] V. I. Anisimov, D. E. Kondakov, A. V. Kozhevnikov, I. A. Nekrasov, Z. V. Pchelkina, J. W. Allen, S.-K. Mo, H.-D. Kim, P. Metcalf, S. Suga, et al. "Full orbital calculation scheme for materials with strongly correlated electrons." *Phys. Rev. B* 71, 125119 (2005). (Cit. on pp. 15, 28, 66).

References

- [Ani+93] V. I. Anisimov, I. V. Solovyev, M. A. Korotin, M. T. Czyżyk, and G. A. Sawatzky. “Density-functional theory and NiO photoemission spectra.” *Phys. Rev. B* 48, 16929 (1993). (Cit. on pp. 21, 83).
- [APG11] M. Aichhorn, L. Pourovskii, and A. Georges. “Importance of electronic correlations for structural and magnetic properties of the iron pnictide superconductor LaFeAsO.” *Phys. Rev. B* 84, 054529 (2011). (Cit. on pp. 28, 29).
- [Ary+04] F. Aryasetiawan, M. Imada, A. Georges, G. Kotliar, S. Biermann, and A. I. Lichtenstein. “Frequency-dependent local interactions and low-energy effective models from electronic structure calculations.” *Phys. Rev. B* 70, 195104 (2004). (Cit. on p. 21).
- [ASo6] C. Ambrosch-Draxl and J. O. Sofo. “Linear optical properties of solids within the full-potential linearized augmented plane-wave method.” *Comput. Phys. Commun.* 175, 1 (2006). (Cit. on p. 44).
- [Ass+13] E. Assmann, P. Blaha, R. Laskowski, K. Held, S. Okamoto, and G. Sangiovanni. “Oxide Heterostructures for Efficient Solar Cells.” *Phys. Rev. Lett.* 110, 078701 (2013). Selected for a synopsis in *Physics*. (Cit. on pp. x, 71–73, 76, 77, 80, 85, 88, 138).
- [Ass+15] E. Assmann, P. Wissgott, J. Kuneš, A. Toschi, P. Blaha, and K. Held. “woptic: optical conductivity with Wannier functions and adaptive k-mesh refinement.” (2015). Submitted. (Cit. on pp. ix, 39, 57, 61, 66, 87, 88, 137).
- [AT95] T.-h. Arima and Y. Tokura. “Optical Study of Electronic Structure in Perovskite-Type RMO_3 ($R = \text{La, Y}$; $M = \text{Sc, Ti, V, Cr, Mn, Fe, Co, Ni, Cu}$).” *J. Phys. Soc. Jpn.* 64, 2488 (1995). (Cit. on p. 72).
- [ATT93] T. Arima, Y. Tokura, and J. B. Torrance. “Variation of optical gaps in perovskite-type 3d transition-metal oxides.” *Phys. Rev. B* 48, 17006 (1993). (Cit. on pp. 72, 74).
- [AZA91] V. I. Anisimov, J. Zaanen, and O. K. Andersen. “Band theory and Mott insulators: Hubbard U instead of Stoner I.” 44, 943 (1991). (Cit. on p. 21).
- [Bed+78] S. Bedair, M. Lamorte, J. Hauser, and K. Mitchell. “Growth and characterization of a two-junction, stacked solar cell.” In: *Electron Devices Meeting, 1978 International*. Vol. 24. 1978, pp. 250–253. (Cit. on p. 72).
- [Ber11] S. Berryman. “Ancient Atomism.” In: *The Stanford Encyclopedia of Philosophy*. Ed. by E. N. Zalta. Winter 2011. 2011. (Cit. on p. vii).

- [Bla+01] P. Blaha, K. Schwarz, G. K. Madsen, D. Kvasnicka, and J. Luitz. *An Augmented Plane Wave + Local Orbitals Program for Calculating Crystal Properties*. Vienna: Technische Universität Wien, 2001. ISBN: 3-9501031-1-2. (Cit. on pp. ix, 9, 33, 75).
- [Bor+93] P. Bordet, C. Chaillout, M. Marezio, Q. Huang, A. Santoro, S.-W. Cheong, H. Takagi, C. S. Oglesby, and B. Batlogg. "Structural Aspects of the Crystallographic-Magnetic Transition in LaVO_3 around 140 K." *J. Solid State Chem.* 106, 253 (1993). (Cit. on pp. 72, 74).
- [BS14] P. Blaha and K. Schwarz. *WIEN 2k*. WIEN2k-Update information. 2014. URL: http://www.wien2k.at/reg_user/updates/ (visited on 04/09/2015). (Cit. on p. 36).
- [BSS81] R. Blankenbecler, D. J. Scalapino, and R. L. Sugar. "Monte Carlo Calculations of Coupled Boson-Fermion Systems." *Physical Review D* 24, 2278 (1981). (Cit. on p. 25).
- [Cap06] K. Capelle. "A bird's-eye view of density-functional theory." *Braz. J. Phys.* 36, 1318 (2006). (Cit. on p. ix).
- [Car10] S. Carroll. *The Laws Underlying The Physics of Everyday Life Are Completely Understood*. Sean Carroll. 2010. URL: <http://www.preposterousuniverse.com/blog/2010/09/23/the-laws-underlying-the-physics-of-everyday-life-are-completely-understood/> (visited on 07/08/2015). (Cit. on p. viii).
- [CG05] M. Cococcioni and S. de Gironcoli. "Linear response approach to the calculation of the effective interaction parameters in the LDA+U method." *Phys. Rev. B* 71, 035105 (2005). (Cit. on p. 21).
- [Chi+03] L. Chioncel, L. Vitos, I. A. Abrikosov, J. Kollár, M. I. Katsnelson, and A. I. Lichtenstein. "Ab initio electronic structure calculations of correlated systems: An EMTO-DMFT approach." *Phys. Rev. B* 67, 235106 (2003). (Cit. on p. 28).
- [Coto2] S. Cottenier. *Density Functional Theory and the family of (l)apw-methods: a step-by-step introduction*. 2002. ISBN: 978-90-807215-1-7. (Cit. on p. 9).
- [DPA07] M. De Raychaudhury, E. Pavarini, and O. K. Andersen. "Orbital Fluctuations in the Different Phases of LaVO_3 and YVO_3 ." *Phys. Rev. Lett.* 99, 126402 (2007). (Cit. on pp. 73, 76).
- [EW14a] M. Eckstein and P. Werner. "Ultrafast Separation of Photodoped Carriers in Mott Antiferromagnets." *Phys. Rev. Lett.* 113, 076405 (2014). (Cit. on p. 73).
- [EW14b] M. Eckstein and P. Werner. "Ultra-fast photo-carrier relaxation in Mott insulators with short-range spin correlations." (2014). (Cit. on p. 73).

References

- [Fau+13] D. A. Faux, P. J. McDonald, N. C. Howlett, J. S. Bhatt, and S. V. Churakov. "Nuclear magnetic resonance relaxometry of water in two and quasi-two dimensions." *Phys. Rev. E* 87, 062309 (2013). (Cit. on p. 35).
- [Fra+12] C. Franchini, R. Kováčik, M. Marsman, S. S. Murthy, J. He, C. Ederer, and G. Kresse. "Maximally localized Wannier functions in LaMnO₃ within PBE+U, hybrid functionals and partially self-consistent GW: an efficient route to construct ab initio tight-binding parameters for eg perovskites." *J. Phys.: Condens. Matter* 24, 235602 (2012). (Cit. on p. 33).
- [Fre+08] F. Freimuth, Y. Mokrousov, D. Wortmann, S. Heinze, and S. Blügel. "Maximally localized Wannier functions within the FLAPW formalism." *Phys. Rev. B* 78, 035120 (2008). (Cit. on p. 33).
- [FSF] Free Software Foundation. *What is free software and why is it so important for society?* URL: <http://www.fsf.org/about/what-is-free-software> (visited on 03/02/2015). (Cit. on p. x).
- [Geo+96] A. Georges, G. Kotliar, W. Krauth, and M. J. Rozenberg. "Dynamical mean-field theory of strongly correlated fermion systems and the limit of infinite dimensions." *Rev. Mod. Phys.* 68, 13 (1996). (Cit. on pp. ix, 22).
- [Geo04] A. Georges. "Strongly Correlated Electron Materials: Dynamical Mean-Field Theory and Electronic Structure." cond-mat/0403123. Lectures on the Physics of Highly Correlated Electron Systems VIII (2004) 3, American Institute of Physics Conference Proceedings Vol. 715 (2004). (Cit. on pp. ix, 25).
- [Gia+09] P. Giannozzi, S. Baroni, N. Bonini, M. Calandra, R. Car, C. Cavazzoni, D. Ceresoli, G. L. Chiarotti, M. Cococcioni, I. Dabo, et al. "QUANTUM ESPRESSO: a modular and open-source software project for quantum simulations of materials." *J. Phys.: Condens. Matter* 21, 395502 (2009). (Cit. on pp. xix, 33).
- [GK92] A. Georges and G. Kotliar. "Hubbard model in infinite dimensions." *Phys. Rev. B* 45, 6479 (1992). (Cit. on pp. 22, 23).
- [Gon+09] X. Gonze, B. Amadon, P.-M. Anglade, J.-M. Beuken, F. Bottin, P. Boulanger, F. Bruneval, D. Caliste, R. Caracas, M. Côté, et al. "ABINIT: First-principles approach to material and nanosystem properties." *Comput. Phys. Commun.* 180, 2582 (2009). (Cit. on p. 33).

-
- [Grå+12] O. Grånäs, I. Di Marco, P. Thunström, L. Nordström, O. Eriksson, T. Björkman, and J. Wills. “Charge self-consistent dynamical mean-field theory based on the full-potential linear muffin-tin orbital method: Methodology and applications.” *Comput. Mater. Sci.* 55, 295 (2012). (Cit. on p. 28).
- [Gss88] R. W. Godby, M. Schlüter, and L. J. Sham. “Self-energy operators and exchange-correlation potentials in semiconductors.” *Phys. Rev. B* 37, 10159 (1988). (Cit. on p. 7).
- [Gul+11] E. Gull, A. J. Millis, A. I. Lichtenstein, A. N. Rubtsov, M. Troyer, and P. Werner. “Continuous-time Monte Carlo methods for quantum impurity models.” *Rev. Mod. Phys.* 83, 349 (2011). (Cit. on pp. xvii, 25, 75).
- [Guo+13] H.-Z. Guo, L. Gu, Z.-Z. Yang, S.-F. Wang, G.-S. Fu, L. Wang, K.-J. Jin, H.-B. Lu, C. Wang, C. Ge, et al. “Electronic transport and photovoltaic properties in Bi₂Sr₂Co₂O_y epitaxial heterostructures.” *EPL* 103, 47006 (2013). (Cit. on p. 72).
- [Har10] M. Hartl. *No, really, pi is wrong: The Tau Manifesto*. Tau Day. 2010. URL: <http://tauday.com/tau-manifesto> (visited on 08/20/2014). (Cit. on pp. xix, 3).
- [He+12] C. He, T. D. Sanders, M. T. Gray, F. J. Wong, V. V. Mehta, and Y. Suzuki. “Metal-insulator transitions in epitaxial LaVO₃ and LaTiO₃ films.” *Phys. Rev. B* 86, 081401 (2012). (Cit. on p. 72).
- [Hel+03] K. Held, I. Nekrasov, G. Keller, V. Eyert, N. Blümer, A. McMahan, R. Scalettar, T. Pruschke, V. Anisimov, and D. Vollhardt. “Realistic investigations of correlated electron systems with textslda+dmft.” Ψ_k Newsletter 56, 65 (2003). (Cit. on p. 28).
- [Hel07] K. Held. “Electronic structure calculations using dynamical mean field theory.” *Adv. Phys.* 56, 829 (2007). (Cit. on pp. ix, 28).
- [Het+98] M. H. Hettler, A. N. Tahvildar-Zadeh, M. Jarrell, T. Pruschke, and H. R. Krishnamurthy. “Nonlocal dynamical correlations of strongly interacting electron systems.” *Phys. Rev. B* 58, R7475 (1998). (Cit. on p. 23).
- [Hew97] A. C. Hewson. *The Kondo Problem to Heavy Fermions*. Cambridge University Press, 1997. 476 pp. ISBN: 9780521599474. (Cit. on p. 24).
- [HK64] P. Hohenberg and W. Kohn. “Inhomogeneous Electron Gas.” *Phys. Rev. B* 136, 864 (1964). (Cit. on p. 4).

References

- [HMS01] K. Held, A. K. McMahan, and R. T. Scalettar. "Cerium Volume Collapse: Results from the Merger of Dynamical Mean-Field Theory and Local Density Approximation." *Phys. Rev. Lett.* 87, 276404 (2001). (Cit. on p. 28).
- [HSH07] Y. Hotta, T. Susaki, and H. Y. Hwang. "Polar Discontinuity Doping of the $\text{LaVO}_3/\text{SrTiO}_3$ Interface." *Phys. Rev. Lett.* 99, 236805 (2007). (Cit. on p. 72).
- [Hwa+12] H. Y. Hwang, Y. Iwasa, M. Kawasaki, B. Keimer, N. Nagaosa, and Y. Tokura. "Emergent phenomena at oxide interfaces." *Nat. Mater.* 11, 103 (2012). (Cit. on p. 71).
- [HYK10] K. Haule, C.-H. Yee, and K. Kim. "Dynamical mean-field theory within the full-potential methods: Electronic structure of CeIrIn_5 , CeCoIn_5 , and CeRhIn_5 ." *Phys. Rev. B* 81, 195107 (2010). (Cit. on p. 28).
- [ILO8] H. Ishida and A. Liebsch. "Origin of metallicity of $\text{LaTiO}_3/\text{SrTiO}_3$ heterostructures." *Phys. Rev. B* 77, 115350 (2008). (Cit. on p. 73).
- [IM10] M. Imada and T. Miyake. "Electronic Structure Calculation by First Principles for Strongly Correlated Electron Systems." *J. Phys. Soc. Jpn.* 79, 112001 (2010). (Cit. on p. 21).
- [IT15] M. Iazzi and M. Troyer. "Efficient continuous-time quantum Monte Carlo algorithm for fermionic lattice models." *Phys. Rev. B* 91, 241118 (2015). (Cit. on p. 25).
- [Jac55] E. D. Jackson. "Areas for improvement of the semiconductor solar energy converter." In: *Proceedings of the Transactions of the Conference on the Use of Solar Energy, The Scientific Basis*. Tucson: University of Arizona Press, 1955, pp. 122–126. (Cit. on p. 72).
- [Jac60] E. D. Jackson. "Solar energy converter." International Classification H01L25/04, H01L31/00. 1960. (Cit. on p. 72).
- [JC89] R. O. Jones and O. Gunnarsson. "The density functional formalism, its applications and prospects." *Rev. Mod. Phys.* 61, 689 (1989). (Cit. on p. ix).
- [JG96] M. Jarrell and J. E. Gubernatis. "Bayesian inference and the analytic continuation of imaginary-time quantum Monte Carlo data." *Phys. Rep.* 269, 133 (1996). (Cit. on pp. xviii, 26, 75).
- [KA75] D. D. Koelling and G. O. Arbman. "Use of energy derivative of the radial solution in an augmented plane wave method: application to copper." *J. Phys. F: Met. Phys.* 5, 2041 (1975). (Cit. on p. 10).

- [Kan63] J. Kanamori. "Electron Correlation and Ferromagnetism of Transition Metals." *Progr. Theor. Phys.* 30, 275 (1963). (Cit. on p. 20).
- [KF12] A. P. Kirk and M. V. Fischetti. "Fundamental limitations of hot-carrier solar cells." *Phys. Rev. B* 86, 165206 (2012). (Cit. on p. 73).
- [KKV12] B. Kaduk, T. Kowalczyk, and T. Van Voorhis. "Constrained Density Functional Theory." *Chem. Rev.* 112, 321 (2012). (Cit. on p. 21).
- [KM98] W. Kohn and A. E. Mattsson. "Edge Electron Gas." *Phys. Rev. Lett.* 81, 3487 (1998). (Cit. on p. 8).
- [Koh99] W. Kohn. "Nobel Lecture: Electronic structure of matter—wave functions and density functionals." *Rev. Mod. Phys.* 71, 1253 (1999). (Cit. on pp. ix, 8).
- [Kor+10] R. Korytár, M. Pruneda, J. Junquera, P. Ordejón, and N. Lorente. "Band selection and disentanglement using maximally localized Wannier functions: the cases of Co impurities in bulk copper and the Cu(111) surface." *J. Phys.: Condens. Matter* 22, 385601 (2010). (Cit. on p. 33).
- [Kot+01] G. Kotliar, S. Y. Savrasov, G. Pálsson, and G. Biroli. "Cellular Dynamical Mean Field Approach to Strongly Correlated Systems." *Phys. Rev. Lett.* 87, 186401 (2001). (Cit. on p. 23).
- [Kot+06] G. Kotliar, S. Y. Savrasov, K. Haule, V. S. Oudovenko, O. Parcollet, and C. A. Marianetti. "Electronic structure calculations with dynamical mean-field theory." *Rev. Mod. Phys.* 78, 865 (2006). (Cit. on pp. ix, 28).
- [Kou+07] L. F. Kourkoutis, D. A. Muller, Y. Hotta, and H. Y. Hwang. "Asymmetric interface profiles in $\text{LaVO}_3/\text{SrTiO}_3$ heterostructures grown by pulsed laser deposition." 91, 163101 (2007). (Cit. on p. 72).
- [ks65] W. Kohn and L. J. Sham. "Self-Consistent Equations Including Exchange and Correlation Effects." *Phys. Rev.* 140, A1133 (1965). (Cit. on pp. 5, 8).
- [Ku+02] W. Ku, H. Rosner, W. E. Pickett, and R. T. Scalettar. "Insulating Ferromagnetism in $\text{La}_4\text{Ba}_2\text{Cu}_2\text{O}_{10}$: An Ab Initio Wannier Function Analysis." *Phys. Rev. Lett.* 89, 167204 (2002). (Cit. on pp. 15, 66).
- [Kun+10] J. Kuneš, R. Arita, P. Wissgott, A. Toschi, H. Ikeda, and K. Held. "Wien2wannier: From linearized augmented plane waves to maximally localized Wannier functions." *Comput. Phys. Commun.* 181, 1888 (2010). (Cit. on pp. ix, 33, 34, 40, 75, 87).
- [Lau05] R. B. Laughlin. *A Different Universe: Reinventing Physics from the Bottom Down*. New York, NY: Basic Books, 2005. 254 pp. ISBN: 978-0-465-03829-9. (Cit. on p. viii).

References

- [LBG13] F. Lechermann, L. Boehnke, and D. Grieger. "Formation of orbital-selective electron states in LaTiO_3 / 7SrTiO_3 superlattices." *Phys. Rev. B* 87, 241101 (2013). (Cit. on pp. 28, 73).
- [LCO5] V. L. Lignères and E. A. Carter. "An Introduction to Orbital-Free Density Functional Theory." In: *Handbook of Materials Modeling*. Ed. by S. Yip. Springer Netherlands, 2005, pp. 137–148. ISBN: 978-1-4020-3287-5, 978-1-4020-3286-8. (Cit. on p. 5).
- [Lec+06] F. Lechermann, A. Georges, A. Poteryaev, S. Biermann, M. Posternak, A. Yamasaki, and O. K. Andersen. "Dynamical mean-field theory using Wannier functions: A flexible route to electronic structure calculations of strongly correlated materials." *Phys. Rev. B* 74, 125120 (2006). (Cit. on pp. 28, 29).
- [Lec+14] F. Lechermann, L. Boehnke, D. Grieger, and C. Piefke. "Electron correlation and magnetism at the LaAlO_3 / 7SrTiO_3 interface: A DFT+DMFT investigation." *Phys. Rev. B* 90, 085125 (2014). (Cit. on pp. 28, 73).
- [Lev79] M. Levy. "Universal variational functionals of electron densities, first-order density matrices, and natural spin-orbitals and solution of the v-representability problem." *PNAS* 76, 6062 (1979). (Cit. on p. 4).
- [Lia+13] H. Liang, L. Cheng, X. Zhai, N. Pan, H. Guo, J. Zhao, H. Zhang, L. Li, X. Zhang, X. Wang, et al. "Giant photovoltaic effects driven by residual polar field within unit-cell-scale LaAlO_3 films on SrTiO_3 ." *Sci. Rep.* 3 (2013). (Cit. on p. 72).
- [Lio03] A. Liebsch. "Surface versus Bulk Coulomb Correlations in Photoemission Spectra of SrVO_3 and CaVO_3 ." *Phys. Rev. Lett.* 90, 096401 (2003). (Cit. on p. 40).
- [LK00] A. I. Lichtenstein and M. I. Katsnelson. "Antiferromagnetism and d-wave superconductivity in cuprates: A cluster dynamical mean-field theory." *Phys. Rev. B* 62, R9283 (2000). (Cit. on p. 23).
- [LO15] F. Lechermann and M. Obermeyer. "Towards Mott design by δ -doping of strongly correlated titanates." *en. New J. Phys.* 17, 043026 (2015). (Cit. on pp. 28, 73).
- [LPM07] A. A. Levin, P. Paufler, and D. C. Meyer. "Low-temperature domain behaviour of a SrTiO_3 (0 0 1) single-crystal plate." *Physica B* 393, 373 (2007). (Cit. on p. 72).
- [Mad+01] G. K. H. Madsen, P. Blaha, K. Schwarz, E. Sjöstedt, and L. Nordström. "Efficient linearization of the augmented plane-wave method." *Phys. Rev. B* 64, 195134 (2001). (Cit. on p. 11).

-
- [Mai+05] T. Maier, M. Jarrell, T. Pruschke, and M. H. Hettler. “Quantum cluster theories.” *Rev. Mod. Phys.* 77, 1027 (2005). (Cit. on p. 23).
- [Man10] E. Manousakis. “Photovoltaic effect for narrow-gap Mott insulators.” *Phys. Rev. B* 82, 125109 (2010). (Cit. on p. 73).
- [Mar+12] N. Marzari, A. A. Mostofi, J. R. Yates, I. Souza, and D. Vanderbilt. “Maximally localized Wannier functions: Theory and applications.” *Rev. Mod. Phys.* 84, 1419 (2012). (Cit. on pp. ix, 14, 17, 36, 55).
- [Mar13] L. D. Marks. “Fixed-Point Optimization of Atoms and Density in DFT.” *J. Chem. Theory Comput.* (2013). (Cit. on p. 76).
- [Mes15] D. Meschede. *Gerthsen Physik*. Springer-Lehrbuch. Berlin, Heidelberg: Springer Berlin Heidelberg, 2015. ISBN: 978-3-662-45976-8 978-3-662-45977-5. (Cit. on p. vii).
- [MI11] K. Momma and F. Izumi. “VESTA 3 for three-dimensional visualization of crystal, volumetric and morphology data.” *J. Appl. Crystallogr.* 44, 1272 (2011). (Cit. on p. 192).
- [Min+05] J. Minár, L. Chioncel, A. Perlov, H. Ebert, M. I. Katsnelson, and A. I. Lichtenstein. “Multiple-scattering formalism for correlated systems: A kkr-dmft approach.” *Phys. Rev. B* 72, 045125 (2005). (Cit. on p. 28).
- [Mos+08a] A. A. Mostofi, J. R. Yates, Y.-S. Lee, I. Souza, D. Vanderbilt, and N. Marzari. “wannier90: A tool for obtaining maximally-localised Wannier functions.” *Comput. Phys. Commun.* 178, 685 (2008). (Cit. on pp. ix, 75).
- [Mos+08b] A. A. Mostofi, J. R. Yates, Y.-S. Lee, I. Souza, D. Vanderbilt, and N. Marzari. “WANNIER90: A tool for obtaining maximally-localised Wannier functions.” *Comput. Phys. Commun.* 178, 685 (2008). (Cit. on pp. 15, 17, 33, 55, 56).
- [MP76] H. J. Monkhorst and J. D. Pack. “Special points for Brillouin-zone integrations.” *Phys. Rev. B* 13, 5188 (1976). (Cit. on p. 14).
- [MS10] A. J. Millis and D. G. Schlom. “Electron-hole liquids in transition-metal oxide heterostructures.” *Phys. Rev. B* 82, 073101 (2010). (Cit. on p. 73).
- [MSC11] MSC. *The Pi Manifesto - No, really, pi is right!* 2011. URL: <http://www.thepimanifesto.com/> (visited on 04/15/2015). (Cit. on p. xix).
- [Mül89] E. Müller-Hartmann. “Correlated fermions on a lattice in high dimensions.” *Z. Physik B* 74, 507 (1989). (Cit. on p. 20).

References

- [Mus+15] J. I. Mustafa, S. Coh, M. L. Cohen, and S. G. Louie. “Automated construction of maximally localized Wannier functions: the optimized projection functions (OPF) method.” arXiv:1508.04148 [cond-mat] (2015). (Cit. on p. 66).
- [mv89] W. Metzner and D. Vollhardt. “Correlated Lattice Fermions in $d = \infty$ Dimensions.” *Phys. Rev. Lett.* 62, 324 (1989). (Cit. on p. 22).
- [mv97] N. Marzari and D. Vanderbilt. “Maximally localized generalized Wannier functions for composite energy bands.” *Phys. Rev. B* 56, 12847 (1997). (Cit. on pp. 14, 15, 75).
- [Nek+05] I. A. Nekrasov, G. Keller, D. E. Kondakov, A. V. Kozhevnikov, T. Pruschke, K. Held, D. Vollhardt, and V. I. Anisimov. “Comparative study of correlation effects in CaVO_3 and SrVO_3 .” *Phys. Rev. B* 72, 155106 (2005). (Cit. on p. 40).
- [NHM06] N. Nakagawa, H. Y. Hwang, and D. A. Muller. “Why some interfaces cannot be sharp.” *Nat. Mater.* 5, 204 (2006). (Cit. on p. 85).
- [NO98] J. W. Negele and H. Orland. *Quantum Many-particle Systems*. Westview Press, 1998. 480 pp. ISBN: 9780738200521. (Cit. on pp. xix, 22).
- [Nom+12] Y. Nomura, M. Kaltak, K. Nakamura, C. Taranto, S. Sakai, A. Toschi, R. Arita, K. Held, G. Kresse, and M. Imada. “Effective on-site interaction for dynamical mean-field theory.” *Phys. Rev. B* 86, 085117 (2012). (Cit. on p. 21).
- [OH04] A. Ohtomo and H. Y. Hwang. “A high-mobility electron gas at the $\text{LaAlO}_3/\text{SrTiO}_3$ heterointerface.” *Nature* 427, 423 (2004). (Cit. on pp. viii, 71).
- [Oht+02] A. Ohtomo, D. A. Muller, J. L. Grazul, and H. Y. Hwang. “Artificial charge-modulation in atomic-scale perovskite titanate superlattices.” *Nature* 419, 378 (2002). (Cit. on pp. viii, 71).
- [OM04a] S. Okamoto and A. J. Millis. “Electronic reconstruction at an interface between a Mott insulator and a band insulator.” *Nature* 428, 630 (2004). (Cit. on p. 73).
- [OM04b] S. Okamoto and A. J. Millis. “Spatial inhomogeneity and strong correlation physics: A dynamical mean-field study of a model Mott-insulator–band-insulator heterostructure.” *Phys. Rev. B* 70, 241104 (2004). (Cit. on p. 73).
- [OMS06] S. Okamoto, A. J. Millis, and N. A. Spaldin. “Lattice Relaxation in Oxide Heterostructures: $\text{LaTiO}_3/\text{SrTiO}_3$ Superlattices.” *Phys. Rev. Lett.* 97, 056802 (2006). (Cit. on p. 76).

- [Pal01] R. Palais. “ π is wrong!” *Math. Intell.* 23, 7 (2001). (Cit. on pp. xix, 3).
- [Par+12] N. Parragh, A. Toschi, K. Held, and G. Sangiovanni. “Conserved quantities of SU(2)-invariant interactions for correlated fermions and the advantages for quantum Monte Carlo simulations.” *Phys. Rev. B* 86, 155158 (2012). (Cit. on pp. x, 25, 75).
- [Pav+04] E. Pavarini, S. Biermann, A. Poteryaev, A. I. Lichtenstein, A. Georges, and O. K. Andersen. “Mott Transition and Suppression of Orbital Fluctuations in Orthorhombic $3d^1$ Perovskites.” *Phys. Rev. Lett.* 92, 176403 (2004). (Cit. on p. 40).
- [Pav+05] E. Pavarini, A. Yamasaki, J. Nuss, and O. K. Andersen. “How chemistry controls electron localization in $3d^1$ perovskites: a Wannier-function study.” *New J. Phys.* 7, 188 (2005). (Cit. on p. 40).
- [Pav+11] E. Pavarini, E. Koch, D. Vollhardt, and A. I. Lichtenstein. *The LDA+DMFT approach to strongly correlated materials: Lecture notes of the Autumn School 2011 Hands-on LDA+DMFT at Forschungszentrum Jülich, 4 - 7 October 2011. Modeling and simulation.* Jülich: Forschungszentrum Jülich, Zentralbibliothek, Verl., 2011. ISBN: 978-3-89336-734-4. (Cit. on p. ix).
- [PBE96] J. P. Perdew, K. Burke, and M. Ernzerhof. “Generalized Gradient Approximation Made Simple.” *Phys. Rev. Lett.* 77, 3865 (1996). (Cit. on pp. xviii, 8, 40).
- [Per+08] J. P. Perdew, A. Ruzsinszky, G. I. Csonka, O. A. Vydrov, G. E. Scuseria, L. A. Constantin, X. Zhou, and K. Burke. “Restoring the Density-Gradient Expansion for Exchange in Solids and Surfaces.” *Phys. Rev. Lett.* 100, 136406 (2008). (Cit. on pp. xviii, 8, 75).
- [Pou+07] L. V. Pourovskii, B. Amadon, S. Biermann, and A. Georges. “Self-consistency over the charge density in dynamical mean-field theory: A linear muffin-tin implementation and some physical implications.” *Phys. Rev. B* 76, 235101 (2007). (Cit. on p. 28).
- [PS01] J. P. Perdew and K. Schmidt. “Jacob’s ladder of density functional approximations for the exchange-correlation energy.” In: *aip Conference Proceedings. Density-Functional Theory and its Application to Materials.* Vol. 577. AIP Publishing, 2001, pp. 1–20. (Cit. on p. 8).
- [Rib+14] T. Ribic, E. Assmann, A. Tóth, and K. Held. “Cubic interaction parameters for t_{2g} Wannier orbitals.” *Phys. Rev. B* 90, 165105 (2014). (Cit. on pp. 20, 40, 41, 88, 137).
- [RK07] Z. Romanowski and S. Krukowski. “Transformation of complex spherical harmonics under rotations.” *J. Phys. A: Math. Theor.* 40, 15071 (2007). (Cit. on p. 35).

References

- [RKLO8] A. N. Rubtsov, M. I. Katsnelson, and A. I. Lichtenstein. "Dual fermion approach to nonlocal correlations in the Hubbard model." *Phys. Rev. B* 77, 033101 (2008). (Cit. on p. 23).
- [RN82] R. T. Ross and A. J. Nozik. "Efficiency of hot-carrier solar energy converters." *Journal of Applied Physics* 53, 3813 (1982). (Cit. on p. 73).
- [Roh+11] G. Rohringer, A. Toschi, A. Katanin, and K. Held. "Critical Properties of the Half-Filled Hubbard Model in Three Dimensions." *Phys. Rev. Lett.* 107, 256402 (2011). (Cit. on p. 23).
- [Rot+14a] H. Rotella, O. Copie, A. Pautrat, P. Boullay, A. David, D. Pelloquin, and W. Prellier. "Two components for one resistivity in $\text{LaVO}_3/\text{SrTiO}_3$ heterostructure." (2014). (Cit. on p. 72).
- [Rot+14b] H. Rotella, O. Copie, P. Boullay, H. Ouerdanne, A. David, A. Pautrat, D. Chateigner, and W. Prellier. "A Combined Structural Analysis Refinement of a Strained LaVO_3 Thin Films." (2014). (Cit. on p. 72).
- [Rub+14] O. Rubel, A. Bokhanchuk, S. J. Ahmed, and E. Assmann. "Unfolding the band structure of disordered solids: From bound states to high-mobility Kane fermions." *Phys. Rev. B* 90, 115202 (2014). FOLD2BLOCH is available at <https://github.com/rubel75/fold2Bloch>. (Cit. on pp. 88, 137).
- [San98] A. W. Sandvik. "Stochastic method for analytic continuation of quantum Monte Carlo data." *Phys. Rev. B* 57, 10287 (1998). (Cit. on pp. xviii, 26, 75).
- [Sca+14] A. Scaramucci, J. Ammann, N. A. Spaldin, and C. Ederer. "On the calculation of crystal field parameters using Wannier functions." arXiv:1405.3804 [cond-mat] (2014). (Cit. on pp. 40, 41).
- [Sek+04] A. Sekiyama, H. Fujiwara, S. Imada, S. Suga, H. Eisaki, S. I. Uchida, K. Takegahara, H. Harima, Y. Saitoh, I. A. Nekrasov, et al. "Mutual Experimental and Theoretical Validation of Bulk Photoemission Spectra of $\text{Sr}_{1-x}\text{Ca}_x\text{O}_3$." *Phys. Rev. Lett.* 93, 156402 (2004). (Cit. on p. 40).
- [Si+15] L. Si, Z. Zhong, J. M. Tomczak, and K. Held. "Route to room-temperature ferromagnetic ultrathin SrRuO_3 films." *Phys. Rev. B* 92, 041108 (2015). (Cit. on p. 73).
- [SKO1] S. Y. Savrasov and G. Kotliar. "Spectral Density Functionals for Electronic Structure Calculations." arXiv:cond-mat/0106308 (2001). (Cit. on p. 28).
- [SKO4] S. Y. Savrasov and G. Kotliar. "Spectral density functionals for electronic structure calculations." *Phys. Rev. B* 69, 245101 (2004). (Cit. on p. 28).

-
- [SK54] J. C. Slater and G. F. Koster. "Simplified LCAO Method for the Periodic Potential Problem." *Phys. Rev.* 94, 1498 (1954). (Cit. on p. 18).
- [SKA01] S. Y. Savrasov, G. Kotliar, and E. Abrahams. "Correlated electrons in δ -plutonium within a dynamical mean-field picture." *Nature* 410, 793 (2001). (Cit. on p. 28).
- [Sla37] J. C. Slater. "Wave Functions in a Periodic Potential." *Phys. Rev.* 51, 846 (1937). (Cit. on p. 10).
- [SMV01] I. Souza, N. Marzari, and D. Vanderbilt. "Maximally localized Wannier functions for entangled energy bands." *Phys. Rev. B* 65, 035109 (2001). (Cit. on pp. 14–17, 75).
- [SNS00] E. Sjöstedt, L. Nordström, and D. J. Singh. "An alternative way of linearizing the augmented plane-wave method." *Solid State Communications* 114, 15 (2000). (Cit. on p. 11).
- [SQ61] W. Shockley and H. J. Queisser. "Detailed Balance Limit of Efficiency of p-n Junction Solar Cells." 32, 510 (1961). (Cit. on p. 72).
- [Tar+13] C. Taranto, M. Kaltak, N. Parragh, G. Sangiovanni, G. Kresse, A. Toschi, and K. Held. "Comparing quasiparticle GW+DMFT and LDA+DMFT for the test bed material SrVO₃." *Phys. Rev. B* 88, 165119 (2013). (Cit. on p. 40).
- [TKH07] A. Toschi, A. A. Katanin, and K. Held. "Dynamical vertex approximation: A step beyond dynamical mean-field theory." *Phys. Rev. B* 75, 045118 (2007). (Cit. on p. 23).
- [Tom+12] J. M. Tomczak, M. Casula, T. Miyake, F. Aryasetiawan, and S. Biermann. "Combined gw and dynamical mean-field theory: Dynamical screening effects in transition metal oxides." *EPL* 100, 67001 (2012). (Cit. on p. 40).
- [Wan] Wannier Developers' Group. *wannier.org*. URL: <http://www.wannier.org/> (visited on 10/19/2014). (Cit. on p. 15).
- [Wan+15] L. Wang, Y. Li, A. Bera, C. Ma, F. Jin, K. Yuan, W. Yin, A. David, W. Chen, W. Wu, et al. "Device Performance of the Mott Insulator LaVO₃ as a Photovoltaic Material." *Phys. Rev. Applied* 3, 064015 (2015). (Cit. on p. 72).
- [Wan37] G. H. Wannier. "The Structure of Electronic Excitation Levels in Insulating Crystals." *Phys. Rev.* 52, 191 (1937). (Cit. on p. 13).
- [wco6] Z. Wu and R. E. Cohen. "More accurate generalized gradient approximation for solids." *Phys. Rev. B* 73, 235116 (2006). (Cit. on pp. xix, 8).

References

- [WHE14] P. Werner, K. Held, and M. Eckstein. “Role of impact ionization in the thermalization of photoexcited Mott insulators.” *Phys. Rev. B* 90, 235102 (2014). (Cit. on p. 73).
- [Wik15a] Wikipedia contributors. *Atomic theory*. In: *Wikipedia, the free encyclopedia*. Page Version ID: 675381609. 2015. (Cit. on p. vii).
- [Wik15b] Wikipedia contributors. *Matsubara frequency*. In: *Wikipedia, the free encyclopedia*. Page Version ID: 664043995. 2015. (Cit. on p. xviii).
- [Wik15c] Wikipedia contributors. *Shockley–Queisser limit*. In: *Wikipedia, the free encyclopedia*. Page Version ID: 668151093. 2015. (Cit. on p. 72).
- [Wis+12] P. Wissgott, J. Kuneš, A. Toschi, and K. Held. “Dipole matrix element approach versus Peierls approximation for optical conductivity.” *Phys. Rev. B* 85, 205133 (2012). (Cit. on p. 39).
- [Wis12] P. Wissgott. “Transport Properties of Correlated Materials from First Principles.” PhD thesis. Vienna: Technische Universität Wien, 2012. (Cit. on pp. ix, 39, 43, 45, 57, 61, 66).
- [Yat+07] J. R. Yates, X. Wang, D. Vanderbilt, and I. Souza. “Spectral and Fermi surface properties from Wannier interpolation.” *Phys. Rev. B* 75, 195121 (2007). (Cit. on p. 17).
- [Zha+15] S. G. Zhao, A. Gu, X. L. Yan, L. M. Hao, Y. Xie, T. Zhang, and K. X. Jin. “Transport and photoresponse properties in $\text{Pr}_{0.5}\text{Ca}_{0.5}\text{CoO}_3/\text{Nb-SrTiO}_3$ heterostructure.” *EPL* 108, 67007 (2015). (Cit. on p. 72).
- [Zho+15] Z. Zhong, M. Wallerberger, J. M. Tomczak, C. Taranto, N. Parragh, A. Toschi, G. Sangiovanni, and K. Held. “Electronics with Correlated Oxides: $\text{SrVO}_3/\text{SrTiO}_3$ as a Mott Transistor.” *Phys. Rev. Lett.* 114, 246401 (2015). (Cit. on p. 73).
- [zzH13] Z. Zhong, Q. Zhang, and K. Held. “Quantum confinement in perovskite oxide heterostructures: Tight binding instead of a nearly free electron picture.” *Phys. Rev. B* 88, 125401 (2013). (Cit. on p. 81).

Acknowledgements

When you hand in a thesis, you have to sign a statement saying that the work is yours alone, yet all involved know full well you could not have done it on your own. In this spirit, let me thank:

- My advisor, Karsten Held, co-advisor, Giorgio Sangiovanni, as well as the “inofficial advisors” Peter Blaha and Robert Laskowski, for taking me on board, providing me with a juicy project to work on, coming up with the necessary funding and ample travel opportunities, in short: doing all that good thesis advisors should, and teaching me some physics besides.
- Markus Aichhorn, and Karsten once more, for their patience while I wrote this document and various deadlines came and went. Writing this thesis has been as much a lesson in humility concerning my own working speed as anything else.
- Philipp Wissgott, on whose work the second part of this thesis is built. Waltz on, Philipp.
- Markus Wallerberger, Patrik Gunacker, and Giorgio again, for invaluable support in using the w2dynamics code.
- My colleagues in Vienna for all the group meetings, group lunches, group Badminton games and climbing sessions we shared. Out of a big group, let me mention but a few: *Ciro*, *Thomas*, *Zhicheng*, and *Nils*, it was good sharing an office with you.
- My immediate family, *Rita*, *Sophie*, and *Felix*, for putting up with and supporting me this whole time; and many others in the family for their inestimable help with all kinds of things non-scientific.

Yours is a share of the credit, but all errors are mine alone.

Acknowledgements

In addition to helpful people, I have profited from a lot of freely available software. This document was typeset in URW Palladio and Carlito using L^AT_EX, KOMA-Script, and too many packages to name. Graphics were made using gnuplot, VESTA [MI11], TikZ, and Spaghetti Primavera.

Vita

Elias Assmann Born 1985-02-05
married, 2 children (born 2009 and 2010)

Education

- 2011–2015 Ph.D. at Vienna University of Technology
Dissertation: *Spectral Properties of Strongly Correlated Materials* supervised by Profs. Karsten Held (Vienna) and Giorgio Sanguiovanni (Würzburg, Germany)
- 2003–2011 Studies of Physics at Graz University of Technology
Master's thesis: *Quantum Monte Carlo Simulation of the Attractive Hubbard Model in a Harmonic Confining Potential* supervised by Profs. Hans Gerd Evertz (Graz) and Richard T. Scalettar (Davis).
- Mar–Jul 2010 Research stay at University of California, Davis, USA
- 2006 / 2007 Year abroad at Université Joseph Fourier, Grenoble, France
Bachelor's thesis: *Model-Independent Constraints on Extra Neutral Gauge Bosons from the Process $e^- e^+ \rightarrow \mu^- \mu^+$* .
- 2004 / 2005 Suspension of studies for civilian national service
- 1995–2003 Secondary school at Graz International Bilingual School

Publications

- E. Assmann, P. Wissgott, J. Kuneš, A. Toschi, P. Blaha, and K. Held. "woptic: optical conductivity with Wannier functions and adaptive k-mesh refinement." (2015). Submitted.
- S. Löffler, M. Bugnet, N. Gauquelin, S. Lazar, E. Assmann, K. Held, G. A. Botton, and P. Schattschneider. "Real-space mapping of electronic orbitals." (2015). Submitted.
- T. Ribic, E. Assmann, A. Tóth, and K. Held. "Cubic interaction parameters for t_{2g} Wannier orbitals." *Phys. Rev. B* 90, 165105 (2014).

O. Rubel, A. Bokhanchuk, S. J. Ahmed, and E. Assmann. "Unfolding the band structure of disordered solids: From bound states to high-mobility Kane fermions." Phys. Rev. B 90, 115202 (2014). FOLD2BLOCH is available at <https://github.com/rubel175/fold2Bloch>.

E. Assmann, P. Blaha, R. Laskowski, K. Held, S. Okamoto, and G. Sangiovanni. "Oxide Heterostructures for Efficient Solar Cells." Phys. Rev. Lett. 110, 078701 (2013). Selected for a synopsis in *Physics*.

E. Assmann, S. Chiesa, G. G. Batrouni, H. G. Evertz, and R. T. Scalettar. "Superconductivity and charge order of confined Fermi systems." Phys. Rev. B 85, 014509 (2012). Editor's Suggestion.

Presentations

- 2014-10 WIEN2k workshop, Warsaw, Poland
Tutorial: *Correlated electrons, LDA+U, Dynamical Mean-Field Theory, Wannier functions*
- 2014-08 27th International Conference on Low Temperature Physics, Buenos Aires
Poster: *Oxide Heterostructures for Efficient Solar Cells*
- 2014-08 Advanced Topics in Magnetism and Superconductivity, Bariloche, Argentina
Talk: *woptic: Transport Properties For Strongly Correlated Materials*
- 2014-07 Strongly Correlated Electron Systems 2014, Grenoble, France
Poster: *Oxide Heterostructures for Efficient Solar Cells*
- 2014-02 Novel Materials and superconductors, Obertraun, Austria
Poster: *wien2wannier: From Linearized Augmented Plane Waves to Maximally Localized Wannier Functions*
- 2014-02 From Electrons to Phase Transitions, Vienna, Austria
Poster: *wien2wannier: From Linearized Augmented Plane Waves to Maximally Localized Wannier Functions*
- 2013-09 New Thermoelectric Materials, Split, Croatia
Talk: *woptic: Transport Properties with Wannier Functions and Adaptive k-Integration*
- 2013-08 ERC Workshop: Ab Initio Dynamical Vertex Approximation, Vorderstoder, Austria

-
- Talk: *Charge Self-Consistency. Fully self-consistent "DFT+many-body" methods*
- 2013-08 WIEN2013 Workshop, Pennsylvania State University, University Park, USA
Tutorials: *Optical properties; Wannier functions, LDA+U, DMFT*
Invited talk: *Oxide Heterostructures for Efficient Solar Cells*
- 2013-05 Quantum in Complex Matter, Ischia, Italy
Invited talk: *Oxide Heterostructures for Efficient Solar Cells*
- 2013-03 Spring Meeting of the German Physical Society, Regensburg, Germany
Talk: *Oxide Heterostructures for Efficient Solar Cells*
- 2013-02 Novel Materials and Superconductors, Planneralm, Austria
Poster: *woptic: optical conductivity with Wannier functions and adaptive k-mesh refinement*
- 2012-12 ViCoM (Vienna Computational Materials Laboratory) Workshop, Stadtschlaining, Austria
Talk: *Oxide Heterostructures for Solar Cells*
- 2012-10 Correlated Electrons at Surfaces and Interfaces, Würzburg, Germany
Poster: *Oxide Heterostructures for Efficient Solar Cells*
- 2012-05 University of Würzburg, Germany seminar
Talk: *Correlated Heterostructures for Solar Cells*
- 2012-02 vsc (Vienna Scientific Cluster) User Workshop, Neusiedl am See, Austria
Talk: *Realistic Materials Simulations using Dynamical Mean Field Theory*
- 2012-02 Novel Materials and Superconductors 2012, Planneralm, Austria
Talk: *Correlated Heterostructures for Fun and Profit*
- 2011-12 International Conference on Advanced Materials, Coimbatore, India
Talk: *Bulk and Interface Properties of Lanthanum Vanadate*
- 2010-12 Vienna University of Technology seminar
Talk: *The 2D Attractive Hubbard Model in a Trap*